PHUSICOS

According to nature

Deliverable   D4.4

Modelling changing pattern of hazard and risk and identifying the return period of the extreme events that the NBS could safely withstand

Work Package 4 – Technical Innovation to Design a Comprehensive Framework

Deliverable Work Package Leader:
UNINA

Revision: 2
Dissemination level: Public

August 2023

Any dissemination of results must indicate that it reflects only the author's view and that the Agency is not responsible for any use that may be made of the information it contains.

The present document has not yet received final approval from the European Commission and may be subject to changes.

Note about contributors

Lead partner responsible for the deliverable:	UNINA
Deliverable prepared by:	Antonio Pignalosa, Carlo Gerundo, Francesco Pugliese, Giuseppe Speranza, Paolo Budetta, Alfonso Corniello, Marialuce Stanganelli, Francesco De Paola (UNINA)
Partner responsible for quality control:	NGI
Deliverable reviewed by:	Farrokh Nadim
Other contributors:	Nicola Del Seppia, Nicola Coscini (ADBS), Nicola Silvestri (UNIPI), Anders Solheim (NGI), Nellie Sofie Body (NGI), Dieter Issler (NGI), Mari Olsen (Innlandet), Didier Vergés (CTP OPCC); Bjørn Gudleik Kalsnes (NGI); Juan Antonio Ballesteros Canovas (University of Madrid); Séverine Bernardie (BRGM); Santiago Fàbregas (AECT Pirineos-Pyrénées); José Carlos Robredo Sánchez (UPM); Bastien Colas (BRGM); Clar a Levy (BRGM); Marco Luppichini (UNIPI); Claudio Vanneschi (CGT),

Project information

Project period:	1 May 2018 – 30 April 2023
Grant Agreement number:	776681
Web-site:	www.phusicos.eu
Project coordinator:	Norwegian Geotechnical Institute, (NGI)

Project partners:

Summary, synthesis and conclusions

One of the main objectives of the PHUSICOS project is to demonstrate the viability and effectiveness of nature-based solutions (NBS) in reducing the risk associated with different hydro-meteorological hazards. Ideally, the evidence for effectiveness of NBS, or for that matter traditional grey infrastructure solutions, in mitigating the risk should be based on their performance during major events. However, gathering data and evidence from field observations may take several years and decades after the NBS is fully implemented. Many types of NBS need several years before they become fully effective and extreme natural hazard events do not occur frequently. In absence of evidence from performance observations under actual events, one could resort to numerical modelling of the expected performance. Numerical simulations, capable of modelling the impacts of the expected critical events and the performance of the risk mitigating NBS under the applied loads from these scenarios as accurately as possible, can provide insight to the expected performance and effectiveness of the implemented measures.

This deliverable presents the work performed in Task 4.4 (Modelling changing pattern of hazard and risk and identifying the return period of the extreme events that the NBS could safely withstand), which aimed to assess the effectiveness of nature-based solutions (NBS) in reducing risks at the demonstrator cases of the project through numerical simulations. The modelled NBS are those implemented at the Serchio River Basin in Italy and the Pyrenees sites in Spain and France, and the one designed, but not implemented, at Gudbrandsdalen Valley in Norway. The NBS considered and modelled at these sites are quite different and mitigate against very different threats. In all cases, the simulations aimed at producing hazard maps for the threat of interest, with and without NBS implementation. Comparison of the hazard maps for the two situations provides a quantitative measure of the effectiveness of the NBS. Where relevant, simulations were also done for different future climate scenarios.

Demonstrator case: Serchio River Basin, Italy

Location and challenges: The lower part of the Serchio river includes the sub-basin of Lake Massaciuccoli. The lake has a surface area of about 13 km^2 and an average depth of about two metres. Since the beginning of the twentieth century, the territory had a strong agricultural development and urbanization. The basin falls within the Migliarino-San Rossore-Massaciuccoli (MSRM) Natural Park as well as several protected areas of national importance. The Serchio River Basin is critical for the region's access to clean and safe water, and it is essential for the agriculture in the area. The challenges present in the Lake Massaciuccoli sub-basin comprise extreme drought and flooding, soil erosion and water pollution from farmland runoff. Some of these challenges are being exacerbated by climate change, requiring adaptation of the local community, especially in the agriculture sector.

NBS (implemented): The NBS measures implemented as part of the PHUSICOS project focus on mitigating the risk posed by soil erosion and farmland runoff. They comprise vegetated buffer strips (VBSs) and sediment retention basins for water purification, as well as revegetation with multiple vegetation layers, referred to as conservative

agricultures (Cas) to reduce erosion using appropriate native plant species. Two canals have been restructured to improve their drainage and purification capacity.

Numerical modelling – Results and discussion

Numerical simulations were carried out with the Soil & Water Assessment Tool (SWAT+) software package. The modelling was done at very local scale and based on data with very high resolution (20cm × 20cm cell size). The numerical simulations focused on assessing the efficacy of the implemented NBS in mitigating runoff and soil erosion hazard in a flat agricultural area. The NBS performances were assessed both for the present-day climate regime and for future climate change scenarios with mild and strong variations (RCP 4.5 and RCP 8.5, respectively). For each implementation and climatic scenario, modelling was carried out for two study sites having similar crop rotations but different soil textures and organic contents. The results of modelling consisted in 12 different scenarios modelled for both runoff and sediment loss.

The study showed that, in very flat agricultural areas, flow accumulation may occur, especially beside channels and streams. This implies high runoff depths and sediment losses over large areas. The analyses showed that runoff is sensitive to soil texture (fine-grained vs coarse-grained soils) and its organic content. The mitigating effect of NBS for both runoff and soil erosion hazard is higher for moderate rainfall intensities and low organic content. When soils are characterized by high organic content and coarser textures, the runoff strongly depends on the rainfall quantity and intensity. The efficacy of the NBS reduces with very high rainfall intensity. In the study area, future climate scenarios forecast lower rainfall, corresponding to low runoff and soil erosion. However, the mitigating effects of the designed NBS are also strongly reduced. In presence of extreme climatic changes, their effects become negligible.

It should be noted that VBSs and CAs exert their action with different performances on different hazards. Whereas VBSs reduce both runoff and sediment losses, CAs have only a secondary effect on runoff, being much more effective in reducing sediment losses.

In conclusion, the results presented in this deliverable show that numerical modelling is a powerful analysis tool for supporting farmers and stakeholders when setting up sustainable agricultural management and planning with respect to mitigation of the risk posed by runoff and soil erosion. Furthermore, numerical modelling can be considered an effective tool for assessing the effectiveness of up-scaling of VBSs and CAs in wider zones.

Demonstrator case: Gudbrandsdalen Valley, Norway

Location and challenges: The Gudbrandsdalen Valley is one of the most populated rural areas in Norway, extending for roughly 140 km from the town of Lillehammer, in the south, to the village of Dombås, in the north. The wide floodplains extending along the river are extensively designated as farmland, but many scattered residential settlements with public facilities connected by public roads are also available, that sporadically bridge over the river.

The valley and side valleys are exposed to a range of hydro-meteorological hazards, flooding in the main river and in the tributary rivers, debris flows and debris slides, rockfall and snow avalanches.

The river Gausa in Gudbransdalen experiences frequent flooding, with occasional damaging events, such as in 1995, 2011 and 2013 (and most recently in August 2023 during the extreme weather event "Hans"). The lower parts of Gausa at Jorekstad, where the river moves across Gudbrandsdalslågen, is particularly vulnerable to floods since the confluence area between the two rivers has been repeatedly damaged during past flooding events. The return period for floods that can cause significant damage in this area seems to be 8 to 10 years. The floods have been a threat to the agricultural land, as well as housing and public facilities in Jorekstad such as a football pitch with bleachers, an outside pool, a sports centre and a school. Moreover, eroded sediments from Gausa have been depositing in the confluence zone over the years, changing the river bottom form and thereby enhancing the flooding effects.

NBS (proposed): One of the NBS interventions that has been proposed for the Gudbrandsdalen demonstrator case site consists of a receded floor barrier to be implemented in the lower side of Gausa River, a tributary river to Gudbrandsdalslågen, at Jorekstad in the town of Lillehammer. The area where the NBS is supposed to be implemented is a private land in the Lillehammer municipality with a total extension of 7.28 km^2. The planned NBS consists of a receded flood barrier along the lower reaches of the Gausa River having a total length of 2878 m split into three sections of 2682, 133 and 63 m. Given that the floodplain along Gausa has a riparian forest with several endangered species and a valuable biodiversity, the flood barrier was located outside of the forest with the aim to re-establish the natural floodplain processes that have been jeopardized by an existing grey barrier. The planned NBS would reduce the energy of the river Gausa before it conveys into the main river and protected farms and surrounding agricultural lands, as well as urban settlements and public facilities at Jorekstad.

Numerical modelling – Results and discussion

Flood is the major natural hazard threatening the Jorekstad study area and the Gausa River watershed. The methodology applied for flood hazard assessment in the frame of PHUSICOS project allowed generating high-resolution hazard maps of several stream flow conditions, such as flow velocity, flow depth and the extension of the possible flooded areas, for both the baseline and the NBS scenario, at different soil moisture conditions. By running the FLO-2D model, the flooded areas were detected, and the maximum flow depth and the maximum velocity were assessed for each analysed 20 m cell-size of the study area at 2, 5, 10, 20, 25, 50, 100, 200-year return periods.

In average soil moisture conditions, the simulations revealed how the planned NBS was fully effective against flooding caused by rainfall events having a return period shorter or equal to 100 years. Even when 200-year rainfall events occur, the flood barrier would limit the flooded areas and protect the exposed settlements. However, under conditions when the soil is fully saturated, the receded flood barriers would not be effective against rainfall events having a return period greater than 5 years.

Changing the physical features of the designed barrier (increasing the length by 140 m and/or increasing the height by 2 m) did not contribute to enhancing its effectiveness. It is worth noting that raising the earth barrier crown more than 2 m would not be technically and economically feasible since its 2:1 sloped sides would entail a much bigger footprint.

Demonstrator Case: The Pyrenees, Spain and France

Location and challenges: The Pyrenees mountain range separates the Iberian Peninsula from the rest of Europe, stretching more than 430 km between Spain and France and rising higher than 3,400 m in elevation. National parks offer hiking trails over the entire length of the range, while dozens of ski resorts can be found on both sides of the Pyrenees. The mountain roads and ski resorts in the Pyrenees are exposed to impacts of typical hydro-meteorological hazards in mountainous areas, namely rockfalls, landslides, debris flows, flash floods and snow avalanche.

NBS (implemented): The NBS implemented in the French and Spanish Pyrenees in PHUSICOS aimed to mitigate the risk associated with gravity-driven processes in steep terrain. In the French Capet Forest, release of snow avalanches is mitigated with afforestation. Various rockfall and erosion mitigation measures have been installed at two locations along an important road between France and Spain, RD-934 and A-136 in France and Spain, respectively. Both locations are high-risk sites, where rockfalls on the road pose significant threat. At the location in Artouste, France, the release of rocks is mitigated by various wooden- and stone structures to fix individual rocks on the till surface and bedrock ledges with a release potential, all in combination with sustainable forest management. In Santa Elena, on the Spanish side, erosion, shallow instability, and release of rock fall from a steep cut through a glacial till ridge (a terminal moraine) are mitigated with terracing using dry masonry walls and timber gabions. The terraces are planted with local bushes and trees, which eventually will ensure stability also beyond the lifetime of the wooden gabions. The final NBS intervention in the Spanish Pyrenees is at Erill-la-Vall in Catalonia, where debris flows are sourced from thick till deposits, exposed in steep gullies. The implemented measures are again terraces built up by local rocks in combination with wooden gabion structures and planted with local vegetation. The numerical modelling in this study focused on assessing the NBS implemented for mitigating the risk posed rockfalls at Artouste (France) and Santa Elena, Biescas (Spain), and snow avalanche in Forêt du Capet in the French Pyrenees.

Numerical modelling – Results and discussion

a) Rockfalls at Artouste

Within this study, the effect of implemented and planned NBS in mitigating rockfall hazard on the forested slope of Artouste in the Pyrénées-Atlantiques (France) department, where different types of NBS are designed to be integrated with afforestation, are investigated. The existing and planned NBS involve some punctual and areal interventions, affecting a limited area compared to possible rockfall source and propagation areas. They consist of wooden tripods, meshes, and masonry walls designed to fix unstable blocks along the slope. Some passive defence works, such as wooden rockfall barriers, are designed close to some source areas with the aim to intercept falling

rocks before the increase of speed. All those measures are designed to be integrated and coupled with an expected mitigating effect of the forest. The numerical analyses were done with Rockyfor3D software.

Field surveys identified two main volume classes for rockfalls, 0.25 m^3 and 1.0 m^3, associated with 10- and 100-year return periods, respectively.

By integrating forest data with rockfall risk mitigation interventions and different blocks volumes, four different modelling scenarios were distinguished:

- Scenario 1 (S1): baseline with block size 0.25 m3;
- Scenario 2 (S2): baseline with block size 1.00 m3;
- Scenario 3 (S3): NBS with block size 0.25 m3;
- Scenario 4 (S4): NBS with block size 1.00 m3.

The main target of the study was to assess the mitigating effect of NBS in terms of variation of maximum rockfall energies and rebound heights on the slope and, specifically, along the road.

Comparing modelling results of the S1 and S3 scenarios related to blocks of 0.25 m^3, the mitigating effect of coupled NBS and forest is exhibited through a dampening of the highest peak values for both maximum rockfall energy and rebound height. On the other hand, NBS do not significantly affect the average values which are reduced only in few areas directly downslope to the designed wooden rockfall barriers. With such a block size, rockfall energy along the road after NBS implementation ranges between 200 and 500 Kj.

When rock blocks of 1 m^3 are considered, no significant improvements are observed with NBS introduction.

Regarding the maximum energy, no improvements are noted, except for some peaks in very limited areas. The most evident effect is a shift of the highest values of kinetic energy and rebound height, probably due to the deviatoric effect of block-trees impacts. Therefore, the stabilization interventions give a very local contribution, limited to a few areas with small extensions compared to the identified potential rockfall sources; passive defence structures such as wooden rockfall barriers are the most effective for stopping small boulders (volume of less than 0.25 m^3), while they have a marginal effect on blocks with a volume of 1.0 m^3. However, the combination of several orders of overlapping barriers was proven to stop most of the blocks providing a significant mitigation effect.

Based on modelling outputs, the designed interventions are not sufficient to significantly reduce the risk of rockfalls due to the very local effect of some types of NBS, their small spatial distribution, and low adsorption energies of wooden barriers and trees. However, it should be noted that the simulations were implemented by detecting the areas most susceptible to detachment and considering rockfall release from those areas. This means that most of the detached blocks in the numerical simulations were released from steep areas located in the northern part of the study area, far from the implemented NBS, thus

gaining kinetic energy along their path and limiting the benefits of the implemented solutions. In the southern side (where there are few detachment zones with much lower energies), it was proven that the designed NBS allows a shift of the highest values of kinetic energy and rebound height. Only about 50 detachment zones were stabilized out of about a hundred in this slope. Therefore, if all the potential detachment zones in the slope were stabilized with the designed NBS, the effective decrease of reach probability would have been more significant. Based on these considerations, NBS might be considered as an additional solution for dampening the rockfall intensity, limiting the sizing and, thus, the economic and environmental impacts of other grey measures such as steel rockfall barriers.

b) Rockfalls at Santa Elena, Biescas

At the case study site of Santa Elena, Biescas, in Spain, a slope on moraine debris facing one of the most important roads in the area is affected by intense erosion which caused debris denudation and excavation of deep gullies. The erosion of clayey and sandy matrix can provoke the detachment of rock boulders threatening the road users. The detached rock can be of very different sizes since highly heteromeric outcropping blocks characterize the moraine debris.

The NBS designed to tackle this threat mainly consists of slope terracing by means of wooden and masonry structures and subsequent revegetation. A retaining masonry wall is also planned at the slope base. The goal of the numerical modelling done for this site was to verify the effectiveness of the NBS by comparing the modelling results of an NBS scenario with a baseline scenario. Model input data were collected during field campaigns and remote sensing on high-resolution UAV imagery and terrestrial laser-scanning models.

The main target of the assessment was to assess the change in maximum rockfall energy and jump height, because of the mitigative effect of planned NBSs, both on the slope and along the investigated road transect.

Modelling results highlight that rockfalls are characterized by short runout related to the limited slope extension and, consequently, mostly show low energy content. The highest rockfall energy and height are recorded along some gullies in the central part of the slope where blocks channelize. Consequently, also the reaching probability is the highest in these areas. In the current scenario, most of the blocks reach the slope base and the road. The terracing was proven to significantly limit the rockfall hazard since terraces both prevent rockfall detachment and hinder the movement of detached rocks. Consequently, in the most hazardous area, corresponding to the main area of NBS implementation, the rock blocks accumulate on the terraces without reaching the road. In the remaining part of the slope, the largest part of detached rock can reach the slope stop when they impact on retaining wall. In only a few cases, rocks can jump over the wall after dissipating most of their kinetic energy. Therefore, compared to the current scenario, the hazard on the road is highly reduced, and the planned NBS can be considered as an effective approach, showing very few downsides.

c) Snow avalanche at Forêt du Capet

The Midaou catchment in the municipality of Barèges in the Département Hautes-Pyrénées in south-western France is highly susceptible to snow avalanche. The NBS to be implemented at this demo site is afforestation at high altitudes as a protection against release of snow avalanches. To assess the protective effect that can be expected once the forest has established itself, the runout of snow avalanches with return periods in the (estimated) range of 10–300 years were simulated with the NGI numerical model for snow avalanche runout. The results of the numerical modelling showed that both the designed NBS (afforestation of the release area for snow avalanche) and the existing "grey" mitigation measures (terraces and snow bridges in the northern part of the catchment) can effectively reduce the probability of avalanche release from the highest parts of the potential release area. Avalanches could still start at lower altitudes, but they will have lower intensity and shorter runouts. Under extreme conditions like those recorded in 2013 (the snow covering the supporting structures completely and/or being unusually light and cohesionless), the snow avalanche release in the mitigated area upslope might still be possible but involving shallower depths of snow cover.

It is difficult to assign return periods to the simulations because we lack the required meteorological data needed for accurately estimating the return. Nevertheless, the comparison between the estimated runouts of avalanches with and without the "grey" and NBS mitigation measures, but otherwise identical conditions, showed that the hybrid solution is expected to be quite robust and effective.

Concluding Remarks

Effective strategies for mitigating the risk of hydro-meteorological hazards often require a combination of several structural and non-structural measures. NBS can be considered as structural measures with sometimes limited capacity (for mitigating the impacts of extreme events, for example) but also with additional co-benefits in comparison with classical grey measures. Although the co-benefits of the NBS are not modelled and reported in this deliverable, they are described in PHUSICOS Deliverable D2.4: "Nature-based solutions implemented in PHUSICOS".

The numerical modelling of some of the NBS implemented or designed in the PHUSICOS project revealed some of their limitations in mitigating the risk. For example, the NBS implemented in the Serchio River Basin for reducing runoff and erosion from farming are effective under the present climate regime but may not be effective under some of the future climate scenarios. The NBS designed for flood risk mitigation at the Gudbrandsdalen is effective for flooding events with return periods of 100 years or more under normal circumstances. However, under severe soil moisture conditions, the designed NBS loses its efficacy for floods with a return period greater than 5 years. The NBS implemented for rockfall risk mitigation at Artouste has a very local effect and should be scaled up to many other locations in the area to make a significant reduction of rockfall risk. On the other hand, the NBS implemented at Santa Elena is very effective in reducing the rockfall risk under the scenarios analysed. Likewise, the NBS implemented for mitigation of snow avalanche risk at Forêt du Capet

is effective for the scenarios analysed, even under extreme conditions like when the snow covers the supporting structures completely.

Given both the local extent of some of the NBS implemented in the frame of PHUSICOS project and the timeframe required to experimentally assess their benefits, numerical modelling can be utilised as a viable and complementary approach to the field investigations for the targeted up-scaling and replicability of the investigated solutions. It should be noted there the results of the numerical modelling presented in this deliverable may include significant uncertainty. The sources of the uncertainty are the variability of the input parameters used in the analyses, assumptions made about the boundary conditions and load scenarios, as well as modelling uncertainty. The analyses presented in this deliverable were based on the best estimates of the input parameters and realistic assumptions regarding boundary conditions and external loads. A probabilistic approach where the uncertainties are explicitly addressed and modelled would help identify the most sensitive parameters for each case and improve the understanding of the effectiveness, or lack thereof, of the implemented NBS.

The numerical simulations presented in this deliverable demonstrate that if disaster risk reduction is the main goal, few nature-based or grey solutions can be universal and work in all situations. In some situations, like the case of snow avalanche at Forêt du Capet, a hybrid combination of NBS and grey infrastructure is the most effective risk mitigation measure. A well-designed hybrid combination of green and grey measures, representing a relevant trade-off between the engineering needs to reduce the negative impacts of natural hazards and the co-benefits related to the NBS, could be the optimal solution in many situations. Numerical modelling is a tool which is useful for decision-makers, who ultimately are responsible for reducing the risk to communities while at the same time will also need to consider the role co-benefits of NBS may have concerning nature, biodiversity and improving the quality of life of local populations.

Contents

Introduction

PHUSICOS, meaning 'According to nature', in Greek φυσικός, is a 5-year Innovation Action project started in May 2018 and funded by the European Union's Horizon 2020 research and innovation programme (Grant agreement No. 776681). The project consortium involves 15 organizations from 7 countries (Norway, Germany, Austria, Italy, France, Spain and Switzerland) and includes end-user partners from local and regional administrative units.

The main aim of PHUSICOS is to assess with a multi-disciplinary comprehensive approach the effectiveness of nature-based or nature-inspired solutions (NBSs) in limiting the natural hazards induced by extreme weather events in mountainous and rural areas. PHUSICOS's underlying premise is that nature itself is a source of ideas and solutions for mitigating the risk caused by changing climate. As nature's designs are often elegant, effective and frugal, implementing NBSs, including hybrid green/blue/-grey infrastructure, can provide ecological, social and economic resilience for society.

Task 4.4 (Modelling changing pattern of hazard and risk and identifying the return period of the extreme events that the NBS could safely withstand) aims to assess the effectiveness of nature-based solutions (NBS) in reducing risks at the three demonstrator cases of the project, namely the Serchio River Basin, the Gudbrandsdalen Valley and the Pyrenees sites. This is done by implementing numerical modelling and analyses to produce the hazard maps for threats of interest, with and without NBS implementation, and for different climatic scenarios.

In the frame of PHUSICOS project, reducing the risk associated with different natural hazards using NBS is assessed in different countries and varying geological, morphological, and hydrological settings. The aim is to evaluate and monitor the NBS effectiveness from different viewpoints, ranging from social, environmental and economic benefits and losses to technical feasibility and effectiveness. In the Task 4.1 of the project, a comprehensive framework for NBS assessment was developed to support governance in the decision-making processes (Deliverable D4.1; Autuori et al., 2019). Some key indicators included in the assessment framework tool are linked to the effectiveness of NBS in hazard and risk reduction, in terms of both reduction of areas affected by a natural phenomenon and reduction of its intensity in a defined area.

According to UNDRR (2020), constitutive components of risk are the hazard, which is related to the dynamics and probability of occurrence of a dangerous natural phenomenon, the exposure, the vulnerability, and the (coping) capacity of the elements at risk, which are in turn related to human assets and exposed activities. Therefore, when the mitigation interventions are oriented to reduce the intensity of natural phenomena or their frequency of occurrence, without intervening on exposed assets, then risk reduction is strictly related to hazard reduction. For these reasons, the modelling described in this deliverable is oriented to the hazard assessment, which represents the main risk component affected by NBS interventions.

The assessment of the effectiveness of mitigation measures against natural hazards, from a technical perspective, is often pursued through the proper modelling of the hazard scenarios before and after the measure's implementation. The comparison of modelling results for different scenarios allows evaluating the change in hazard and risk patterns as a result of both the implementation of mitigation measures and the residual risk associated to the post-operam scenario. Moreover, starting from the same initial configuration (baseline scenario, S0), different countermeasures among grey solutions and NBS can be modelled to compare their effects on hazard reduction, providing further relevant inputs for stakeholders involved in the decision-making processes.

When the natural phenomena that pose the risk are strongly linked to weather events (e.g. rainfalls, snowfalls, temperature), the comparison of results from the hazard modelling developed for different climatic scenarios represents an effective approach to assess the effectiveness of mitigation interventions also against the impacts of climate change.

The study of the NBS effectiveness in a changing climate can be tackled with different approaches depending on both the type of meteorological event set as model input (single event or hydrological annuities, etc.) and the related return period. Taking flood risk as an example, the approach chosen for the assessment of climate change effects varies depending on whether hydraulic modelling is linked to a single meteorological event, lasting a few hours up to a few days, or whether soil erosion is modelled based on the plant growth cycle, thus considering a full solar or hydrological year. The approach also depends on the NBS measure and on the possible setting of defined operational thresholds. For example, when the events determining the threshold achievement in the future climatic scenarios are investigated for NBS designed for protection of riverbanks and basins for flood expansion, defining the related critical return period could be challenging. On the other hand, NBS not characterized by a defined operational limit are quite different, e.g., with some solutions designed to prevent soil erosion (agricultural best practice management, vegetated filter strips, or conservative agricultural techniques), or reforestation interventions. In such cases, NBS continue to exert their actions, although the effectiveness reduces gradually with the intensity of the triggering cause.

In cases where definition of a critical threshold is not relevant, the NBS effectiveness under changing climate scenarios is evaluated through modelling scenarios with extreme climatic conditions occurring in a distant future.

The modelling approach also varies according to the scale of the assessment, generally moving from physically based models for detailed-scale analysis, to more empirical or heuristic approaches for catchment- or regional-scale ones.

The choice of the most appropriate model also depends on the quantity and quality of data available or achievable, compared with the different data demands of the models. The choice of the methodological approach for hazard modelling should thus take its first steps from a preliminary overall assessment of the scenario to deal with, considering

the requirements related to the natural hazards to be modelled, to the features of the hypothesized countermeasure (NBS in this case), considering the morphological, geological and hydrological scenario, and the causes that trigger the hazardous phenomena, the scale of assessments and the data availability (Aleotti and Chowdhury, 1999a; Chung and Fabbri, 1999; Fell et al., 2008; Hervás and Bobrowsky, 2009; Hungr, 2018; I Pérez-Rey, 2019; van Westen et al., 2006; Volkwein et al., 2011).

For these reasons, before proceeding with the adoption of a specific model, a general framework is developed to set the modelling workflow that can address the choice towards the optimal approach, according to the above-mentioned different aspects. One of the preliminary steps of the implemented modelling activities was first to perform a scenario analysis for each demonstrator case, starting from a general methodological framework, and then to differentiate the modelling technique depending on the features of each demonstrator case. For each demonstrator case and approach typology, the future climate scenario was then chosen to test the effectiveness of NBSs, also considering the climate change.

The next steps concern the modelling through approaches adapted to each demonstrator case, according to the considered NBSs, and choosing the most appropriate scale of the analysis which best fits the effects of the adopted measure.

Modelling and analysis were thus carried out to generate, for each demonstrator case, hazard or susceptibility maps, at varying the climatic scenarios and the NBS implemented, e.g. at the ante-operam baseline scenario (S0), and at the post-operam one (S1). The aim was to estimate some technical key indicators to be integrated into the comprehensive framework assessment tool developed in the frame of Task 4.1 of PHUSICOS project.

1   General Methodological Framework

1.1   Analysis of the modelling scenario

The modelling scenario of each demonstrator case was based on a decision-making process guided by a general methodological framework (Figure 1) considering the different categories of aspects influencing the hazard modelling. The first step of modelling is the scenario at each demonstrator case carried out by the site owners supported by local consultants. This was possible using a multidisciplinary approach for the analysis of the geological and geomorphological settings, the geotechnical characterization of the geological units affected by the phenomenon, and thus developing hydrological and hydraulic analyses. In this way, the aspects characterizing the evolution of a phenomenon were defined as follows: 1) the type of phenomenon; 2) the dimensional parameters (such as volume, runout distance, flood height, etc.); 3) the areal extension of the zones affected by the hazardous event; 4) the possible triggering causes; and 5) the possible relationships between the latter and the climatic events. The "Hazard Scenario" (Figure 1) was then set, representing the fundamental factor to implement the modelling scenario. The Hazard Scenario is also the core of the subsequent design stages of suitable countermeasures (the "NBSs' Design" in this case) to set the modelling scale. The latter represents the scale of both the phenomena and the implementation of NBS (here referred to as "Scale of Assessment"), and the approach to be used in the assessment of the effects of climate change (here defined as the "Climate Approach"). The elements of the methodological approach, based on a flow of decision-making processes, were thus outlined. They represent the starting point of several choices which led, for each demonstrator case, to the modelling approaches and techniques to be used for 1) the S0, for the definition of the baseline hazard or susceptibility; and 2) the NBS implementation scenario under climate conditions and considering the climate change, for the definition of the residual hazard or susceptibility.
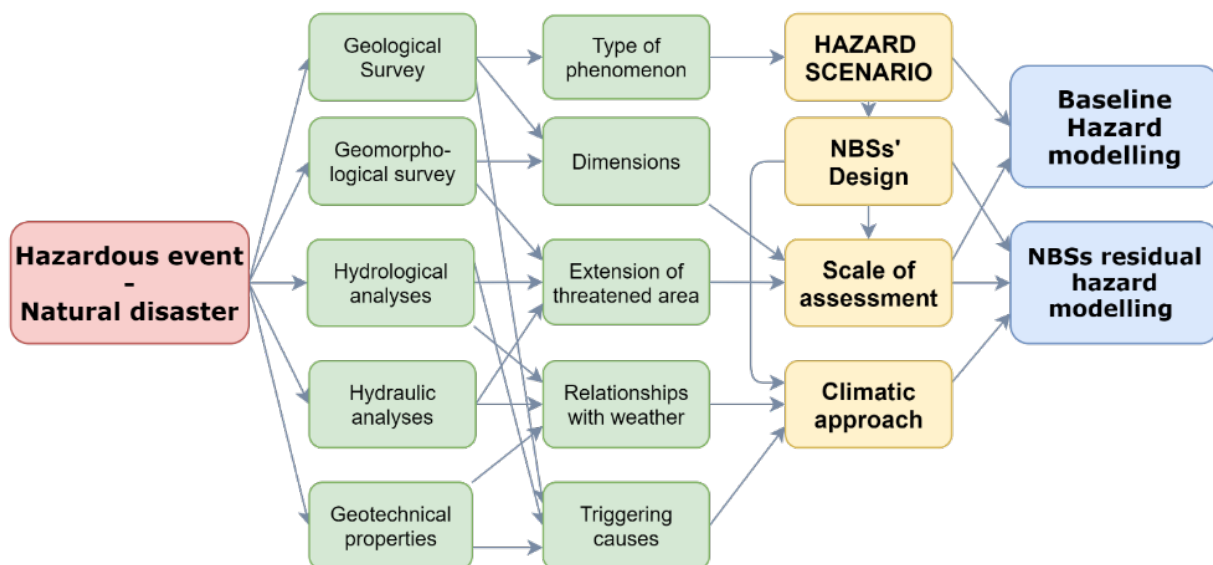

Figure 1: General scheme for the definition of the modelling scenario.

Among the primary components of the main structure of the methodological framework, highlighted in Figure 1 with yellow colour, the first, and probably the most relevant for choosing the modelling approach, is the Hazard Scenario. Indeed, the selection of the modelling approaches depends on the possibility that the phenomenon analysed may also propagate to distant areas. If so, the modelling must be oriented to both the onset of the hazardous phenomenon (onset hazard) and its propagation, where the latter defines the reach probability (propagation hazard). The structure, used in the decision-making process that leads to the choice of the most suitable approach against the hazard scenario, is sketched in Figure 2.

To deal with modelling of the hazard onset, the triggering causes of the event (meteorological, seismic events, etc.) need specific attention. Indeed, if they are unknown, to reach the proper definition of the hazard, at least the intensities (runout, volume, flood height etc.) of a sufficient number of previous events need to be inventoried to define the occurrence probability for a given intensity and thus the related hazard class (Aleotti and Chowdhury, 1999b; Hervás and Bobrowsky, 2009; Hungr, 2018; Volpi, 2019). With unknown causes and lack of historical data, just an intensity zoning, without reference to time scales can be defined as an onset susceptibility (Chung and Fabbri, 2008, 1999; Guzzetti et al., 2006, 2005).
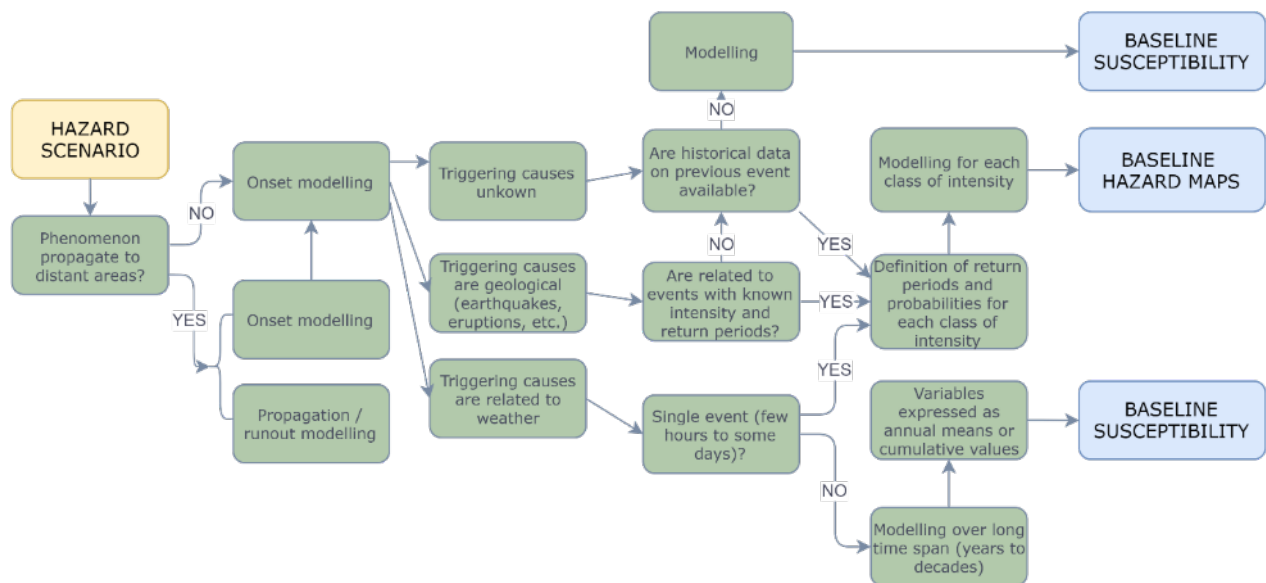

Figure 2: decision-making process at the base of methodological framework focusing on triggering causes and propagation dynamics.

When the trigger is related to geological events (earthquakes, eruptions, collapses, etc.), distinguishing between causes with undefined return period and those with defined return period (e. g. earthquakes) is required. In the former case, it is necessary to fall back again to the inventory of possible events and, if absent, to move forward with the susceptibility modelling. In the latter case, however, it is possible to establish the relationship between intensity and probability of occurrence and then to perform the hazard modelling.

When triggering causes are related to climatic events (storms, droughts, etc.), distinguishing between phenomena linked to single events, with short duration and high intensity (e. g. periods of intense rainfalls), usually characterized by predictable return periods, or linked to long-lasting events (seasons or even years) is needed, instead. In the first case, again, the relationship between intensity and probability of occurrence could be defined and thus the hazard modelling can be performed. In the second case, it is possible to exclusively account for the intensity of the phenomenon, as a function of variables expressed as annual averages and/or as cumulative values and, eventually, evaluate trends over several years. In this case, it is not possible to refer to the probability and therefore to the hazard. The modelling is thus exclusively oriented to susceptibility.

The modelling approach is also based on the right choice of the scale of assessment which is in turn linked to the scale at which the studied phenomena exert their action. If the hazardous phenomenon impacts over small areas (slopes, valleys etc.), it could be feasible to carry out survey campaigns to get geological, topographical, environmental, geotechnical and local weather data required for the detailed analysis at larger scale. In such case, physically based, site-specific geotechnical or kinematical models may be applied, and detailed analysis may be developed by applying either deterministic or probabilistic approaches.

On the other hand, if the impact scale of the hazardous phenomenon is large (catchments, regions, countries), or if the NBS implementation is upscaled to large areas, then the modelling should be oriented to comparable scales. This proves the difficulty to get detailed information on such extensive ranges. In this case, a certain degree of simplification and a lower degree of resolution must be accepted. Therefore, the choice is mainly oriented towards empirical heuristic models or geostatistical ones.
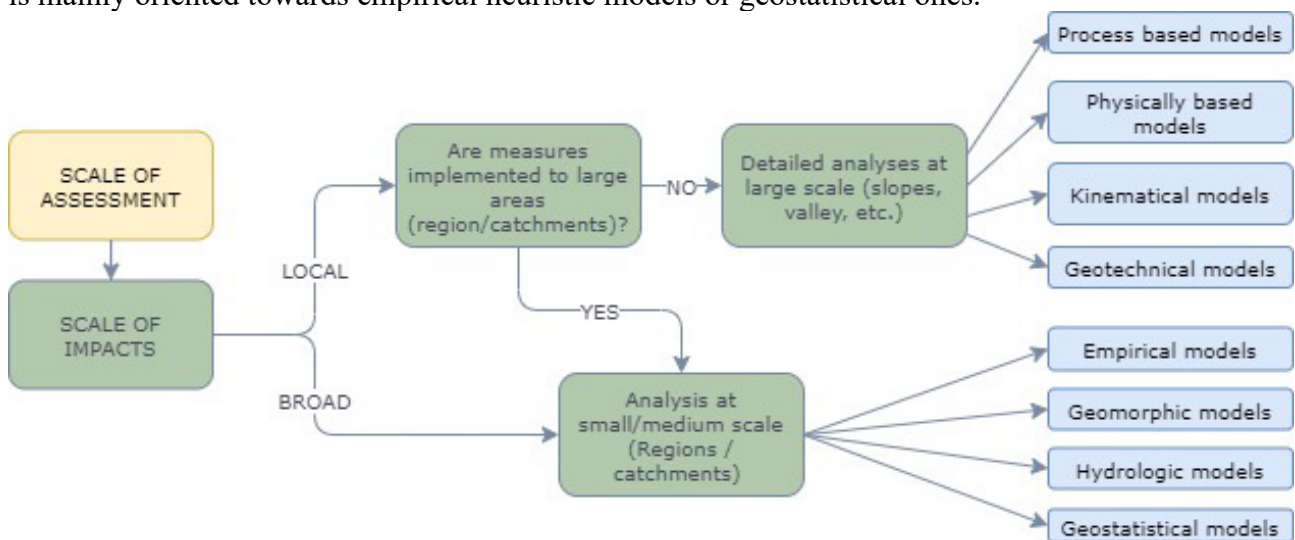

Figure 3. decision-making process at the base of methodological framework focusing on the scale of assessment.

Another fundamental element of the general methodological approach is the climatic scenario to be accounted for modelling the residual hazard after the NBS implementation

(Figure 4). Of course, this aspect is applied only to hazardous phenomena whose triggering causes are strictly related to weather conditions.

In such cases, the first step is to identify the most suitable climate change forecasting model (General Circulation Models, GCM) for the studied area which could be defined, for instance, by comparing historical data from local weather stations with those modelled by different downscaled GCMs (Ahmed et al., 2013; Ashraf Vaghefi et al., 2017; Chen et al., 2011; Corte-Real et al., 1995; Hempel et al., 2013; Pierce et al., 2013; Schmidli et al., 2006; Wilby and Wigley, 2016). Differences between weather station data and modelled historical data could be then applied to overcome bias and calibrate the most suitable GCM based on local data (Ashraf Vaghefi et al., 2017; Hempel et al., 2013; Ines and Hansen, 2006). Once the most suitable GCM is selected, and eventually downscaled and bias corrected, the climatic scenarios are simulated (e.g. RCP IPCC 4.5 and 8.5, Clarke L. et al., 2007; Meinshausen et al., 2011; Moss et al., 2008, 2010; Rao and Riahi, 2006).
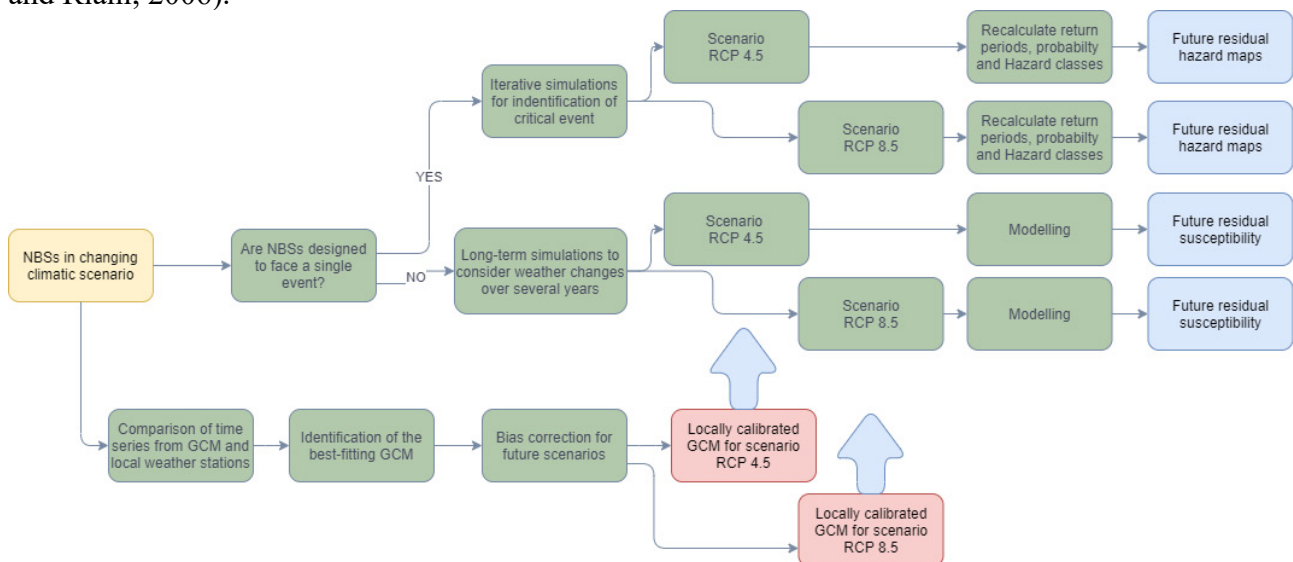

Figure 4: Decision-making process at the base of methodological framework focusing on the scale of assessment.

Once the most suitable climatic model and scenario have been selected for the demonstrator case, the next step is to define the type of event the NBS are designed to deal with. The modelling approach adopted depends on whether NBS are designed to face a single critical event (such as a period of intense rainfall) or if their mitigation action should be effective over long periods. In the first case, the effectiveness of NBS for different climate change scenarios can be based on the detection of the critical event in the modelled future climate which could allow recalculating the return period and the probability to define the residual hazard after the NBS implementation (Peres and Cancelliere, 2018, 2016). If long periods and seasonal trends need to be considered, then the appropriate approach is to carry out new simulations in distant future period, considering the selected GCM and scenario (Ashraf Vaghefi et al., 2017). This approach

makes it possible to run new modelling for assessing the future residual susceptibility after the NBS implementation.

2 Hazard and Susceptibility modelling at Serchio River Basin, Italy

2.1 Case study

The demonstrator case study site of the Serchio River Basin is located in the westernmost part of the river catchment, few kilometres to the north of the river outlet and to the south of the Massaciuccoli Lake. Here, one of the most important residual marshy areas of Italy was partially reclaimed in the 1920s, in favour of two large agricultural areas: the Vecchiano to the south-west and Massaciuccoli reclamation areas, to the south-east (Brunelli G. and Cannicci G., 1942; Cenni M., 1997). The area has then turned to a flat agricultural plain mechanically drained by a network of artificial channels. Drainage is guaranteed by a series of pumping stations, which in turn pump water toward either the lake or the agricultural plain, depending on the irrigation needs and rainfall regimes, in order to keep the water table depth suitable for cultivation.

The reclamation areas are characterized by fluvial to lacustrine surficial deposits ranging from silty clays to the south, which gradually change to sands moving to north. The organic content increases remarkably when approaching the lake, ranging from <3% in the southern part to up to 55% close to the southernmost lake embankments (Figure 5).

The growing industrial agricultural activities in the area, starting from 1970s with the increasing use of fertilizers and pesticides, caused an exponential increase of nutrient content in the lake, which suffered eutrophication, essentially due to nitrogen and phosphorus compounds losses (Brunelli G. and Cannicci G., 1942; Cenni M., 1997; Pistocchi et al., 2012; Silvestri et al., 2017).
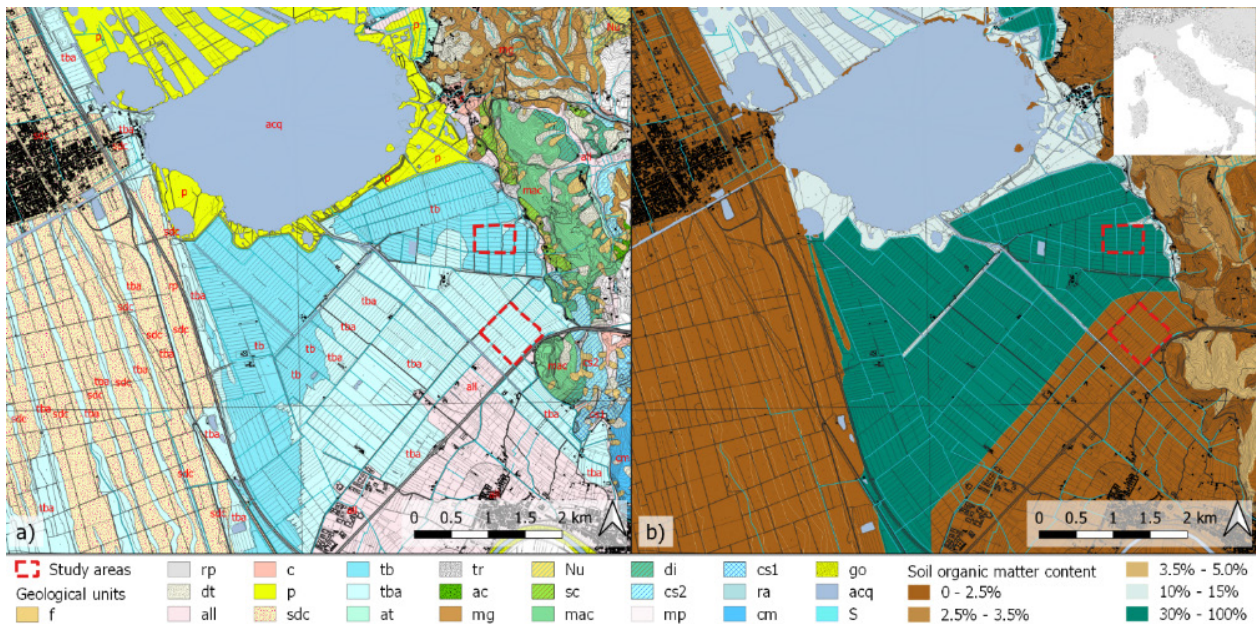
Figure 5: Geological and pedological inset of study areas: a) geological map of the study area ("A.B.D.A.S.," 2006) b) pedological map of the study area reporting the soil organic content as percentage ("Regione Toscana - SITA: Database Pedologico," n.d.). f - landslide deposits, rp – backfill, dt – slope debris, all – alluvial deposits, c – conoid deposits, p – lacustrine deposits, sdc – coastal dune sands, tb – peaty deposits, tba – peaty-clayey deposits, at – terraced alluvial deposits, tr – recent (quaternary deposits), ac – limestones and clays of Canetolo Unit (Auctt.), mg – turbitidic sandstones and siltites of Macigno Fm (auctt.), Nu – Nummulites breccias, sc – marly limestone of the Scaglia Rossa Fm., mac – marly limestones of the Maiolica Fm, di – jaspers, cs2 – dark grey limestone with black flints, mp – marls with Posidonomya, cs1 – light grey limestones with light flints, ra – reddish limestones of the Rosso Ammonitico Fm, cm – massive limestones of the Calcare Massiccio Fm, go – floodplain alluvial deposits, acq – waterbodies, S – Serchio river path.

The reclamation activity in the area also resulted in the depression of the water table over the whole agricultural plain, especially with respect to the surrounding hilly areas to the east and the coastal dune area to the west, which induced hazard for salinization and contamination due to lake embankment seepage (Pistocchi et al., 2012; Rossetto et al., 2010). The depression of water table in turn resulted in the soil compaction and, consequently, in the enhanced subsidence of the entire agricultural area, which dropped up to 3 m below the sea level (Baldaccini, 2018). Currently, the crop lands elevation is also below the height of the main drainage channels resulting in a locally inverted topography.
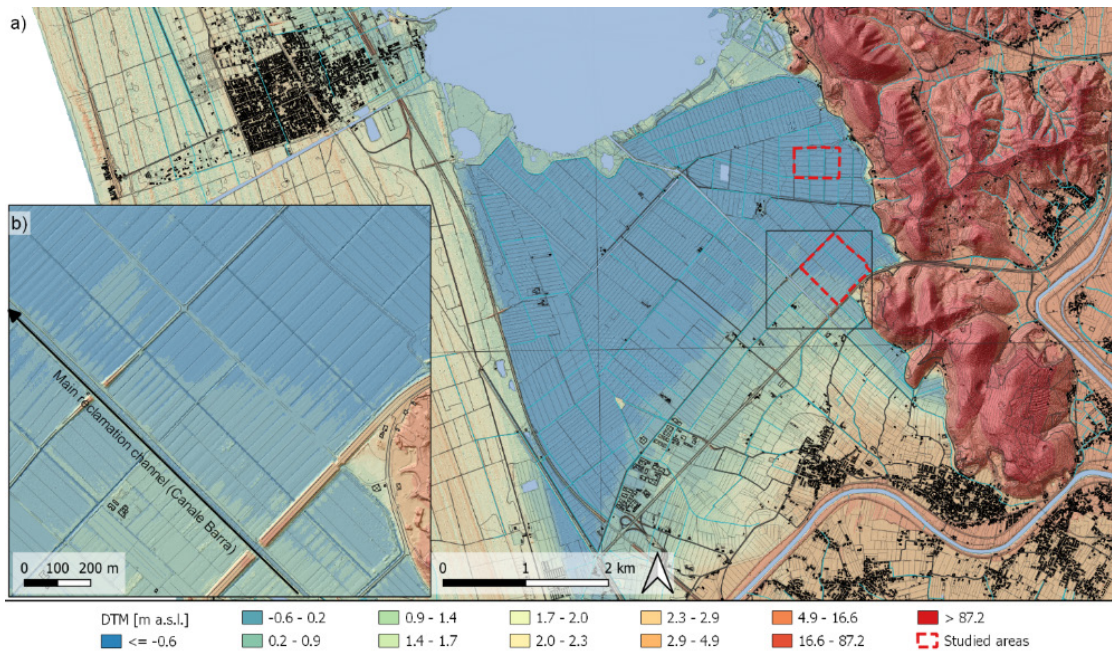
Figure 6 Digital terrain models with a cell size = 1m² representing elevation with false color ramp: a) enlarged view to the whole reclamation area; b) zoom at field scale pointing out the depression of the agricultural land with respect to the main draining channel ("Canale Barra")

The combined impacts of water table depression, land subsidence and conventional industrial agriculture resulted in various hazardous phenomena, ranging from ground and surficial water pollution to soil erosion and flooding, which are threating the area with its resources and inhabitants, resulting in a complex ad extended risk-exposed area.

2.2   NBS Design

Local authorities led by Autorità del Bacino del Serchio (ADBS) were engaged in addressing all these risks through the implementation of NBS measures throughout the whole basin. In the study area NBS implemented in the frame of PHUSICOS project ("PHUSICOS R&D project - Horizon 2020," 2019) are mainly aimed at reducing nutrient losses through reduction of sediment transport and runoff.

NBS were implemented in two study areas, namely the Studiati area to the north and the Gioia area to the south, in the Massaciuccoli reclamation area. They consist in: 1) vegetated buffer strips (VBS), that is in band of grassing with perennial species along the edges of some cultivated fields; 2) adoption of techniques of conservative agriculture (CA), by implementing winter cover crops and gentle tillage (Silvestri et al., 2017); 3) the excavation of a sediment retention basin.

2.2.1   Scale of assessment

In the frame of PHUSICOS project, VBSs and CAs were implemented at plot scale on the Studiati and Gioia areas (Figure 7) which are $19.9´10^4\,\text{m}^2$ and $36.7´10^4\,\text{m}^2$ wide,

respectively. Each area encompasses 33 and 39 different plots, respectively, with individual extension ranging from ~5000 m² to ~11000 m². In the Studiati area, both VBSs and CAs were implemented on 14 plots, with just 3 of them intersected by combining both measures (Fig 7a). This resulted in a cumulative area of $7.7´10^4$ m² intersected by CAs and a cumulative one of $6.0´10^4$ m² draining towards VBSs, corresponding to the 38.7% and the 30.1% of the whole area, respectively. As in the previous case, also in the Gioia area VBSs and CAs were implemented on 14 plots with just 2 plots interested by the combination of both measures (Fig 7b). The resulting cumulative area intersected by CAs is $13.0´10^4$ m² and the cumulative area draining towards VBSs is $11.6´10^4$ m², corresponding to the 35.4% and 31.6% of the whole areas, respectively.
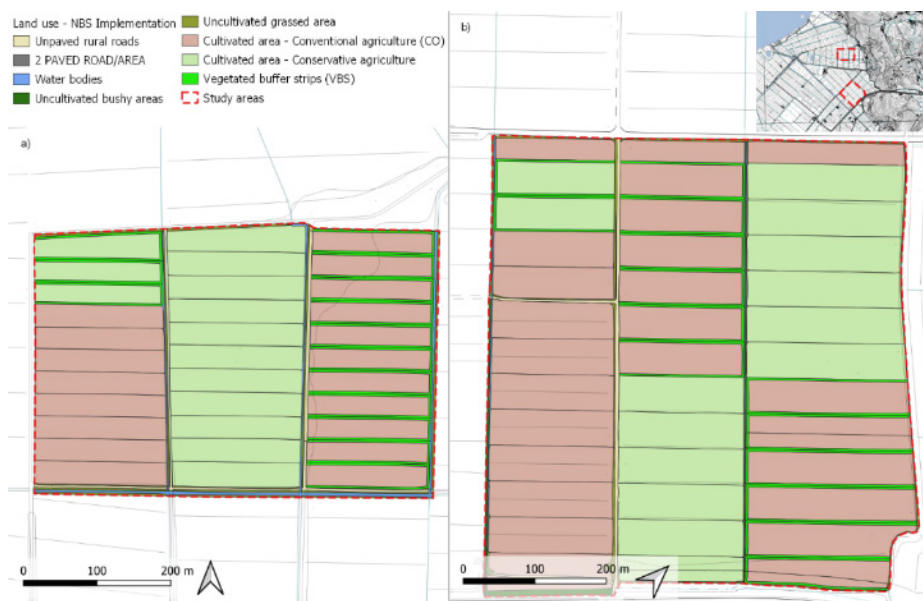

Figure 7: Land use map reporting the layout of the NBS designed for the a) "Studiati" and b) "Gioia" study areas.

Runoff and soil erosion occurring in the two areas of the demonstrator case are directed toward the artificial drainage network, consisting of reclamation channels. They are a sub-part of a more extended draining area with catchments of $1.0´10^6$ m² and $2.0´10^6$ m² measured uphill to the outlet points of the Studiati and Gioia areas, respectively. The study areas thus represent only a minor rate of the relative sub-catchments, corresponding to 20% and 18% for the Studiati and the Gioia area, respectively. In summary, considering both basins together, the NBS designed in the frame of the PHUSICOS project are implemented on a small portion of the cultivated area, <7% for the CAs and <6% for the VBSs. For these reasons, considering the ratios between areas of the sub-basins and the areas influenced by the NBSs, the NBS are expected to exert their action only at local scale, e.g. scale of the single plot to scale of individual study areas, thus having a negligible footprint even at the sub-basin scale. Nevertheless, considering that both CAs and VBSs were suitable for upscaling to the whole basin, the modelling approach can be considered suitable for application at different scales.

2.2.2   Triggering causes

Runoff and sediment loss, in temperate areas, are mostly triggered by rainfalls (Linsley, 1967; Peel and McMahon, 2020); many other predisposing factors affecting runoff and soil erosion are also known, the most relevant of which are soil properties, organic content, land cover and land use, slope angle, slope length, and agricultural and conservation practices (Arnaez et al., 2007; Bryan and Poesen, 1989; Dodd and Sharpley, 2016; Githui et al., 2009; Kinnell and Risse, 1998; Lasanta et al., 2000; Liu et al., 2000; Loague, 1992; Nasta et al., 2017; Ruiz-Colmenero et al., 2013; Sajikumar and Remya, 2015; Saxton and Rawls, 2006; Shanshan et al., 2018; Sharpley, 1985; Tuppad et al., 2010; Wallace et al., 2017; Williams, 1975). In agricultural areas, where annual crops are the most widespread practices, the stage of plant growth strongly affects the rainfall/runoff ratios (Burkart, 2010) and consequently the soil erosion. Hazard modelling should thus consider a time interval covering the entire plant lifecycle to properly account for the different plant growth stages when different rainfall events occur. On the other hand, to include the effects of short-term rainfalls, time sampling should be accurate enough to reproduce each single event.

2.2.3   Climatic approach

The approach used for assessing climate change impacts on the effectiveness of implemented NBS considered 1) that NBS are designed to exert their action over long periods and at varying the intensity of climatic events; 2) that NBS implemented do not have a defined critical operating threshold. Therefore, the criteria to be used in modelling should consider long periods of time in extreme future weather conditions, hence over a long-term period.

The type of climatic events considered (seasonal trends) and the characteristics of NBS implemented allow for neither the definition of a critical event to be used in the modelling nor the estimation of a critical return period. Therefore, the concept of probability is not applicable and the assessment was oriented essentially to the definition of susceptibility before the NBS implementation (baseline scenario S0), (a) in current climatic condition; and the residual susceptibility with the implementation of NBS (scenario S1), (b) in current climatic conditions, (c) in climate change scenarios with mild climatic variations (RCP 4.5); (d) in climate change scenarios with significant climatic variations (RCP 8.5). Furthermore, to consider long-term climatic variations, the simulations considered the furthest period available with GCM and climatic scenarios (years up to 2100).

2.3   Methods

2.3.1   Introduction to modelling approach

Modelling of runoff and sediment loss in the Massaciuccoli agricultural area was based on the hazard scenarios defined above and took into account the different aspects stated in the previous sections, such as the capability: 1) to deal with almost flat morphologies

and agricultural areas; 2) to allow assessments at local scale (plot to agricultural field scale); 3) to simulate effects of weather conditions over time intervals compatible with annual crops' lifecycles (seasons to years); and 4) to spatialize the results for the production of output maps.

Many models are available in the literature focusing on runoff and soil erosion working at different scales and with different approaches ranging from fully empirical models (e.g. Ghosal and das Bhattacharya, 2020; Renard et al., 1991) to physically-based models for soil erosion and water runoff (Abu-Zreig et al., 2001; Arnold et al., 2012; Bieger et al., 2017; Gassman et al., 2014; Shrestha et al., 2021) up to physically-based models directly simulating pollutant runoff (OECD, 2000; Probst et al., 2005; Stehle et al., 2016). In Table 1, the main strengths and limitations are synthesized for 4 different soils and water assessment models applied worldwide. All four models are able to consider the implementation of NBS such as VBSs and CAs. Among these, the simplest models are based on the Revised Universal Soil Loss Equation (RUSLE, Ghosal and das Bhattacharya, 2020; Renard et al., 1991), as they need lower site-specific data than others. However, they can only model soil loss and do not provide any information about runoff. Furthermore, they are designed to be used at regional to watershed scales with no knowledge of applications at larger scales. Results of such models are very sensitive to slope morphology, especially in terms slope steepness (Renard et al., 1991), thus having a few applicability to flat areas.

Table 1 Comparison of different runoff and soil erosion models

Model	Advantages	Disadvantages
RUSLE (M)	• Simple • Few data • Soil assessment	• No studies at very local scales • Strong dependance on slope (not working in flat areas) • No water runoff
SWAT (S, M, M, D)	• Soil and runoff assessment • N/P and Pesticide transport assessment • Studies at local scales (White and Arnold, 2009) • Studies il agricultural flat areas (Donmez et al., 2020) • GIS based 2D spatial assessment • Climate change effects assessment • Possibility to implement VBS	• Highly data demanding on Soil, Land-use, Climate • Need hydrological consistent DTMs • High computational requirements
VFSMOD (S, M, M)	• Strong fitting of modeled with measured data • Strong support literature • N/P and Pesticide transport assessment • Studies at design/plot scales • Very focused on VBS	• Very high data demanding Soils, hydrogeology, hydrology • Single storm event modelling • Mono-dimensional modelling • Difficulties to spatialize the assessment
REXTOX (S, M, D)	• N/P and Pesticide transport assessment • Studies at local scales (Stehle et al., 2016) • GIS based 2D spatial assessment • VBS effectiveness assessment	• Single storm event modelling • No sediment transportation

The NBSs' effectiveness was successfully modelled by VSFMOD (Abu-Zreig et al., 2001; Munoz-Caprina et al., 1992), given the significantly reliable results especially when modelling concentrated flows across VBSs (Abu-Zreig et al., 2001). The model is also able to directly simulate the transport of chemical compounds such as pesticides and nutrients. On the other hand, it is specifically focused on VBSs and it cannot reproduce the effects of different mitigation measures such as CA. It is significantly high-data demanding, especially for large-scale applications (Abu-Zreig et al., 2001; Gericke et al., 2020; Munoz-Caprina et al., 1992). Moreover, it is implemented to work with single short-term rainfall events represented by inflow hydrographs. With reference to dimensionality, it does not satisfy requirement of the methodological approach since it allows only for one-dimensional simulations, without considering the interactions in space and time (Rouzies et al., 2019). Therefore, it is not appropriate for multi-dimensional spatial assessment. Process-based chemical transport models, such as REXTOX (OECD, 2000; Probst et al., 2005), were successfully applied to evaluate the spatial distribution of pesticides and nutrient transport at field scales (e.g. Stehle et al., 2016). However, they are also designed to simulate individual rainfall events and do not simulate sediment transportation. SWAT+ (Bieger et al., 2017; Dile et al., 2016; Gassman et al., 2014) is a fully revised version of SWAT (Arnold et al., 2012; Gassman et al., 2014; Tan et al., 2020), that adopts a comprehensive modelling approach. There is an extensive supporting literature about applications of SWAT with many examples at different scales, including field scales (Karki et al., 2020; Sinnathamby et al., 2017) and flat agricultural areas (Bosch et al., 2004; Donmez et al., 2020). The model was especially used to assess the effects of mitigation measure such as VBS and CA (Arabi et al., 2008; Himanshu et al., 2019; Merriman et al., 2018; Phomcha et al., 2012; Ullrich and Volk, 2009; White and Arnold, 2009). Moreover, it is designed to be fully integrated in qGIS software (QGIS.org, 2021) since input data, as well as outputs, are in the form of maps. Further advantages of SWAT+ are the capability to provide estimation of runoff and sediment loss streamflow estimations, as a result of runoff and lateral flow (Arnold and Allen, 1999; Zhao et al., 2013). Moreover, it's able to simulate over long periods (many years) but using a daily time step (Arnold et al., 2012, 1998), which makes it suitable for simulating the effect of seasonal trends while maintaining a relevant temporal resolution which is able to represent even single meteoric events. On the other hand, it is quite high data-demanding especially on soil properties, agricultural practices and weather. Moreover, it requires high computational capacity, especially when high resolution data are available (Yalew et al., 2013). Despite these last limitations, SWAT+ complies with the main requirements related to dimensionality, morphology, study scale, and matrices of the case study investigated in the frame of this work.

Type of input data and their accuracy for running the SWAT model mostly depend on the scale of the assessment. They concern: 1) soil properties which can be derived from general soil maps developed by USDA (e.g. Schwarz and Alexander, 1995; STATSGO2 Database), by FAO (FAO/UNESCO Soil Map of the World) or from user sample data; 2) DTM at proper resolution (1-30 m for application at regional to watershed scale, less than 1 m for application at field scales); 3) land use maps at the appropriate scale; 4) weather data which can be derived from both local weather stations or by Climate Forecasting System Reanalysis (CFSR, Saha et al., 2010). When local weather data are

incomplete, a weather generator module, included in the software, can fill in the gaps by generating weather data with the same statistical properties as the observed data (Vesely et al., 2019). Soil databases and CFSR meteorological data have been shown to provide reliable results especially for small-scale applications in data-scarce contexts, such as in developing countries (Alemayehu et al., 2015; Bressiani et al., 2015; Cuceloglu and Ozturk, 2019; Dile and Srinivasan, 2014; Mararakanye et al., 2020; Roth and Lemann, 2016). Conversely, for large scale applications, high resolution data assure the reliability of the modelling results (Gassman et al., 2014; Kannan et al., 2019; Muttiah and Wurbs, 2002).

One of the aims of this study was to assess runoff and soil loss at very local scale, comparing different scenarios of NBS implementation and climatic conditions. Considering the scale of the study areas (less than 40 ha), the model setup was based on local soil and weather data, as well as on high resolution DTM, remote imagery and design layouts of the NBSs.

2.4   Input data processing

2.4.1   Digital terrain modelling

The DTM used for simulations was reconstructed by means of close-range photogrammetry (Giordan et al., 2017; James and Robson, 2014; Remondino and El-hakim, 2006; Westoby et al., 2012) carried out in the whole Massaciuccoli reclamation area, hence comprising both study areas. The adopted vehicle for photogrammetry was a Barko GT autogiro (AV) equipped with a Sony Alpha 7 digital camera with 24.3 Mpx CMOS full frame sensor sized 35.8 mm ´ 23.9 mm (focal length 35 mm; flight height constant at 300 m above ground level, ground sampling distance 4.7 cm/pixel).

The model scaling and georeferencing was carried out measuring 9 ground control points (GCP) with differential real-time kinematic GNSS (Kozlov and Tkachenko, 1998); 2 more points were applied for error check. The average georeferencing error was 16 cm.

Data processing carried out in Metashape software (Agisoft LLC, 2016) allowed reconstructing a Digital Surface Model (DSM) with 27 pt/m^2 mean point density. Subsequent noise filtering and point cloud classifications allowed the DTM extraction of the entire area with 20 cm cell size.
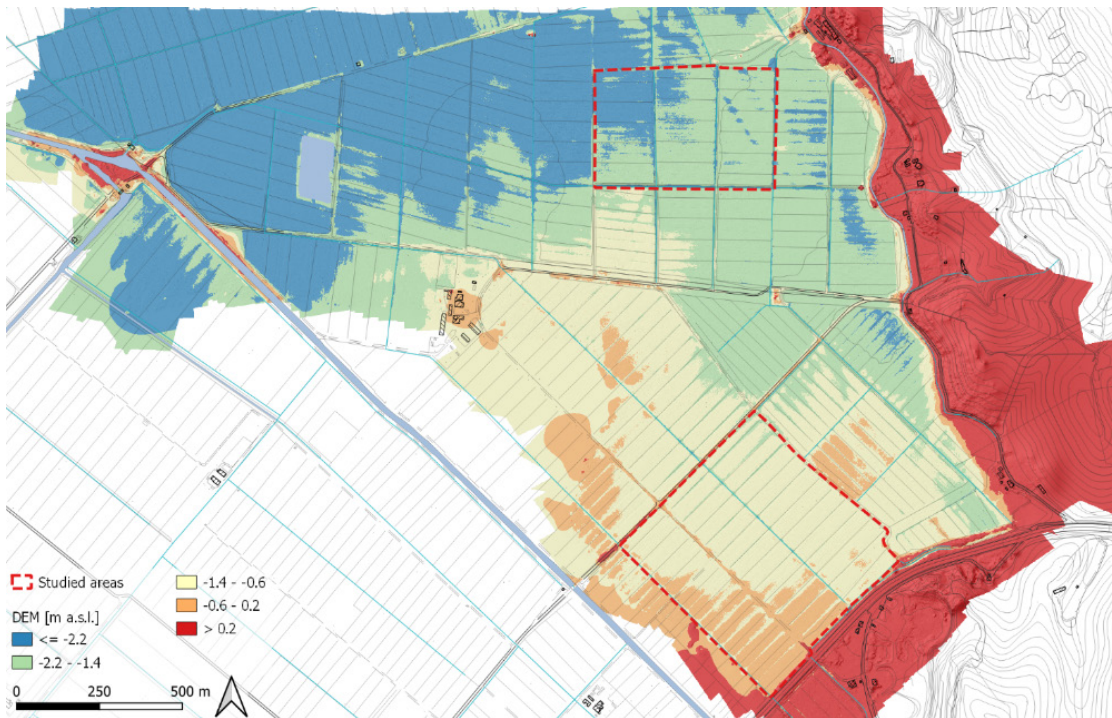
Figure 8: high resolution digital elevation model of the Massaciuccoli reclamation area (cell size of 20 · 20 cm) surveyed and processed by Centro di Geo Tecnologie – University of Siena (unpublished data, pers. comm.)

Due to the high resolution of the digital model and the resulting dm-scale roughness of the surface coupling with the flat morphology of the area, post-processing of digital model was required to make it consistent with the hydrological network detected in the field. This is specifically required in agricultural flat areas, where hydrographic natural network is poor and drainage system is formed by artificial channels of limited width and depth (Donmez et al., 2020). With such settings, indeed, automatic processing for watershed delineation may not match the real stream networks producing unreal modelling results (Luo et al., 2011) and post-processing activities are thus needed for the effective delineation of the draining network and watersheds.

Hydrological consistent stream networks and watershed delineation can be pursued with different approaches consisting of: 1) applying the automatic channel network "burn-in" function of SWAT+ (Dile et al., 2016); 2) manually modifying the DTM by carving channels and streams based on field measurements. Both approaches require the preliminary on field definition of the hydrographic network and its properties.
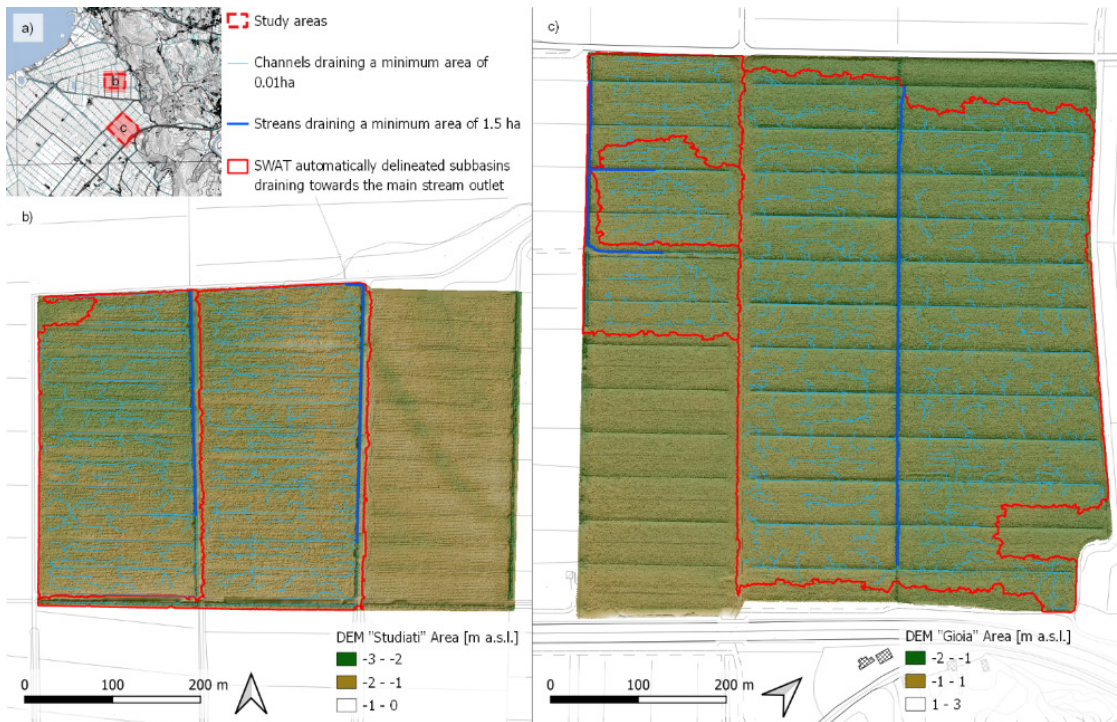
Figure 9: result from automatic watershed delineation on photogrammetry derived high resolution DTMs: a) geographical framework of the two study areas; b) watershed delineation at Studiati area; b) watershed delineation at Gioia area.

Automatic watershed delineation at study site produced unphysical results for both areas. At the Gioia area, the 17% of the agricultural land was neglected from watershed delineation, due to a slight slope opposite to the drainage direction (Figure 9c). At the Studiati Area, morphologies are totally flat and digital model of the stream paths was quite noisy. Moreover, channels were often crossed to the south by rural roads resulting in discontinuity in the hydrographic network delineation. In addition, channel morphology was often obliterated by the vegetation cover which resulted in a poor modelling of the channels themselves. In such setting, the watershed delineation produced a totally inverted draining direction with stream flow directed to the north instead of to the south and 30% of the studied area was neglected by watershed delineation.

Based on the severity of inconsistencies of the automatic watershed delineation, DTM post-processing was differentiated between the two areas. At the Gioia site, the mild approach based on the burn-in function was applied, using the shapefile of the real draining network surveyed in the field. It provided reliable result with both watershed and stream network matching the real ones (Figure 10a). At Studiati site, the manual carving was required to correctly delineate the watershed and the channel network. It was accomplished by topographical surveying of the channel sections in field and reconstructing a triangular irregular network (TIN) 3D model of the channel network. Depths were used in TIN creation instead of elevations, and TIN was then converted into a raster to be used for map algebra in qGIS software (QGIS.org, 2021). Conversely,

road crossings were neglected and replaced by a linear interpolation of the channels' geometries. The resulted post-processed DTM was then used for automatic watershed delineation and produced results matching the real draining network and watershed (Figure 10b).
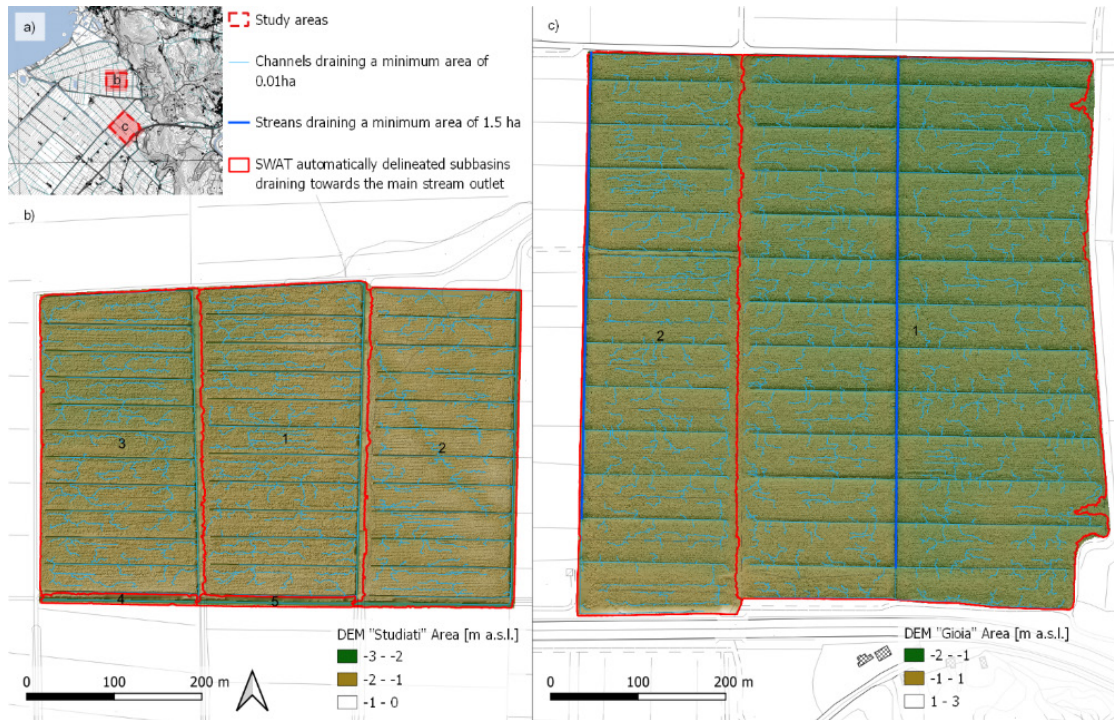

Figure 10: hydraulically consistent watershed delineation after DTM post processing: a) geographical inset of the study areas; b) watershed delineation at the Studiati area; c) watershed delineation at the Gioia area.

2.4.2   Soil maps

Soil data input in SWAT are in form of indexed raster maps with associated look-up tables used to link the soil index to the soil properties (Bieger et al., 2017; Dile et al., 2021). Indexes of soil raster maps represent homogeneous soil units which can be characterized by a unique set of soil parameters. At the study areas, soil maps were reconstructed based on the soil samples parameters suggested by Silvestri et al. (2002). Soil sample spatial density was constant over the whole Massaciuccoli reclamation area with and average value of ~0.2 samples/ha, which resulted in 12 and 17 soil samples collected in the Studiati and in the Gioia area, respectively (Figure 11). Soil parameters available for samples concerned soil granulometry (percentage of sand, silt and clay), USDA classification of soil textures (USDA, 1999), percent content of organic matter (OM), PH, electrical conductivity (EC), albedo ratio (A), and CaCO3 percent content.
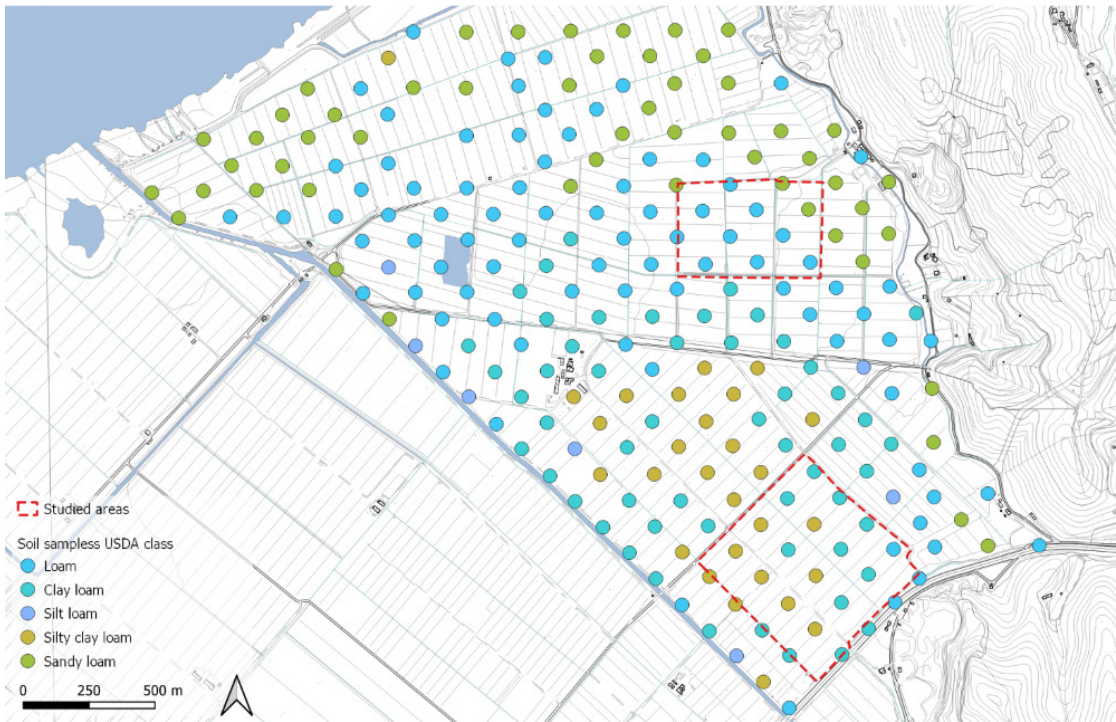
Figure 11: soil samples sites available for the Massaciuccoli area, with sample identification and texture classification according to USDA texture classification (USDA, 1999).

The missing parameters required for SWAT+ modelling were derived for each sample applying pedo-transfer functions available in scientific literature, based on soil texture and organic matter content. Specifically, bulk density (BD) was derived by applying the empirical equations from Hollis et al. (2012). The available water content (AWC) was calculated as the difference between the field capacity (FC) and the wilting point (WP), applying the equations proposed by Hutson and Wagenet (1992).

Soil erodibility input data, expressed as the k factor of the USLE equation (Ghosal and das Bhattacharya, 2020; Renard et al., 1991), was calculated by applying the pedotransfer equations of Williams (1995). They consider the effect of factors related to sand content, clay-to-silt ratios, organic content and the possible presence of high sand contents. The lower the erodibility returned by each factor, the higher the value of the considered variable.

Regardging the hydraulic conductivity (K_{sat}), the values reported in Table 2 were used. These values were derived from direct measurements on soils with similar textures and organic content in similar contexts. For soils with high organic contents (OM > 20%), a constant value of K_{sat} = 1.8 mm/h was set, based on the authors' experience.

Table 2: K$_{sat}$ values as function of soil texture and OM

Organic matter content	K$_{sat}$ (mm/h)			
	OM<5%	OM 5-10%	OM 10-20%	OM>20%
Clay	0.5	0.5	3.6	1.8
Silty clay	2.5	2.3	3.6	1.8
Clay loam	8.0	7.5	3.6	1.8
Silty clay loam	10.0	9.3	3.6	1.8
Silt Loam	12.5	11.7	3.6	1.8
Loam	15.0	14.0	3.6	1.8
Sandy Loam	25.0	23.3	3.6	1.8
Sand	50.0	46.7	3.6	1.8

All the soil parameters were interpolated over the whole area to achieve continuous representation of the variation of each variable (Fig 12). Considering the even spacing of samples, interpolation was carried out using the natural neighbor function in the qGIS software. Raster maps of sand, silt and clay contents were then used to derive the texture classification for each cell according to the USDA soil classification system (USDA, 1999), which allowed reproducing the soil texture map as a polygonal shapefile (Figure 13a). The organic matter content was classified according to the classes reported in (Figure 13b) in a polygonal shapefile. The intersection of both resulted in a soil map which units were differentiated per both texture and organic content (Fig 13c). Such units were then used for zonal statistics based on soil parameters' raster to compute the mean values to be set as input parameters in the SWAT user-soil database (Dile et al., 2021).
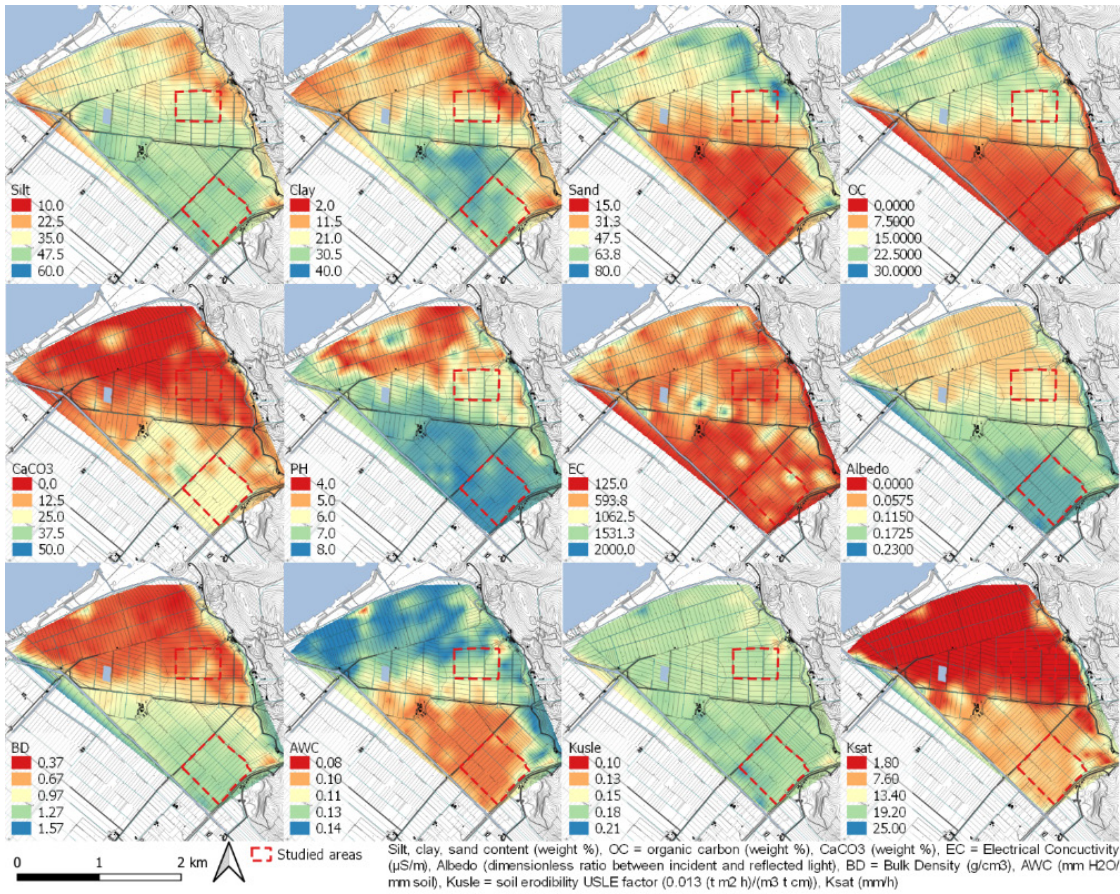
Figure 12: Raster maps of the main soil parameters used as QSWAT+ inputs.
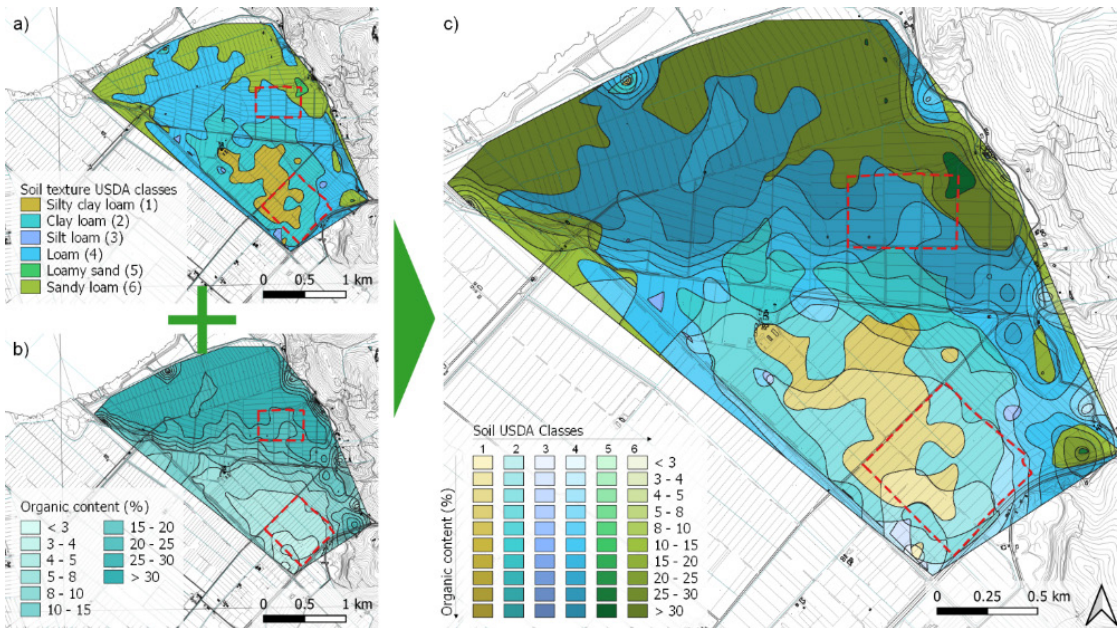
Figure 13: Map overlay to derive soil units homogeneous for texture and organic content; a) soil USDA texture map with IDs attributed to each soil class; b) Organic matter map representing OM percent classes; c) Soil units used as SWAT input differentiated per texture and per organic content.

2.4.3 Land use maps

Land use maps were generated based on the high resolution orthophoto and DTM (20 cm cell size both) achieved by remote sensing, identifying the different land use units, and on cadastral maps and crop plans to identify the different land use units crops. This allowed detecting single land parcels characterized by different crop rotations and agricultural techniques (Fig 14a,d), which resulted in several agricultural land use units. Along with these narrow rural unpaved roads, small ditches, stream vegetated embankments were identified as individual land-use units (Figure 14b,e). Moreover, given the large-scale of the study, the real extension of VBS implemented was delineated as polygonal areas and handled as individual land-cover units. Similar approach was then applied to differentiate the areas interested by different agricultural techniques (Figure 14c,f). This allowed to overcome difficulties in modelling the concentrated flow across VBS, which represents a key feature for correctly predicting the effects on runoff and sediment transport reduction (Dosskey et al., 2002; Helmers et al., 2005; White and Arnold, 2009).

Land use maps were thus generated for both the S0 (Figure 14b,e) and the S1 scenarios (Figure 14c,f).
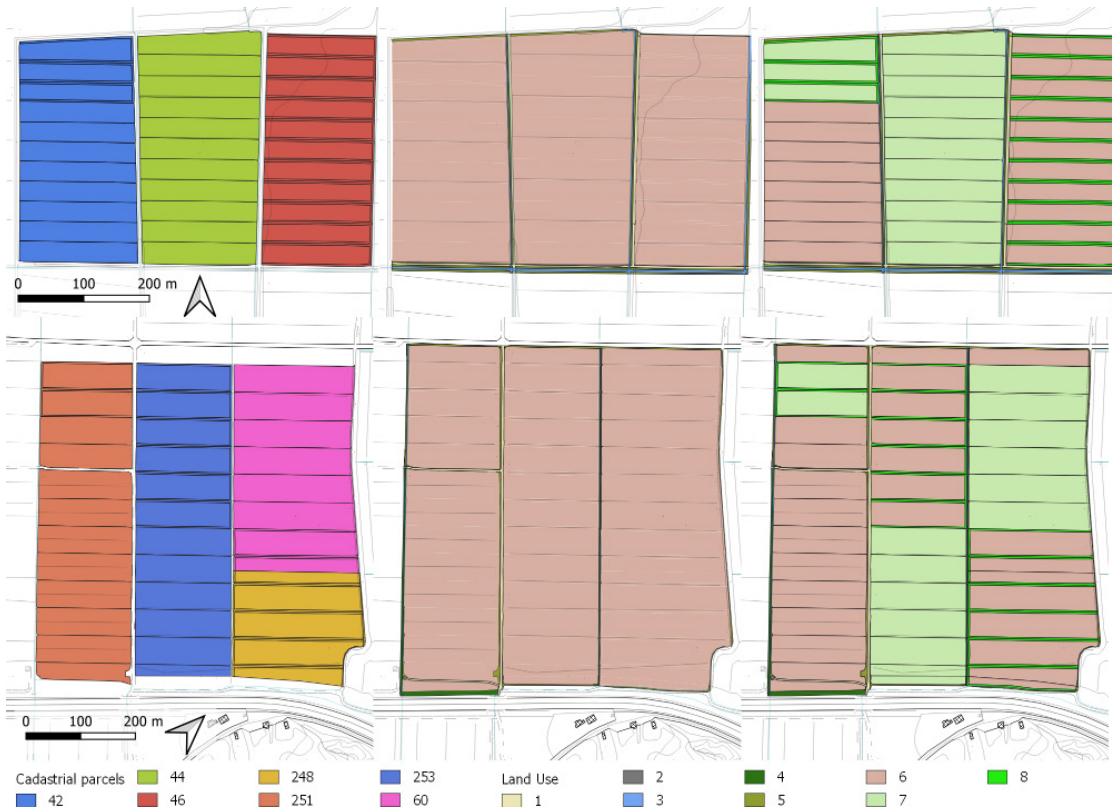
Figure 14 Land-use map used as input in qSWAT+. They are differentiated based on cadastral parcels interested by different crop rotations in the Studiati (a) and Gioia (c) areas, land use for the baseline scenario S0 (b and d), land use for the scenario S1 accounting for different agricultural techniques (c and f). Cadastral parcels: identified according to official ID: 42, 44, 46, 248, 251, 253, 250; Land use: 1 = unpaved rural roads, 2 = paved roads/areas, 3 = water bodies, 4 = uncultivated bushy areas, 5 = uncultivated grassed areas, 6 = conventional agriculture, 7 = conservative agriculture (S1), 8 = vegetated buffer strips (S2).

Agricultural land units characterized by both conventional and conservative agricultures are processed according to the crop rotations schemes and calendars provided by site owners (Table 3).

*Table 3. Crop rotation calendar provided by site owner differentiated based on cadastral parcels. In green winter cover crops (WCC) are reported when implemented in the scenario S1. Crops are reported according to SWAT+ coding: CORN = corn, RYEG = Italian (annual) ryegrass, SUNF = sunflower, DWHT = durum wheat, SKIP = code used for skipping modelling until the next agricultural phase, WWHT = winter wheat, OATS = oats, FPEA = field peas. * WCC implemented on limited area not interesting the whole parcel.*

Cadastral Parcels		PARC. 42 (1)	PARC. 44 (2)	PARC. 46 (3)	PARC. 251 (4)	PARC. 258 (5)	PARC. 60 + 248 (6)
Year	Year of rotation						
2010	1	CORN	CORN	CORN	SKIP	SKIP	SUNF
		WCC (RYEG)*	WCC (RYEG)		WCC (OATS + FPEA)*	WCC (OATS + FPEA)*	
2011	2	SUNF	SUNF	CORN	SUNF	SUNF	DWHT
		WCC (RYEG)*	WCC (RYEG)				WCC (OATS + FPEA)
2012	3	CORN	CORN	SUNF	WWHT	DWHT	SUNF
		WCC (RYEG)*	WCC (RYEG)		WCC (OATS + FPEA)*	WCC (OATS + FPEA)*	
2013	4	CORN	CORN	CORN	SUNF	SUNF	DWHT
		WCC (RYEG)*	WCC (RYEG)				WCC (OATS + FPEA)
2014	5	SUNF	SUNF	CORN	WWHT	DWHT	SUNF
		WCC (RYEG)*	WCC (RYEG)		WCC (OATS + FPEA)*	WCC (OATS + FPEA)*	
2015	6	CORN	CORN	DWHT	SUNF	SUNF	DWHT
		WCC (RYEG)*	WCC (RYEG)		WCC (OATS + FPEA)*	WCC (OATS + FPEA)*	WCC (OATS + FPEA)

2.4.4   Weather data

The historical weather data used for simulations were based on the recordings of the Metato weather station, located 4.8 km south of the studied areas and with similar morphological and environmental settings to the study areas. Rainfall, temperature, humidity, wind velocity and direction, solar radiation, with 15 min time interval are available and freely accessible from the portal of the Regional Hydrological and Geological Sector of Tuscany (Tuscany Region, 2021). Temperature and precipitation data were recorded since 1990, with few gaps generally due to periodical maintenance activities. Conversely, solar radiation, humidity and wind data are available since 2010. The 2010-2015 timespan was recognized to be the most complete and continuous for SWAT+ simulations. Moreover, the same interval was used for extracting storm events for other environmental simulations being carried in VFSMOD out by CREAF in the frame of Task 4.2, making this timespan suitable for results comparisons.

Future scenario weather data were modelled through Climate Change Toolkit (CCT, Ashraf Vaghefi et al., 2017) for the long future climate change, according to the climatic approach adopted. To achieve calibrated future weather data, the procedure for data downscaling and bias correction was adopted (Ahmed et al., 2013; Hempel et al., 2013; Ines and Hansen, 2006; Teutschbein and Seibert, 2012). Downscaling was carried out based on 3 different weather stations close to the investigated area, located in similar morphological and climatic setting which, at the same time, provided required data over a sufficiently large overlapping time interval (1996-2005). The three weather stations are located at Lido di Camaiore, Strettoia and Metato localities (Tuscany Region, 2021).

Future data used for modelling the effect of mild (RCP 4.5) and strong climate change scenarios (RCP 8.5) refer to the time span 2094-2099.

2.4.5   Model calibration

The local scale model established for the assessment was limited to a small portion of the catchment of the Massaciuccoli reclamation area. The data available from the monitoring and gauging systems in the area covered the entire catchment and were not suitable for model calibration. Furthermore, the main target of our assessment was to assess the relative effects of NBS with reference to the baseline case S0. Therefore, no model calibration was performed. However, a monitoring system is gathering data since April 2021 in both study areas to monitor the effects of NBSs. It will thus provide local data useful and for model calibration. However, model calibration and validation are usually based on several years of monitoring and the data being gathered now could be applied in a few years.

2.5   Modelling results

The approach used in modelling runoff and sediment yield was at very local scale based on high resolution DTM, soil, land use and management data. It provided detailed estimates of agricultural practices and NBS performances regarding site runoff and soil erosion dynamics (Lasanta et al., 2000; Probst et al., 2005; Williams et al., 2015) with resolution of few square meters. Spatial units used in the modelling were the uniform hydrological response units (HRU), which are characterized by same soil, plant and hydrological conditions and processes (Arnold et al., 2012; Bieger et al., 2017; Dile et al., 2021). Their extension ranges from <1 m^2 to ≈1500 m^2, thus representing a partition of both landcover and soil units with water flows converging to individual channel intersections. Modelling outputs referred to HRUs are related to nutrient balance, water balance, plant cycle and losses. On the other hand, hydrological processes are usually referred to water bodies (channels, reservoir, aquifers, point sources etc.). The results can be also related to different time steps ranging from days to years, and aggregated in averages, total, maxima etc.

Among the possible SWAT+ outputs, the study focused on the runoff and sediment yield leaving the area caused by water erosion. Variables were referred to HRU. When considering sediment yields at HRUs, the areal annual average weight was considered, along with the total amount produced at each study area; runoff was estimated for the surface component and thus intended as the annual amount of water leaving the area.

2.5.1   Current climatic scenario

Runoff susceptibility maps for current climatic conditions are provided in the Annexes 1 to 6, wherein results for both the Studiati and the Gioia areas are reported. At the Studiati area, the current runoff in general reached quite low values of ≈74 mm/y (Annex 1 Figure a); high values were observed just along the rural road where they reached average values of ≈831 mm/y quite close to the average annual precipitation (1178 mm).

At the Gioia area, the runoff was generally comparable to the Studiati's, with most frequent values ranging from 40 to 80 mm/y (Annex 1 Figure b). However, in the Gioia area, there were limited areas along the borders of some fields, near the drainage channels, where runoff reached values higher than 110 mm/y. The highest values, also in this area, were recorded along rural roads where it exceeded 800 mm/y.

The NBS implementation (VBSs and CAs) in both areas resulted in a significant runoff reduction along the plot borders where VBSs are implemented. Here, runoff amounts drop to values ranging from 15 to 40 mm/y. On the other hand, in areas where a CA is implemented, its effect on the runoff was almost negligible (Annex 2 Figure a, b).

Sediment yield susceptibility maps for current climatic conditions are provided in Annex 1 Figs. c and d for the Studiati and the Gioia area, respectively. In the former, consistent with the low runoff values, the sediment yield was also calculated to be quite low with an average of 0.10 t/ha per year with highest values (6.7 t/ha) recorded along the slopes of the main embankments. In general, the lowest values (0-0.2 t/ha) were recorded along the innermost parts of the plots whereas they both increased along the channels and close to the plot's borders. Similarly, in the Gioia area, the innermost parts of the plots exhibited low values of sediment yield ranging between 0-0.2 t/ha. The areas of high sediment production along plot borders were more widespread with values exceeding 32 t/ha per year. They were located along the plot borders in the western part of the area, where clay and silty clay soils are located. In the remaining part, although the sediment yield still showed high values at the plot border, it never exceeded 8 t/ha. Consequently, the average annual sediment weight yielded at the Studiati area was 2.7 t/y, whereas the calculated sediment yield was much higher at the Gioia area, exceeding 126 t/y.

The NBS implementation (VBSs and CAs) area resulted in a drastic reduction of sediment yield, especially along the zones of channelized flows along the channels and the plots' borders (Annex 2, Figure c, d). Indeed, in the Studiati area the total annual sediment loss decreased to 1.6 t/y (Annex 2, Figure c), whereas in the Gioia area it was reduced by an order of magnitude dropping to 15.7 t/y (Annex 2, Figure d). Specifically, where CAs or VBSs were implemented, areas characterized by peak of sediment yield disappeared and highest values never exceeded 4 t/ha (Annex 2, Figure c, d).

2.5.2   RCP 4.5 Future climatic scenario

The effects of climate change were estimated comparing the S0 and S1 scenario in long future climate (2095-2100) accounting for climate changes outlined by the RCP 4.5 (Annexes 3 and 4) and RCP 8.5 scenarios (Annexes 5 and 6) and modelled using the GCM5 (MIROC). Possible future scenario characterized by mild climate change, resulted in a rainfall reduction to 898 mm/y. Accordingly, considering S0, runoff modelled at Studiati area (Annex 3, Figure a) was characterized by uniformly distributed low values. At the Gioia area, the runoff distribution was much more complex (Annex 3, Figure b), ranging between 20 and 160 mm/y. Higher values (80-160 mm/y) were recorded where soils were in the clay loam and silty clay loam classes.

When referring to the S1 scenario at the Studiati area, no significant variation in runoff was observed (Annex 4, Figure a). Moreover, runoff did not vary for different types of NBS implemented. In the Gioia area the implementation of NBS resulted in the runoff reduction along the plot borders where VBSs were implemented. There are no significant variations for areas influenced by the implementation of CAs (Annex 4, Figure b).

The sediment yield at the Studiati area (Annex 3, Figure c) followed the runoff trend, with very low mean annual values over the entire area (0-0.2 t/ha), The total sediment loss for the entire area was ≈0.3 t/y. At the Gioia area (Annex 3, Figure d), low sediment yield values were recorded in the innermost areas of the plots whereas highest values were recorded at plot borders. The total sediment loss modelled in the area was 64 t/y.

Considering the implementation of NBS in the Studiati area (Annex 4, Figure c), no significant variation in sediment yield values was detected. In the Gioia area, there was a general decrease in sediment yield both over the entire area and along the perimeter of the plots where it was limited to 8 t/ha. Sediment loss reduction was significant for both VBSs and CAs (Annex 4, Figure d).

2.5.3 RCP 8.5 Future climatic scenario

Modelling carried out for the RCP 8.5 climatic scenario focusing on runoff and sediment yield point out two different behaviours for the two study areas. Specifically, a further decrease of rainfall (738 mm/y) was forecasted for the future climate with the average runoff decreasing accordingly. In the Studiati area (Annex 5, Figure a), modelled runoff values were generally low.

In the Gioia area, runoff prediction was characterized by low values as well, although higher than the Studiati's. Runoff varied over the Gioia area according to the soil texture and organic matter distribution. In fact, it reached slightly higher values (40-80 mm/y) where silty clay loams with low organic content (< 3%), and where clay loams with medium-low organic content (< 5%) outcrop.

Considering the NBS implementation (S1, Annex 6) no significant changes were recorded in the Studiati area (Annex 6 Figure a). Conversely, in the Gioia area a slight reduction of runoff was observed (Annex 6, Figure b) where VBSs were implemented. The effect of CA in runoff reduction was, however, negligible.

In the Studiati area, the sediment yield trend was consistent with the runoff (Annex 5, Figure c). No variations were detected against S0, since the modeled total sediment production was constantly equal to 0.3 t/y. In the Gioia area, sediment yield was generally low in the central part of each plot, disregarding differences in crop rotations and soil types (Annex 5, Figure d). On the contrary, along the plot borders it ranged in the interval 2-32 t/ha. Consequently, in the whole area, the total sediment loss was 107 t/y.

When considering the S1 scenario (Annex 6 Figure c, d), the two areas behaved differently. Indeed, while in the Studiati area no significant improvements were predicted (Annex 6, Figure c), as documented by the scarce total sediment loss decreased (from 0.3 to 0.26 t/y), in the Gioia area a general reduction of sediment yield was observed over the whole area (Annex 6, Figure d). Indeed, in central areas of plots, it reduced to <0.01 t/ha, whereas along borders it ranged in the interval 0.2-4 t/ha. The reduction was uniform in areas of CA implementation. However, in the parcels 4 and 5, it still remained higher (0.8 – 4 t/ha) than in parcel 6 (0 – 0.8 t/ha). In all plots intersected by VBSs, sediment yield reduced to values close to those recorded in the central parts, ranging in the interval 0-0.2 t/ha. In terms of total losses, a reduction of 82% was predicted for the NBS scenario with values dropping to 19 t/y for the entire Gioia area.

2.6   Discussion

SWAT+ simulations carried out in the Massaciuccoli reclamation agricultural area, carried out in the two key study areas of Studiati and Gioia, according to the flat morphology of the sites, pointed out average medium-to-low annual depths of runoff in both areas, with the Studiati area being characterized by lowest values. The runoff depths in the Gioia area showed higher values and a more complex distribution. Specifically, peak values of runoff depths were modelled along the plot edges in area just uphill the first order of channels draining the area. This pointed out the significant influence of the local topography, which induced high runoff depths in areas characterized by huge flow accumulation. The effect of flow accumulation was also evident for the sediment yield in both areas. In the Studiati's, which in general was characterized by very low average values (< 0.2 t/ha), higher values were recorded along the channel paths (0.4–4 t/ha), remarking the role of channelized flows in sediment removal. In the Gioia area, sediment yield was much more influenced by flow accumulation with values exceeding 32 t/ha along the channel paths. Unlike the Studiati area, here the average sediment loss along plots border increased moving towards east consistently with the increase of clay content (Figure 13c). However, no significant correlation was detected with OM. The NBS implementation in both study areas (Annex 2) resulted in a mild reduction of runoff depth. Although VBS performances were generally reduced by flow accumulation (Abu-Zreig et al., 2001; Stehle et al., 2016; White and Arnold, 2009) in the study areas, and mostly in the Gioia one, runoff reduction occurred generally along the VBSs, where they were still able to halve values from ≈80 mm/y to <40 mm/y. On the other hand, no significant variations in terms of runoff were detected for plots where CA was implemented. When considering the sediment yield, the effect of implementation of both NBS was much more evident especially in the Gioia area, where the total annual sediment loss was reduced by an order of magnitude in areas interested by both CAs and VBSs, also where they were not coupled. The sediment loss reduction was more evident in the parcel 5 where sunflower-durum wheat rotations were interspersed by winter cover crops (oats and legumes). Both type of NBS exerted their action in sediment loss reduction also in the Studiati area with predominant effects in areas of flow accumulation along the channel's paths (Annex 2).

Modelling of future scenario considering mild climate changes (RCP 4.5) resulted in diminishing the rainfall from 1178 mm/y to 898 mm/y. Such climatic variation induced two different behaviours in the two study areas. Indeed, whilst the Studiati area low runoff depths were forecasted widespread, in the Gioia area the forecasted runoff depth distribution was much more articulated. Here, they ranged over a larger interval (20 – 160 mm/y), if compared to the results from modelling in current weather (40-80 mm/y). Moreover, the distribution followed the soil texture distribution with highest values recorded where clay loams and silty clay loams outcropped. This remarks the relevant influence of soil texture distribution in different climatic conditions characterized by drier weather. Consistently with runoff, the sediment yield in the presence of mild climate changes decreased in the Studiati area from 2.7 t/y to 0.3 t/y with slightly higher values limited to major stream embankments. In the Gioia area also, according to lower rainfall, sediment yield decreased over the whole area, although zones of high sediment yield remained detectable along the plot's borders. Considering the generally low runoff and sediment yield at the Studiati area with future mild climatic variation, detectable effects of NBS were strongly reduced accordingly. Conversely, in the Gioia area, whilst runoff reduction remained still limited to the areas of the VBSs implementation, sediment losses were significantly lowered by the 75% (from 64 t/y to 16 t/y) by the coupled effect of both VBSs and CAs. Similar diverging trends were recognized also when modelling strong climate changes (RCP 8.5), which resulted in a further reduction of rainfall (738 mm/y). In such conditions low values were still recorded in the Studiati area, even if slightly higher averages were recorded compared to RCP 4.5 climatic scenario. Consistently, also sediment loss remained low and with negligible effects of NBSs. On the contrary, in the Gioia area, although a general decrease of runoff depth was observed, which remained controlled by soil granulometry, the sediment yield suffered a significant increase (from 64 to 107 t/y), pointing out the enhanced erosive capacity of more intense rainfall. In this area the implementation of NBS exerted a reduced effect in runoff mitigation, which was limited to the areas of the VBSs implementation, whereas their effect in reducing sediment losses was much more significant being able to limit it by the 80% (reducing it from 107 mm/y to 19 mm/y).

2.7   Concluding remarks

The present study is one of the few applications of SWAT+ model to very local scale and based on data with very high resolution. The modelling was carried out to support the knowledge of the efficacy of NBS in mitigating runoff and soil erosion hazard in a flat agricultural area in Central Italy, where vegetated buffer strips (VBSs) and conventional agricultures (CAs) were implemented in the frame of the PHUSICOS project. On this context, NBS implementation scenarios were tested against the baseline one. Furthermore, the comparison of NBS performances in changed climate scenarios in distant future was also assessed. Climate change scenarios with both mild and strong variations (RCP 4.5 and RCP 8.5, respectively) were considered in the analysis. For each implementation and climatic scenario, modelling was carried out for two study sites having similar crop rotations but different soil textures and organic contents. The results of modelling consisted in 12 different scenarios modelled for both runoff and sediment loss.

The comparison between different NBS implementation scenarios, in different pedological areas and climatic conditions exhibited the influence exerted by all those variables in controlling runoff, soil erosion and NBS performances. Specifically, the study showed that also in very flat agricultural areas, flow accumulation may occur, especially beside channels and streams. Their negative effects implied high runoff depths and sediment losses over large areas. Moreover, the runoff was much more sensitive to soil textures when finer grained soils with low organic content outcropped. Here, also the negative effects of flow accumulation were much more evident. In presence of lower but more concentrated rainfall (as forecasted for the future climatic scenarios) the different behaviour of various soil textures was stressed especially with regards to runoff. Their depths were indeed distributed over wider ranges and were strongly controlled by soil textures and organic content with highest values occurring where low organic content and fine-grained soils are detected. In such pedological and climatic conditions, the NBS performances in runoff and soil erosion hazard mitigation are enhanced also when lower but more intense rainfalls occur. On the contrary, when soils are characterized by high organic content and coarser textures, the runoff strongly depends on the rainfall quantities, as well as their intensity. In such cases, forecasted future low rainfalls correspond to low runoff and soil erosion. Moreover, the mitigating effects of the designed NBS are strongly reduced. In presence of extreme climatic changes, their effects become negligible.

A further result consists in the effects of different NBSs. In fact, when the mitigation effect of NBS is noticeable, VBSs and CAs exert their action with different performances on different hazards. Although VBSs can reduce both runoff and sediment losses, CAs have only a secondary effect on runoff being much more performing in reducing sediment losses.

In conclusion, when referring to runoff and soil erosion, NBS performances and consequently their feasibility, among other aspects, are strongly influenced by soil texture, organic content, water flow accumulation and rainfall distribution. These aspects were all considered in SWAT+ modelling which is emerged to be a viable approach also for assessments at field scales. It can be thus intended as a supporting analysis tool for farmers and stakeholders when setting up sustainable agricultural management and planning.

2.8   References

A.B.D.A.S. [www document], 2006. URL https://www.appenninosettentrionale.it/itc/ (accessed 9.7.21).

Abu-Zreig, M., Rudra, R.P., Whiteley, H.R., 2001. Validation of a vegetated filter strip model (VFSMOD). Hydrological Processes 15, 729–742. https://doi.org/10.1002/HYP.101

Agisoft LLC, 2016. AgiSoft Metashape Professional.

Ahmed, K.F., Wang, G., Silander, J., Wilson, A.M., Allen, J.M., Horton, R., Anyah, R., 2013. Statistical downscaling and bias correction of climate model outputs for climate change impact assessment in the U.S. northeast. Global and Planetary Change 100, 320–332.

Alemayehu, T., Griensven, A. van, Bauwens, W., 2015. Evaluating CFSR and WATCH Data as Input to SWAT for the Estimation of the Potential Evapotranspiration in a Data-Scarce Eastern-African

Catchment. Journal of Hydrologic Engineering 21, 05015028. https://doi.org/10.1061/(ASCE)HE.1943-5584.0001305

Aleotti, P., Chowdhury, R., 1999a. Landslide hazard assessment: Summary review and new perspectives. Bulletin of Engineering Geology and the Environment 58, 21–44. https://doi.org/10.1007/S100640050066

Aleotti, P., Chowdhury, R., 1999b. Landslide hazard assessment: Summary review and new perspectives. Bulletin of Engineering Geology and the Environment 58, 21–44. https://doi.org/10.1007/S100640050066

Arabi, M., Frankenberger, J.R., Engel, B.A., Arnold, J.G., 2008. Representation of agricultural conservation practices with SWAT. Hydrological Processes 22, 3042–3055. https://doi.org/10.1002/HYP.6890

Arnaez, J., Lasanta, T., Ruiz-Flaño, P., Ortigosa, L., 2007. Factors affecting runoff and erosion under simulated rainfall in Mediterranean vineyards. Soil and Tillage Research 93, 324–334. https://doi.org/10.1016/J.STILL.2006.05.013

Arnold, J.G., Allen, P.M., 1999. Automated methods for estimating baseflow and ground water recharge from streamflow records. Journal of the American Water Resources Association 35, 411–424. https://doi.org/10.1111/J.1752-1688.1999.TB03599.X

Arnold, J.G., Moriasi, D.N., Gassman, P.W., Abbaspour, K.C., White, M.J., Srinivasan, R., Santhi, C., Harmel, R.D., Griensven, A. van, Liew, M.W. van, Kannan, N., Jha, M.K., 2012. SWAT: Model Use, Calibration, and Validation. Transactions of the ASABE 55, 1491–1508. https://doi.org/10.13031/2013.42256

Arnold, J.G., Srinivasan, R., Muttiah, R.S., Williams, J.R., 1998. Large area hydrologic modeling and assessment part I: Model development. Journal of the American Water Resources Association 34, 73–89. https://doi.org/10.1111/J.1752-1688.1998.TB05961.X

Ashraf Vaghefi, S., Abbaspour, N., Kamali, B., Abbaspour, K.C., 2017. A toolkit for climate change analysis and pattern recognition for extreme weather conditions – Case study: California-Baja California Peninsula. Environmental Modelling & Software 96, 181–198. https://doi.org/10.1016/J.ENVSOFT.2017.06.033

Autuori, S., Caroppi, G., de Paola, F., Pugliese, F., Giugni, M., Stanganelli, M.L., Urciuoli, G., 2019. Deliverable D4.1 Comprehensive Framework for NBS Assessment.

Baldaccini, G.N., 2018. Zone umide: dal degrado al recupero ecologico. Il caso del lago di Massaciuccoli (Toscana nord-occidentale). Biologia Ambientale 32, 85–98. https://doi.org/10.30463/ao181.009

Bieger, K., Arnold, J.G., Rathjens, H., White, M.J., Bosch, D.D., Allen, P.M., Volk, M., Srinivasan, R., 2017. Introduction to SWAT+, A Completely Restructured Version of the Soil and Water Assessment Tool. JAWRA Journal of the American Water Resources Association 53, 115–130. https://doi.org/10.1111/1752-1688.12482

Bosch, D.D., Sheridan, J.M., Batten, H.L., Arnold, J.G., 2004. EVALUATION OF THE SWAT MODEL ON A COASTAL PLAIN AGRICULTURAL WATERSHED. Transactions of the ASAE 47, 1493-. https://doi.org/10.13031/2013.17629

Bressiani, D. de A., Srinivasan, R., Jones, C.A., Mendiondo, E.M., 2015. Effects of spatial and temporal weather data resolutions on streamflow modeling of a semi-arid basin, Northeast Brazil. International Journal of Agricultural and Biological Engineering 8, 125–139. https://doi.org/10.25165/IJABE.V8I3.970

Brunelli G., Cannicci G., 1942. Il Lago di Massaciuccoli. Boll. Pesca Piscic. Idrobiol. 16, 5–66.

Bryan, R.B., Poesen, J., 1989. Laboratory experiments on the influence of slope length on runoff, percolation and rill development. Earth Surface Processes and Landforms 14, 211–231. https://doi.org/10.1002/ESP.3290140304

Burkart, M., 2010. The hydrologic footprint of annual crops, in: A Watershed Year: Anatomy of the Iowa Floods of 2008. https://doi.org/10.2307/j.ctt20mvd5n.14

Cenni M., 1997. Lago di Massaciuccoli: 13 ricerche finalizzate al risanamento : 2° contributo.

Chen, J., Brissette, F.P., Leconte, R., 2011. Uncertainty of downscaling method in quantifying the impact of climate change on hydrology. Journal of Hydrology 401, 190–202.

Chung, C.J., Fabbri, A.G., 2008. Predicting landslides for risk analysis - Spatial models tested by a cross-validation technique. Geomorphology 94, 438–452.

Chung, C.J.F., Fabbri, A.G., 1999. Probabilistic prediction models for landslide hazard mapping. Photogrammetric Engineering and Remote Sensing.

Clarke L., Edmonds J., Jacoby H., Pitcher H., Reilly R., Richels R., 2007. Scenarios of greenhouse gas emissions and atmospheric concentrations, in: Sub-Report 2.1a of Synthesis and Assessment Product 2.1 by the U.S. Climate Change Science Program and the Subcommittee on Global Change Research,. Department of Energy, Office of Biological & Environmental Research, Washington DC.

Corte-Real, J., Zhang, X., Wang, X., 1995. Downscaling GCM information to regional scales: a non-parametric multivariate regression approach. Climate Dynamics 11, 413–424. https://doi.org/10.1007/BF00209515

Cuceloglu, G., Ozturk, I., 2019. Assessing the Impact of CFSR and Local Climate Datasets on Hydrological Modeling Performance in the Mountainous Black Sea Catchment. Water 2019, Vol. 11, Page 2277 11, 2277. https://doi.org/10.3390/W11112277

Dile, Y., Srinivasan, R., George, C., 2021. QGIS Interface for SWAT+: QSWAT+.

Dile, Y.T., Daggupati, P., George, C., Srinivasan, R., Arnold, J., 2016. Introducing a new open source GIS user interface for the SWAT model. Environmental Modelling and Software 85, 129–138.

Dile, Y.T., Srinivasan, R., 2014. Evaluation of CFSR climate data for hydrologic prediction in data-scarce watersheds: an application in the Blue Nile River Basin. JAWRA Journal of the American Water Resources Association 50, 1226–1241. https://doi.org/10.1111/JAWR.12182

Dodd, R.J., Sharpley, A.N., 2016. Conservation practice effectiveness and adoption: unintended consequences and implications for sustainable phosphorus management. Nutrient Cycling in Agroecosystems 104, 373–392. https://doi.org/10.1007/S10705-015-9748-8

Donmez, C., Sari, O., Berberoglu, S., Cilek, A., Satir, O., Volk, M., 2020. Improving the Applicability of the SWAT Model to Simulate Flow and Nitrate Dynamics in a Flat Data-Scarce Agricultural Region in the Mediterranean. Water 2020, Vol. 12, Page 3479 12, 3479. https://doi.org/10.3390/W12123479

Dosskey, M.G., Helmers, M.J., Eisenhauer, D.E., Franti, T.G., Hoagland, K.D., 2002. Assessment of concentrated flow through riparian buffers. Journal of Soil and Water Conservation 57.

FAO/UNESCO Soil Map of the World [WWW Document], n.d. URL http://www.fao.org/soils-portal/data-hub/soil-maps-and-databases/faounesco-soil-map-of-the-world/en/ (accessed 8.30.21).

Fell, R., Corominas, J., Bonnard, C., Cascini, L., Leroi, E., Savage, W.Z., 2008. Guidelines for landslide susceptibility, hazard and risk zoning for land use planning. Engineering Geology 102, 85–98.

Gassman, P.W., Sadeghi, A.M., Srinivasan, R., 2014. Applications of the SWAT Model Special Section: Overview and Insights. Journal of Environmental Quality 43, 1–8. https://doi.org/10.2134/JEQ2013.11.0466

Gericke, A., Nguyen, H.H., Fischer, P., Kail, J., Venohr, M., 2020. Deriving a Bayesian Network to Assess the Retention Efficacy of Riparian Buffer Zones. Water 2020, Vol. 12, Page 617 12, 617. https://doi.org/10.3390/W12030617

Ghosal, K., das Bhattacharya, S., 2020. A Review of RUSLE Model. Journal of the Indian Society of Remote Sensing 2020 48:4 48, 689–707. https://doi.org/10.1007/S12524-019-01097-0

Giordan, D., Hayakawa, Y., Nex, F., Remondino, F., Tarolli, P., 2017. Review article: The use of remotely piloted aircraft systems (RPAS) for natural hazards monitoring and management. Natural hazards and earth systems sciences discussions 1–26. https://doi.org/10.5194/NHESS-2017-339

Githui, F., Mutua, F., Bauwens, W., 2009. Estimating the impacts of land-cover change on runoff using the soil and water assessment tool (SWAT): Case study of Nzoia catchment, Kenya. Hydrological Sciences Journal 54, 899–908. https://doi.org/10.1623/HYSJ.54.5.899

Guzzetti, F., Reichenbach, P., Ardizzone, F., Cardinali, M., Galli, M., 2006. Estimating the quality of landslide susceptibility models. Geomorphology 81, 166–184.

Guzzetti, F., Reichenbach, P., Cardinali, M., Galli, M., Ardizzone, F., 2005. Probabilistic landslide hazard assessment at the basin scale. Geomorphology 72, 272–299. https://doi.org/10.1016/j.geomorph.2005.06.002

Helmers, M.J., Eisenhauer, D.E., Dosskey, M.G., Franti, T.G., Brothers, J.M., McCullough, M.C., 2005. Flow pathways and sediment trapping in a field-scale vegetative filter. Transactions of the ASAE 48, 955–968. https://doi.org/10.13031/2013.18508

Hempel, S., Frieler, K., Warszawski, L., Schewe, J., Piontek, F., 2013. A trend-preserving bias correction - The ISI-MIP approach. Earth System Dynamics 4, 219–236. https://doi.org/10.5194/ESD-4-219-2013

Hervás, J., Bobrowsky, P., 2009. Mapping: Inventories, Susceptibility, Hazard and Risk. Landslides - Disaster Risk Reduction 321–349. https://doi.org/10.1007/978-3-540-69970-5_19

Himanshu, S.K., Pandey, A., Yadav, B., Gupta, A., 2019. Evaluation of best management practices for sediment and nutrient loss control using SWAT model. Soil and Tillage Research 192, 42–58. https://doi.org/10.1016/J.STILL.2019.04.016

Hungr, O., 2018. Some methods of landslide hazard intensity mapping. Landslide Risk Assessment 215–226. https://doi.org/10.1201/9780203749524-12

Hutson, J.L., Wagenet, R.J., 1992. LEACHM: Leaching Estimation And Chemistry Mo- del: A process-based model of water and solute movement, transformations, plant uptake and chemical reactions in the unsaturated zone. Version 3.0: Research Series No. 93-3. Ithaca, NY: Cornell University.

I Pérez-Rey, A.R.L.G.X.E.-V.R.T.L.A., 2019. A multi-approach rockfall hazard assessment on a weathered granite natural rock slope. Landslides 16, 2005–2015. https://doi.org/10.1007/s10346-019-01208-5

Ines, A.V.M., Hansen, J.W., 2006. Bias correction of daily GCM rainfall for crop simulation studies. Agricultural and Forest Meteorology 138, 44–53.

James, M.R., Robson, S., 2014. Mitigating systematic error in topographic models derived from UAV and ground-based image networks. Earth Surface Processes and Landforms 39, 1413–1420. https://doi.org/10.1002/ESP.3609

Kannan, N., Santhi, C., White, M.J., Mehan, S., Arnold, J.G., Gassman, P.W., 2019. Some Challenges in Hydrologic Model Calibration for Large-Scale Studies: A Case Study of SWAT Model Application to Mississippi-Atchafalaya River Basin. Hydrology 2019, Vol. 6, Page 17 6, 17. https://doi.org/10.3390/HYDROLOGY6010017

Karki, R., Srivastava, P., Veith, T.L., 2020. Application of the Soil and Water Assessment Tool (SWAT) at Field Scale: Categorizing Methods and Review of Applications. Transactions of the ASABE 63, 513–522. https://doi.org/10.13031/TRANS.13545

Kinnell, P.I.A., Risse, L.M., 1998. USLE-M: Empirical Modeling Rainfall Erosion through Runoff and Sediment Concentration. Soil Science Society of America Journal 62, 1667–1672. https://doi.org/10.2136/SSSAJ1998.03615995006200060026X

Kozlov, D., Tkachenko, M., 1998. Centimeter-level, real-time kinematic positioning with GPS+GLONASS C/A receivers. Navigation, Journal of the Institute of Navigation 45, 137–147. https://doi.org/10.1002/J.2161-4296.1998.TB02378.X

Lasanta, T., García-Ruiz, J.M., Pérez-Rontomé, C., Sancho-Marcén, C., 2000. Runoff and sediment yield in a semi-arid environment: The effect of land management after farmland abandonment. Catena 38, 265–278.

Linsley, R.K., 1967. The relation between rainfall and runoff: Review paper. Journal of Hydrology 5, 297–311. https://doi.org/10.1016/S0022-1694(67)80128-8

Liu, B.Y., Nearing, M.A., Shi, P.J., Jia, Z.W., 2000. Slope Length Effects on Soil Loss for Steep Slopes. Soil Science Society of America Journal 64, 1759–1763. https://doi.org/10.2136/SSSAJ2000.6451759X

Loague, K., 1992. USING SOIL TEXTURE TO ESTIMATE SATURATED HYDRAULIC CONDUCTIVITY AND THE IMPACT ON RAINFALL-RUNOFF SIMULATIONS1. JAWRA Journal of the American Water Resources Association 28, 687–693. https://doi.org/10.1111/J.1752-1688.1992.TB01490.X

Luo, Y., Su, B., Yuan, J., Li, H., Zhang, Q., 2011. GIS Techniques for Watershed Delineation of SWAT Model in Plain Polders. Procedia Environmental Sciences 10, 2050–2057. https://doi.org/10.1016/J.PROENV.2011.09.321

Mararakanye, N., le Roux, J.J., Franke, A.C., 2020. Using satellite-based weather data as input to SWAT in a data poor catchment. Physics and Chemistry of the Earth, Parts A/B/C 117, 102871. https://doi.org/10.1016/J.PCE.2020.102871

Meinshausen, M., Smith, S.J., Calvin, K., Daniel, J.S., Kainuma, M.L.T., Lamarque, J., Matsumoto, K., Montzka, S.A., Raper, S.C.B., Riahi, K., Thomson, A., Velders, G.J.M., van Vuuren, D.P.P., 2011. The RCP greenhouse gas concentrations and their extensions from 1765 to 2300. Climatic Change 109. https://doi.org/10.1007/s10584-011-0156-z

Merriman, K.R., Daggupati, P., Srinivasan, R., Toussant, C., Russell, A.M., Hayhurst, B., 2018. Assessing the impact of site-specific BMPs using a spatially explicit, field-scale SWAT model with edge-of-field and tile hydrology and water-quality data in the Eagle Creek Watershed, Ohio. Water (Switzerland) 10. https://doi.org/10.3390/w10101299

Moss, R., Babiker, M., Brinkman, S., Calvo, E., Carter, T., Edmonds, J., Elgizouli, I., Emori, S., Erda, L., Hibbard, K., Jones, R., Kainuma, M., Kelleher, J., Lamarque, J.F., Manning, M., Matthews, B., Meehl, J., Meyer, L., Mitchell, J., Nakicenovic, N., O'Neill, B., Pichs, R., Riahi, K., Rose, S., Runci, P., Stouffer, R., Vuuren, D. van, Weyant, J., Wilbanks, T., Ypersele, J.P. van, Zurek, M., 2008. Towards New Scenarios for Analysis of Emissions, Climate Change, Impacts and Response Strategies, IPCC Expert Meeting Report.

Moss, R.H., Edmonds, J.A., Hibbard, K.A., Manning, M.R., Rose, S.K., van Vuuren, D.P., Carter, T.R., Emori, S., Kainuma, M., Kram, T., Meehl, G.A., Mitchell, J.F.B., Nakicenovic, N., Riahi, K., Smith, S.J., Stouffer, R.J., Thomson, A.M., Weyant, J.P., Wilbanks, T.J., 2010. The next generation of scenarios for climate change research and assessment. Nature 2010 463:7282 463, 747–756. https://doi.org/10.1038/nature08823

Munoz-Caprina R, Parsons JE, Gilliam JW, 1992. Vegetation Filter Strips: Modelling Hydrology and Sediment Movement, in: ASAE Paper. American Society of Agricultural Engineers.

Muttiah, R.S., Wurbs, R.A., 2002. Scale-dependent soil and climate variability effects on watershed water balance of the SWAT model. Journal of Hydrology 256, 264–285. https://doi.org/10.1016/S0022-1694(01)00554-6

Nasta, P., Palladino, M., Ursino, N., Saracino, A., Sommella, A., Romano, N., 2017. Assessing long-term impact of land-use change on hydrological ecosystem functions in a Mediterranean upland agro-forestry catchment. Science of the Total Environment 605–606, 1070–1082.

OECD, 2000. Report of the OECD Pesticide Aquatic Risk Indicators Expert Group. .

Peel, M.C., McMahon, T.A., 2020. Historical development of rainfall-runoff modeling. Wiley Interdisciplinary Reviews: Water 7. https://doi.org/10.1002/WAT2.1471

Peres, D.J., Cancelliere, A., 2018. Modeling impacts of climate change on return period of landslide triggering. Journal of Hydrology 567, 420–434. https://doi.org/10.1016/J.JHYDROL.2018.10.036

Peres, D.J., Cancelliere, A., 2016. Estimating return period of landslide triggering by Monte Carlo simulation. Journal of Hydrology 541, 256–271. https://doi.org/10.1016/J.JHYDROL.2016.03.036

Phomcha, P., Wirojanagud, P., Vangpaisal, T., Thaveevouthti, T., 2012. Modeling the impacts of alternative soil conservation practices for an agricultural watershed with the SWAT model. Procedia Engineering 32, 1205–1213. https://doi.org/10.1016/J.PROENG.2012.02.078

PHUSICOS R&D project - Horizon 2020 [WWW Document], 2019. URL https://phusicos.eu/ (accessed 9.10.21).

Pierce, D.W., Das, T., Cayan, D.R., Maurer, E.P., Miller, N.L., Bao, Y., Kanamitsu, M., Yoshimura, K., Snyder, M.A., Sloan, L.C., Franco, G., Tyree, M., 2013. Probabilistic estimates of future changes in California temperature and precipitation using statistical and dynamical downscaling. Climate Dynamics 40, 839–856. https://doi.org/10.1007/S00382-012-1337-9

Pistocchi, C., Silvestri, N., Rossetto, R., Sabbatini, T., Guidi, M., Baneschi, I., Bonari, E., Trevisan, D., 2012. A Simple Model to Assess Nitrogen and Phosphorus Contamination in Ungauged Surface Drainage Networks: Application to the Massaciuccoli Lake Catchment, Italy. Journal of Environmental Quality 41, 544–553. https://doi.org/10.2134/JEQ2011.0302

Probst, M., Berenzen, N., Lentzen-Godding, A., Schulz, R., 2005. Scenario-based simulation of runoff-related pesticide entries into small streams on a landscape level. Ecotoxicology and Environmental Safety 62, 145–159. https://doi.org/10.1016/J.ECOENV.2005.04.012

QGIS.org, 2021. QGIS Geographic Information System [WWW Document]. Open Source Geospatial Foundation Project.

Rao, S., Riahi, K., 2006. The role of non-CO2 greenhouse gases in climate change mitigation: Long-term scenarios for the 21st century. Energy Journal 27, 177–200. https://doi.org/10.5547/ISSN0195-6574-EJ-VOLSI2006-NOSI3-9

Regione Toscana - SITA: Database Pedologico [WWW Document], n.d. URL http://www502.regione.toscana.it/geoscopio/pedologia.html (accessed 9.7.21).

Remondino, F., El-hakim, S., 2006. Image-based 3D modelling: A review. Photogrammetric Record 21, 269–291. https://doi.org/10.1111/J.1477-9730.2006.00383.X

Renard, K., Foster, G., Weesies, G., Porter, J., 1991. RUSLE: Revised universal soil loss equation. Journal of Soil and Water Conservation 46.

Rossetto, R., Basile, P., Cannavò, S., Pistocchi, C., Sabbatini, T., Silvestri, N., Bonari, E., 2010. Surface water and groundwater monitoring and numerical modeling of the southern sector of the Massaciuccoli Lake basin, in: Società Geologica Italiana (Ed.), Rendiconti Online Società Geologica Italiana,. Pisa.

Roth, V., Lemann, T., 2016. Comparing CFSR and conventional weather data for discharge and soil loss modelling with SWAT in small catchments in the Ethiopian Highlands. Hydrology and Earth System Sciences 20, 921–934. https://doi.org/10.5194/HESS-20-921-2016

Rouzies, E., Lauvernet, C., Barachet, C., Morel, T., Branger, F., Braud, I., Carluer, N., 2019. From agricultural catchment to management scenarios: A modular tool to assess effects of landscape features on water and pesticide behaviour. Science of The Total Environment 671, 1144–1160. https://doi.org/10.1016/J.SCITOTENV.2019.03.060

Ruiz-Colmenero, M., Bienes, R., Eldridge, D.J., Marques, M.J., 2013. Vegetation cover reduces erosion and enhances soil organic carbon in a vineyard in the central Spain. Catena 104, 153–160.

Saha, S., Moorthi, S., Pan, H.-L., Wu, X., Wang, Jiande, Nadiga, S., Tripp, P., Kistler, R., Woollen, J., Behringer, D., Liu, H., Stokes, D., Grumbine, R., Gayno, G., Wang, Jun, Hou, Y.-T., Chuang, H., Juang, H.-M.H., Sela, J., Iredell, M., Treadon, R., Kleist, D., Delst, P. van, Keyser, D., Derber, J., Ek, M., Meng, J., Wei, H., Yang, R., Lord, S., Dool, H. van den, Kumar, A., Wang, W., Long, C., Chelliah, M., Xue, Y.,

Huang, B., Schemm, J.-K., Ebisuzaki, W., Lin, R., Xie, P., Chen, M., Zhou, S., Higgins, W., Zou, C.-Z., Liu, Q., Chen, Y., Han, Y., Cucurull, L., Reynolds, R.W., Rutledge, G., Goldberg, M., 2010. The NCEP Climate Forecast System Reanalysis. Bulletin of the American Meteorological Society 91, 1015–1058. https://doi.org/10.1175/2010BAMS3001.1

Sajikumar, N., Remya, R.S., 2015. Impact of land cover and land use change on runoff characteristics. Journal of Environmental Management 161, 460–468. https://doi.org/10.1016/J.JENVMAN.2014.12.041

Saxton, K.E., Rawls, W.J., 2006. Soil Water Characteristic Estimates by Texture and Organic Matter for Hydrologic Solutions. Soil Science Society of America Journal 70, 1569–1578. https://doi.org/10.2136/SSSAJ2005.0117

Schmidli, J., Frei, C., Vidale, P.L., 2006. Downscaling from GCM precipitation: a benchmark for dynamical and statistical downscaling methods. International Journal of Climatology 26, 679–689. https://doi.org/10.1002/JOC.1287

Schwarz, G.E., Alexander, R.B., 1995. State Soil Geographic (STATSGO) Data Base for the Conterminous United States. Open-File Report. https://doi.org/10.3133/OFR95449

Shanshan, W., Baoyang, S., Chaodong, L., Zhanbin, L., Bo, M., 2018. Runoff and Soil Erosion on Slope Cropland: A Review. https://doi.org/10.5814/j.issn.1674-764x.2018.05.002 9, 461–470. https://doi.org/10.5814/J.ISSN.1674-764X.2018.05.002

Sharpley, A.N., 1985. Depth of Surface Soil-runoff Interaction as Affected by Rainfall, Soil Slope, and Management. Soil Science Society of America Journal 49, 1010–1015. https://doi.org/10.2136/SSSAJ1985.03615995004900040044X

Shrestha, N.K., Rudra, R.P., Daggupati, P., Goel, P.K., Shukla, R., 2021. A comparative evaluation of the continuous and event-based modelling approaches for identifying critical source areas for sediment and phosphorus losses. Journal of Environmental Management 277, 111427. https://doi.org/10.1016/J.JENVMAN.2020.111427

Silvestri, N., Pistocchi, C., Antichi, D., 2017. Soil and Nutrient Losses in a Flat Land-Reclamation District of Central Italy. Land Degradation & Development 28, 638–647. https://doi.org/10.1002/LDR.2549

Silvestri, N., Risaliti, R., Ginanni, M., Accogli, D., Sabbatini, T., Tozzini, C., 2002. Application of a georeferenced soil database in a protected area of Migliarino San Rossore Massaciuccoli Park, in: Proceedings of VII Congress of the European Society for Agronomy. Cordoba (ES).

Sinnathamby, S., Douglas-Mankin, K.R., Craige, C., 2017. Field-scale calibration of crop-yield parameters in the Soil and Water Assessment Tool (SWAT). Agricultural Water Management 180, 61–69. https://doi.org/10.1016/J.AGWAT.2016.10.024

STATSGO2 Database [WWW Document], n.d. URL https://water.usgs.gov/GIS/metadata/usgswrd/XML/ussoils.xml (accessed 8.30.21).

Stehle, S., Dabrowski, J.M., Bangert, U., Schulz, R., 2016. Erosion rills offset the efficacy of vegetated buffer strips to mitigate pesticide exposure in surface waters. Science of The Total Environment 545–546, 171–183. https://doi.org/10.1016/J.SCITOTENV.2015.12.077

Tan, M.L., Gassman, P.W., Yang, X., Haywood, J., 2020. A review of SWAT applications, performance and future needs for simulation of hydro-climatic extremes. Advances in Water Resources 143.
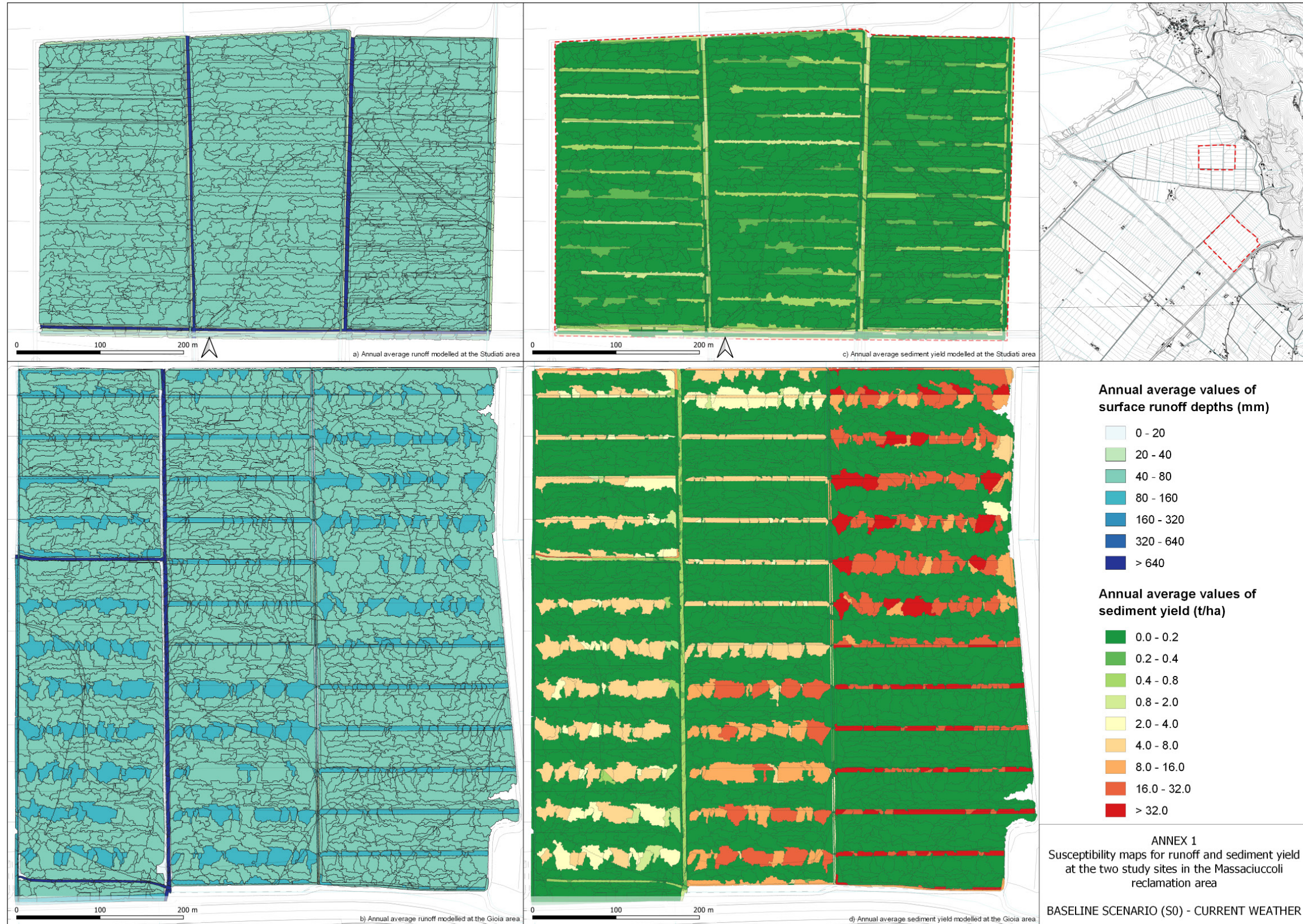
Teutschbein, C., Seibert, J., 2012. Bias correction of regional climate model simulations for hydrological climate-change impact studies: Review and evaluation of different methods. Journal of Hydrology 456–457, 12–29.

Tuppad, P., Kannan, N., Srinivasan, R., Rossi, C.G., Arnold, J.G., 2010. Simulation of Agricultural Management Alternatives for Watershed Protection. Water Resources Management 24, 3115–3144. https://doi.org/10.1007/S11269-010-9598-8
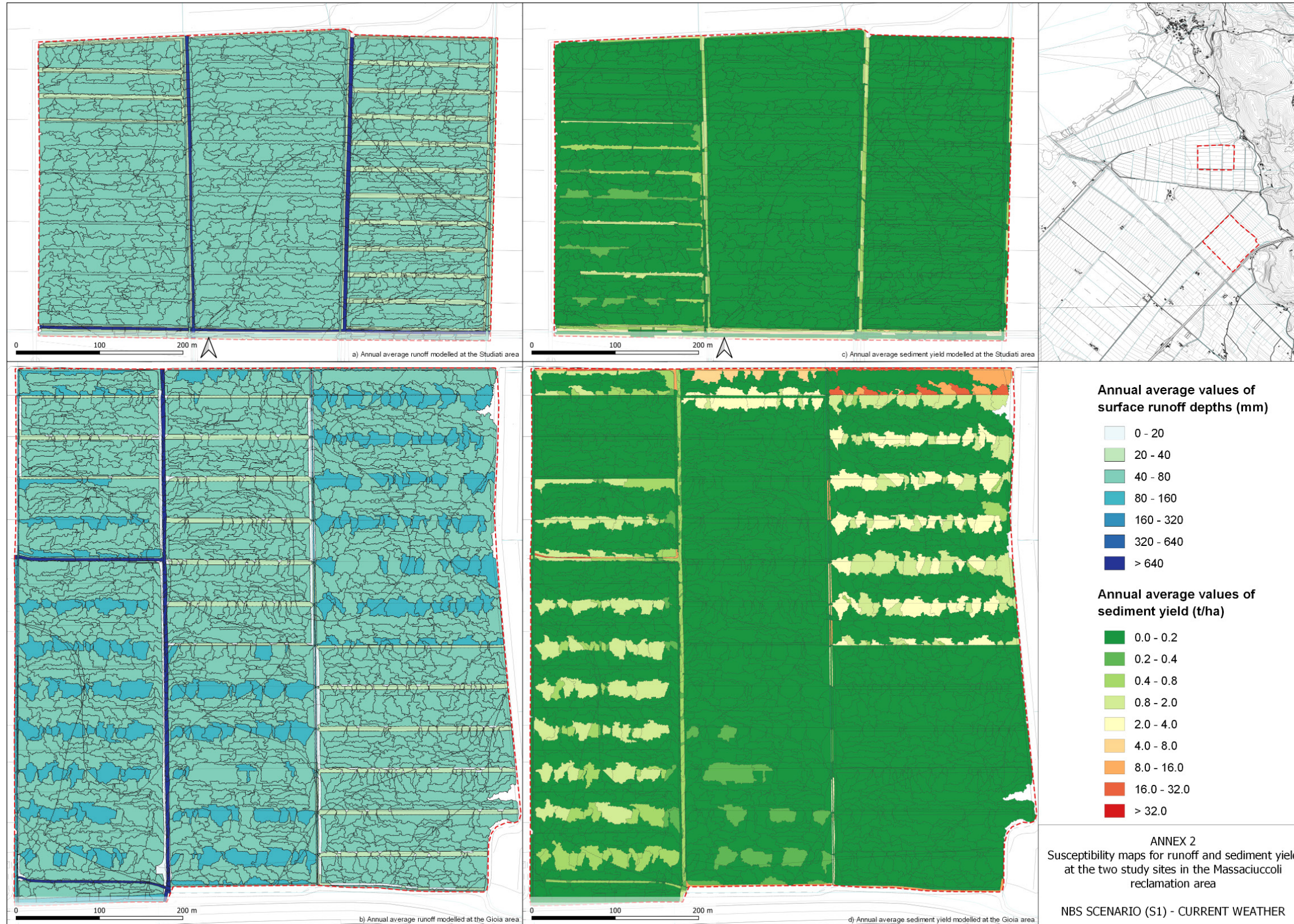
Tuscany Region, 2021. SIR -DATA / Historical Archive [WWW Document]. URL http://www.sir.toscana.it/consistenza-rete (accessed 10.4.21).

Ullrich, A., Volk, M., 2009. Application of the Soil and Water Assessment Tool (SWAT) to predict the impact of alternative management practices on water quality and quantity. Agricultural Water Management 96, 1207–1217. https://doi.org/10.1016/J.AGWAT.2009.03.010

UNDRR, 2020. Hazard Definition & classification review. Hazard Definition & Classification Reviewazard Definition & Classification Review.

USDA, S.S.S., 1999. Soil taxonomy: A basic system of soil classification for making and interpreting soil surveys, Second Edition. ed, Agriculture handbook. United States Department of Agriculture - Natural Resources Conservation Service.

van Westen, C.J., van Asch, T.W.J., Soeters, R., 2006. Landslide hazard and risk zonation - Why is it still so difficult? Bulletin of Engineering Geology and the Environment 65, 167–184. https://doi.org/10.1007/S10064-005-0023-0

Vesely, F.M., Paleari, L., Movedi, E., Bellocchi, G., Confalonieri, R., 2019. Quantifying Uncertainty Due to Stochastic Weather Generators in Climate Change Impact Studies. Scientific Reports 2019 9:1 9, 1–8. https://doi.org/10.1038/s41598-019-45745-4

Volkwein, A., Schellenberg, K., Labiouse, V., Agliardi, F., Berger, F., Bourrier, F., Dorren, L.K.A., Gerber, W., Jaboyedoff, M., 2011. Rockfall characterisation and structural protection - A review. Natural Hazards and Earth System Science 11, 2617–2651. https://doi.org/10.5194/NHESS-11-2617-2011

Volpi, E., 2019. On return period and probability of failure in hydrology. Wiley Interdisciplinary Reviews: Water 6, e1340. https://doi.org/10.1002/WAT2.1340

Wallace, C.W., Flanagan, D.C., Engel, B.A., 2017. Quantifying the effects of conservation practice implementation on predicted runoff and chemical losses under climate change. Agricultural Water Management 186, 51–65. https://doi.org/10.1016/J.AGWAT.2017.02.014

Westoby, M.J., Brasington, J., Glasser, N.F., Hambrey, M.J., Reynolds, J.M., 2012. "Structure-from-Motion" photogrammetry: A low-cost, effective tool for geoscience applications. Geomorphology 179, 300–314.

White, M.J., Arnold, J.G., 2009. Development of a simplistic vegetative filter strip model for sediment and nutrient retention at the field scale. Hydrological Processes 23, 1602–1616. https://doi.org/10.1002/HYP.7291

Wilby, R.L., Wigley, T.M.L., 2016. Downscaling general circulation model output: a review of methods and limitations: 21, 530–548. https://doi.org/10.1177/030913339702100403

WILLIAMS, J.R., 2015. Runoff and Water Erosion. Modeling Plant and Soil Systems 439–455. https://doi.org/10.2134/AGRONMONOGR31.C18

Williams, J.R., 1995. The EPIC Model, in: Singh, V.P. (Ed.), Computer Models of Watershed Hydrology. Water Resources Publications, pp. 909–1000.

Williams, J.R., 1975. Sediment-yield prediction with universal equation using runoff energy factor. Sediment-Yield Workshop, Present and Prospective Technol for Predict Sediment Yields and Sources, Proc, USDA Sediment Lab,.

Yalew, S., van Griensven, A., Ray, N., Kokoszkiewicz, L., Betrie, G.D., 2013. Distributed computation of large scale SWAT models on the Grid. Environmental Modelling & Software 41, 223–230. https://doi.org/10.1016/J.ENVSOFT.2012.08.002

Zhao, W.J., Sun, W., Li, Z.L., Fan, Y.W., Song, J.S., Wang, L.R., 2013. A Review on SWAT Model for Stream Flow Simulation. Advanced Materials Research 726–731, 3792–3798. https://doi.org/10.4028/www.scientific.net/amr.726-731.3792
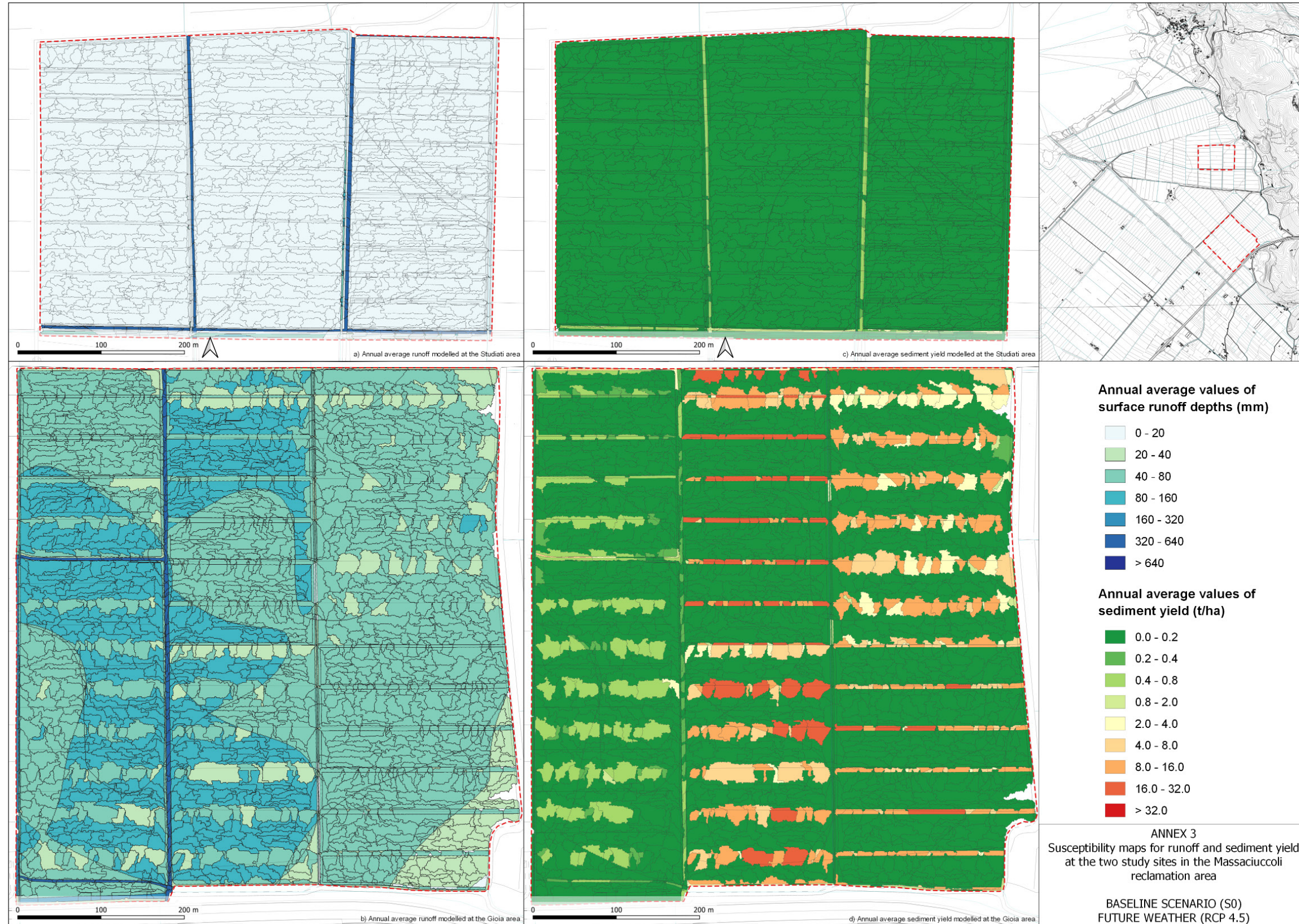
2.9 ANNEX 1 – Susceptibility maps for runoff and sediment yield at the two study sites in the Massaciuccoli reclamation area - BASELINE SCENARIO (S0) – CURRENT WEATHER

a) Annual average runoff modelled at the Studiati area

c) Annual average sediment yield modelled at the Studiati area

b) Annual average runoff modelled at the Gioia area

d) Annual average sediment yield modelled at the Gioia area

Annual average values of surface runoff depths (mm)

- 0 – 20
- 20 – 40
- 40 – 80
- 80 – 160
- 160 – 320
- 320 – 640
- > 640

Annual average values of sediment yield (t/ha)

- 0.0 – 0.2
- 0.2 – 0.4
- 0.4 – 0.8
- 0.8 – 2.0
- 2.0 – 4.0
- 4.0 – 8.0
- 8.0 – 16.0
- 16.0 – 32.0
- > 32.0

ANNEX 1
Susceptibility maps for runoff and sediment yield at the two study sites in the Massaciuccoli reclamation area

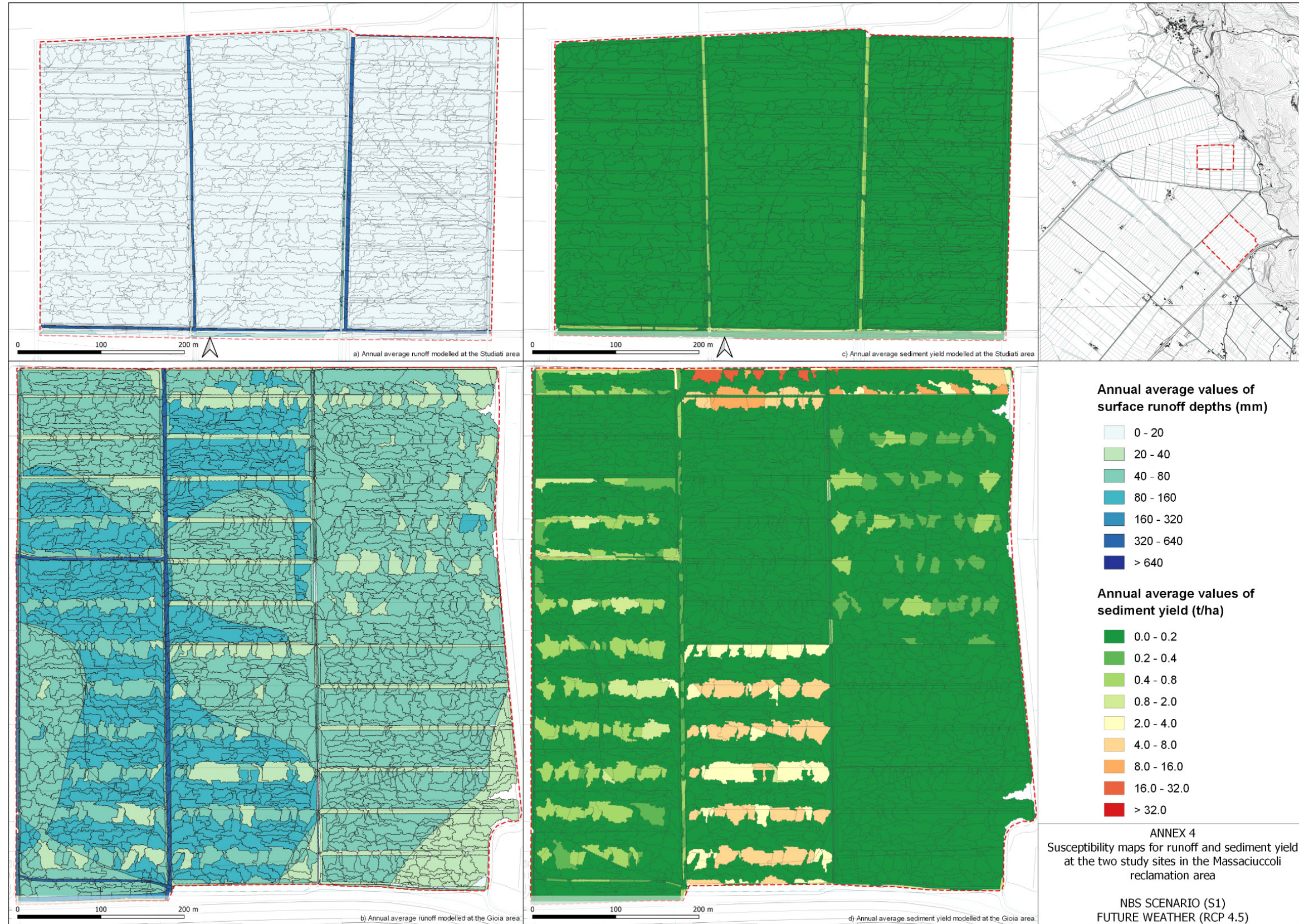BASELINE SCENARIO (S0) - CURRENT WEATHER

2.10 ANNEX 2 – Susceptibility maps for runoff and sediment yield at the two study sites in the Massaciuccoli reclamation area - NBS SCENARIO (S1) – CURRENT WEATHER
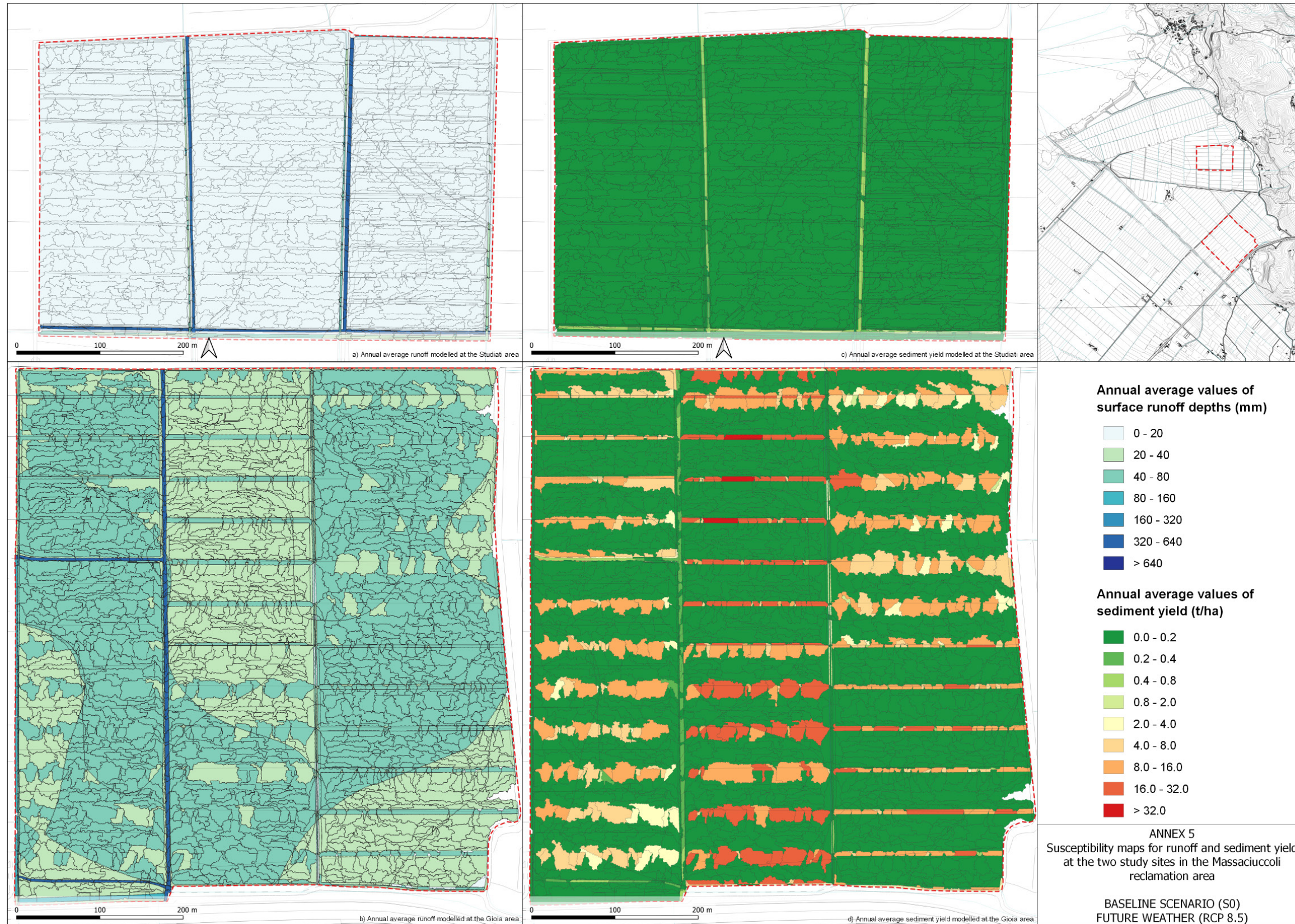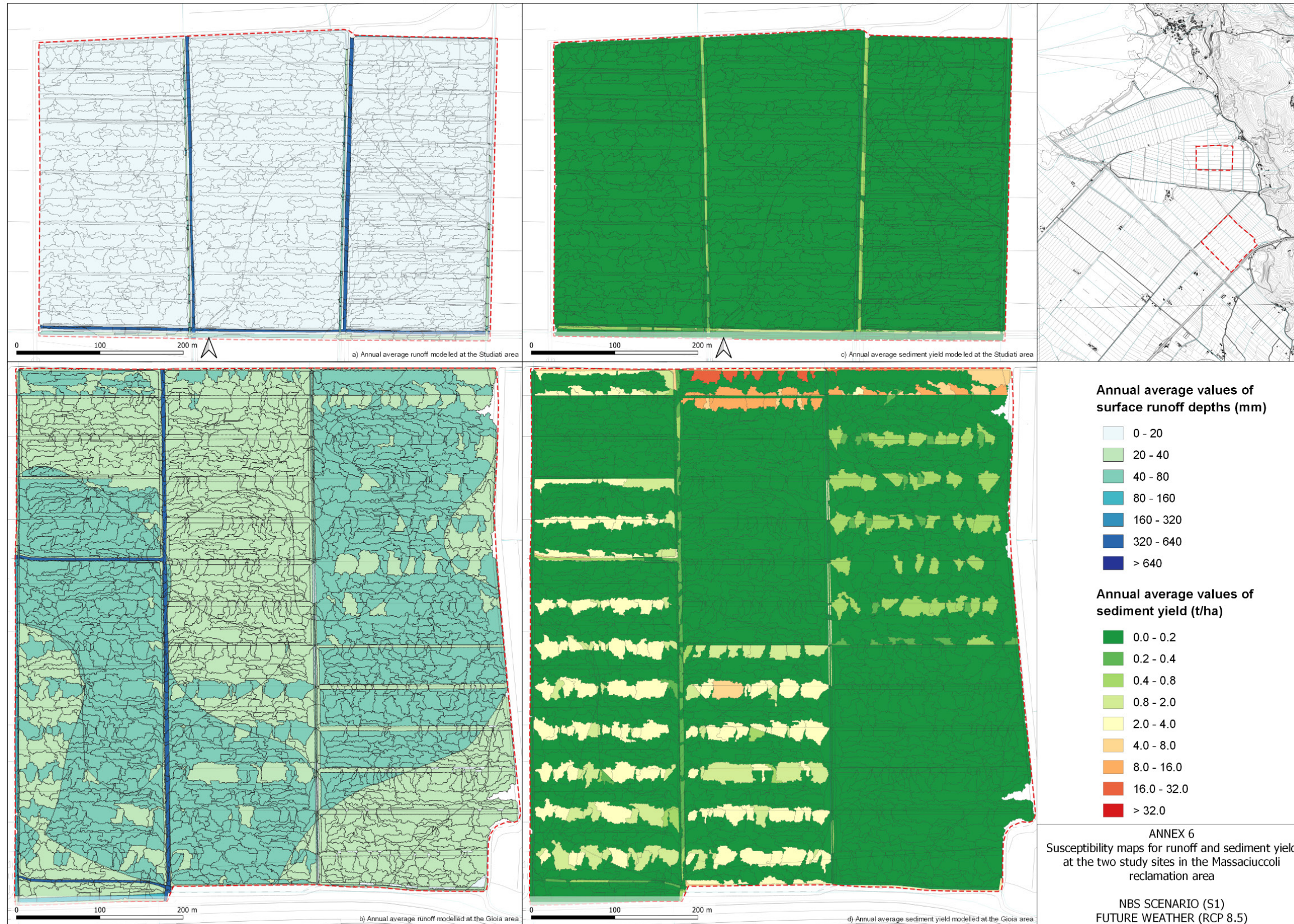

a) Annual average runoff modelled at the Studiati area

c) Annual average sediment yield modelled at the Studiati area

b) Annual average runoff modelled at the Gioia area

d) Annual average sediment yield modelled at the Gioia area

Annual average values of surface runoff depths (mm)

- 0 - 20
- 20 - 40
- 40 - 80
- 80 - 160
- 160 - 320
- 320 - 640
- > 640

Annual average values of sediment yield (t/ha)

- 0.0 - 0.2
- 0.2 - 0.4
- 0.4 - 0.8
- 0.8 - 2.0
- 2.0 - 4.0
- 4.0 - 8.0
- 8.0 - 16.0
- 16.0 - 32.0
- > 32.0

ANNEX 2
Susceptibility maps for runoff and sediment yield at the two study sites in the Massaciuccoli reclamation area

NBS SCENARIO (S1) - CURRENT WEATHER

2.11   ANNEX 3 – Susceptibility maps for runoff and sediment yield at the two study sites in the Massaciuccoli reclamation area - BASELINE SCENARIO (S0) – FUTURE WEATHER (RCP 4.5)

a) Annual average runoff modelled at the Studiati area

c) Annual average sediment yield modelled at the Studiati area

b) Annual average runoff modelled at the Gioia area

d) Annual average sediment yield modelled at the Gioia area

Annual average values of surface runoff depths (mm)

- 0 - 20
- 20 - 40
- 40 - 80
- 80 - 160
- 160 - 320
- 320 - 640
- > 640

Annual average values of sediment yield (t/ha)

- 0.0 - 0.2
- 0.2 - 0.4
- 0.4 - 0.8
- 0.8 - 2.0
- 2.0 - 4.0
- 4.0 - 8.0
- 8.0 - 16.0
- 16.0 - 32.0
- > 32.0

ANNEX 3
Susceptibility maps for runoff and sediment yield
at the two study sites in the Massaciuccoli
reclamation area

BASELINE SCENARIO (S0)
FUTURE WEATHER (RCP 4.5)

2.12 ANNEX 4 – Susceptibility maps for runoff and sediment yield at the two study sites in the Massaciuccoli reclamation area - NBS SCENARIO (S1) – FUTURE WEATHER (RCP 4.5)

a) Annual average runoff modelled at the Studiati area

c) Annual average sediment yield modelled at the Studiati area

b) Annual average runoff modelled at the Gioia area

d) Annual average sediment yield modelled at the Gioia area

Annual average values of surface runoff depths (mm)

- 0 - 20
- 20 - 40
- 40 - 80
- 80 - 160
- 160 - 320
- 320 - 640
- > 640

Annual average values of sediment yield (t/ha)

- 0.0 - 0.2
- 0.2 - 0.4
- 0.4 - 0.8
- 0.8 - 2.0
- 2.0 - 4.0
- 4.0 - 8.0
- 8.0 - 16.0
- 16.0 - 32.0
- > 32.0

ANNEX 4
Susceptibility maps for runoff and sediment yield at the two study sites in the Massaciuccoli reclamation area

NBS SCENARIO (S1)
FUTURE WEATHER (RCP 4.5)

2.13 ANNEX 5 – Susceptibility maps for runoff and sediment yield at the two study sites in the Massaciuccoli reclamation area - BASELINE SCENARIO (S0) – FUTURE WEATHER (RCP 8.5)

a) Annual average runoff modelled at the Studiati area

c) Annual average sediment yield modelled at the Studiati area

b) Annual average runoff modelled at the Gioia area

d) Annual average sediment yield modelled at the Gioia area

Annual average values of surface runoff depths (mm)

- 0 - 20
- 20 - 40
- 40 - 80
- 80 - 160
- 160 - 320
- 320 - 640
- > 640

Annual average values of sediment yield (t/ha)

- 0.0 - 0.2
- 0.2 - 0.4
- 0.4 - 0.8
- 0.8 - 2.0
- 2.0 - 4.0
- 4.0 - 8.0
- 8.0 - 16.0
- 16.0 - 32.0
- > 32.0

ANNEX 5
Susceptibility maps for runoff and sediment yield at the two study sites in the Massaciuccoli reclamation area

BASELINE SCENARIO (S0)
FUTURE WEATHER (RCP 8.5)

2.14 ANNEX 6 – Susceptibility maps for runoff and sediment yield at the two study sites in the Massaciuccoli reclamation area - NBS SCENARIO (S1) – FUTURE WEATHER (RCP 8.5)

a) Annual average runoff modelled at the Studiati area

c) Annual average sediment yield modelled at the Studiati area

b) Annual average runoff modelled at the Gioia area

d) Annual average sediment yield modelled at the Gioia area

Annual average values of surface runoff depths (mm)

- 0 - 20
- 20 - 40
- 40 - 80
- 80 - 160
- 160 - 320
- 320 - 640
- > 640

Annual average values of sediment yield (t/ha)

- 0.0 - 0.2
- 0.2 - 0.4
- 0.4 - 0.8
- 0.8 - 2.0
- 2.0 - 4.0
- 4.0 - 8.0
- 8.0 - 16.0
- 16.0 - 32.0
- > 32.0

ANNEX 6
Susceptibility maps for runoff and sediment yield at the two study sites in the Massaciuccoli reclamation area

NBS SCENARIO (S1)
FUTURE WEATHER (RCP 8.5)

3 Hazard modelling in Gudbrandsdalen Valley, Norway

3.1 Case study

The Gudbrandsdalen Valley is one of the most populated rural areas in Norway, extending for roughly 140 km from the town of Lillehammer, in the south side, to the village of Dombås, in the north. The wide floodplains extending along the river are extensively designated as farmland, but many scattered residential settlements with public facilities connected by public roads are also available, that sporadically bridge over the river.

The valley and side valleys are exposed to a range of hydro-meteorological hazards, flooding in the main river and in the tributary rivers, debris flows and debris slides, rockfall and snow avalanches.

One of the NBS interventions that has been proposed for the Gudbrandsdalen case site consists in a receded floor barrier to be implemented in the lower side of river Gausa, a tributary river to Gudbrandsdalslågen, at Jorekstad in the town of Lillehammer (Figure 15).

The river Gausa experiences frequent flooding, with occasional extreme events, such as in 1995, 2011 and 2013. The frequency and severity of extreme events are expected to increase over the coming decades. The lower parts of Gausa at Jorekstad, where the river moves across Gudbrandsdalslågen, is particularly vulnerable to floods since the confluence area between the two rivers has been repeatedly damaged during past flooding events (Oppland County Administration, 2021). This has been threatening the agricultural land, as well as housing and public facilities in Jorekstad, such as a football pitch with bleachers, an outside pool, a sports centre and a school. Moreover, eroded sediments from Gausa have been depositing in the confluence zone over the years, changing the river bottom form and thereby enhancing the flooding effects (Solheim, et al., 2021).

3.1.1 NBS design

The area where the NBS is supposed to be implemented is a private land in the Lillehammer municipality with a total extension of 7.28 km^2. The planned NBS consists of a receded flood barrier along the lower reaches of the Gausa River having a total length of 2878 m split into three sections of 2682, 133 and 63 m, respectively. Given that the floodplain along Gausa has a riparian forest with several endangered species and a valuable biodiversity, the flood barrier was located outside of the forest with the aim to re-establish the natural floodplain processes that have been jeopardized by an existing grey barrier (Solheim, et al., 2021) (Figure 16).
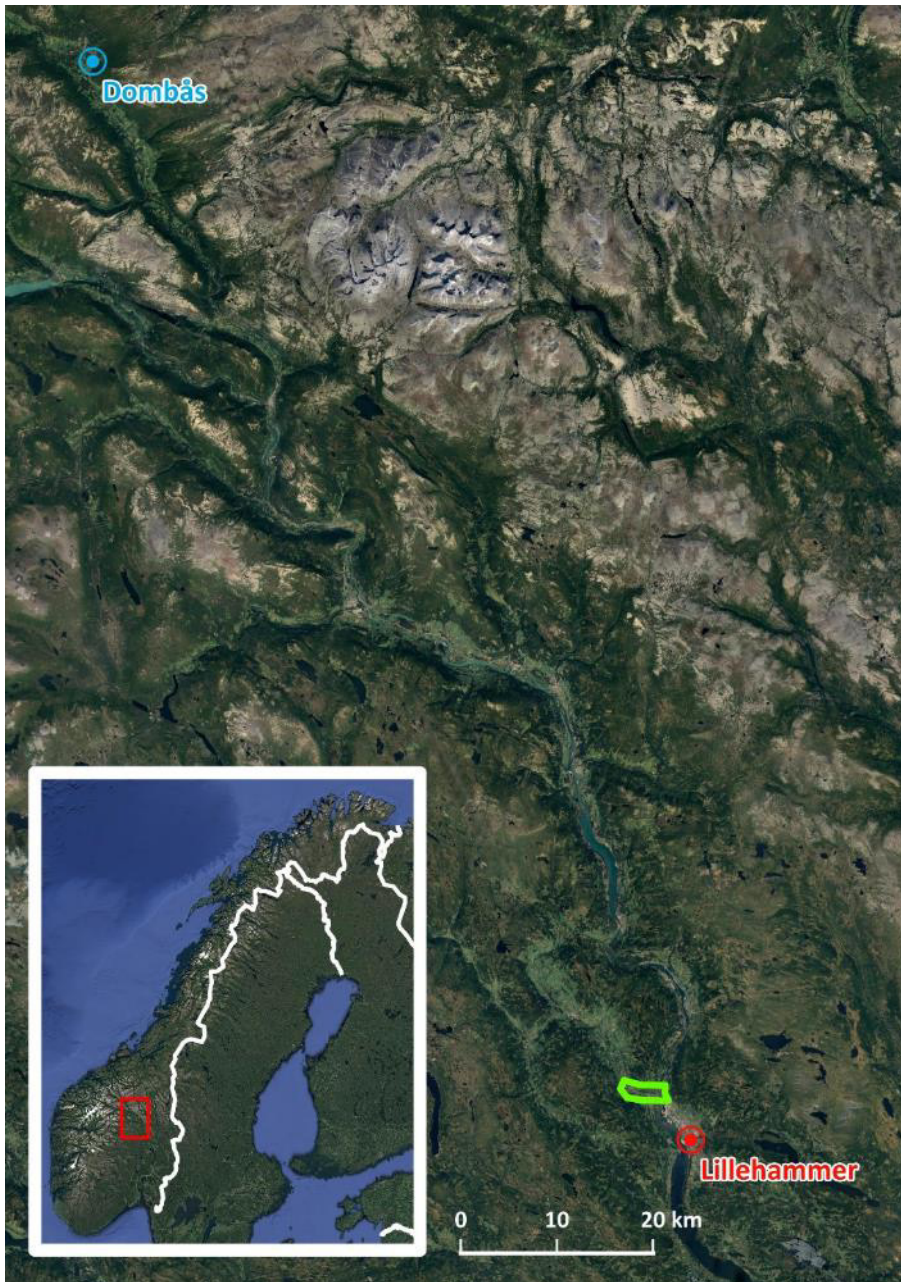
Figure 15: Location of the valley of Gudbrandsdalen in Norway (bottom left) and location of Jorekstad study area, marked in green, in the valley of Gudbrandsdalen.

The planned NBS should have been made of earth and its elevation ranges from 0 to about 3 m above ground level. It has a flat crown of 4 m wide with 2:1 sloped sides (Figure 17). It would have reduced the energy of the river Gausa before it conveys into the main river and protected farms and surrounding agricultural lands, as well as urban settlements and public facilities at Jorekstad.
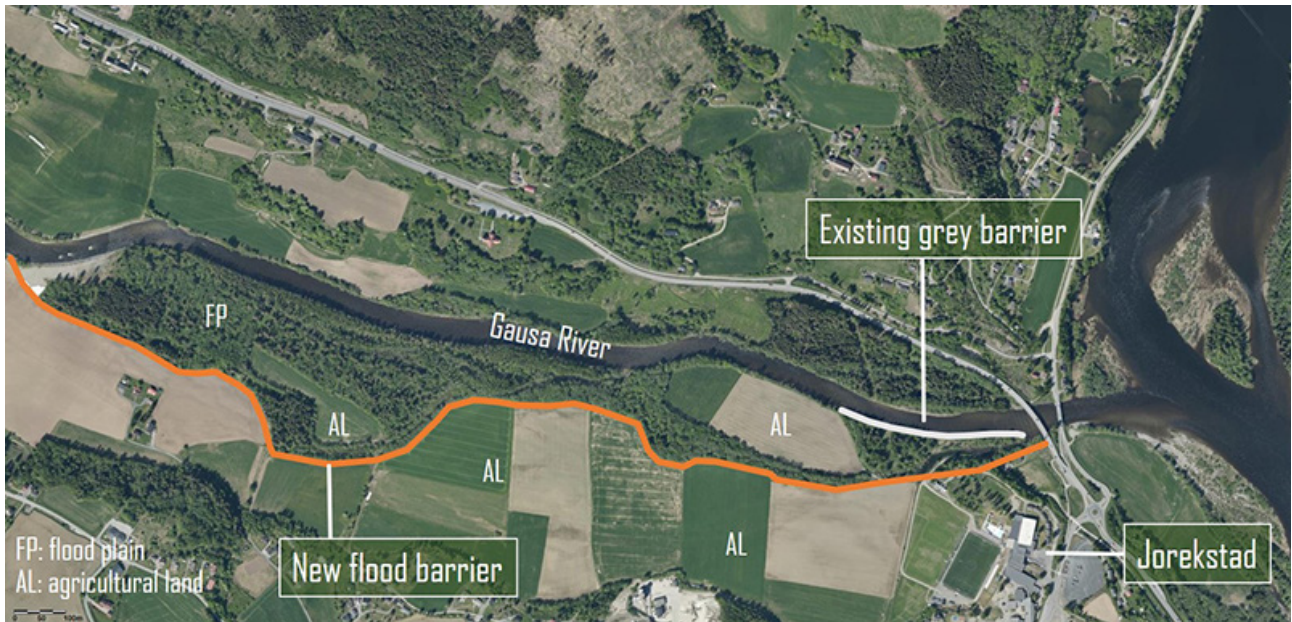
Figure 16: Aerial photo of the area with the location of the receded flood barrier and of the existing one **Ugyldig kilde er angitt..**
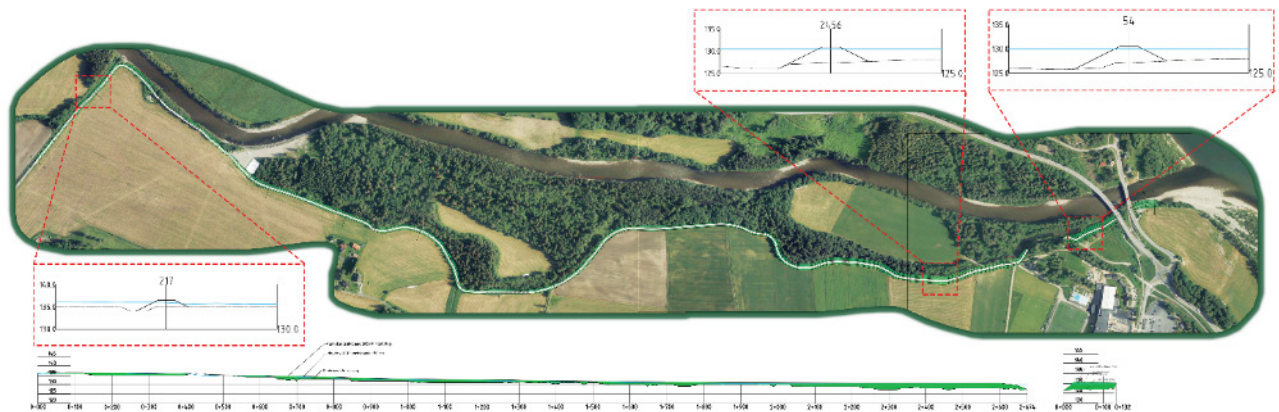
Figure 17: Top view, lengthwise section and some average cross sections of the planned receded flood barrier.

3.1.2 Hydro-meteorological hazards of concern

Floods are acknowledged to be one of the most dangerous and widespread climate-related natural hazards (Jonkman, 2005). They are estimated to be responsible for almost 15% of the total economic losses due to natural hazard events, involving about 50% of the total population exposed by their effects in 2018 (CRED, 2018). Due to climate change, the intensity of the extreme rainfall events is predicted to increase all over the world (Groisman, et al., 2005), and it will potentially lead towards an increase in the magnitude of extreme flows with relevant implications for landowners, flood mitigation strategies, and infrastructure design (Eccles, Zhang, & Hamilton, 2019). Flooding is not only responsible for disease on urban environment, causing damage and losses of life, property, infrastructures and disruption of public services (Talbot, et al., 2018). It can

also provoke the loss of food crops and livestock and the depletion of soil quality due to oxygen deficiency (Atta-ur-Rahman & Khan, 2011; Akpoveta, Osakwe, Ize-Iyamu, Medjor, & Egharevba, 2014; Walls, Heller Wardrop, & Brooks, 2005). Flood hazard modelling was implemented using statistical-probabilistic techniques applied to assess the annual maximum series values of both flow rate and precipitation, depending the data availability.

3.1.3   Climatic approach

At the Jorekstad case study, the effectiveness of the planned receded floor barrier was assessed only considering the current climatic scenario. This choice was due to the assumption that the average expected useful life of this kind of NBS is about 25-30 years, thus a time span not long enough to consider long-term climatic variations (years up to 2100). Namely, assessing the effectiveness of the planned NBS by the end of the century is outside the scope of this modelling activity, given the distant time horizon is not relevant for assessing the flood barrier efficacy.

3.2   Analysis methods

3.2.1   Introduction to modelling approach

To achieve the target of mapping the flood hazard for both the baseline and the NBS scenarios, the study contemplated different modelling procedures. These included climate, hydrological, hydraulic and flood modelling structured in an integrated workflow as showed in Figure 18 and discussed in the following sections.

Climate modelling allowed calculating the intensity-duration-frequency (IDF) curves through a disaggregation procedure of rainfall data measured at a local weather station. By processing a Digital Elevation Model (DEM) in a GIS environment, the watershed boundary was identified, and its extension, length and slope were derived. These worked as input data of the hydrological model, useful to assess the amounts of stream flow generated by rainfall extreme events. The hydrological model computed the extreme values by taking into account rainfall data time series, topography, soil type and land use-land cover features of the watershed. The outputs of hydrological model were the *soil curve number* (*CN*) and the design hydrographs.

In the frame of this work, the hydraulic model was applied to process the DEM and the hydrograph at the inlet section identified on the river network, aimed at computing the stream flow conditions such as flow velocity, flow depth and the possible flooded areas, by using the software FLO-2D, as in depth described in the next sections.
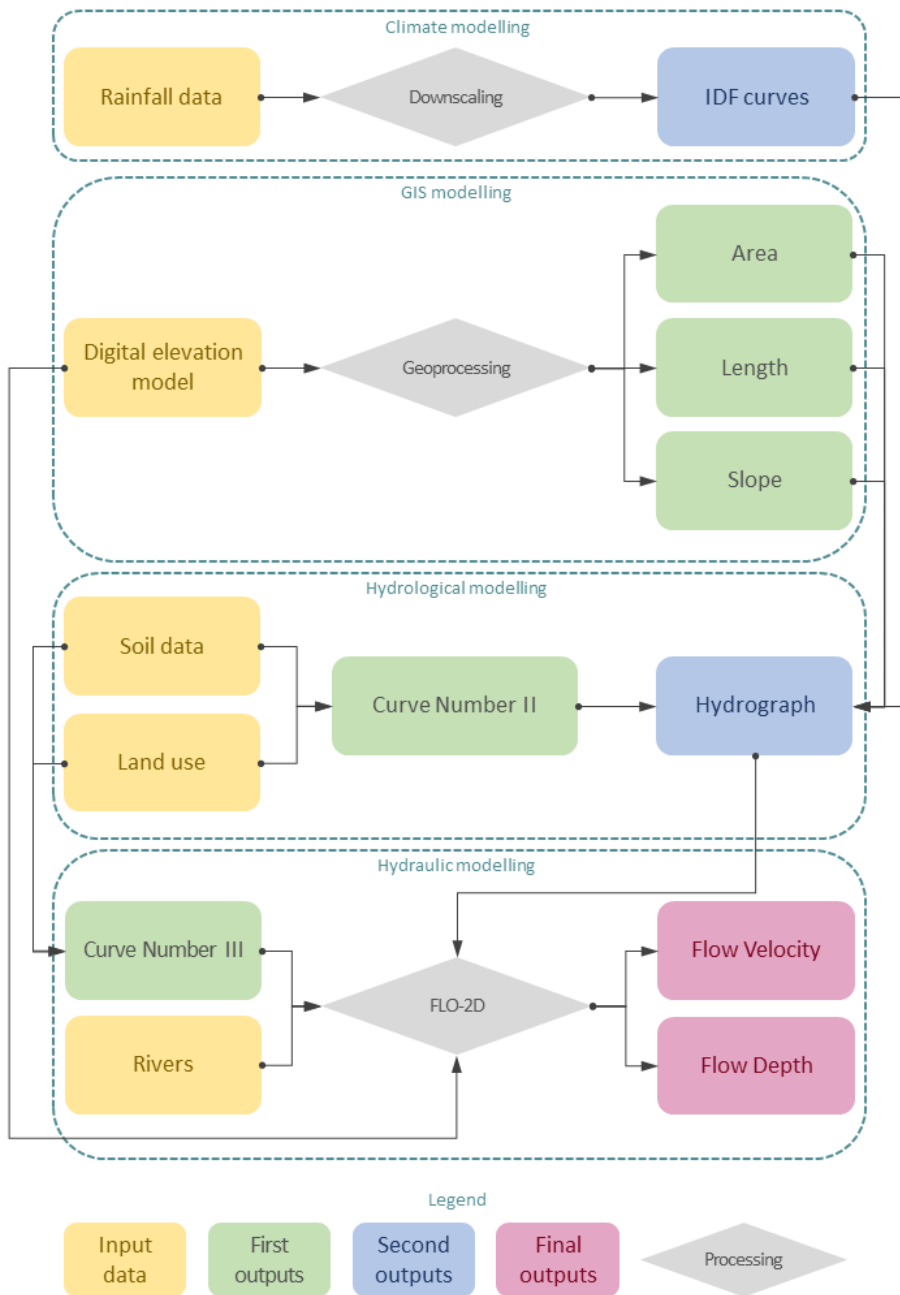
Figure 18: Flow chart of the methodology used for Jorekstad case study.

3.3   Data processing

3.3.1   Climate modelling

Climate modelling is a challenging task since it needs intensive and high-quality rainfall data. It requires long time series data and a minimum of hourly data to simulate future

flood scenarios. In this work, the climate modelling procedure involved the steps described hereunder.

- Selection of meteorological stations: the meteorological stations of Lillehammer, located 7 km far from Jorekstad, just outside the investigated watershed, was selected because the rainfall data from this station were able to significantly contribute to flooding simulation at Jorekstad (Figure 19). Moreover, the rainfall data of Gjøvik and Hamar stations were excluded from the analysis since they are located outside the watershed and thus too far from the study area, 42 and 56 km, respectively. The FLO-2D model used in the analysis requires an input of extreme values of rainfall distribution and rainfall intensities.

- IDF curve development: the Norwegian Centre for Climate Services (NCCS) provides the rainfall intensity in the form of Intensity-Duration-Frequency (IDF values) from more than 80 stations all over Norway, based on a minimum of 10 seasons. For Lillehammer station IDF values were developed considering 23 seasons, from 1969 to 1991[1]. Starting from the extreme value results made available by NCSS, the IDF curve was derived with reference to the return periods of 2, 5, 10, 20, 25, 50, 100 and 200-year to be used for both the simulations in the FLO-2D environment and the calculation of the rainfall intensity.
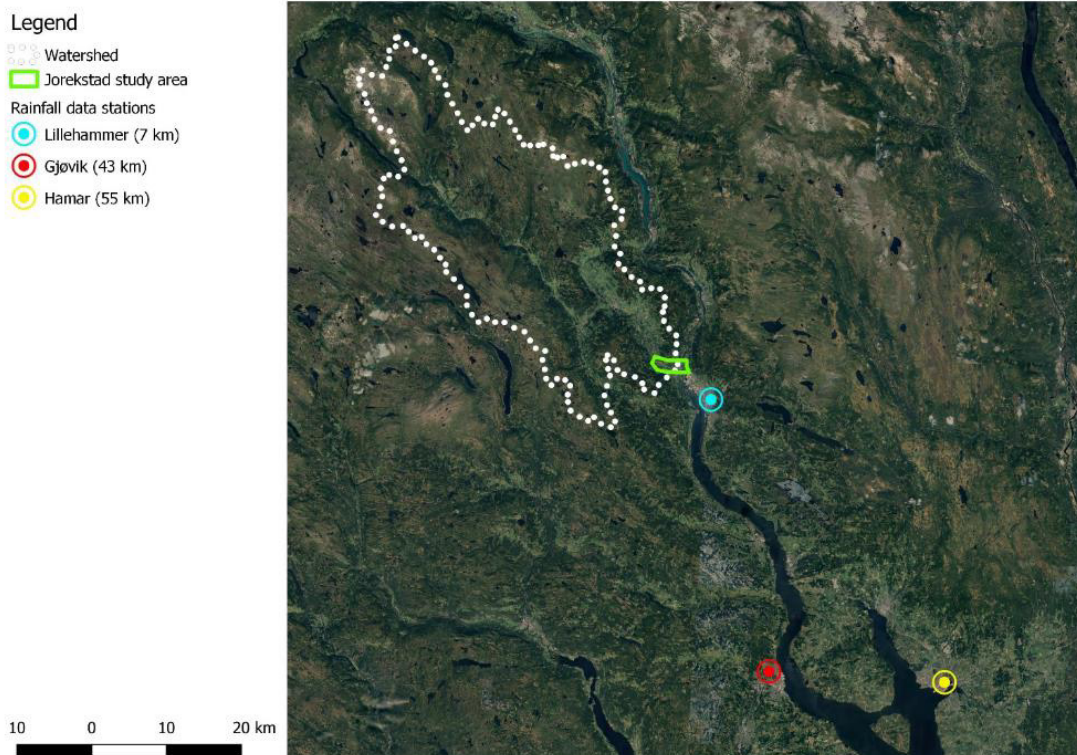
Figure 19: Aerial photo of the watershed with the location of the closest rainfall data stations.

---

[1] NCCS specifies that for measures and infrastructure with a short lifetime, as the planned receded floor barrier at Jorekstad is, current design value can be used without any climate change allowance.

Table 4: Rainfall Depth h *[mm] of Lillehammer station (source: NCCS)*

Return Period T [years]	Duration d [hr; min]														
	0.017 hr (1 min)	0.034 hr (2 min)	0.050 hr (3 min)	0.083 hr (5 min)	0.167 hr (10 min)	0.250 hr (15 min)	0.333 hr (20 min)	0.50 hr (30 min)	0.75 hr (45 min)	1 hr (60 min)	1.50 hr (90 min)	3 hr (180 min)	6 hr (360 min)	12 hr (720 min)	24 hr (1440 min)
2	1.3	2.2	2.8	3.9	5.7	6.7	7.4	8.4	9.8	10.5	11.7	15.4	20.8	26.8	33.7
5	1.5	2.6	3.4	4.8	6.6	7.8	8.4	9.6	11.7	12.6	13.8	18.3	25.5	30.7	38.9
10	1.7	3	3.8	5.4	7.2	8.4	9.1	10.5	13	14	15.2	20.1	28.9	33.3	43.2
20	1.9	3.3	4.2	6	7.7	9.1	9.8	11.2	14.3	15.3	16.5	21.9	32.0	35.4	46.7
25	2	3.4	4.4	6.2	7.9	9.3	10	11.5	14.7	15.7	17	22.5	33.0	36.3	47.5
50	2.1	3.7	4.7	6.7	8.4	9.9	10.7	12.2	15.9	17	18.2	24.2	36.1	38.4	51
100	2.3	4	5.1	7.3	9	10.6	11.3	13	17.1	18.3	19.5	25.9	39.1	40.6	54.4
200	2.6	4.4	5.6	7.8	9.5	11.1	11.8	13.6	18.1	19.4	20.7	27.6	42.3	42.8	57.9

- <u>Intensity estimation</u>: rainfall intensity is calculated as the average rainfall depth *hr* that falls per time increment *i = hr/d*, where *d* is the rainfall duration measured in millimetre per hour (De Paola, Giugni, Topa, & Bucchignani, 2014). The rainfall intensity *hr* for a given return period *T* and duration *d* can be calculated from a bi-parameter power-law **Ugyldig kilde er angitt.**.

$$hr(T) = a(T) \cdot d^n \qquad (1)$$

where:
- *T* is the return period [years]
- *d* is the rainfall duration [h]
- *a* [mm/h^n] and *n* [-] are the parameters of the rainfall curve

These parameters can be estimated by a simple linear regression analysis in bi-logarithmic scale as shown below (Figure 20, Table 5).

It is worth nothing that, although the *n* parameter approximates a constant value (0.41), the hydraulic model described below was built considering the exact functional curves calibrated using the probabilistic approach.
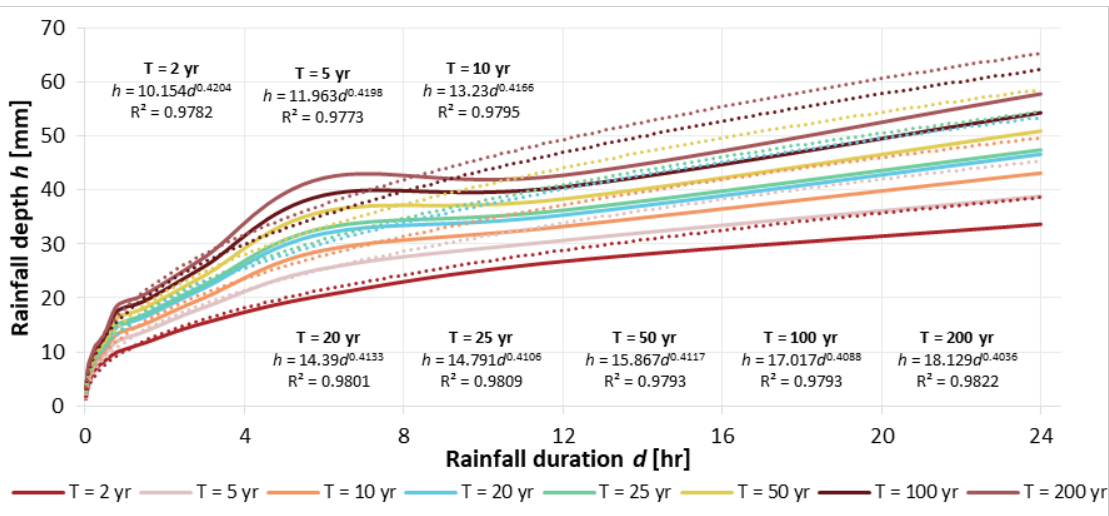
Figure 20: Intensity-Duration-Frequency curves for the selected return periods at Lillehammer station.

Table 5: Parameters of the bi-parameter power-law that describes the rainfall intensity hr *for a given return period* T *and duration* d *at Lillehammer station.*

Parameters	Return Period T [years]							
	2	5	10	20	25	50	100	200
$a(T)$ [mm/h^n]	10.154	11.963	13.23	14.39	14.791	15.867	17.017	18.129
N	0.4204	0.4198	0.4166	0.4133	0.4106	0.4117	0.4088	0.4036

3.3.2 GIS modelling

To achieve the data required for the hydrological modelling, some spatial data were extracted from the Norwegian national website for map data and other spatial information (Table 6; www.geonorge.no).

Table 6: Features of spatial data extracted from the Norwegian national website for map data and other spatial information.

Data	Format	File extension	Resolution
River Gausa watershed	Vector	shp	-
DEM	Raster	geotiff/ascii	5pt (around 25x25 cm)
Land use map	Vector	shp	-
Buildings	Vector	shp	-
Rivers and creeks	Vector	shp	-
River Gausa watershed	Vector	shp	-
Sediment cover map	Vector	shp	Based on maps of different scales (1:20000 - 1:250000)
Buildings footprints	Vector	shp	-

The GIS modelling was carried out by processing a DEM with 0.25 m spatial resolution in Arcmap 10.7. It was clipped using the River Gausa watershed boundary, then the extension and the average slope were calculated via geoprocessing tools. The total area of the watershed was 946 km^2 and its average slope of around 16.5%.

Rivers and creeks network were similarly clipped along the watershed boundaries and the length of the main river was estimated in 71.33 km.

3.3.3 Hydrological modelling

Soil Curve Number

To model the runoff in the studied watershed and to predict the hydrographs generated by rainfall extreme events, the Soil Conservation Service Curve Number (SCS-CN) method was applied. It was originally developed by the U.S. Department of Agriculture, Soil Conservation Service in the late 1950s and since then updated several times with the latest one being released in 2004 (Natural Resources Conservation Service, 2021). It is used worldwide in several hydrological applications since it is a simple but well-structured method, resulting in not much data demanding and easily working to get well-documented environmental inputs. Moreover, it accounts for several factors which influence runoff generation, gathering them in a single parameter, the Curve Number (Ponce & Hawkins, 1996; Soulis, 2021). Basically, for ungauged watersheds, CNs are derived from the National Engineering Handbook (NEH) tables using watershed features such as hydrologic soil group (HSG), land use cover and antecedent moisture condition (AMC) (Lal, et al., 2017).

The SCS-CN method consists of the following equations:
$$Q = \frac{(P-I_a)^2}{(P-I_a+S)} \text{ for } P > I_a; \quad \text{otherwise } Q = 0 \quad (2)$$
where:
- Q [mm] is the direct surface runoff;
- P [mm] is the rainfall;
- I_a [mm] is the initial abstraction;
- S [mm] is the potential maximum retention.

To estimate I_a and S, the following Equations 3 and 4 can be used, respectively:
$$I_a = 0.2 \cdot S \quad (3)$$
$$S = 254 \cdot \left(\frac{100}{CN} - 1\right) \quad (4)$$
where:
- CN is a dimensionless number, ranging from 0 and 100, as a function of HSG, land use cover, and AMC.

SCS classified the hydrologic soils in four groups (HSGs), from A to D, listed at decreasing the infiltration rate, on the basis of their infiltration capacity (Table 7). Moreover, it provided CN for each Land Cover type as HSG changes (Table 8).

Table 7: Description of HGSs according to SCS.

Hydrologic soil group	Description
A	Soils having low runoff potential when thoroughly wet. Water is transmitted freely through the soil. They typically have less than 10% clay and more than 90% sand or gravel and have gravel or sand textures.
B	Soils having moderately low runoff potential when thoroughly wet. Water transmission through the soil is unimpeded. They typically have between 10% and 20% clay and 50% to 90% sand and have loamy sand or sandy loam textures.
C	Soils having moderately high runoff potential when thoroughly wet. Water transmission through the soil is somewhat restricted. They typically have between 20% and 40% clay and less than 50% sand and have loam, silt loam, sandy clay loam, clay loam, and silty clay loam textures.
D	Soils having high runoff potential when thoroughly wet. Water movement through the soil is restricted or very restricted. They typically have greater than 40% clay, less than 50% sand, and have clayey textures. I

Table 8: Curve Number for each Land Cover Type as HSG changes, according to SCS.

Land Cover Type	HSG			
	A	B	C	D
Straight row without conservation tillage	72	81	88	91
Straight row with conservation tillage	62	71	78	81
Pasture, grassland, or range-continuous forage for grazing in poor conditions	68	79	86	89
Pasture, grassland, or range-continuous forage for grazing in good conditions	39	61	74	80
Meadow-continuous grass in good conditions, protected from grazing and generally mowed for hay	30	58	71	78
Woods (forest litter, small trees, and brush are destroyed by heavy grazing or regular burning)	45	66	77	83
Woods (litter and brush adequately cover the soil)	25	55	70	77
Open areas: grass, golf courses, parks in good conditions (> 75% grassy cover)	39	61	74	80
Open areas: grass, golf courses, parks in fair conditions (grassy cover among 50% and 75%)	49	69	79	84
Open areas (< 50% grassy cover)	68	79	86	89
Commercial areas (average soil permeability rate 15%)	89	92	94	95
Industrial areas (average soil permeability rate 28%)	81	88	91	93
Residential areas (average soil permeability rate 35%)	77	85	90	92
Residential areas (average soil permeability rate 62%)	61	75	83	87
Residential areas (average soil permeability rate 70%)	57	72	81	86
Residential areas (average soil permeability rate 75%)	54	70	80	85
Residential areas (average soil permeability rate 80%)	51	68	79	84
Residential areas (average soil permeability rate 88%)	46	65	77	82
Paved car park, rooftops	98	98	98	98
Roads (paved)	98	98	98	98
Roads (gravel)	76	85	89	91
Roads (dirt)	72	82	87	89

The soil moisture condition in the watershed before the runoff occurrence is another relevant factor influencing the CN. SCS classified the soil moisture condition in three *Antecedent Moisture Condition* (AMC) classes:

- AMC I: the soils in the watershed are basically dry;
- AMC II: average condition;
- AMC III: the soils in the watershed are basically saturated from antecedent rainfalls.

These classes are based on the 5-day antecedent rainfall (i.e. the accumulated total rainfall preceding the runoff under consideration). SCS made a distinction between the dormant and the growing season to simulate the differences in evapotranspiration process (Table 9).

Table 9: Seasonal rainfall limits for each AMC class according to SCS.

AMC Class	5-day antecedent rainfall [mm]	
	Dormant season	Growing season
I	< 13	< 36
II	13 ÷ 28	36 ÷ 54
III	> 28	> 54

The abovementioned CN values are representative of Class II (average) antecedent moisture condition, AMC II. The following Equations 5 and 6 allow calculating the CN in dry (AMC I) and saturated (AMC III) condition, as a function of the average one.

$$CN(I) = \frac{4.2 \cdot CN(II)}{10 - 0.058 \cdot CN(II)} \tag{5}$$

$$CN(III) = \frac{23 \cdot CN(II)}{10 + 0.13 \cdot CN(II)} \tag{6}$$

For watersheds with different Land Cover types and HSGs, the total CN can be estimated by carrying out an area-weighted average of CN related to the different isoparametric sub-areas, i.e. areas having a given Land Cover type and a given HSG. Weights are intended as a function of the extension of the isoparametric sub-areas in the watershed over the total area of the watershed.

For the Jorekstad case study, the sediment cover map of River Gausa watershed, provided by the Geological Survey of Norway (NGU), was reclassified according to the four HSGs defined by SCS (Table 10). Similarly, the land use map of River Gausa watershed was reclassified by assigning to each land use class a Land Cover type as defined by SCS (Table 11). CN equal to 100 was set for swamplands, rivers and lakes.

Once the HSGs and Land Cover types were assigned, this two-polygon shapefile was processed in GIS with an intersection tool in order to detect the isoparametric sub-areas.

Then the CN area-weighted average was calculated (Figure 21), assessing for the River Gausa watershed a total CN of 78.95.

Table 10: Classification of sediment covers at River Gausa watershed into HSGs.

Sediment cover	HSG
Glaciers and rivers deposits	
Glacial deposits	A
Rivers and creeks deposits	
Back-shaped glaciers deposits	
Moraine material, continuous cover	B
Rogen moraine	
Bare mountains	
Rockfall deposits	
Rockfall deposits, incoherent or thin cover	
Flood deposits glacial drainage	
Slope debris, rock and block cover	
Slope debris, incoherent or thin cover over the bedrock	C
Landslide deposits	
Landslide deposits, incoherent or thin cover	
Avalanche deposits	
Peat and swampland	
Thin cover of organic material over bedrock	
Filling mass (anthropogenic material)	
Unconsolidated rock/bedrock under water	D
Moraine material, incoherent or thin cover over the bedrock	

Table 11: Classification of land uses at River Gausa watershed into Land Cover types.

Land use	Land Cover Type
Crops	Straight row without conservation tillage
Woods	Woods (forest litter, small trees, and brush are destroyed by heavy grazing or regular burning)
Golf course	Open areas: grass, golf courses, parks in good conditions (> 75% grassy cover)
Sports field	
Alpine slopes	Open areas (< 50% grassy cover)
Open areas	
Industrial areas	Industrial areas (average soil permeability rate 28%)
Quarries	
Densely built areas	Residential areas (average soil permeability rate 75%)
	Residential areas (average soil permeability rate 80%)
Cemeteries	Residential areas (average soil permeability rate 88%)
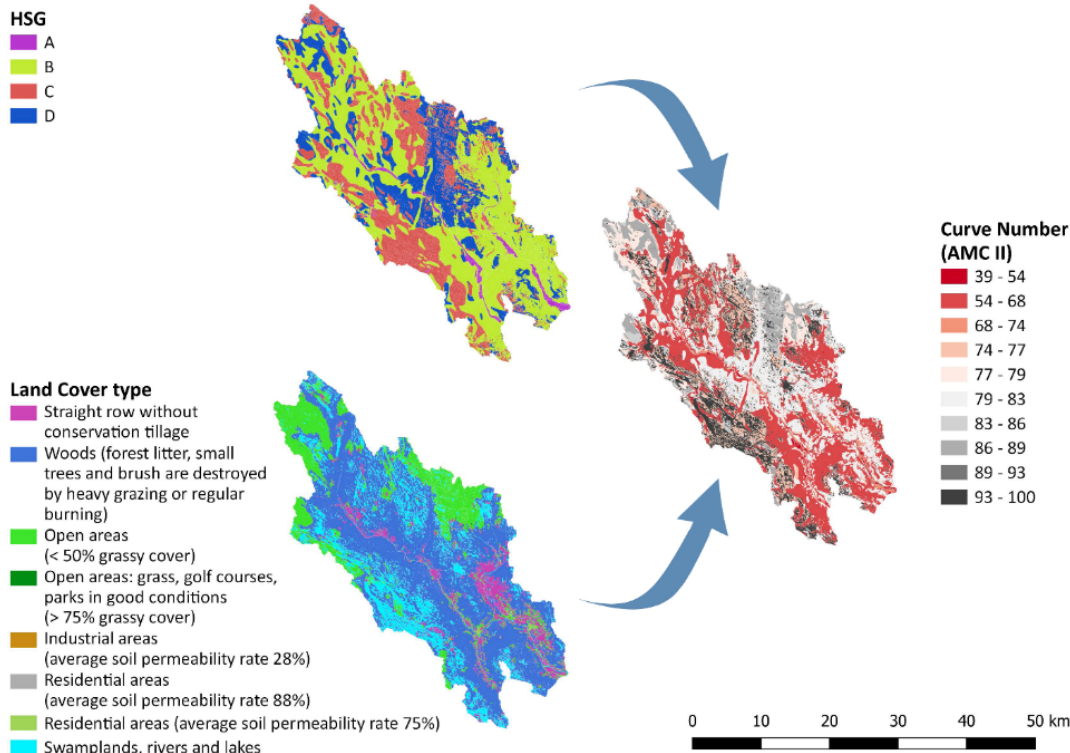
Figure 21: Graphical abstract of HSGs and Land Cover types intersection to achieve isoparametric sub-areas at River Gausa watershed and related CN.

- <u>Hydrograph development</u>. Hydrograph was used to generate and estimate the peak flow Q_p of the watershed. It was derived from the physical features of the catchment calculated as outputs of GIS processing: slope and total extension of the catchment and length of the longest stream. The SCS method estimates the peak flow Q_p by considering a typical dimensionless unit hydrograph, presenting a time base t_b made by an accumulation time t_a and a time from peak to the tail of the hydrograph t_e. The runoff volume of this triangular hydrograph was computed as follow:

$$V = \frac{Q_p}{2} \cdot (t_a + t_e) = \frac{Q_p \cdot t_b}{2} \tag{7}$$

The typical dimensionless unit hydrograph developed by the SCS consists of 37.5% of the total runoff volume before the peak discharge and the remaining volume after the peak flow occurs. Thus, the unit hydrograph can be solved using the simplified form of a *triangular unit hydrograph*.
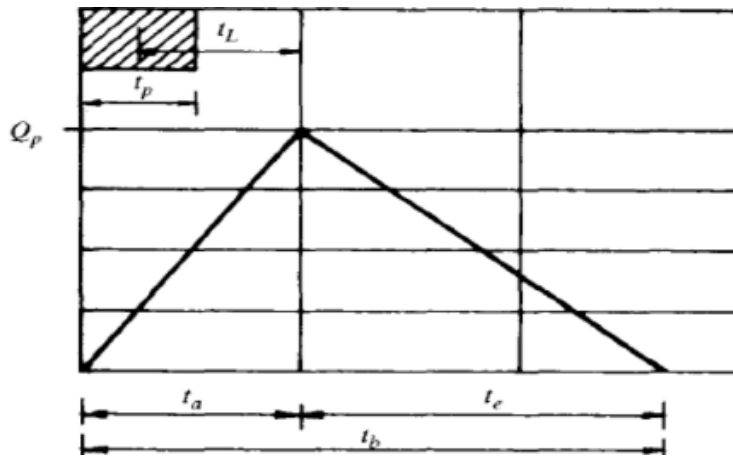
Figure 22: Triangular dimensionless unit hydrograph developed by SCS.

Assuming the same 37.5% of the volume on the left region of t_p for the triangular unit hydrograph, it was possible to solve for the t_b, which contains the entire 100% runoff volume. Therefore:

$$t_b = 2.67 \cdot t_a \tag{8}$$

According to Equation (9), the peak flow depends on the rainfall volume V, the watershed area A, and the lag time t_L, whereas from Equation (11), the lag time t_L depends on the mainstream length L, the river basin's slope i_b, and the Curve Number CN. The peak flow Q_p [m³/s] is given by:

$$Q_p = \frac{0.208 \cdot A \cdot V}{t_a} \tag{9}$$

where:
- A [km²] is the area of the watershed;
- V [mm] is the depth of runoff.

Furthermore, other hydrological parameters such as the concentration time (t_c), the accumulation time (t_a) and the lag time (t_L), required to develop the hydrograph, were calculated based on the Simas equation (Simas, 1996). The concentration time (t_c) represents the time required for the runoff to move from the most distant hydraulic point located in the upstream of the watershed to the outlet located at the extreme dawn stream. The concentration time was estimated using Equation 10:

$$t_a = 0.5 \cdot t_p + t_L \tag{10}$$

where:
- t_a [h] is the accumulation time;
- t_p [h] is the rainfall event duration;
- t_L [h] is the lag time.

The lag time represents the time elapsed between the occurrence of the rainfall and the peak discharge. It was computed using the following Mockus equation **Ugyldig kilde er angitt.**:

where:
- i_b [%] is the average slope of the watershed;
- L is related to the watershed area A through an empirical equation introduced by Hack (Hack, 1957), as reported below:

$$L = 1.4 \cdot A^{0.6} \tag{12}$$

Once t_p and Q_p were calculated for a given return period T and a set AMC, the D-hr unit hydrograph for the analyzed watershed was achieved by using the dimensionless Mockus unit hydrograph (Mockus, 1957). This dimensionless curvilinear hydrograph was derived from many natural unit hydrographs from watersheds at widely varying widely the size and the geographical locations. It expresses dimensionless t/t_a ratio on the abscissa axis and the Q/Q_p ratio on the ordinate one (Figure 23, Table 12).
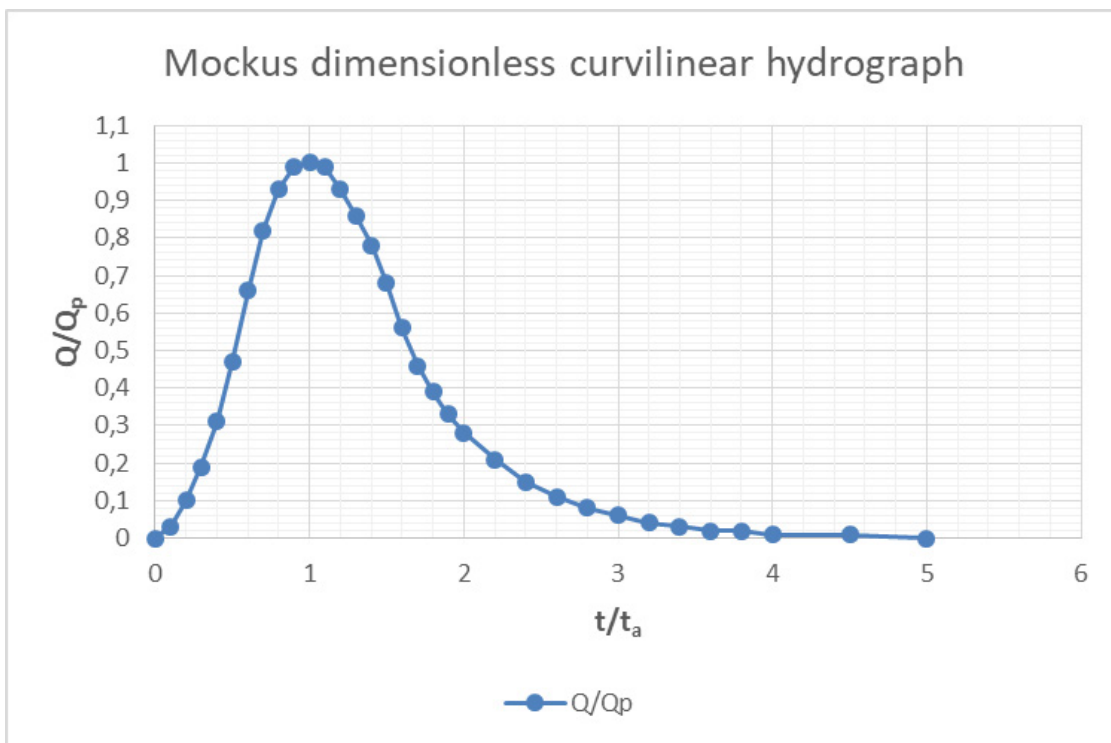
Figure 23: Mockus dimensionless unit hydrograph.

Table 12: Ratios for dimensionless unit hydrograph.

t/t_a [-]	Q/Q_p [-]
0.0	0.00
0.1	0.03
0.2	0.10
0.3	0.19
0.4	0.31
0.5	0.47
0.6	0.66
0.7	0.82
0.8	0.93
0.9	0.99
1.0	1.00
1.1	0.99
1.2	0.93
1.3	0.86
1.4	0.78
1.5	0.68
1.6	0.56
1.7	0.46
1.8	0.39
1.9	0.33
2.0	0.28
2.2	0.21
2.4	0.15
2.6	0.11
2.8	0.08
3.0	0.06
3.2	0.04
3.4	0.03
3.6	0.02
3.8	0.02
4.0	0.01
4.5	0.01
5.0	0.00

Mockus hydrographs of River Guasa watershed are plotted for 2, 5, 10, 20, 25, 50, 100, 200-year return period considering AMC I, AMC II and AMC III in Figure 24 a, b and c, respectively.
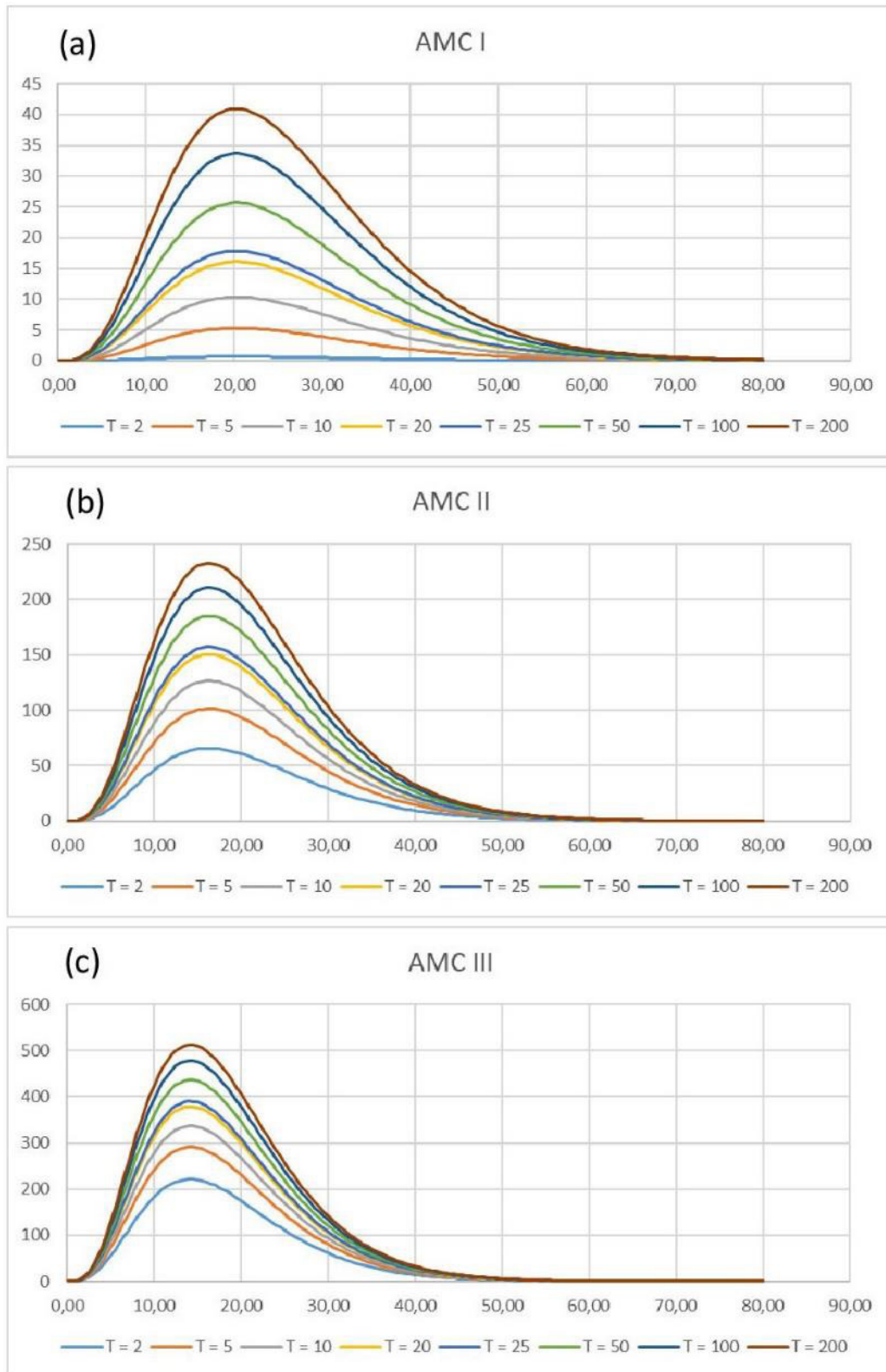
Figure 24: Mockus hydrographs at River Guasa watershed for different return periods and AMCs.

3.3.4   Hydraulic modelling

The hydraulic model was used to compute the flow parameters, namely the flow velocity, the depth and the area of possible inundation. To achieve this information, the FLO-2D software was adopted given its suitability to assess the possible range of flow properties (velocity and depth) and predict the potential inundated areas (O'Brien, 2011). The flood simulations were done using the procedure hereafter described. To build the baseline scenario, the DEM of the study area was resampled to achieve a 1 m resolution DEM, which was then imported into the software in the form of an ASCII grid file. The ASCII file was used for the easier conversion of XYZ grid file in Global Mapper software. Grid Computation was done from the ASCII file. The analysis cell-size of the model was set equal to 20 m. FLO-2D performed a grid interpolation to assign the representative elevation of each grid element. In addition, a cumulative of 2, 5, 10, 20, 25, 50, 100 and 200-year return period of climate modelling and hydrological model result of hydrograph and soil curve number were used to simulate the FLO-2D baseline scenario. The inlet section was set where River Gausa crosses the boundary of the study area. Similarly, outlet sections were set at the intersection between the Gudbrandsdalenslågen River and the boundary of the study area. The baseline scenario model was refined by importing both building footprints and a land use map containing Manning roughness coefficient[2] for each land use class (Table 13).

Table 13: Manning roughness coefficient for each land use class at Jorekstad study area.

Land use	Manning roughness coefficient [s/m$^{1/3}$]
Golf course	
Sports field	0.485
Crops	
Woods	
Alpine slopes	0.400
Open areas	
Cemeteries	0.300
Industrial areas	
Quarries	0.035
Densely built areas	

In the NBS scenario, the model built for the baseline scenario was modified by importing 3 cloud points files (.xyz) containing the location and the elevation of the barrier crown. The imported levee is capable to cut off up to 8 possible overland flow directions for each crossed grid element. The result of the simulation was post-processed in the Mapper software. From the results of the numerical model, the maps of maximum flow depth and maximum flow velocity occurred at each cell of the model were generated.

---

[2] Roughness coefficients represent the resistance to flood flows in channels and floodplains.

3.4 Modelling results

As the flood hazard simulation target is to forecast the maximum discharge at different return periods, a first simulation run was carried out considering the most severe situation of 5-day antecedent rainfalls, namely AMC III.

In the baseline scenario, the flood plain was inundated at each return period. Starting from 10-year return period, the flooded area threatened the sports facilities at Jorekstad. The average max flow depth ranged from 1.28 m at 2-year return period (with an absolute maximum of 3.37 m at the floodplain) to 2.60 m at 200-year return period (with an absolute maximum of 5.2 m at the floodplain) (Figure 25). Concerning the average max flow velocity, it ranged from 0.40 m/s at 2-year return period (with an absolute maximum of 0.50 m/s at the floodplain) to 0.57 m/s at 200-year return period (with an absolute maximum of 0.84 m/s at the floodplain) (Figure 26).

The NBS scenario simulation revealed how the receded flood barrier is able to prevent from the floodplain inundation only when a 2-year return period rainfall occurs. In the other cases, the segment of the barrier perpendicular to the river was bypassed to the south by the flood and the levee was almost totally overstepped. Therefore, the flood plain was always fully inundated and the Jorekstad sport center was threatened by the flood. Moreover, it did not contribute to limit flow depth and velocity. Actually, the average max flow depth ranged from 1.52 m at 2-year return period (with an absolute maximum of 0.17 m in the small portion of floodplain that was inundated) to 2.90 m at 200-year return period (with an absolute maximum of 6.2 m at the floodplain) (Figure 27). Similarly, the max flow velocity ranged from 0.51 m/s at 2-year return period (with an absolute maximum of 0.40 m/s at the floodplain) to 0.60 m/s at 200-year return period (with an absolute maximum of 1.6 m/s at the floodplain) (Figure 28).

By comparing the total amount of flooded areas in the baseline scenario and in the NBS one, it was observed that the flood barrier might actually increase the flooded area just after it is overstepped, i.e. starting from 5-year return period (Figure 29). Similar results were observed when the levee was slightly modified by both prolonging its initial segment to the south and raising the barrier crown by 1 or 2 m.

A second simulation run was carried out considering the average situation of 5-day antecedent rainfall, AMC II, to assess the effectiveness of the flood barrier in less severe soil moisture conditions. In this case, the levee proved to avoid the plain flooding for each return period shorter than or equal to 100-year. Furthermore, even in case of a 200-year rainfall event, the extension of the flooded area was efficiently limited and the flood did not threaten the Jorekstad settlements (Figure 30, Figure 31).
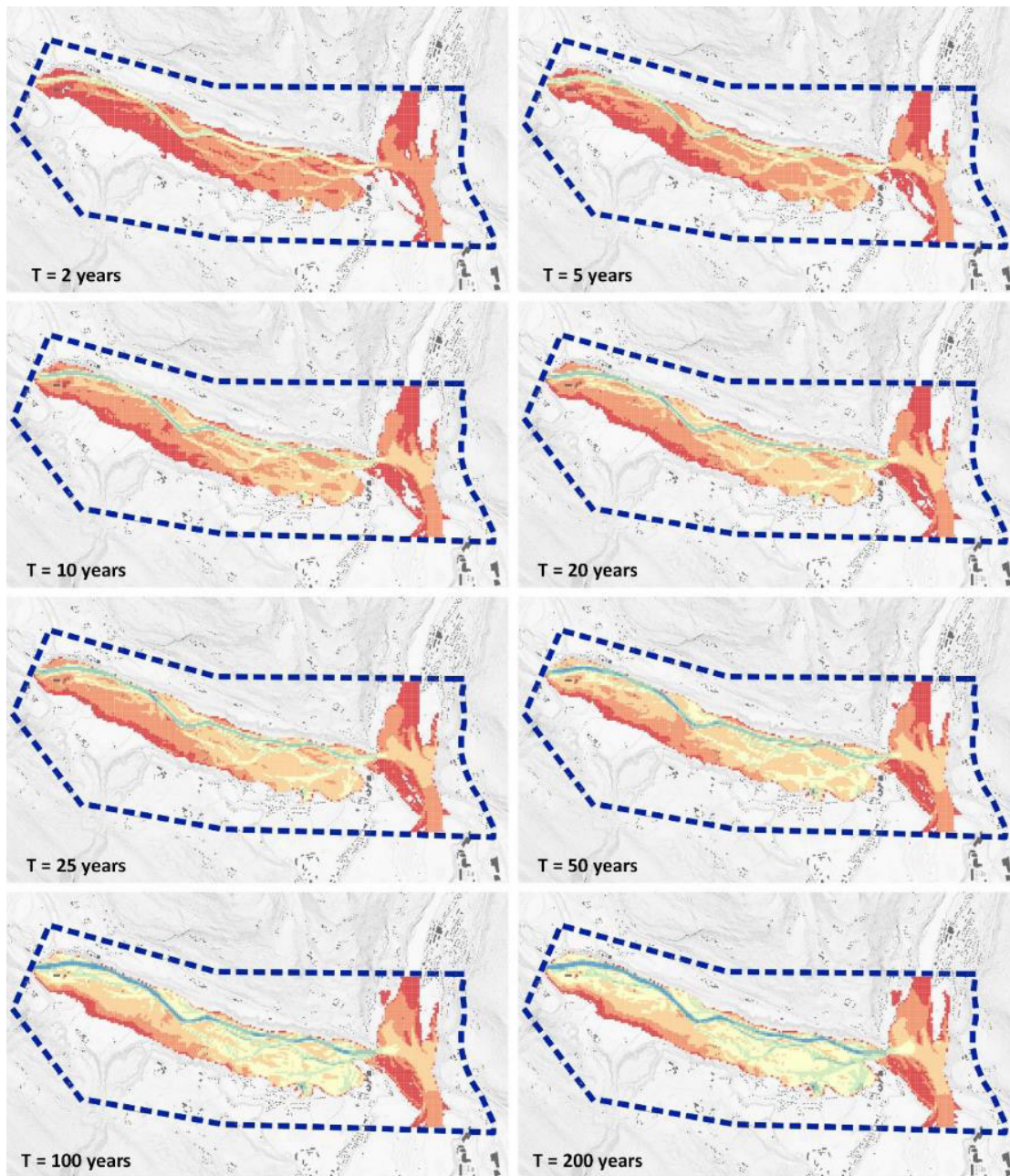
Figure 25: Max Flow Depth maps for baseline scenario considering AMC III.
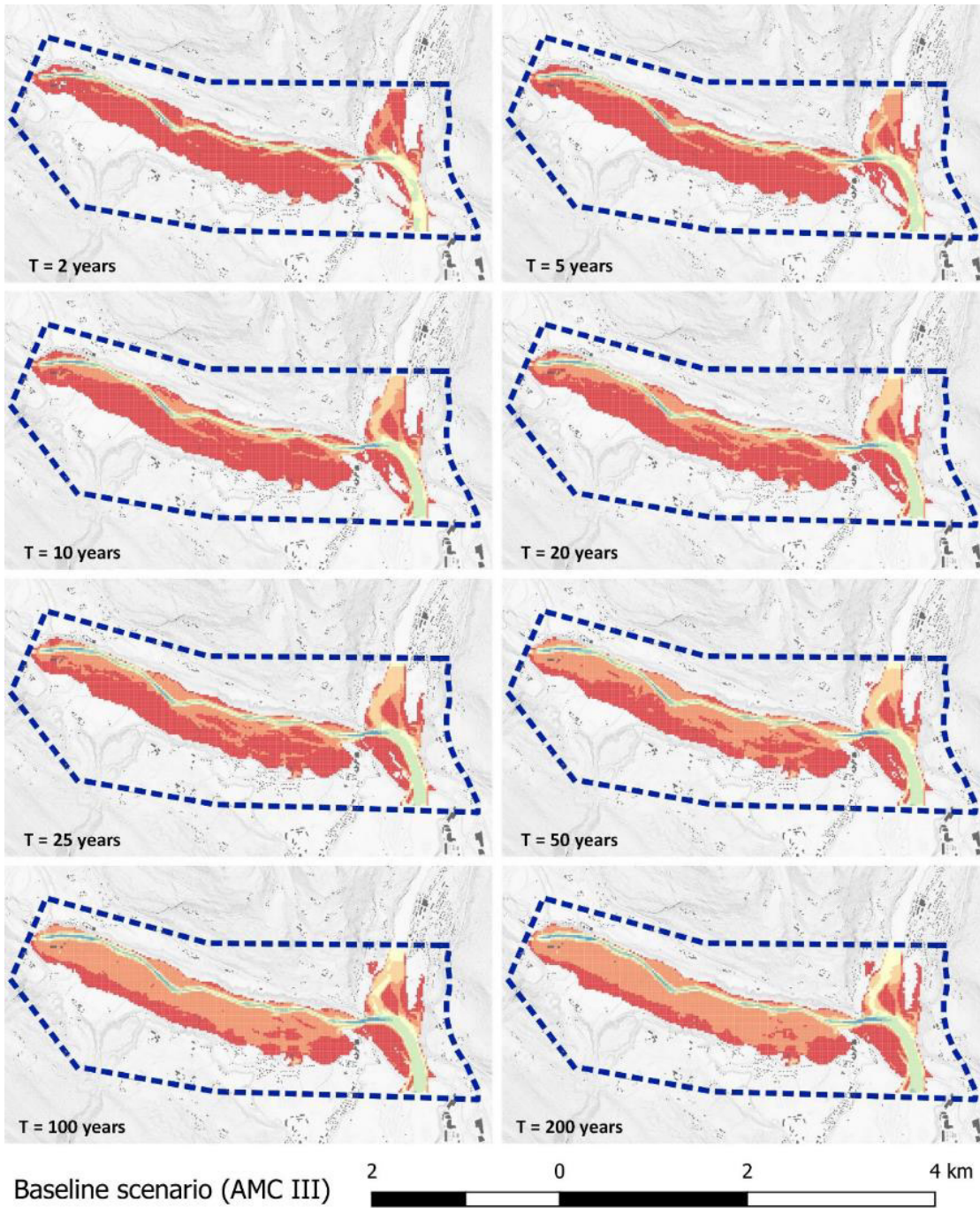
Figure 26: Max Flow Velocity maps for baseline scenario considering AMC III.
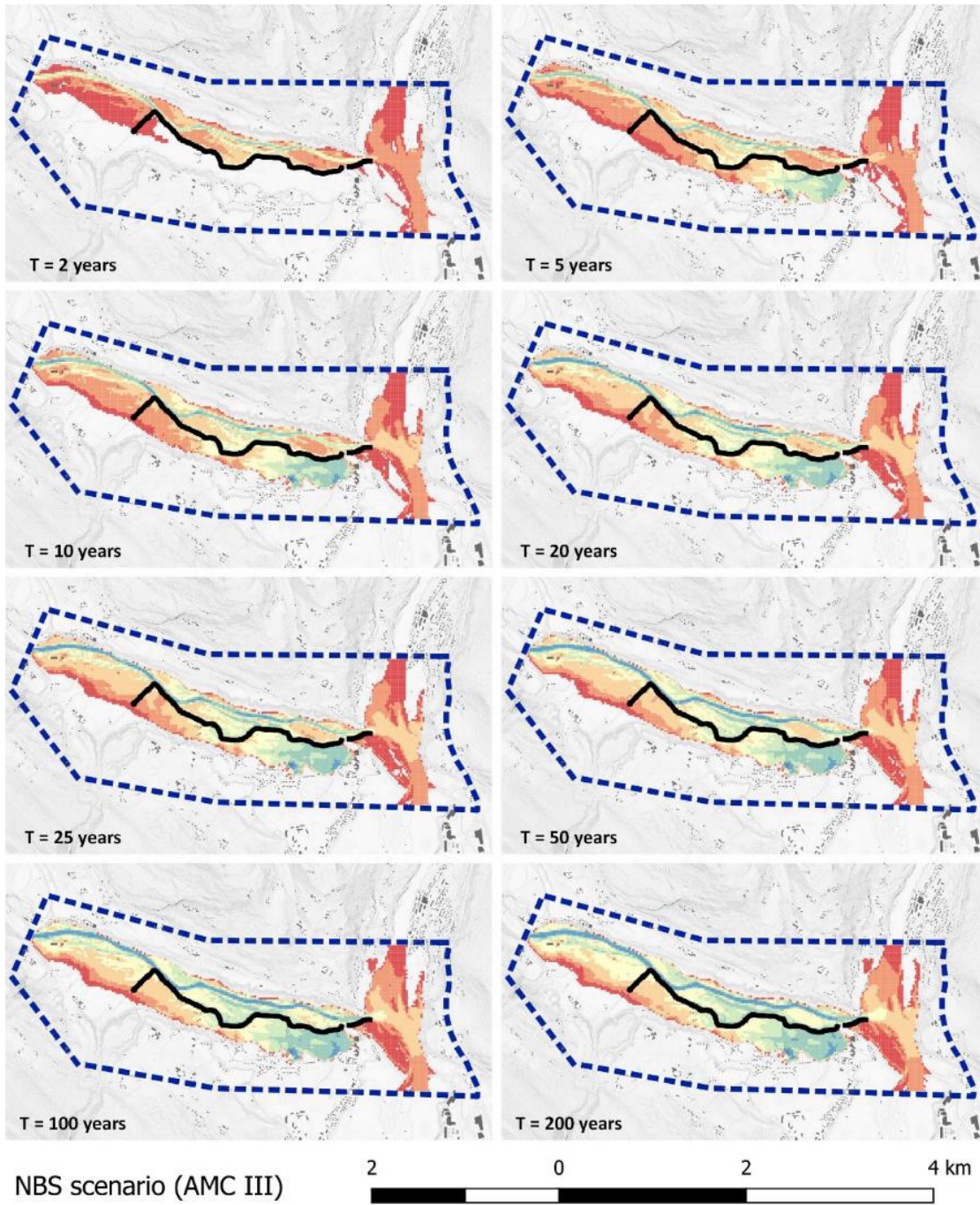
Figure 27: Max Flow Depth maps for NBS scenario considering AMC III.
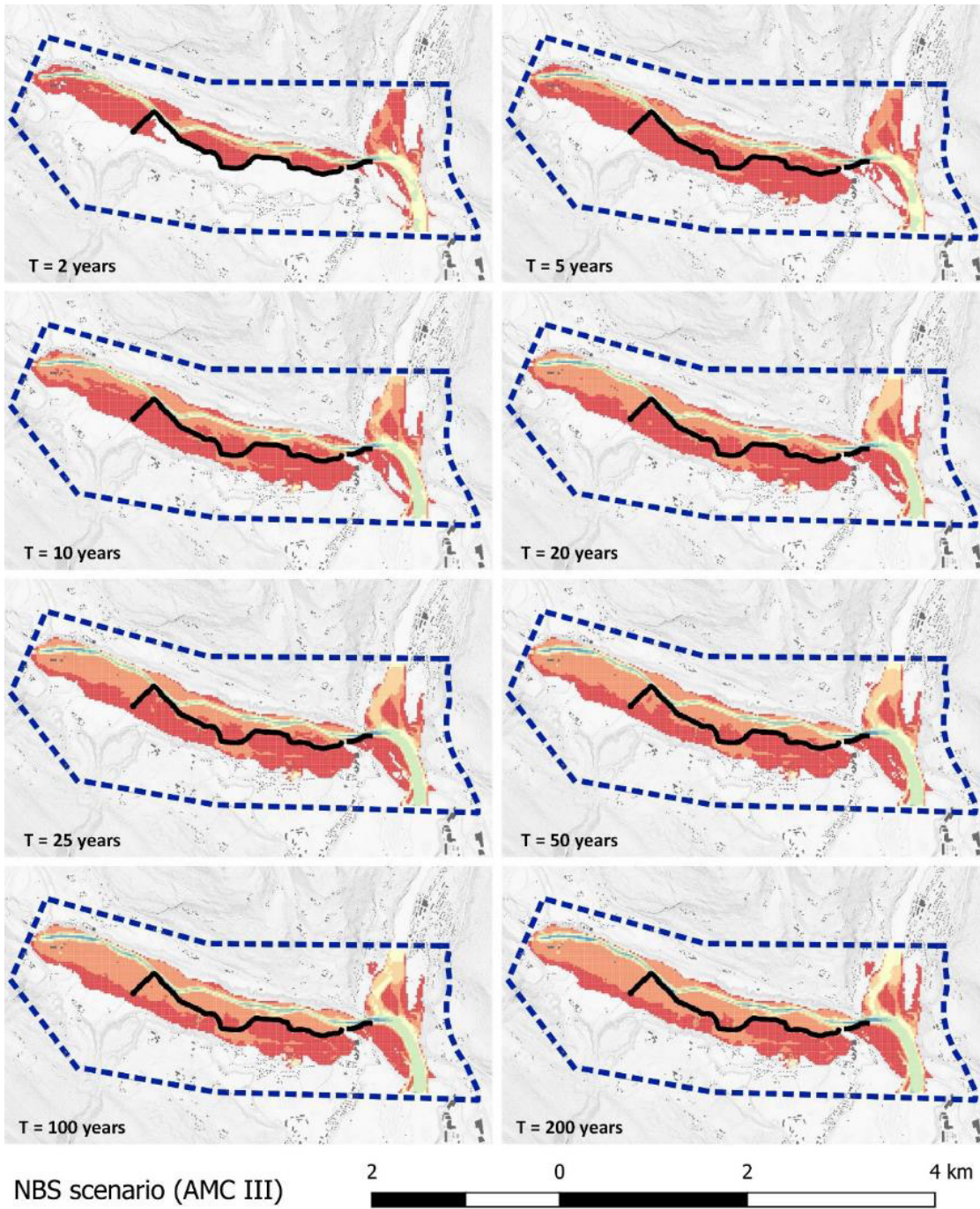
Figure 28: Max Flow Velocity maps for NBS scenario considering AMC III.
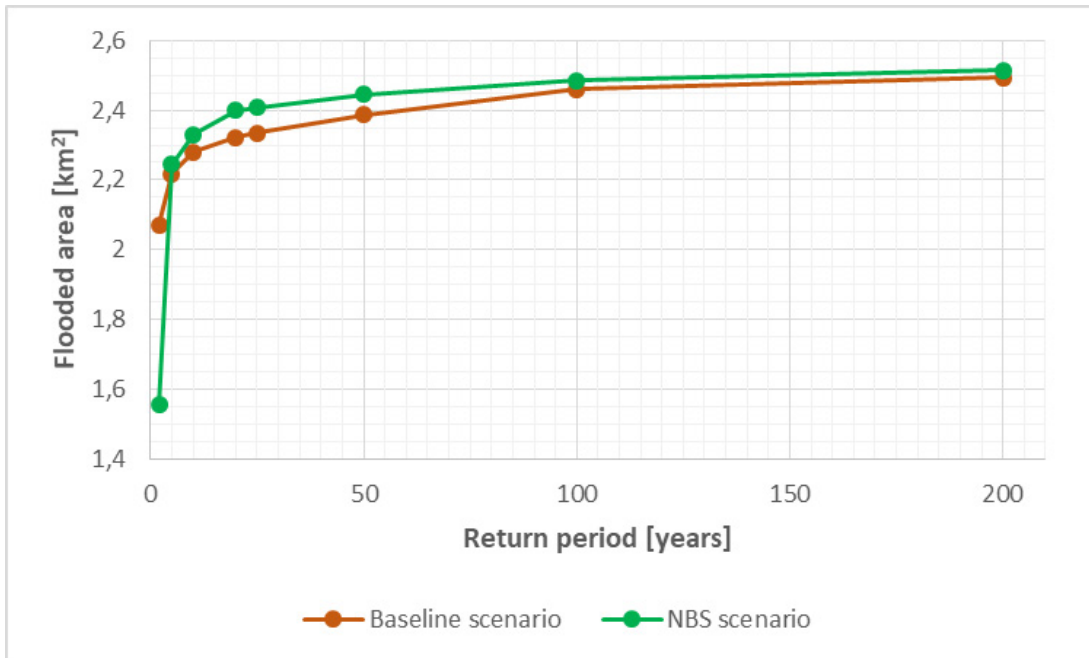
Figure 29: Comparison between the flooded area at baseline scenario and NBS one as a function of return period, considering AMC III.
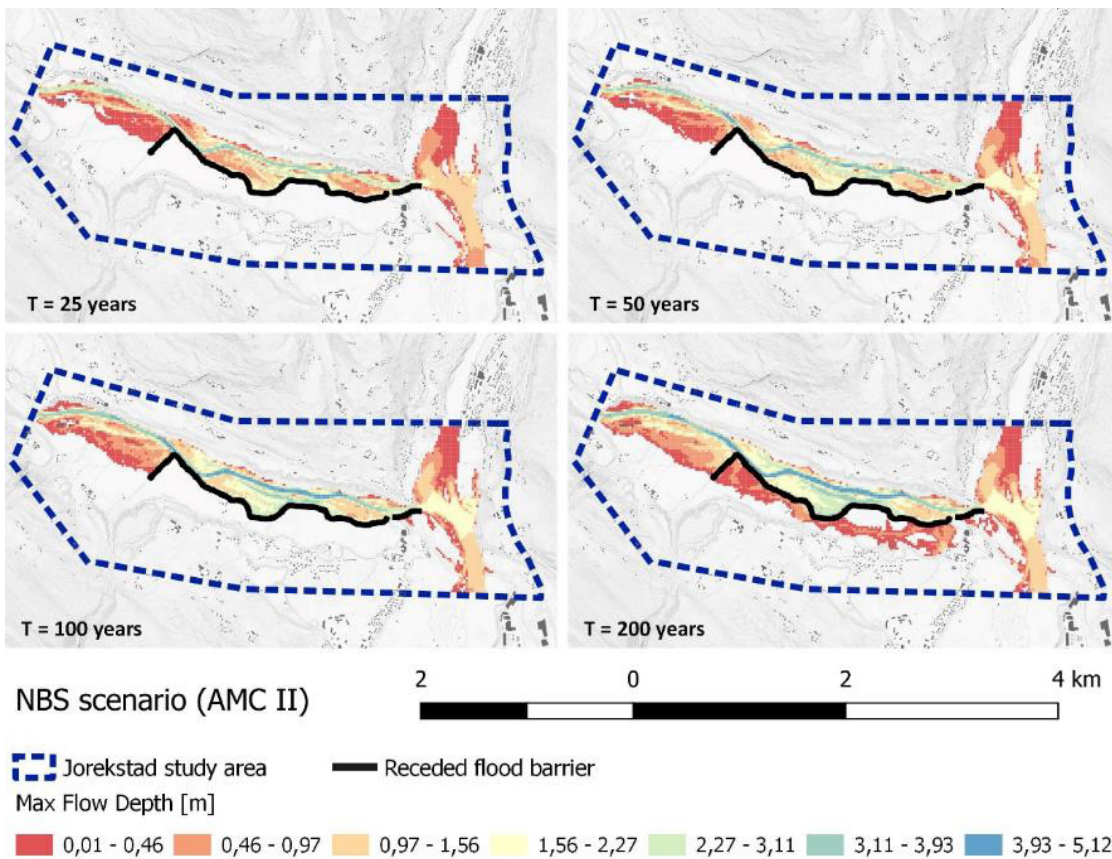
Figure 30: Max Flow Depth maps for NBS scenario considering AMC II.
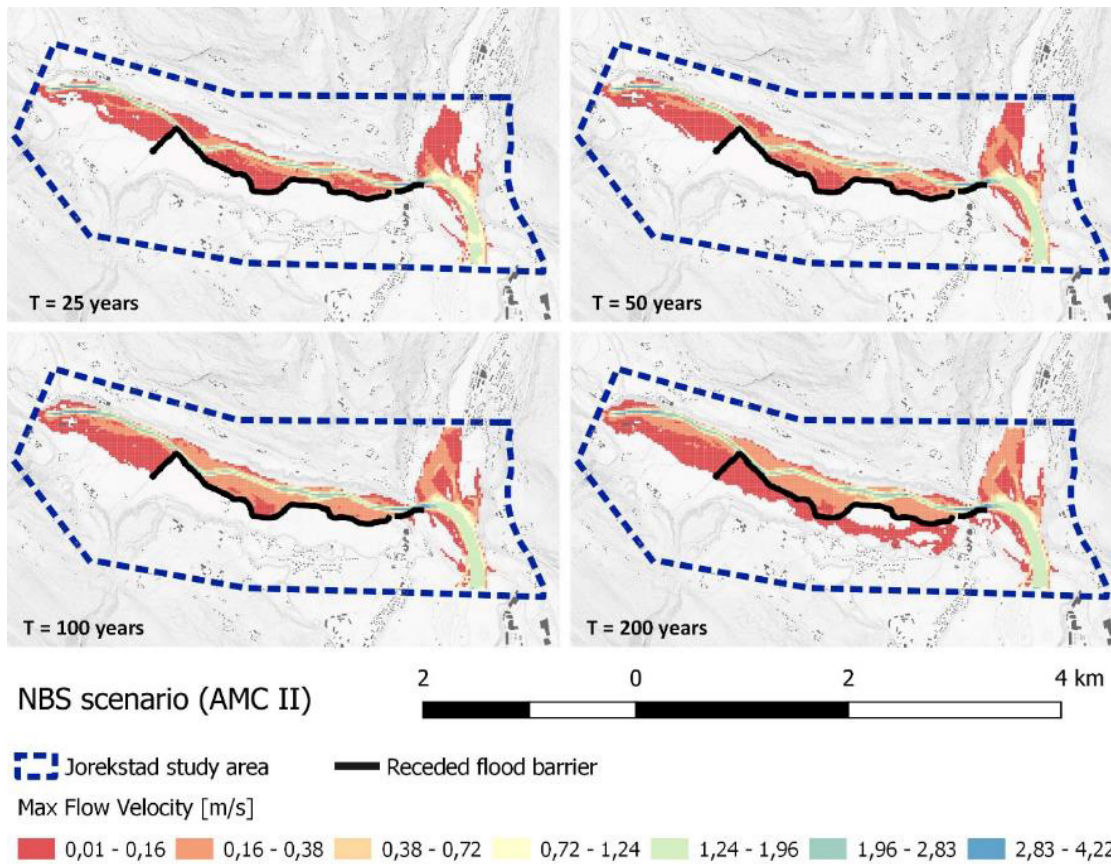
Figure 31: Max Flow Depth maps for NBS scenario considering AMC II.

3.5 Discussion and concluding remarks

Flood is the major natural hazard threatening the Jorekstad study area and the River Gausa watershed. The methodology applied for flood hazard assessment in the frame of PHUSICOS project allowed generating high-resolution hazard maps of several stream flow conditions, such as flow velocity, flow depth and the extension of the possible flooded areas, for both the baseline and the NBS scenario, at different soil moisture conditions. By running the FLO-2D model, the flooded areas were detected and the maximum flow depth and the velocity were assessed for each analyzed 20 m cell-size of the study area at 2, 5, 10, 20, 25, 50, 100, 200-year return period.

In the most severe soil moisture conditions (AMC III), the flood barrier proved to be ineffective against rainfall events having return periods longer or equal to 5 years. Moreover, it showed the opposite effect of reducing stream flow conditions, since the flow overstepping the barrier were no longer spilled into the river. This provoked higher maximum flow depth and velocity and bigger flooded areas than in the baseline scenario.

Different physical features of the barrier (+140 m long, +2 m high) did not contribute to enhance its effectiveness. It is worth nothing that raising the earth barrier crown more

than 2 m would not be technically and economically feasible since its 2:1 sloped sides would entail a much bigger footprint.

In average soil moisture conditions (AMC II), the simulations revealed how the planned NBS was fully effective against flooding caused by rainfall events having a return period shorter or equal to 100-year. Even when 200-year rainfall events occur, the flood barrier would limit the flooded areas and protect the exposed settlements.

Future applications of the methodology herein discussed should account for the hydraulic model having an even higher resolution, as long as glitches, due to data processing capacity, could be easily overcome.

3.6 References

Akpoveta, V. O., Osakwe, S. A., Ize-Iyamu, O. K., Medjor, W. O., & Egharevba, F. (2014). Post Flooding Effect on Soil Quality in Nigeria: The Asaba, Onitsha Experience. *Open Journal of Soil Science, 4*(2), 72-80. doi:10.4236/ojss.2014.42010

Atta-ur-Rahman, & Khan, A. N. (2011). Analysis of flood causes and associated socio-economic damages in the Hindukush region. *Natural Hazards*(59), 1239-1260. doi: 10.1007/s11069-011-9830-8

CRED. (2018). *Natural disasters 2018.* Brussels: Centre for Research on the Epidemiology. Retrieved 10 10, 2021, from https://www.cred.be/sites/default/files/CREDNaturalDisaster2018.pdf

De Paola, F., Giugni, M., Topa, M. E., & Bucchignani, E. (2014). Intensity-Duration-Frequency (IDF) Rainfall Curves, for Data Series and Climate Projection in African Cities. *SpringerPlus*(3), 133. doi:10.1186/2193-1801-3-133

Eccles, R., Zhang, H., & Hamilton, D. (2019). A review of the effects of climate change on riverine flooding in subtropical and tropical regions. *Journal of Water and Climate Change, 10*(4), 687–707. doi:10.2166/wcc.2019.175

Erena, S. H., Worku, H., & De Paola, F. (2018). Flood hazard mapping using FLO-2D and local management strategies of Dire Dawa city, Ethiopia. *Journal of Hydrology: Regional Studies, 19*, 224-239. doi:10.1016/j.ejrh.2018.09.005

European Commission. (2021). *Evaluating the impact of nature-based solutions. A handbook for practicioners.* (A. Dumitru, & L. Wendling, Eds.) Brussels: Publication Office of European Union. doi:10.2777/244577

Groisman, P. Y., Knight, R. W., Easterling, D. R., Karl, T. R., Hegerl, G. C., & Razuvaev, V. N. (2005). Trends in intense precipitation in the climate record. *Journal of Climate, 18*(9), 1326–1350. doi:10.1175/JCLI3339.1

Hack, J. T. (1957). *Studies of Longitudinal Stream Profiles in Virginia and Maryland.* Washington D.C.: United States Geological Survey Professional.

Jonkman, S. N. (2005). Global perspectives on loss of human life caused by floods. *Natural Hazards, 34*, 151–175. doi:10.1007/s11069-004-8891-3

Lal, M., Mishra, S. K., Pandey, A., Pandey, R. P., Meena, P. K., Chaudhary, A., . . . Kumar, Y. (2017). Evaluation of the Soil Conservation Service curve number methodology using data from agricultural plots. *Hydrogeology Journal, 25*, 151-167. doi:10.1007/s10040-016-1460-5

Mockus, V. (1957). *Use of storm and watershed characteristics in synthetic hydrograph analysis and application.* Sacramento: American Geophysical Union.

Natural Resources Conservation Service. (2021). *National Engineering Handbook Part 630 Hydrology.* Washington D.C.: United States Department of Agriculture. Retrieved October 14, 2021, from https://www.nrcs.usda.gov/wps/portal/nrcs/

O'Brien, J. (2011). FLO-2D Reference Manual, Version 2009.

Oppland County Administration. (2021, October 7). *Regional Plans.* Retrieved from Regional Master Plan for the Gudbrandsdalslågen and Its Tributaries. Measures to Reduce Damage from Flooding and Landslides: https://innlandetfylke.no/_f/p1/i34056176-b265-41c3-a53b-e63f4b9ab5cb/lagen-plan_english_main-document.pdf

Ponce, V. M., & Hawkins, R. H. (1996). Runoff Curve Number: Has It Reached Maturity? *Journal of Hydrologic Engineering, 1*(1), 11-19. doi:10.1061/(ASCE)1084-0699(1996)1:1(11)

Simas, M. (1996). *Lag Time Characteristics in Small Watersheds in the United States. A Dissertation Submitted to School of Renewable Natural Resources.* Tucson: University of Arizona.

Solheim, A., Capobianco, V., Oen, A., Kalsnes, B., Wullf-Knutsen, T., Olsen, M., . . . Strout, J. M. (2021). Implementing Nature-Based Solutions in Rural Landscapes: Barriers Experienced in the PHUSICOS Project. *Sustainability, 13*, 1461-1481. doi:https://doi.org/10.3390/su13031461

Soulis, K. X. (2021). Soil Conservation Service Curve Number (SCS-CN) Method: Current Applications, Remaining Challenges, and Future Perspectives. *Water*(13), 192. doi:10.3390/w13020192

Talbot, C. J., Bennet, E. M., Cassel, K., Hanes, D. M., Minor, E. C., Paerl, H., . . . Xenopoulos, M. A. (2018). The impact of flooding on aquatic ecosystem services. *Biogeochemistry*(141), 439-461. doi:10.1007/s10533-018-0449-7

Walls, R. L., Heller Wardrop, D., & Brooks, R. P. (2005). The impact of experimental sedimentation and flooding on the growth and germination of floodplain trees. *Plant Ecology*(176), 203-213. doi:10.1007/s11258-004-0089-y

Ward, A. D., & Elliot, W. J. (1995). *Environmental Hydrology.* New York: CRC Press.

4 Hazard and susceptibility modelling at Pyrenees case studies affected by rockfalls

4.1 Introduction

Rockfalls are specific landslide events originated by the detachment of rock blocks from their initial position. They propagate over underlying slopes, poorly interacting with each other and with slope itself along their trajectories, and moving through a series of bounces, rolls and slips until stopping in the foothill areas. The hazardousness of such a phenomenon lies in the relatively high speed of their initiation, lack of warning signs of detachment, randomness of the trajectories, and high frequency of such events (Cruden & Varnes, 1996).

Such phenomena are more frequent in the presence of very steep slopes of coherent rocks outcrops, especially in mountainous areas, and represent a primary source of hazard due to propagation speed and the high kinetic energy transferred, which causes possible dire effects on human lives and activities, as well as infrastructures.

Mitigating such a risk requires detailed characterization of rock slopes, aimed at defining both the unstable boulder volumes and the dynamic evolution of their trajectories and the optimal performances of rockfall defences. To this aim, it is essential for defence works planning and design to accurately assess and delineate their spatial spread.

Many predictive numerical models have been developed to support accurate studies and define their possible consequences in the hazard assessment, with different capabilities to integrate defence structures. Moreover, many defence strategies have been applied worldwide to deal with rockfall hazards based on both active and passive solutions, to stabilize unstable rock masses or mitigate the effects of their propagation. Among them, nature-based solutions (NBS) include slope geometry reconfiguration using wooden structures and natural materials, wooden rock block fixing structures or barriers, and forests management plans finalized to improve their protective effects. These NBS represent a sustainable and economical solution; however, their effectiveness has not been adequately demonstrated yet.

With this study, we aim to provide new insights into the effectiveness of such types of NBS by investigating two real case studies in the mountainous area of the Pyrenees, characterized by different geological, morphological, and ecological properties. As part of the "PHUSICOS - Horizon 2020" project, based on different general contexts, new different NBS are designed to tackle the issue that integrate with the mitigating effect of the vegetation.

The two study sites are located in Artouste (Laruns municipality) and Santa Elena (Biescas municipality) in the Pyrenees, close to the France-Spain border.

To assess the changing hazard patterns at the sites as a consequence of mitigating effects of the vegetation cover and NBS designed, we performed several simulations and

compared results of different post-operam scenarios including either NBS or Vegetation cover with ante-operam baseline scenarios (S0).

After an introduction on the rockfall onset and propagation dynamics and a comparison of the most updated modelling approaches, the study focuses on each different study area with its peculiarities and types of NBS designed and address the analysis of the NBS effectiveness through a tailored approach of rockfall modelling.

4.1.1 Rockfall onset

Rockfall is generally triggered by the removal from rock faces of individual rock blocks or limited surface portions with limited volumes. Sometimes the rockfall triggering occurs when isolated blocks deposited on acclive slopes lose their balance due to foot erosion or other natural and non-natural disorder causes. The detachment of rocky material from the slope is often controlled by fracture sets which represent areas of weakness of rock masses. Rockfall triggering is thus typical of steep rock outcrops since they are characterized by coherent rocks, often crossed by fractures. Moreover, they have steep slopes that favour the rock mass free falls and their subsequent propagation along the slope by rolling, rebounding, and slipping with increasing speed. Therefore, they can be characterized by very high speeds and a certain unpredictability of the direction of propagation. The dynamics of propagation is indeed influenced by both the block volume and the geometry. It also depends on the slope morphology and geotechnical properties of materials outcropping along the paths: basically, the rockfall dynamics depend on the slope and the block features.

For each rockfall, three different areas are distinguished along the path:

- the onset area where the rockfall is triggered.
- the transit area, where most of the movement of the block occurs.
- the accumulation area, where the sedimentation of the event takes place with the accumulation of the falling boulders.

It is noteworthy that the boundaries between these areas cannot be clearly defined at the slope scale. In fact, rock block deposition can occur in the transit area of other blocks; in the same way, rockfalls can trigger in areas of previous deposition as a consequence of blocks balance loss which often results in the remobilization provoked by the rockfall phenomena.

Generally, rockfalls reach the highest jump heights and speeds in the transit area. Since rockfalls can evolve through different motion types that alternate irregularly, their runouts can be considered as a stochastic event, although rock shapes and the slope gradient can exert some control on them. Jumping rock blocks can get high rotation speeds controlled by the inertia momentum and, thus, by their shape. The runout distance is generally longer when rockfalls involve cubic or spheric rocks. Nevertheless, in some cases, discoidal boulders can also reach high rotational speeds when the minor axis gets oriented parallel to the ground.

The total energy of a falling rock block moving along the transit area is described by its potential and kinetic energy, which convert to either translational or rotational along the path. Therefore, the evolution of their runouts is strictly related to the energy dissipation. It is mainly due to collision that reduces the kinetic energy - caused by deformation work on the soil surface and/or on obstacles lying on the slope (including other blocks, vegetation and anthropic structures). The kinetic energy loss generally depends on the rock mass (size of the rock), the slope, the damping conditions and the collision with obstacles (for example trees).
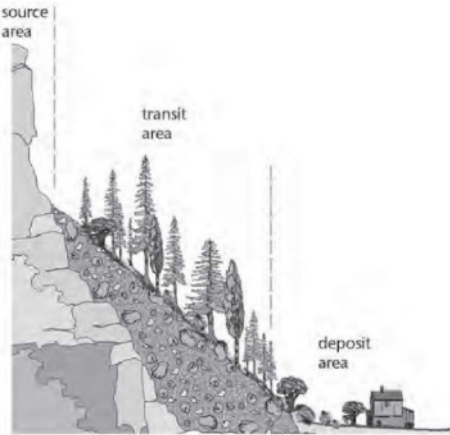
Figure 32: slope zoning according to Berger et al (2013)

4.1.2 Rockfall triggering causes

Rockfalls start with the detachment of blocks from rocky slopes characterized by some intrinsic features such as the outcropping lithology, the fracture intensity, opening and orientation. They are subject to the evolution due to weathering induced by atmospheric and biological agents, which can increase fracturing, fracture opening and propagation, then to the disconnection of rocky blocks and, consequently, to their fall. Some of the leading predisposing causes of rockfall triggering are:

- slope morphology: slope, exposure and relief shape (curvatures);
- geological features: rock types, structural setting, slope debris cover types, rock and soil erodibility;
- geological structure of rock walls: number of fracture sets and their orientation, fracture frequencies, spacings, openings and roughnesses;
- mechanical properties of rocks, discontinuities and soils: cohesion, friction angles, shear strength and compressive strength, elasticity, mechanical behaviour;
- activity status: rockfall frequency and reactivations of previously occurred movements;
- hydrogeology: effects due to the permeability of soils and rocks and hydrostatic pressures.

Among the triggering causes of collapse, several studies showed the relevance of the alternation of frost-thaw cycles where rocky slopes are characterized by a high steepness and fracture intensity (e.g. Pratt et al., 2019).

In some cases, where significant thermal variations occur on daily basis, the thermal expansion and contraction of rock wall surfaces can generate the detachment of rock blocks for thermoclastic phenomena (e.g. Collins & Stock, 2016).

The detachment of the rocky blocks are also provoked by seismic events, especially in areas close to ridge edges and crests, where topographic amplification of the seismic accelerations can occur (e.g. Forte et al., 2021).

Further causes are linked to erosive phenomena, which can determine sole displacements, and to the bioclastic action of the vegetation, involving both the mechanical action exerted by roots expansion and the rock and fracture weathering due to the formation of organic acids.
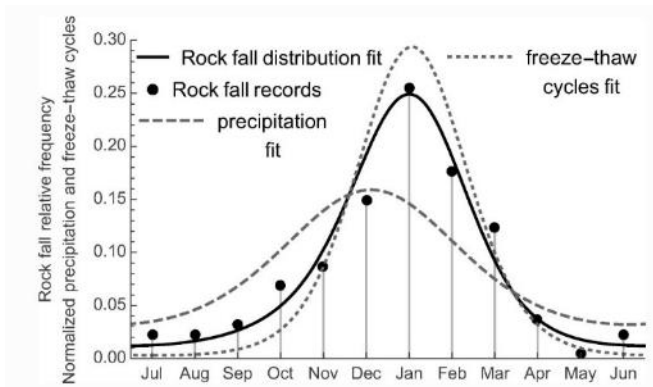
Figure 32. Frequency of rockfall triggering as a function of precipitation patterns (Pratt et al., 2019).

Sporadically, animals and humans can also cause the triggering of collapses, especially for the remobilization of blocks in unstable equilibrium. However, the latter is not a relevant cause.

The role interplayed by different causes coexisting in the same context points out that rockfall onset predictability is not a straightforward task since different causes are characterized by different return periods and time cycles. For these reasons, the correlation of rockfall with climatic factors is challenging and requires long-period monitoring activities on the study site.

4.1.3   Rockfall propagation

After the triggering, falling rocks move along the slope with different modes. These strongly depend on slope steepness and average slope gradient, which vary spatially. The three main motion modes are free fall or flight, rebound, rolling and sliding on the slope surface.

Free fall occurs on very steep slopes. Specifically, for angles greater than 70°, rock movement gradually changes from bounce to fall. During the free fall two different movements can occur: the first is the translation of the block barycentre; the second is the rotation of the block around its centre. After the rotation in air and the subsequent impact on the slope, a rock can jump in a different direction than the arrival one.

Air friction affects the rock speed during free fall, but some authors (Bozzolo and Pamini, 1986) observed that it has no relevant effect on the variation of the movement type.

As mentioned above, movements near the surface can involve different modes:

- *Bounce.* If the average slope decreases downwards, in the direction of movement, a rock collides on the slope surface after free fall, this event is referred to as a rebound. During the first bounce, the rocks tend to fragment. During the first impact, 75-86% of the energy acquired in the initial phase of free fall is dissipated, regardless of the degree of rock fragmentation (Broilli, 1974; Evans and Hungr, 1993).
- *Rolling.* Typically, if the average slope is less than 45°, a bouncing block gradually turns its movement into rolling because the rock gets rotational momentum. In such conditions, rounded boulders are almost constantly in contact with the slope surface. On the other hand, irregular blocks during the transition between rebound and rolling tend to rotate very quickly, and only the more pronounced edges maintain contact with the slope. In both cases, the gravity centre of the block moves along an almost straight path, which results an effective motion mode for energy conservation (Hungr and Evans, 1988).
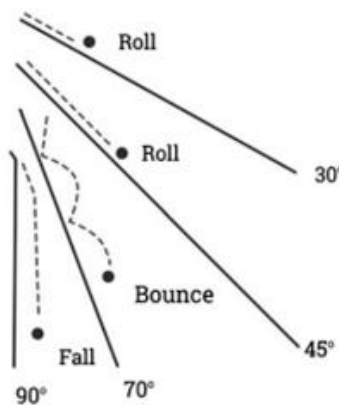
Figure 33: rockfall motion modes.

- *Sliding.* Sliding is another motion that generally occurs only in the initial and final stages of a rockfall. If the slope increases in the direction of movement, the sliding boulder begins to fall, bounce or roll depending on the downslope characteristics. If the average slope does not change during the sliding, the rock usually stops due to energy loss caused by friction.

At some distance from the triggering point, and often after several stages of the movement, a boulder stops. The boulder speed and stopping mainly depend on the average slope steepness since rockfalls generally accelerate on steeper slopes and decelerate on gentler slopes. However, the speed also depends on the size of boulders and the characteristics of the slope cover material, such as the presence of soils or roughness related to debris and vegetation.

Small blocks slow down and stop more easily than larger blocks; firstly, because during a rockfall the total kinetic energy of the small blocks is lower than that of larger ones; secondly, the size ratio with the obstacles laying on the slope is more favourable, as in the case of trees that can stop small blocks.

The boulders slowing down and stopping are improvised rather than gradual processes. They occur because energy is dissipated through collisions and frictional forces acting

on the rock during the movement on inclined surfaces. The frictional force of a moving rock depends not only on the shape of the boulder, but also on the slope surface features, which can significantly vary in short distances. Thus, the friction force between a rock and the inclined surface can be effectively characterized by a dynamic friction angle. The angle of dynamic friction is related to the surface roughness, which can be defined as the change in height perpendicular to the slope within a certain distance along the slope. Kirkby and Statham (1975) defined the dynamic friction angle as (Kirkby and Statham, 1975; Chang, 1998; Pfeiffer and Bowen, 1989):

$$\tan \phi_{\mu d} = \tan \phi_0 + k \frac{d}{2R_{rock}} \tag{13}$$

where, $\phi_{\mu d}$ is the dynamic friction angle (°), ϕ_0 is the internal friction angle (°) (between 20,3° and 33,8°), k is a constant (between 0,17 and 0,26), d is the average diameter of the debris laying on the slope (m), R_{rock} is the average boulder radius (m).

The energy dissipation during impacts on the slope is addressed in modelling by recurring to the apparent restitution coefficient, which describes the variation of block speed before and after collisions:

$$R = \frac{v'}{v} \tag{14}$$

where v and v' are the block speeds before and after the collision, respectively.

Such approach can be considered either kinematical or hybrid kinematical-rigid body, depending on the modelling of the different stages of motion.

The R coefficient comprehensively describes the dynamic actions of impacts and rebounds and simplifies the complex process of interaction between two colliding bodies.

It is necessary to distinguish two components of the restitution coefficients, along the normal (r_n) and the tangential direction (r_t) to the impact plane, respectively. r_n represents the loss of energy determined by the elasticity of the slope material, while r_t is the loss of energy primarily due to the roughness of the slope surface (Dorren et al., 2004, 2006). r_t and the slope angle also represent the main factors controlling the rock velocity in the rebound position. Both parameters are controlled by the composition and the size of the slope covering material and by the radius of the falling rock since the effective surface roughness is proportional to the block size. Therefore, r_t can be calculated by the following formula:

$$r_t = \frac{1}{1 + (MOH/R_{rock})} \tag{15}$$

where MOH is the mean obstacle height along the rockfall path (m) and R_{rock} is the falling rock radius (m).

Other authors addressed the rock-ground interaction with a more rigorous physical approach by recurring to frictional operators acting on the rock-slope interface. These can be considered full-deterministic rigid-body approaches since they explicitly model the change of rotational momentum as the effect of contact and frictional forces acting on rock's edges and corner points (Christen et al., 2007a). They also describe rockfall energy dissipation on a physical basis, considering the action of forces, such as sliding friction and drag, contrasting rock movements.

4.1.4   The effects of the vegetation cover

To limit the use of expensive and impactful artificial interventions against rockfall, the mitigating effect of forest, thus defined as protection forest, is being tested in several mountainous areas since it usually represents a cheaper and more sustainable solution.

Forests are indeed natural protection against rockfall. The different vegetation layers (tree, shrub and grass) can stop, slow down and divert falling blocks, reducing the energy content of the phenomenon. However, it can exert a detrimental action when the vegetation affects the triggering areas. Here the root systems of trees and shrubs can induce the triggering of rocky slope collapses due to the roots that can penetrate the discontinuities of the rock masses and spread them apart by acting as wedges.

Except for this specific case, the forest can generally carry out two types of protection, with the latter being the most important:

- Active protection by preventing the boulder from mobilizing, fixing the blocks through its root systems and decreasing the erosive power of the water by intercepting the surficial runoff water or the sub-surficial water circulation in soil layers. This type of function can be observed along slopes with low to medium dip angles.
- Passive protection by deviating, braking, slowing down and stopping boulders, acting as an obstacle against the rockfall propagation, or a drag force, depending on the ratio between rocks and trees. This function is more pronounced in steeper slopes.

The interaction between rock boulders and trees is complex and depends on many parameters (block shape, speed, impact height, slope degree, soil roughness, tree diameter, root patterns, wood mechanical properties, etc). The effectiveness of the protective role of different forest types depends on the size of the falling block. As an example, ancient forests with tall and large trees are better suited for entrapping the boulders with larger volumes, whereas younger and denser forests are more suited to stop smaller blocks: the higher the number of trees, the greater the increase of impact probability.

Species used in protection forests can also greatly influence their mitigating effectiveness. Generally, broad-leaved species are mechanically more resistant than conifers (Dorren et al., 2005; Stokes et al., 2005).

Species with shallow root systems are the least resistant to overturning. Therefore, in a rockfall protection forest, the use of highly branched and rooted tree species should be encouraged. A sufficient distance between the trees should be left to allow optimal growth of the root system, without compromising the ideal plant spacing pattern.

Dead trees can also have a protective role. In such a case, the trunks of conifers are the most resistant to weathering and decay and, if properly located in rockfall corridors, they are better suited to be used as passive defences, given their capability in deviating and dissipating rockfall energies (Dorren et al., 2005; Kupferschmid Albisetti et al., 2003; Schönenberger et al., 2005).
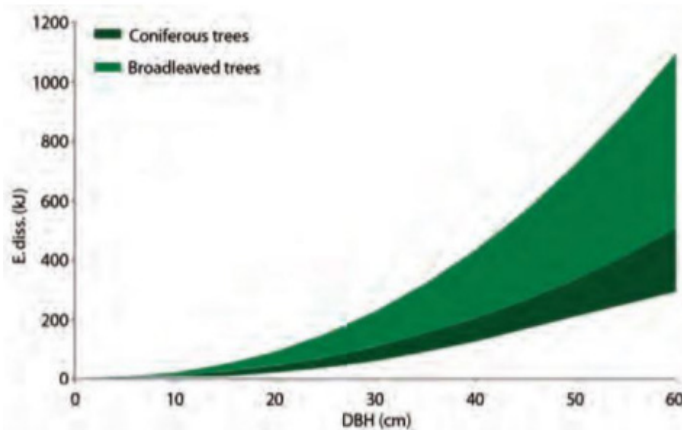
Figure 34: Relationship between dissipated energy and DBH for deciduous and coniferous trees (Dorren et al., 2007).

In Figure 35 (Dorren et al., 2007) a graph that relates the dissipated energies and the tree diameter at breast height (DBH) is presented for deciduous and coniferous trees. It shows that, given the same DBH class, the dissipated energy by broad-leaved trees is much greater.

Despite recent studies on tree strength and forest effects on rockfall in many mountainous regions, the evidence on how much active forest management can effectively protect against rockfall is scarce. To study the effectiveness of rockfall protection forests field, experiments can be performed, for example throwing boulders through different types of forest and monitoring the number of boulders stopped by the forest and their runouts. Nevertheless, these methods are cost-demanding since they are highly time- and work-consuming, especially considering the large forests' extents and variability. An alternative solution is to run rockfall simulations across forests using computer models. The main target of such a modelling is to predict the rockfall propagation dynamics and assess the forests' mitigating effectiveness in order to consider them as a viable solution for protecting human lives and infrastructures on a regional scale.

The protective effect of forest should be considered as a dynamic phenomenon that relies on both spatial and temporal variability of forest structures. However, given the difficulty of modelling forest evolution over short periods, it is advisable to consider a mature forest structure during modelling to determine its effect on the boulder trajectories (Dorren and Berger, 2006). In long-term assessments of residual risk, however, how the forest change over time due to climate change should be also considered. To tackle this challenging task, detailed information on current forest structure, composition, and response to current and recent climatic conditions should be known along with site-calibrated possible trends for future climate conditions.

4.1.5   Rockfall modelling approaches

Several commercially available software packages simulate rockfall propagation through different approaches. Each approach is characterized by some simplifications or assumptions, which should be carefully weighted because of their ability to significantly affect the modelling accuracy and reliability. These approaches can be grouped into several categories:

- At varying the spatial dimensions, software can be divided into two- (2D) and three-dimensional (3D). In two-dimensional models, the trajectories of the block are simulated along a plane (x, z), defined by two axes: one representing the progressive distance and the other the elevation. The slope profile is therefore defined on this plane, leaving out the third spatial dimension. Among these models, the movement on the third dimension is implicitly assumed to be negligible. In three-dimensional models the trajectories of the block are simulated in a three-dimensional space (x, y, z). The third spatial dimension is thus accounted for, including the lateral dispersion of boulders (i.e. deviations of trajectories from the direction of maximum slope). This implies a larger degree of freedom for parameters controlling rockfall propagation with relevant influence on rockfall kinematics, conditioned by the morphological characteristics of the area. This method allows simulating all the trajectories of the block, even the less predictable ones.

- The approaches can be distinguished between kinematic (lumped mass) and dynamic (or rigid body) depending on the physical model adopted. The choice of the most suited approach depends on the data available about the block size and shape, the extension of the study area and the computational capabilities. The lumped mass methods do not consider the shape and size of falling rocks, which is assumed to be a point without mass. The trajectory is therefore independent of the block mass. In this case the rock motion has two components of speed (normal and tangential), while the rotational speed is not considered. The method considers the mass of the block only for the derivation of kinetic energy as a function of the speed. Rigid body methods treat a rock as a rigid body, with shape, size and mass that determine the momentum of inertia at the different motion stages. Some of them can also consider a boulder as a set of particles and therefore simulate fragmentation of the initial boulder. The trajectory is modelled with ballistic approach, associating all the feasible movements, including the rotation in the air. During the different motion stages,

rock impacts on the slope can change the direction of movement. Many models use a hybrid-type approach, using rigid-body physical models for the rolling and sliding phases while considering the block as lumped-mass during the flight phases. Namely, they neglect the momentum of inertia during flight and thus the variation in rotation speeds that it can induce.

- Depending on the approach used in the analysis of interactions with vegetation cover, it is possible to distinguish three cases: (a) models neglecting the effect of vegetation; (b) models considering vegetation as a medium crossed by the block characterized by a resisting drag force; (c) models treating vegetation as a set of trunks which the boulders can impact on, inducing deviation of trajectories and energy dissipation. In the second case, the impacts on vegetation are neglected and the dissipation effect is exerted uniformly according to the viscosity of the vegetation cover. In the latter case, the energy dissipating effect of each trunk is modelled as a function of impacting block size, energy, and direction of incidence, and of tree strength, in turn depending on DBH of tree species.

- A further categorization defines deterministic and probabilistic models. The former do not consider the variation of parameters during the analysis, which are thus constant during simulations. Conversely, the latter can simulate the variation of some parameters within limited ranges defined by the user, using simplified statistical distributions. Each simulated trajectory during the analysis has a certain probability of occurrence as a function of the statistical frequency defined by the distribution of the modelled parameters. To address the uncertainties of the rockfall modelling, most rockfall trajectory models adopt probabilistic approaches at least for some input parameters, such as the trigger direction. From a deterministic viewpoint, rockfall trajectory depends on: a) where the rock comes off, b) which rock collapses, c) the failure mode and d) the slope properties. a), b) and c) are related to the location of the source point (i.e. planar coordinates and height), the properties of the rock (i.e. material, structure, size and shape) and the initial conditions (i.e. initial velocity), respectively. Slope properties include topography, roughness, material, and ground cover. Variations in the source location, rock properties, initial conditions, and slope properties occur between different rockfall events, thus creating inherent uncertainty in rockfall phenomena. The detachment of several rock blocks from different locations on various slopes with different initial conditions results in different rockfall trajectories. Real-scale field experiments reveal that small variations in initial conditions can result in significant dispersion of rockfall trajectories, even if the same rock sample is involved (Li and Lan, 2015).

Rockfall dynamics include rock free fall, rock-slope interactions, rock-vegetation interactions, and often rock fragmentation. The dynamics of free fall are straightforward and can be predicted with reasonably accuracy by simple analytical models if the influence of air is neglected. Conversely, rock-slope interactions modelling is challenging and includes the impact, rebound, rolling, and sliding of rock on the slope. As far as the impact and the rebound of rock are concerned, the time functions of the interaction forces are significantly complex and are likely never precisely determined.

Any model describing rock-slope interactions adopts some level of simplification. Errors in modelling can arise from model inputs or can be associated with the physics or solution of the model. Namely, the analytic equations describing the physics and their solutions can not be adequately accurate.

Regardless of the adopted approach, each model provides: polylines of rockfall trajectories, runout distances, spatial variation of kinetic energies, rebound heights and speed, with their statistical distributions. Depending on whether a bi-dimensional or tri-dimensional model is adopted, modelling results are provided in the form of profiles or maps. Rockfall modelling can allow:

- Hazard analysis: the results describe the area involved, the spatial distribution of maximum kinetic energy and speed and the reach probability on each point of the study area.
- Design defence structures: the location and design of rockfall defence structures such as fences, barriers, ditches and tunnels can optimize the trajectories of blocks, their maximum kinetic energy, and the rebound height (technical codes suggest defence works should be designed on the maximum values corresponding to the 95% quantile of considered parameter recorded on each cell).

4.1.6   A review of available rockfall models

A relevant side of this study was dedicated to the the identification of the most appropriate approaches for the analysis at each case study, based on the general methodological framework here developed. The peculiarities of the hazard scenario at each case study, the scale of impacts, the NBS implementation, and the influence of climate change were thus properly addressed. This approach was integrated with the analysis of the most up-to-date modelling software used in the most recent scientific studies. The following paragraphs discuss the main aspects of models analyzed summarizing the main features and differences.

Among these, RocFall is a 2D probabilistic model based on rigid-body approach, developed by Stevens (1998), and then commercialised by Rocscience Inc., where almost all inputs can be randomly varied, allowing for deterministic and probabilistic analyses. Input data such as triggering locations, rock masses, initial conditions can be randomly derived from predefined statistical distributions and the shape of the rock can be randomly selected from a library of available shapes. Slope properties and their influence on rock-slope impacts can be randomly derived from predefined distributions (Li and Lan, 2015). In RocFall the aforementioned parameters, as well as the slope profile, can also be evaluated using a deterministic approach. STONE is a 3D rockfall simulator based on a lumped-mass approach (Guzzetti et al., 2002), which can probabilistically treat some input parameters such as rockfall source positions and frequencies and the initial horizontal direction; similarly, slope restitution coefficients can be varied within predefined intervals. An updated version of this program, HY-STONE (Crosta and Agliardi, 2004), incorporates a hybrid algorithm (mixed kinematic

and dynamic) and additional functionalities for probabilistic analyses. It can also probabilistically simulate the effects of vegetation and rock fragmentation (Frattini et al., 2013). Rockfall Analyst (Lan et al., 2007) is a semi-deterministic 3d model based on the lumped-mass approach fully integrated within the ArcGIS environment (ESRI, 2004). Rock-slope interaction is defined by three slope properties: the normal and tangential restitution coefficient and the friction angle. The relevant number of trajectories is the only parameter that can allow probabilistic analyses. It can be modelled by varying the initial horizontal direction within a range set by the user. RocPro3D (2014) evolved from Pir3D (Cottaz and Faure, 2008) and adopts a hybrid lumped-mass/rigid-body approach. The probabilistic approach relies on the possibility to vary starting position, rock mass and size and the starting conditions within a uniform distribution. Soil parameters such as the dynamic friction coefficient, restitution coefficients and rebound angles can be varied within uniform or Gaussian probabilistic distributions. A unique feature of this model is the possibility to vary the uncertainties as a function of speed, thus partly accounting for the principle of inertia. RAMMS::Rockfall (Caviezel et al., 2019) is a 3D simulation model that adopts a full rigid-body approach, allowing the explicit definition of arbitrary three-dimensional polyhedral bodies, including the natural rock shapes (Christen et al., 2007), simplifying the assessment of the effect of rock shapes in rockfall propagation behaviour. It introduces a new friction model, which involves a slip-dependent coefficient of friction, and allow modelling the effect of rock erosion on the ground (Bartelt et al., 2013). The contact between the falling rock and the ground is determined by the interaction between the rock corners and edges, where frictional and contact force act inducing rotational momenta. The block rotation is also modelled during the flight stages also considering the effect of air drag force. The model can account for vegetation's effect crossed by falling rock by introducing additional drag forces varying upon vegetation density. On the other hand, it cannot explicitly model the impacts on tree stems. RockyFor3D (Dorren, 2015) is a 3d semi-probabilistic model based on a hybrid approach. It applies rigid-body algorithms for the rotation phases, where a lumped-mass approach is used for the flight stages, whereas rockfall sliding mode is not modelled. The model combines deterministic algorithms with stochastic approaches: it is deterministic in the frame of the description of rockfall processes. To account for the variability of the input data it uses both a deterministic (fixed data) and a probabilistic (data variation) approach, since they can be sampled within user-defined intervals. The main feature of this model is the capability to model the effect of protection forest by simulating the block-tree impacts, by accounting for the energy dissipation as a function of the tree species, the DBH, the block size and the angle of impact. The distribution of trees in the forest can be managed using deterministic and probabilistic approaches. Picus Rock'n'Roll (Rammer et al., 2010; Woltjer et al., 2008) can be considered as an extension of Rockyfor3D since it integrates the same algorithms for rockfall propagation and rock-trees impacts with a patch-based forest simulator. Therefore, it can model the evolution of a forest structure and the changing effect in rockfall mitigation.

4.2 Rockfall modelling at the Artouste, Laruns, France

4.2.1 Case study and hazard scenario

The survey area is located along a primary regional road (RD-934 - A-136) that crosses the Pyrenees, connecting several small towns located along the Spain-France borders. The RD-934 road shows an average daily traffic intensity ranging between 1500 - 2500 vehicles/day and it can reach more than 3000 vehicles/day during summer and winter weekends. This marks the high traffic exposure to possible hazardous natural phenomena occurring along the road.

The case study discussed here is at Artouste, a locality within the Municipality of Laruns, in the Atlantic Pyrenees department. Here the road runs at the base of steep rocky slopes and vertical rock walls, which often release blocks of variable size invading the road.
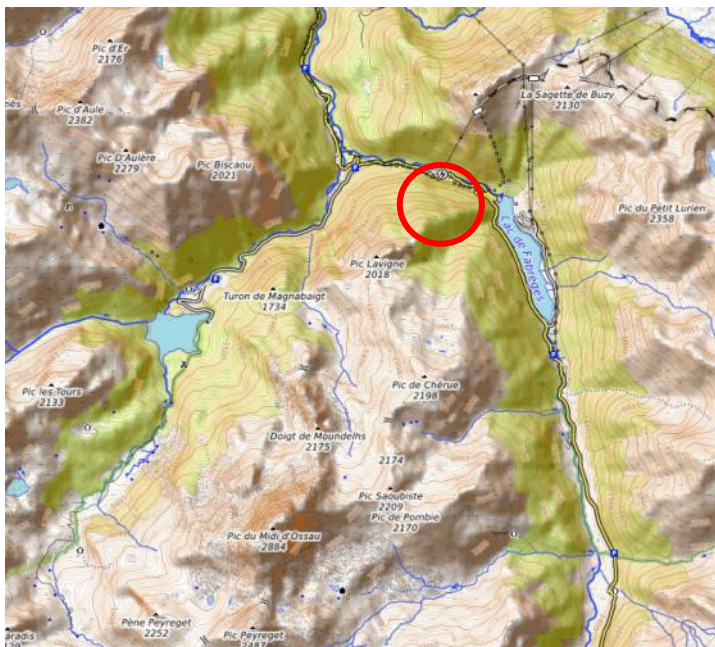
This study analyses a forested slope located approximately at the progressive kilometre 46 + 800 of the departmental road managed by the Departmental Conseil des Pyrénées-Atlantiques, where a speed limit of 60 km/h is set. The slope is in the foothill area of the mount Pic Lavigne (2018 m a.s.l.) and is located in the Ossau valley, which represents one of the main mountain valleys of the Béarn region ( ). At the base of the studied slope the artificial Fabréges Lake and its dam are located.

Figure 35 Study area location

The area is highly exposed to the risk of rockfalls due to the presence of a steep slope, with slope angle > 40°, covered by a forest, where many rocky scarps and isolated blocks can trigger rockfall events. Specifically, a rocky front, about 200 m far from the road, is significantly susceptible to collapse. The current forest cover is characterized by medium-low tree density and the tree average diameter is rather limited, thus being not able to provide sufficient protection against large rockfalls.

A rockfall event also caused a fatality in January 2014, when a woman driving along the road was hit by a boulder 300 kg weight.

In this site, the potential landslides have a variable size, ranging from small blocks to boulders lager than 1 m^3 as documented by the presence of both impacts on the trees and blocks and/or boulders deposited along the slope.

The road segment exposed to the invasion of collapsed boulders is about 700 m long and is only partially protected by pre-existing and under-construction engineering interventions (rockfall tunnel and rockfall fences, respectively), along the main rockfall corridors (Figure 36).
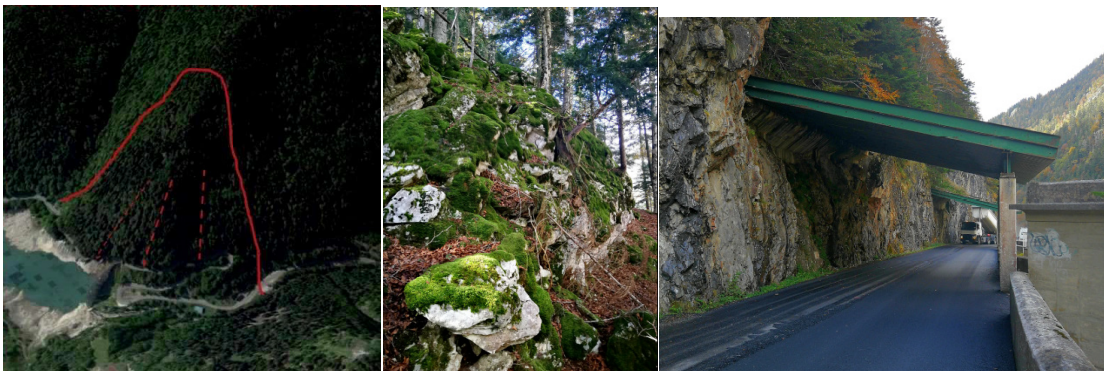
Figure 36: left) study area; center) rockfall release area; right) existin rocfall defences (rockfall tunnel).

4.2.2   Geological setting

From a geological viewpoint, the study area is located in the Pyrenees mountain range, an asymmetric double vergence chain built up from the collision between the Iberian microplate and the European plate, the upper Cretaceous and the Miocene. In particular, the study area is located in the central sector of the axial zone of the orogen, at the end of the Ossau Valley. Here the variscan basement outcrops extensively at the core of a regional antiform, crossed by several intrusions of igneous rocks.

In the area we can distinguish four different sectors characterized by two different lithological complexes (Figure 37):

1. The first complex consists of a Devonian metamorphic-carbonatic series, lithologically dominated by white coloured marbles (Fabrèges Marbles). These are covered by terrigenous-detrital sequences (Sia series), which are 500 m thick, consisting of banded quartzites and sandstones, separated by thin layers of black schists.
2. The second complex consists of intrusive rocks composed of granodiorites belonging to the Eaux-Chaudes batholith, which intrudes the sedimentary series.

The rocks of the metamorphic and crystalline bedrock are covered by Quaternary clastic glacial and fluvial deposits mainly formed by moraine deposits, colluvial debris and alluvial fans debris.
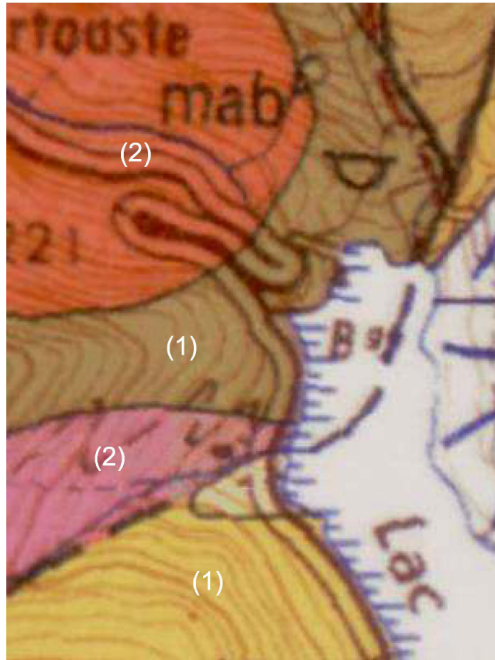
The Quaternary covers affecting the study area essentially of detrital-colluvial nature. The site morphology is characterized by recent glacial activity (Pleistocene). The Ossau Valley was indeed occupied by a very thick alpine glacier, which deeply carved the valley leaving the typical U-section, with very steep flanks. As a consequence of the ice retreat, the slopes engraved by the glacial load are now affected by the development of both deep-seated and superficial slope movements, such as those here studied.

Figure 37: Sketch from the Geological Map of France (scale 1:50.000), Laruns-Somport sheet, reporting the bedrock units at the study area

4.2.3   Nature-Based solution (NBS) designed

The NBS solutions designed in the frame of the PHUSICOS project to deal with rockfall hazard will integrate with existing and under-construction rockfall defence structures. They consist in the insertion of support and retention innovative wooden structures aimed at either fixing boulders in unstable equilibrium and preventing rock block detachment or stopping the released boulders before they reach high speeds. In detail, they consist of wooden tripods (fixing individual boulders) and wooden meshes (fixing grouped boulders and fractured rock masses) made of larch trunks with 15 cm diameter and an estimated service life of 15 years. The structures will be fixed to the ground or anchored in the bedrock at different depths depending on the nature of the ground and of the support; these interventions are designed to fix and stabilize rock boulders with masses larger than 1500 kg. Along with these structures, masonry walls are designed to locally support some overhanging portions of rock faces. They are completed with 2.25 m tall and 3-5 m long wooden barriers, made of larch trunks with a diameter of 25 cm, placed near the main release areas to stop boulders as soon as they collapse. All the trunks will be joined together and resting on the living trees; some barriers will have a horizontal pattern and others a vertical one; the latter will first be tied to two horizontal support poles. No information is available about the energy adsorbed by such barriers. Thus, by considering similar road defence interventions on mixed wood-steel barriers, an average absorption value of 100 kJ was accounted for simulations.
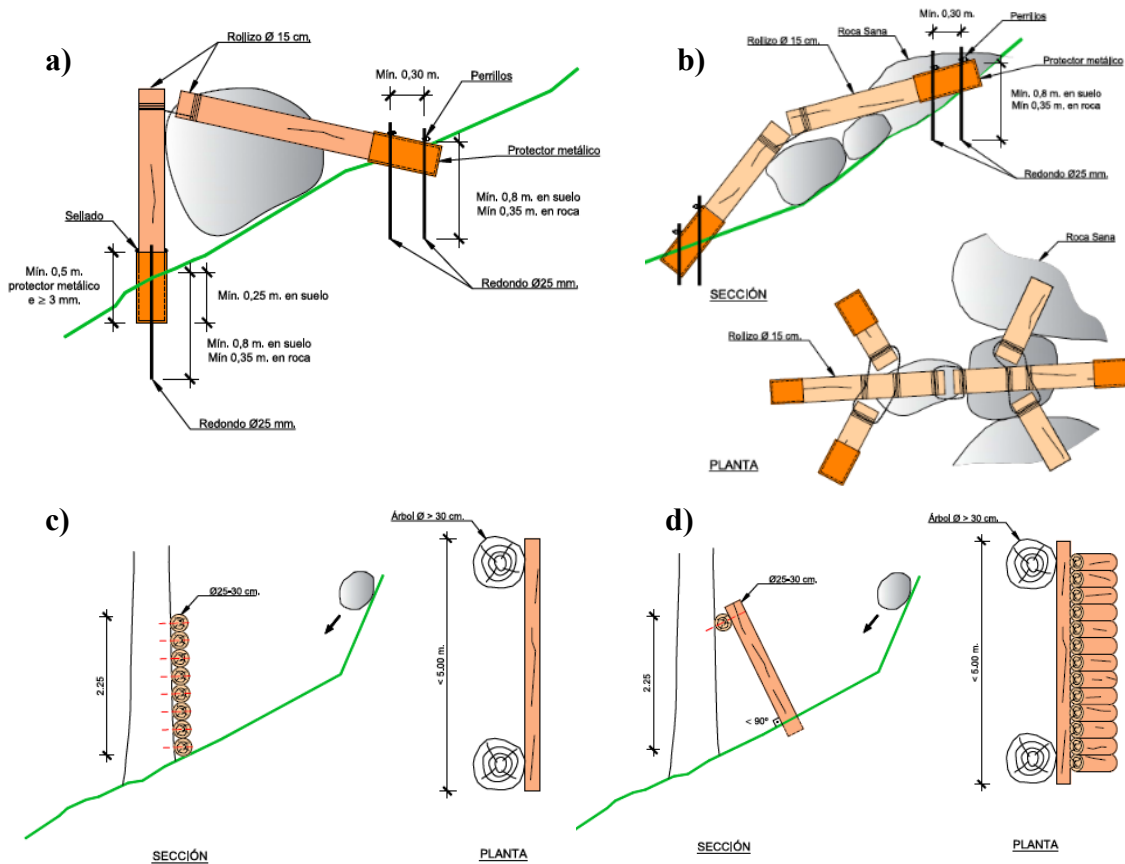
Figure 38: Examples of designed NBS consisting of in (top) rock fixing structures and (bottom) passive rockfall barriers. a) wooden tripods fixing individual boulders; b) wooden meshes fixing grouped boulders; c) rockfall wooden barriers with a horizontal pattern; d) rockfall wooden barriers with a vertical pattern.

These interventions will couple with the protection forest, which will be maintained and improved to increase the protection function. With the NBS project, no detail is provided for future forest density and composition. Therefore, for the sake of safety, during modelling, the current forest structure is included.

4.2.4 Methods

The rockfall hazard analysis for the assessment of the NBS effectiveness, considering the mitigating effect of the forest planted at the study area, was carried out by applying the three-dimensional hybrid model Rockyfor 3D (Dorren, 2015) based on a set of high-resolution input data provided by the PHUSICOS partners BRGM and CTP-OPCC. This analysis was aimed at evaluating the potential effects in terms of rockfall intensities and probability along the studied slope and road at the foothill and their variations induced by the implementation of NBS. To tackle this task, the assessment is based on comparing results of rockfall modelling for baseline (without designed rockfall defence structures) and NBS scenarios (with the designed interventions). To assess the effect of the forest implementation, during the modelling of the baseline scenario, the forest was not included.
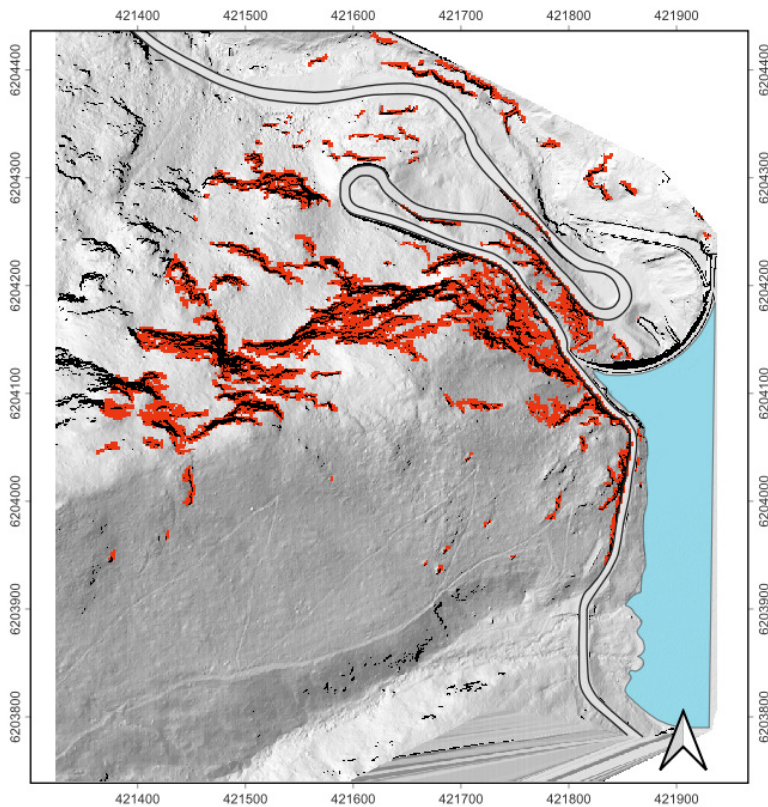
Figure 39: Source areas (red zones) with vertical rock faces (black areas).

Regarding the baseline conditions, two different scenarios were defined by site owners which, according to the results of field surveys, distinguished two different classes of boulder volumes, namely 0.25 m^3 (Scenario 1, S1) and 1.00 m^3 (Scenario 2, S2) related to return periods of 10-year and 100-year, respectively.

Similarly, for the NBS modelling, two different scenarios were defined, namely Scenario 3 (S3) and Scenario 4 (S4), also characterized by the release of blocks of 0.25 m^3 and 1.00 m^3, respectively.

The assessment of NBS and forest effectiveness was based on the comparison between S1 and S3 and between S2 and S4 for the two different classes of rock volumes.

4.2.4.1   Modelling inputs

Input data required for modelling consists of a set of raster files (ESRI ASCII format) which spatially define the different parameters controlling the rockfall propagation. The slope and its morphology are accurately described by a DTM, suitably converted for be processed in RockyFor3D. For this purpose, site owners carried out detailed airborne and terrestrial lidar and photogrammetric surveys to provide high-resolution digital terrain models (DTM and DSM with a 50 x 50 cm cellsize) able to describe the terrain morphology and tree cover with great detail. These were used as a three-dimensional topographic basis for rockfall simulations (DTM) and for current forest modelling

(DSM). Other data inputs were provided with a lower resolution and were thus resampled according to the DTM resolution. With reference to the initial conditions, they concern:

- the rockfall source areas and the relative rock densities (in kg/m^3). Source areas were defined by BRGM applying the method proposed by Loye et al. (2009) on morphometric analysis of DTMs. It compares the slope angle frequency distribution of the studied area with available distributions related to different morphological settings. This allowed defining different thresholds corresponding to increasing probability for a pixel to belong to a cliff. The analyses indicated a probability >90° for slope angles larger than 65.5°, which were then considered cliffs. Cliff neighbouring pixels with slope steeper than 49.5° were also included in sources areas, since the probability was >10% (Figure 39).

- As block shapes in each cell of the source area raster, the parallelepiped was chosen within the library provided, according to the evidence from field surveys.
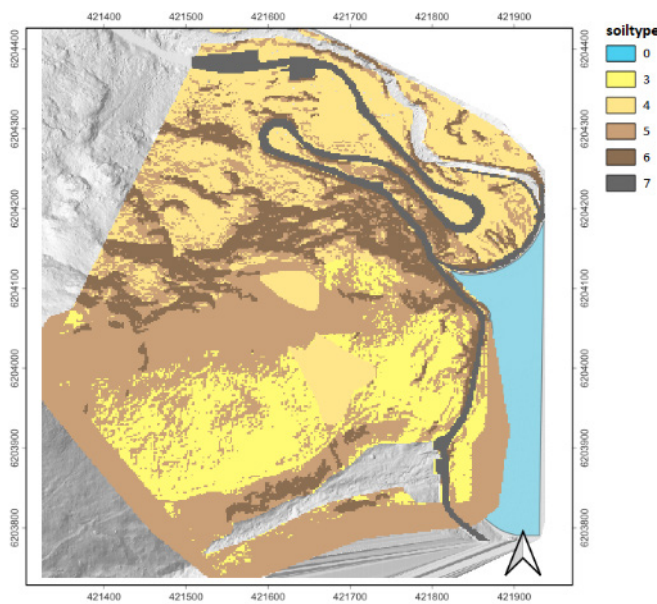
- The three main dimensions of the rock blocks consisting in the (d1) maximum, (d2) medium, and (d3) minimum lengths varied depending on the block class considered according to field data. Values adopted in modelling are reported in the following table:

Figure 40: map of soil types. 0 – water bodies; 3 – medium to fine -grained colluvial deposits; 4 – coarse grained colluvial deposits; 5 – bedrock with thin weathering or soil cover; 6 – bedrock; 7 – anthropic paved surfaces and roads

Table 14. Block parameters used for the two volume classes

Shape	d1(m)	d2 (m)	d3 (m)	Volume (m³)	Weight (kg)
parallelepiped	1.00	0.50	0.50	0.25	625
parallelepiped	1.60	0.80	0.80	1.00	2500

With reference to the propagation area and slope features, they concern:

- Classes of the soil material with their normal restitution coefficients at each raster cell. The soil type mapping was carried out by BRGM combining different sources of information: 1) the geological map of the area, 2) the clustering in homogeneous slope zones, 3) the clustering in zones of homogeneous roughness, 4) the detailed inspection of the 3D shaded view of

the DTM, 5) the detailed inspection of the high resolution orthophotography of the study site. This allowed defining five different soil classes characterizing the study area ranging from coarse-grained colluvial deposits and screes to outcropping bedrock (Figure 41).

- Slope roughness expressed for three different classes of frequency, namely (rg70) 70%, (rg20) 20%, (rg10) 10%. They define the roughness of the inclined surface along the direction of block motion. This roughness does not represent the micro topography, but the boulders located along the slope that hinder the rockfall. This roughness is expressed by three classes defining the probability of a boulder to meet an obstacle of a certain height along the path. Each class corresponds to the representative obstacle height (MOH) in the average direction of rockfalls for the 70%, 20% and 10% of cases, respectively. The roughness data collection for the study area along with other input data was carried out by BRGM. It based on differences between digital elevation models with different cellsize and degree of smoothing. The altitude difference was then corrected for slope angle to calculate the height of the asperities orthogonal to the slope (MOH). The distribution of the MOH was then analysed in order to extract the quantiles corresponding to 70% 20% and 10% (RG70, RG20 and RG10). For areas around departure zones, displaying anomalies on the evaluation of RG70, RG20 and RG10, the values were adjusted manually. The modelled MOHs were then validated based on field data from some sample areas.

The approach used to implement NBS measures in the post-operam scenarios modelling depends on the type of NBS considered and, in some cases, it needs the preparation of new input files. The supporting structures (tripods, walls and meshes) are considered stabilized areas, thus subtracted from the triggering areas considering circles with a radius of 1 m for the tripods and 2.5 m for meshes and walls around the point of implementation derived from the design layouts.

Wooden rockfall barriers were considered linear barriers 2.25 m high with absorption energy of 100 kJ. They were implemented in the software through a set of rasters defining: (1 - net_number) the identification number of the barrier; (2 – net_energy) the maximum absorbed energy in kJ; (3 – net_height) the barrier height measured in the direction normal to the slope expressed in m.

The forest was considered with a deterministic approach using the position of the individual trees got from the comparison between DSM and DTM. This requires two more files containing (1) the coordinates (x and y) and the DBH of each tree (2) the per cent content of conifer species in the form of a raster map.

Within this study, input and output maps were managed with an open-source GIS tool (qGIS).

4.2.4.2   Forest modelling

Since one of the main targets of this study was to evaluate the effect of the current forest as a mitigating element of rockfall, several activities were carried out to detect the trees' location and diameter. Positioning and dimensioning each trunk over such a large area (about $34 \times 10^4 \, \text{m}^2$) is highly time- and cost-demanding. A methodology is thus proposed to extend detailed information collected on sample areas to the whole slope. At first step, some project partners conducted detailed measurements on the trees located in a sufficiently large sample area, considering it representative of the forest structure.

In the sample areas identified in Figure 41, mobile terrestrial laser scanning (TLS) and botanical surveys were carried out to detect the position of each trunk, the tree species, the DBH and the height of each tree.
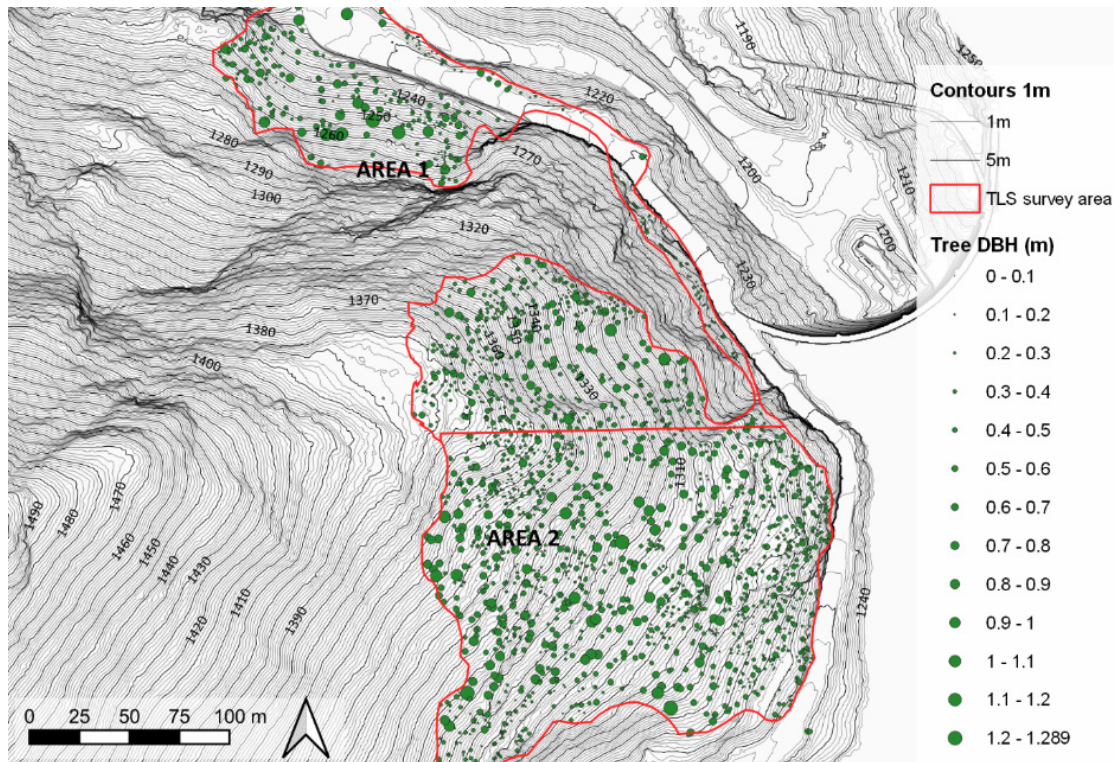
Figure 41. Map of the sample areas covered by field surveys with represented the trees' DBH (circles' diamater). Area 1) TLS surveying area; Area 2) TLS and botanical surveying area.

In particular, the area covered by laser scanning and the definition of the tree position and DBH was about $5.0 \times 10^4 \, \text{m}^2$, whereas the recordings of tree species and botanical measurements were carried out on $2.5 \times 10^4 \, \text{m}^2$ (Figure 41, Area 1). These surveys allowed defining the forest composition in terms of tree species and the input data to set site-specific allometric formulas correlating tree heights and diameters.

More in detail field surveys recognized 1213 trees on $2.5 \times 10^4\ \mathrm{m}^2$ of which 778 firs (*Abies Alba*); 433 beeches (*Fagus Sylvatica*) e 2 yews (*Taxus Baccata*); thus, resulting in a conifer per cent content of ≈64% with the remaining ≈36% of broad-leaved trees.

Field data allowed to define the following allometric formula for the fir trees:

$$DBH = 0.0185714 * H \qquad (4)$$

where DBH is the diameter at breast height measured at 1.2 m above the ground (m); H is the height of the considered fir (m).

For beech trees, the following formula was derived:

$$DBH = 0.0156558 * H \qquad (5)$$

A semi-automated forest model was reconstructed and calibrated to extend the information obtained from the detailed surveys over the entire survey area. It was based on a canopy height model (CHM) developed by comparing the DSM and the DTM using the Ecorisq FINT software (Dorren, 2017; Dorren et al., 2006), which extract the position of individual trees from the CHM by analysing the peaks recognized as tree vertices, using the Tree-top Window Analysis (TWA) following the approach proposed by Dorren et al. (2006). The authors suggested that in the presence of forests with a high frequency of broad-leaved trees, characterized by several secondary peaks within a single crown, it is advisable to smooth the data by applying Gaussian filters.

Twenty different models were defined at varying degree of smoothing to obtain a calibrated model based on tree density. The Gaussian filter plugin included in the qGIS software was used, and the varied parameters were the search radius values and the number of standard deviations used in smoothing and the minimum tree height considered for individual tree positioning (Table 15).

Table 15: parameter used for gaussian filtering of 20 different CHMs. Model no – identification number of the considered CHM; Search radius - the number of cells used for smoothing; Sigma – number of standard deviations used for smoothing; Search mode – geometry of the search area (C= Circular); Min. heights - minimum tree height considered for individual tree positioning (m)

Model No.	1	2	3	4	5	6	7	8	9	10	11	12	13	14	15	16	17	18	19	20
Search radius	-	10	7	6	5	5	5	10	2	-	-	5	5	5	10	5	-	10	10	10
Sigma	-	2	2	2	2	1.5	1.75	1.25	1.25	-	-	1	2	1.5	1.5	1.5	-	1	1.2	1.1
Search mode	C	C	C	C	C	C	C	C	C	C	C	C	C	C	C	C	C	C	C	C
Min. height	-	0.5	0.5	0.5	0.5	0.5	0.5	0.5	0.5	3	0.5	-	0.5	-	3	5	5	5	5	5
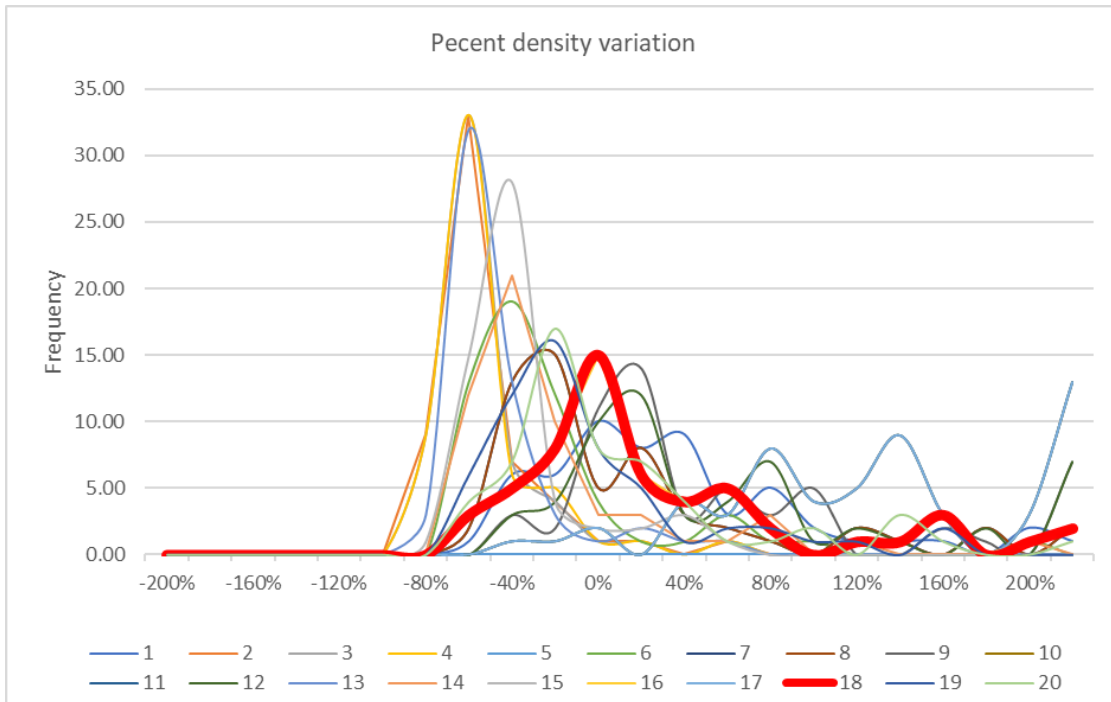
Figure 42. Statistical distribution of per cent density variation between modelled and surveyed tree datasets. Each curve represents a different canopy height model, obtained with different gaussian smoothing. The identification number of the model is reported in the legend.
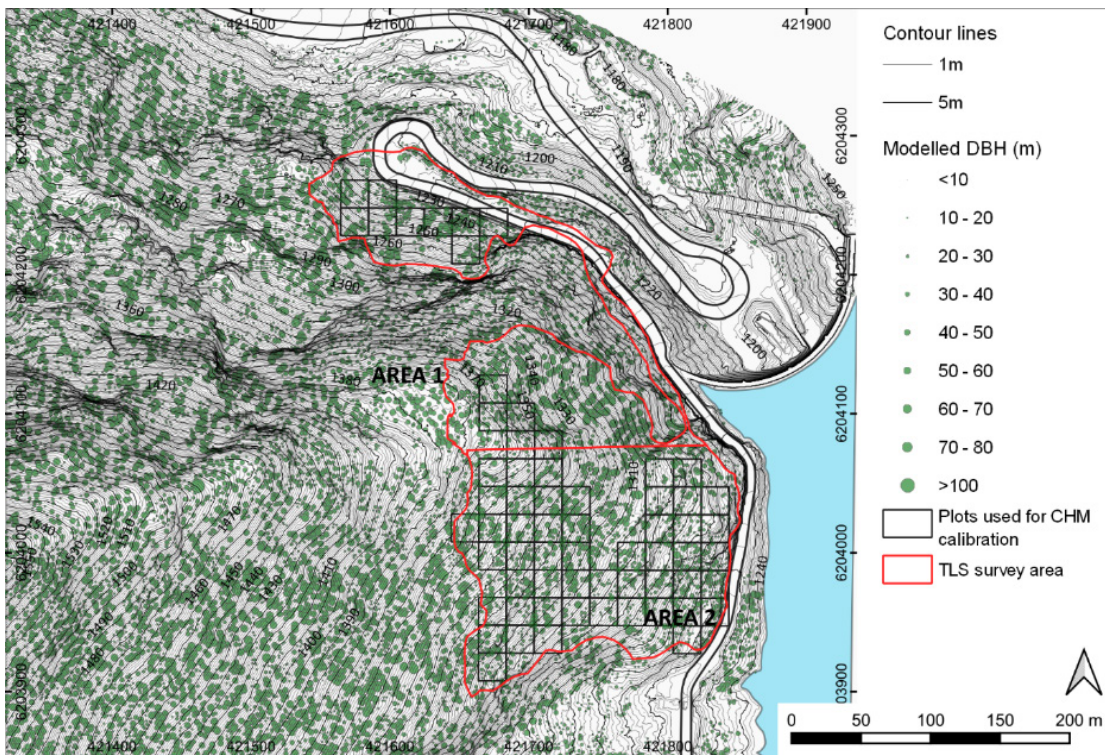
Figure 43: Modelled tree position and DBHs.

Each model produced a map of tree positions over the entire study area, including the sample areas covered by field surveys. Therefore, the modelled data were compared with the collected ones. To this aim, 64 square land plots, 20 m x 20 m size, were identified within the areas with the best coverage of field data. The trees falling in each one were counted from both the modelled and surveyed files. The discrepancies between the two datasets were then calculated as the percentage of the surveyed trees' density. The statistical distribution of density variation allowed us to identify the forest model which best fitted the surveyed data. With this regard, the model n. 18 returned the best fitting, showing the same tree density as the surveyed data on many plots, with distribution somewhat symmetrical around 0 (Figure 42). The model was obtained applying a Gaussian filter with a search radius of 10 cells and averaged over a confidence interval given by 1 standard deviation. The modelling output consists of a point shapefile with the positions and height of individual trees (Figure 43).

Considering the prevalence of conifers with 64% of cases, the allometric equation chosen to derive DBH from tree heights was that computed for those tree species (DBH = 0.0185714*H). In that way, it was possible to get the forest input data for RockyFor3d, namely:

- a text file containing coordinates and diameters of individual trees (treefile.txt);
- a raster map including the percentage distribution of conifers (conif_percent.asc).

4.2.5   Modelling results and discussion

4.2.5.1   Scenario 1

The first modelling scenario (S1) represents a baseline, i.e. without including vegetation and NBS interventions, considering blocks of small volume V = 0.25 m^3, related to a 10-year return period. Maps representing the most significant simulation results for this scenario are reported in the Figure 44.

Figure 44a represents the maximum kinetic energies corresponding to the 95th percentile of the maximum energies recorded at each cell. It indicates that rockfalls reach their highest intensities in a few small areas, mainly along the steepest slopes, where they range between 500-1000 kJ; along gentler slopes, energy values were always below 500 kJ.

Figure 44b shows the maximum rebound heights (sampled at the 95th percentile), which always resulted lower than 2 m in the areas where the boulder detachment occurred. With the rockfall propagation in the transit area, the rebound heights increase, reaching very high values, up to 24 m, where steep slopes are crossed by boulders coming from uphill.

The rockfall reach probability is shown in Figure 44c, pointing out that, due to the high frequency of rockfall source areas uphill from the road, the reach probability ranges between 33% and 40% over the whole area. Slightly higher values are recorded in the

foothill area of the main rock faces, where they are higher than 37%. They reduce moving from the source areas due to the dispersion of the rockfall trajectories. A reach probability of around 34% is recorded along the road in the north-western part. To the southeast, the probability increases due to the proximity of the road to the main source areas. Consequently, the blocks preferentially accumulate along the road (Figure 44d), especially in the central and southern parts. Several blocks also accumulate along the slope, confirming the field evidence.

The main target of this study concerns the hazard affecting the road. To this aim, graphs showing the variation of the main parameters such as the rebound heights and the block energies along with the longitudinal road profile (Figure 45) were generated. They show energies reaching 750 kJ in the northern part of the road (green line), whereas they are considerably lower to the south-est where, except for some peaks, they do not exceed 250 kJ. The average rebound heights (red line) are almost constant along the road, around 10 m, with many peaks due to steep scarps close to the road, especially to the south-western, where they can reach 20 m.
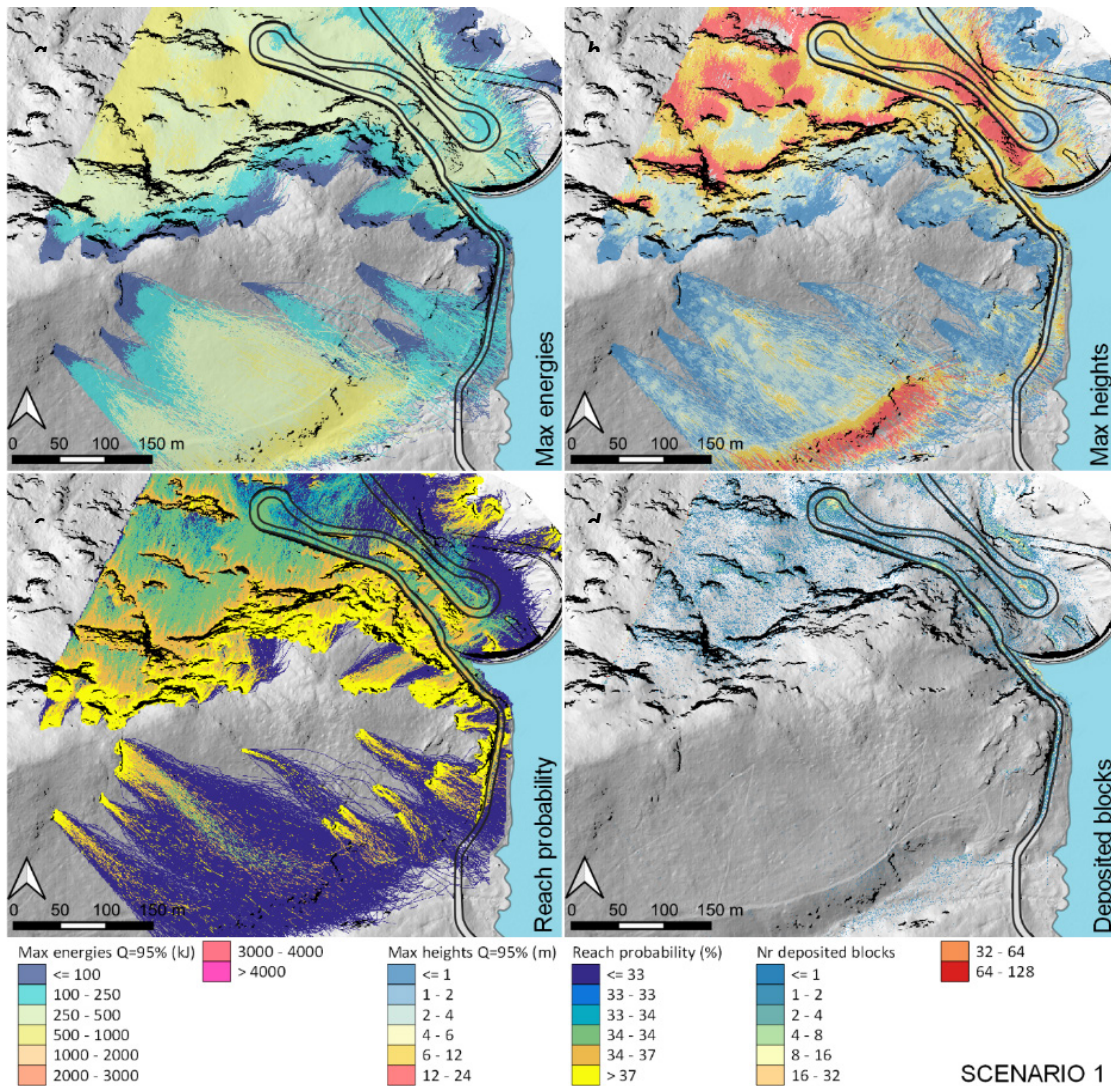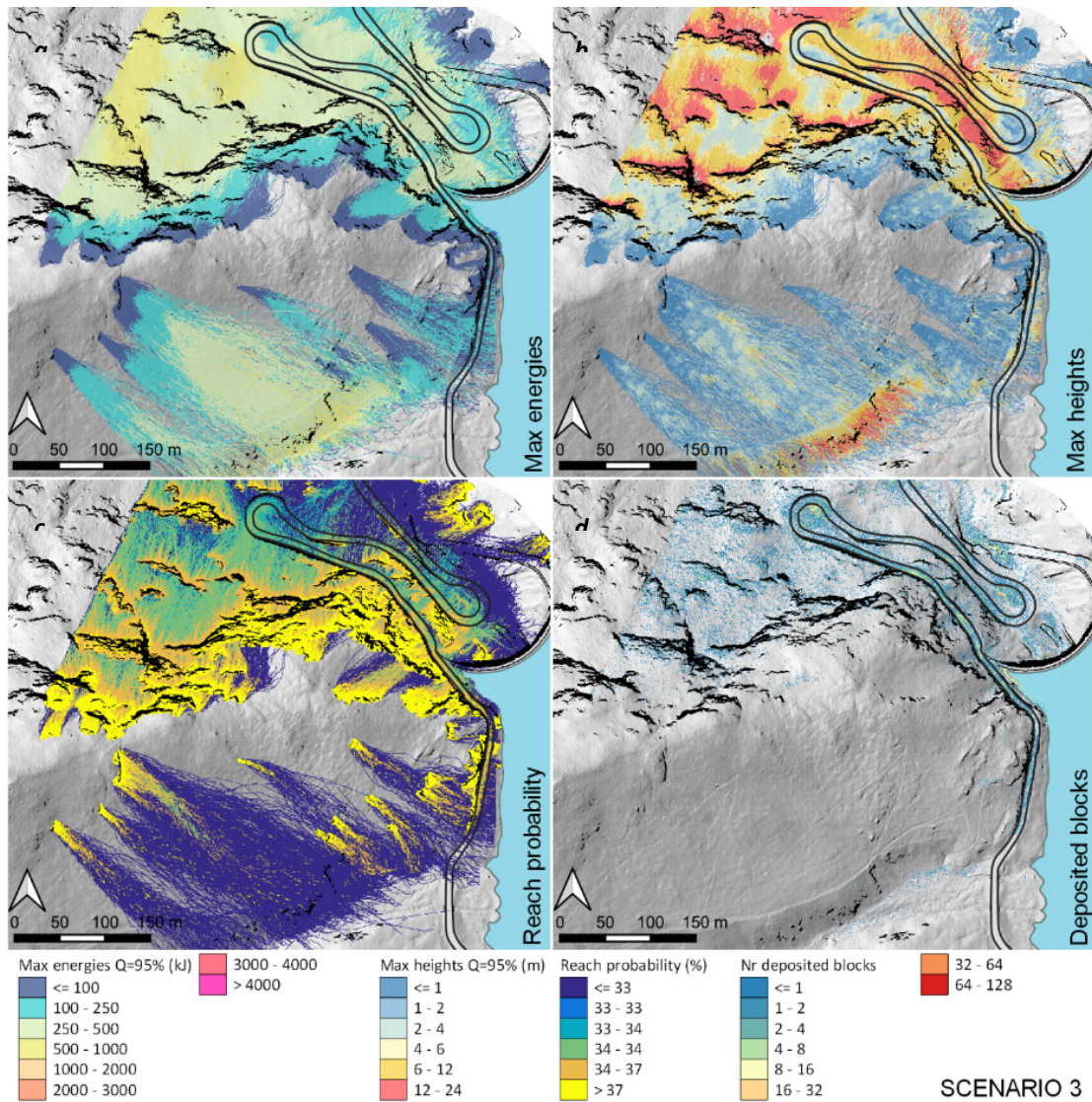
Figure 44: Output maps of rockfall modelling for the Scenario 1. Main rockfall parameters represented are: a) maximum rockfall energies sampled at 95th percentile (kJ); b) maximum rockfall rebound heights sampled at the 95th percentile (m); c) rockfall reach probabilities (%); d) number of deposited blocks at each cell
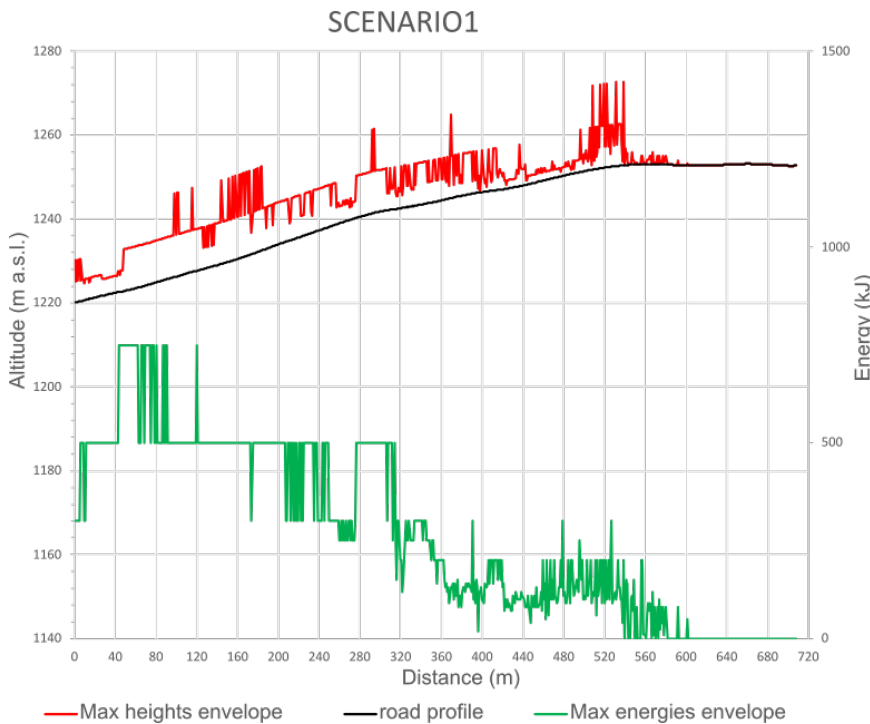
Figure 45: Modelled maximum energies, rebound heights and road altitude profile, along the road path (S1).

4.2.5.2 Scenario 2

Similar to S1, the S2 is a baseline scenario considering blocks with volume V = 1 m^3 related to a 100-year return period.

Observing the spatial distribution of the maximum kinetic energies (95th percentile, Figure 46a), it is noteworthy that, as shown in S1, the highest intensities occur in a few small areas, scattered along the slope, and at the base of the south-eastern slope area, where they exceed 4000 kJ, although far from the road. Energies ranging between 2000-3000 kJ are recorded in the northern part on slopes to the foothill of the highest rocky walls. They locally affect the road close to the main road bend. In the largest part of the studied area, the energy ranges between 500-2000 kJ.

As shown in Figure 46b, rebound heights distribution did not significantly vary compared to S1. Conversely, the rockfall reach probability slightly varied only at the base of the scarps and in the area of rock accumulation because the smallest blocks have slightly longer runouts (Figure 46c). This is confirmed by the map of deposited blocks (Figure 46d), which shows a larger number of blocks deposited along the slope, with a slight reduction of those reaching the road.

As in the previous scenario, the modelled rockfall parameters were recorded along the road path and reported in the graph of Figure 47. It shows that the energy ranges between 1500-3000 kJ in the northern part of the road, whereas, in the southern half of the profile, the energy is below 750 kJ, with just some isolated peaks reaching 1500 kJ. When

considering block rebound heights along the road (Figure 47) results highlight high values along the northern part of the road where they often reach 10 m, with several peaks up to 20 m; in the southern part, flight height are lower (<4 m) with only few cases above 10 m recorded at a location 520 m far from the main bend.
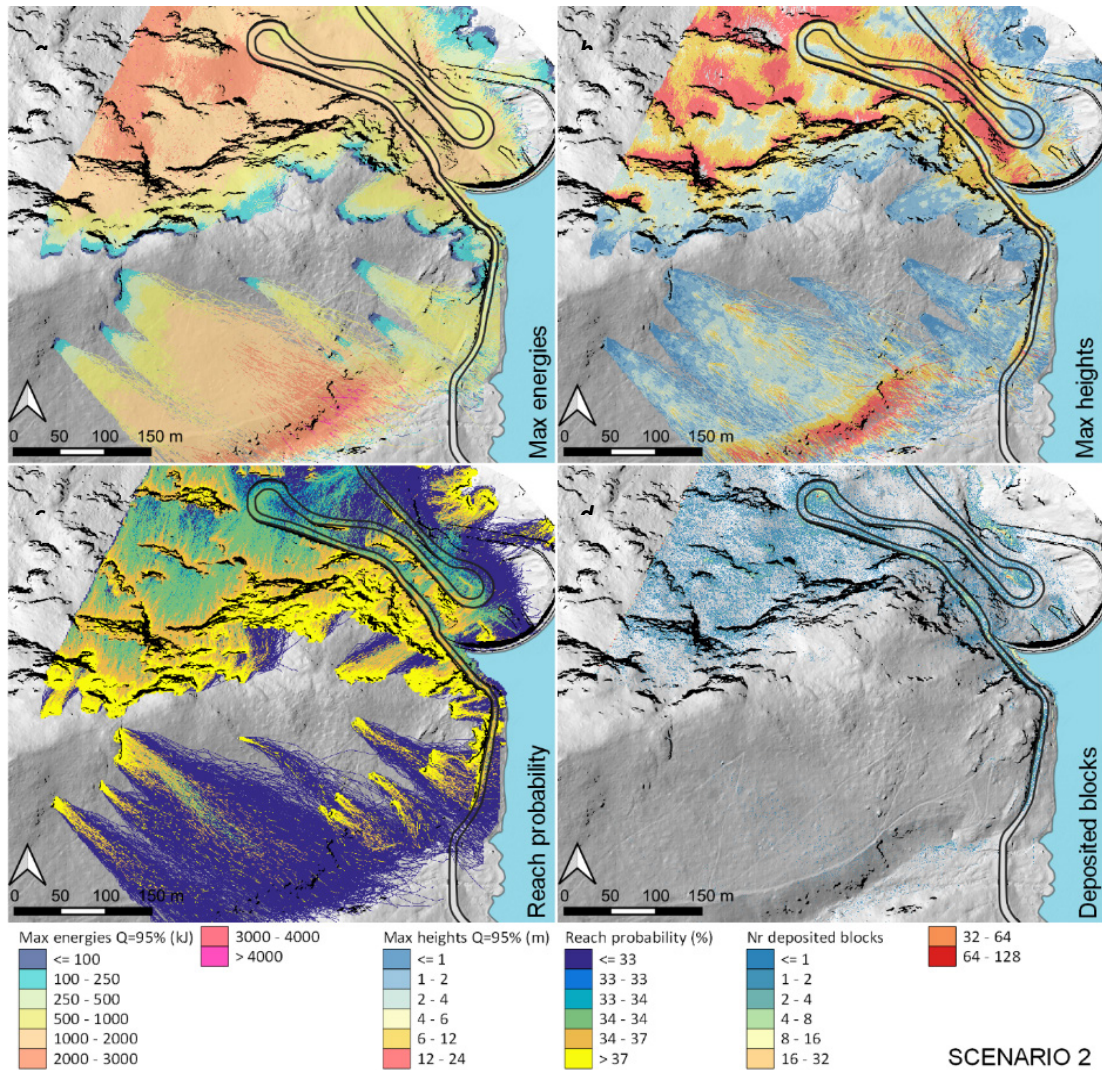
Figure 46: Output maps of rockfall modelling for the Scenario 2. Main rockfall parameters represented are: a) maximum rockfall energies sampled at 95th percentile (kJ); b) maximum rockfall rebound heights sampled at the 95th percentile (m); c) rockfall reach probabilities (%); d) number of deposited blocks at each cell
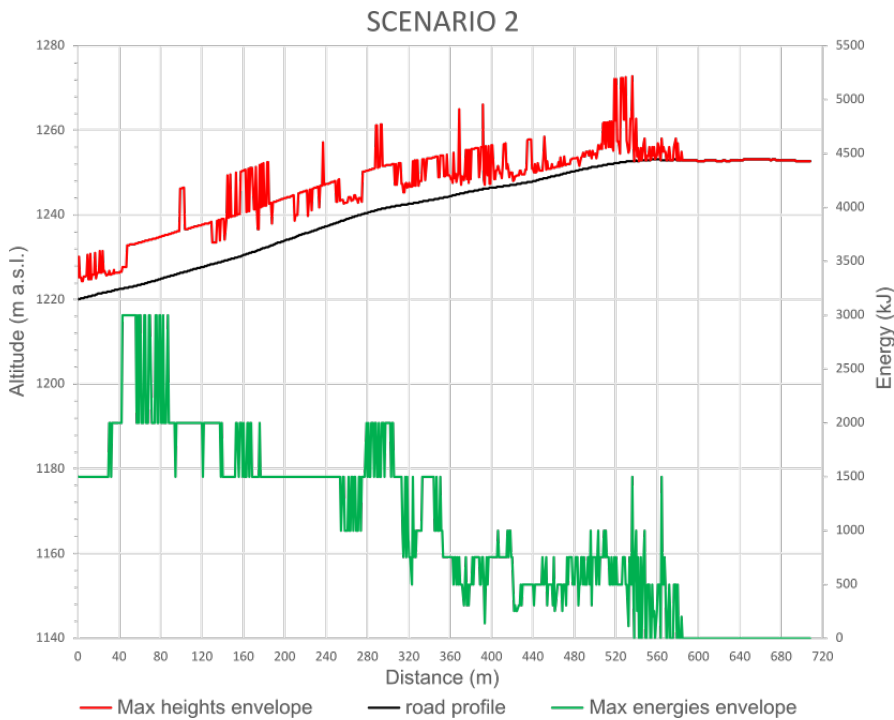
Figure 47: Modelled maximum energies and rebound heights along the road path (S2).

4.2.5.3   Scenario 3

The third scenario (S3) is post-operam, then including the protective effect of both the forest and the designed NBSs, considering small blocks with a volume V = 0.25 m^3 and a return period of 10 years. The results are mapped in Figure 48. The spatial distribution of the maximum kinetic energy (Figure 48a) shows highest values occurring where the slope is steeper, however, it ranges between 500-1000 kJ. In the trigger areas, the energy never exceeds 100 kJ, while increasing during the rockfall propagation on the slope; however, it rarely exceeds 500 kJ.

The maximum rebound heights showed in Figure 48b point out a general decrease of average rockfall heights compared to S1 over the whole area, although very high values are still observed where scarps are crossed by boulders coming from upslope, reaching 24 m.

The reach probability distribution (Figure 48c) is quite similar to that observed at the baseline scenarios. Some changes occur in the area of rockfall deposition, at the margins of the runout area, where it decreases due to shorter runouts. This is confirmed by the distribution of deposited blocks (Figure 48d) which shows higher values along the slope, enhancing some effects of the forest in stopping small blocks. However, the road remains one of the main areas of block accumulation.
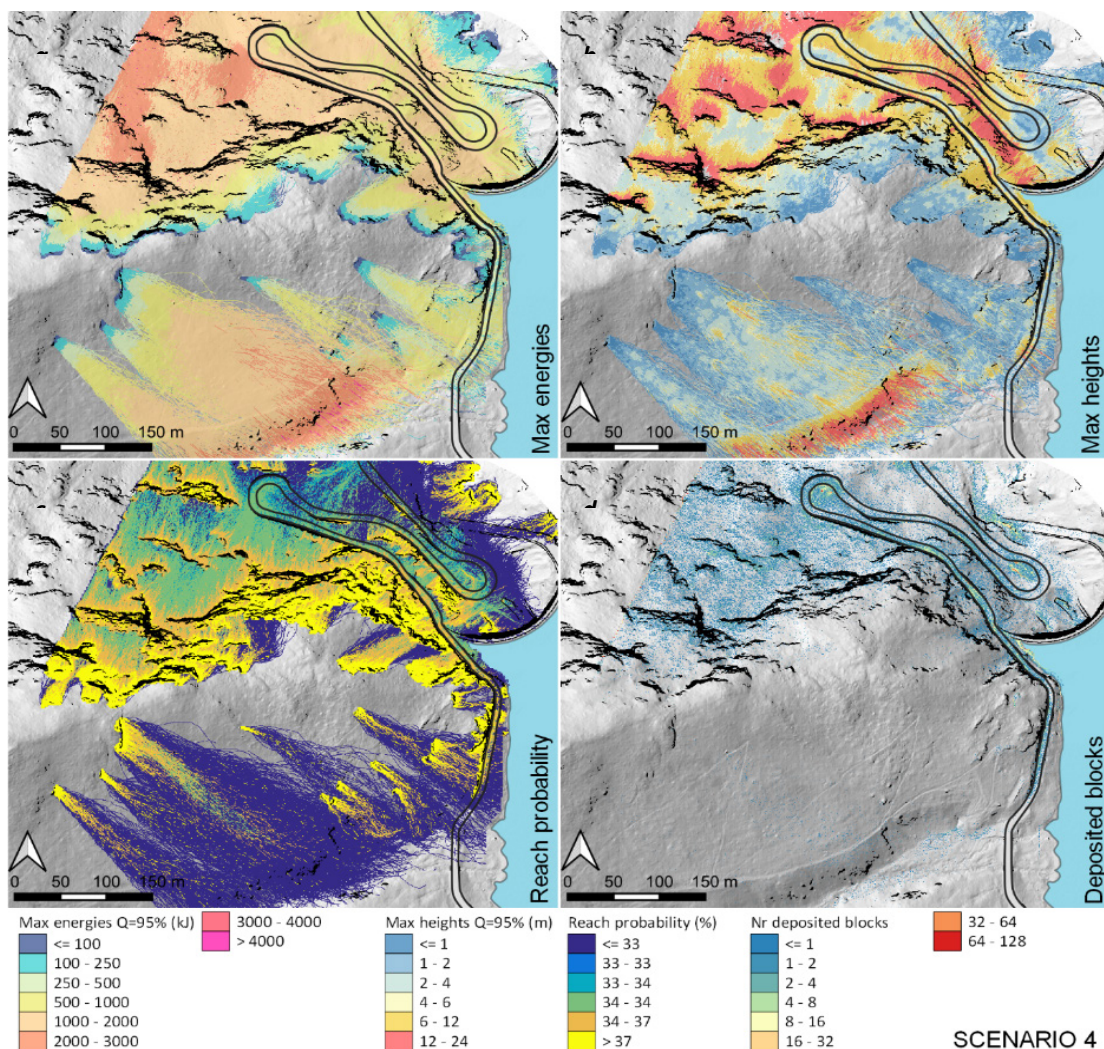
Figure 48: Output maps of rockfall modelling for the Scenario 3. Main rockfall parameters represented are: a) maximum rockfall energies sampled at 95th percentile (kJ); b) maximum rockfall rebound heights sampled at the 95th percentile (m); c) rockfall reach probabilities (%); d) number of deposited blocks at each cell
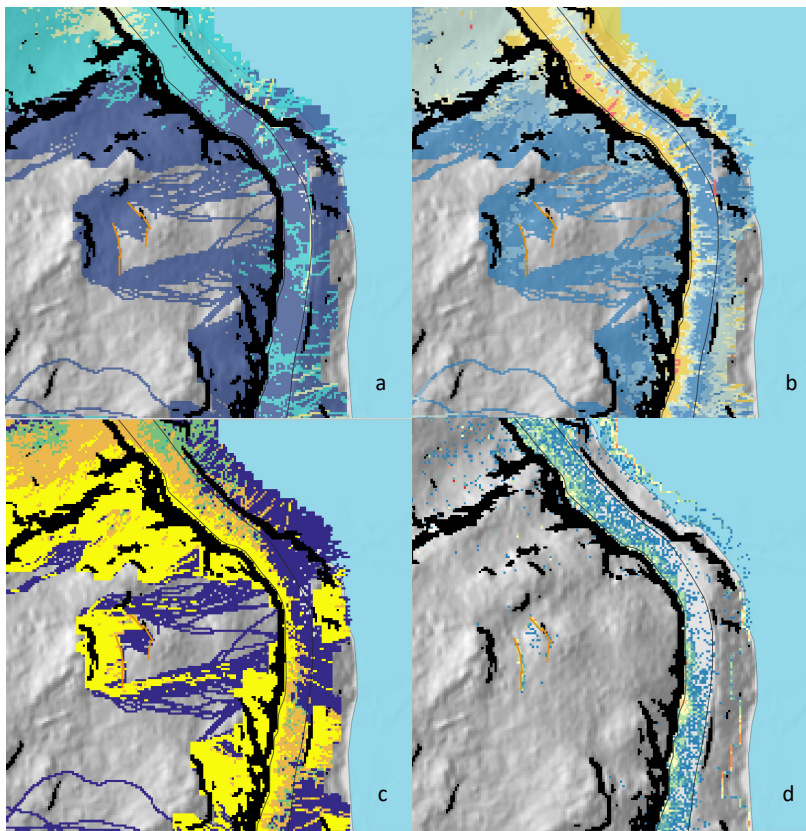
Since the NBS and especially the wooden barriers are implemented in just a small portion of the study area, an enlarged view of the results (Figure 49) may help the assessment of their overall effect. In this area, it is worth noting that the barriers can only partially stop the blocks due to their moderate longitudinal development. In fact, the use of these structures allows the stopping of the rocks coming from the rock faces immediately upslope.

Figure 49 Enlarged rockfall modelling output maps (S3). a) Map of rockfall maximum energies; b) Map of maximum rebound heights; c) map of rockfall reach probability; d) map of deposited blocks

However, in the proximity of their terminations, the blocks bypass the barriers, continuing their trajectories and reaching the road, albeit with much lower energy around 100 kJ (Figure 49a).

Considering the destruction of the heights (Figure 49b), it is observed that positioning the barriers close to the slopes is effective only for blocks collapsed from the slope itself and not for those coming from more upslope areas. Also in this case, the mitigation effect of such a barrier consists in reducing the expected block heights and frequencies on the road below (Figure 49c), given its capability to intercept a certain number of blocks (Figure 49d).

4.2.5.4 Scenario 4

The last simulations (S4) were performed for the NBS scenario considering blocks with volume V = 1.00 m^3 relating to a return period of 100 years. Results are reported in Figure 50. When considering the maximum kinetic energies (95th percentile, Figure 50a), it is worth noting that some peak values (> 4000 kJ) are still detectable along the slope, although less prevalent than those of S2. Values ranging between 2000-3000 kJ are recorded in a few areas with a moderately large extension, in the middle of the slope to the foothill of the tallest rock faces. In general, however, as discussed for other

scenarios, in the highest triggering areas, the energies range between 100-250 kJ, and increase during propagation. This results in very large areas with energy ranging between 1000-2000 kJ.

The height distribution (Figure 50b), when compared to S2, shows a slight decrease over the whole area, especially if the highest values along the slope are considered. The highest values zones exceeding 24 m are still recorded close to the steepest faces due to rebounds boulders coming from upslope.

The distribution of reach probability (Figure 50c) is quite similar to that at the baseline scenarios. Similar results were observed for the distribution of deposited blocks (Figure 50d), which show similar patterns to the baseline scenario with the road being the main block accumulation area.

Figure 50 Output maps of rockfall modelling for the Scenario 4. Main rockfall parameters represented are: a) maximum rockfall energies sampled at 95th percentile (kJ); b) maximum rockfall rebound heights sampled at the 95th percentile (m); c) rockfall reach probabilities (%); d) number of deposited blocks at each cell.
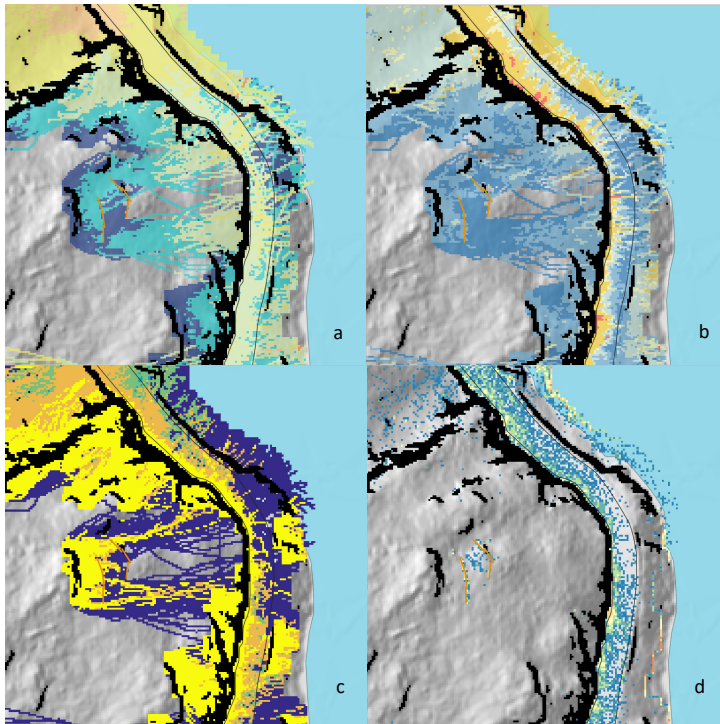
Enlargements of output maps, focusing on the area of NBSs' implementation, is reported in Figure 51. It points out that wooden barriers are not able to stop blocks of such a volume, although capable to individually limit the kinetic energy (Figure 51a). Accordingly, they are capable to limit the downslope rebound heights of impacting rockfalls (Figure 51b). Since their limited effect on stopping rockfall, the reaching probability on the road (Figure 51c) and the area of rockfall accumulation (Figure 51d) did not significantly change.

Figure 51: enlarged rockfall modelling output maps (S3). a) Map of rockfall maximum energies; b) Map of maximum rebound heights; c) map of rockfall reach probability; d) map of deposited blocks

However, it is noteworthy that where the wooden barriers overlap, the combined effect of two orders can stop most of the boulders, which, indeed, accumulate between them (Figure 51c), thus resulting in a narrow strip below the area of overlapping unaffected by rockfalls.

4.2.5.5   Main changes in hazard patterns

After analysing the S1 and S3 scenarios for the same return period (10-yr) and block size, a quantitative comparison between the modelling results helped better document the forest's mitigating effect and NBS interventions and the residual hazard.

The results of this comparison are reported in the maps of Figure 52. These show the variation in maximum energies (Figure 52a) and maximum heights (Figure 52b), between baseline and NBS scenario; negative values testify to an adverse effect of NBS with an increase of the considered parameter. Positive values, on the other hand, indicate a mitigating effect.

The distribution of the maximum energy variations (Figure 52a) points out that, after the NBS implementation, energy shows negligible variations over the largest part of the area (> 49%). In many areas, however, it is possible to observe a decrease in energy values ranging between 0 and 200 kJ. Such mitigating effect can be observed in an overall area of approximately 6.5×10^4 m^2 (approximately 33% of the modelled area). Locally there are also areas (14% of the modelled one), along steepest slopes and some sporadic

trajectories, where an increase in energy content could be expected, compared to the baseline scenario, probably as a consequence of the propagation dynamics of some blocks due to impacts with the vegetation.

The distribution of variations in rebound heights (Figure 52b) shows that the heights tend to remain constant over most of the investigated area, for an extension of about 12 x 10^4 m^2), whereas a reduction in heights due to NBS is recorded on about 4 x 10^4 m^2 ha of surface (about 20% of the area examined). Some increased values can be sporadically expected as already pointed out for the energy distribution.

Energy variations = S1-S3 (kJ)

<= -100	-60 - -40
-100 - -80	-40 - -20
-80 - -60	-20 - 0

0 - 20	60 - 80
20 - 40	80 - 100
40 - 60	> 100

Height variations = S1-S3 (m)

<= -1,60	-0,80 - -0,40
-1,60 - -1,20	-0,40 - 0,00
-1,20 - -0,80	0,00 - 0,40

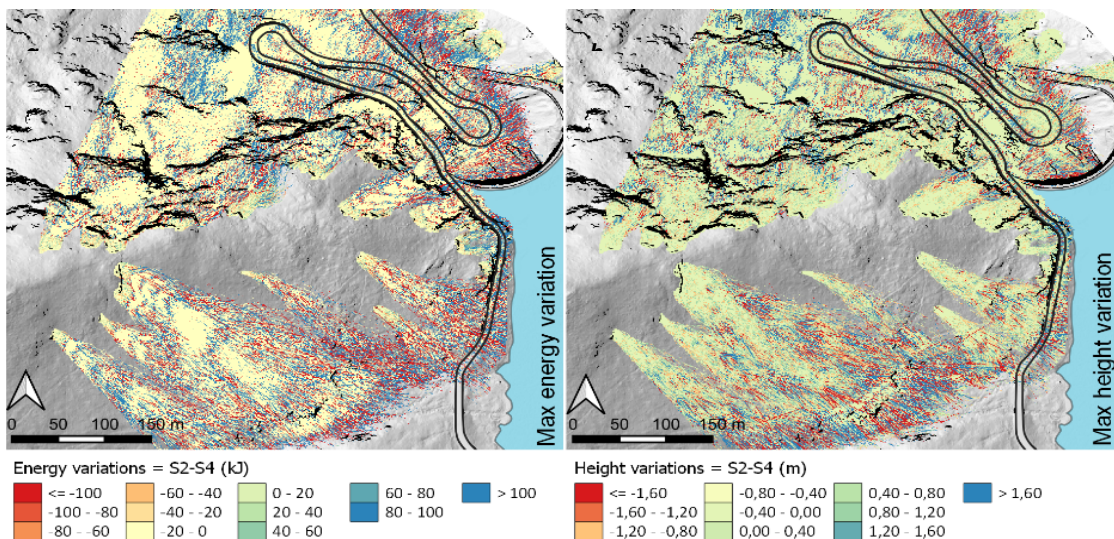|	
0,40 - 0,80	> 1,60
0,80 - 1,20	
1,20 - 1,60	
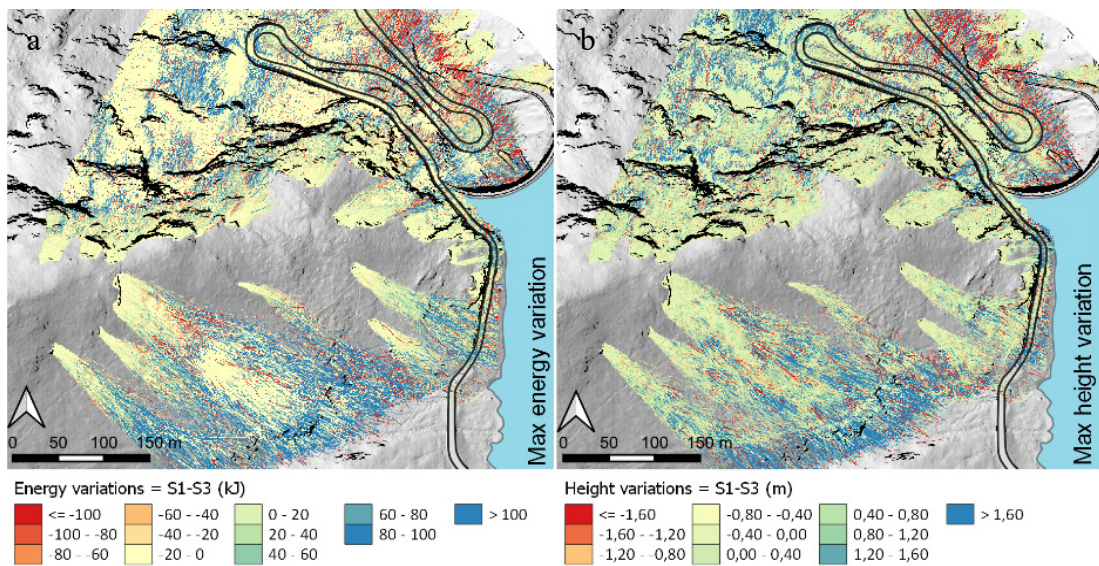
Figure 52: Main variations between the ante-operam (S1) and pos-operam (S3) scenarios, for the volume class V=0.25m³ calculated from the difference S1-S3 for (a) maximum rockfall energies and (b) maximum rebound heights.

These evidences demonstrate a limited effect of the solutions adopted, especially if the assessment is referred to the scale of the entire study area.

To better observe the mitigating effects of the NBS and forest on the rockfalls affecting the road, the absolute variation of the transit heights and energies are reported along the road path. Here, the main outputs of the comparing scenarios are reported together to facilitate the analysis of the residual hazard on the road.

The direct comparison shows that the expected maximum energies along the road remain almost unchanged, with values generally lower than 500 kJ. However, a reduction in the number of peaks of maximum energy along the entire route could be noticed. This effect is much more evident in the northern part of the road, where the energy decrease can reach values of -250 kJ. Along the central and southern section (progressive distance 200- 500 m), the reduction is more widespread, albeit less intense, with a maximum reduction that rarely exceeds 100 kJ.

The rebound heights also remain unchanged on most of the road path (Figure 53). The NBS, however, results in a local reduction of peak values, even more evident in the central and southern area, where a significant decrease of height was partially detected directly downslope to the wooden rockfall barriers in this area rebound heights are reduced by 20 m, thanks to a mitigating effect of both the forest and NBSs.
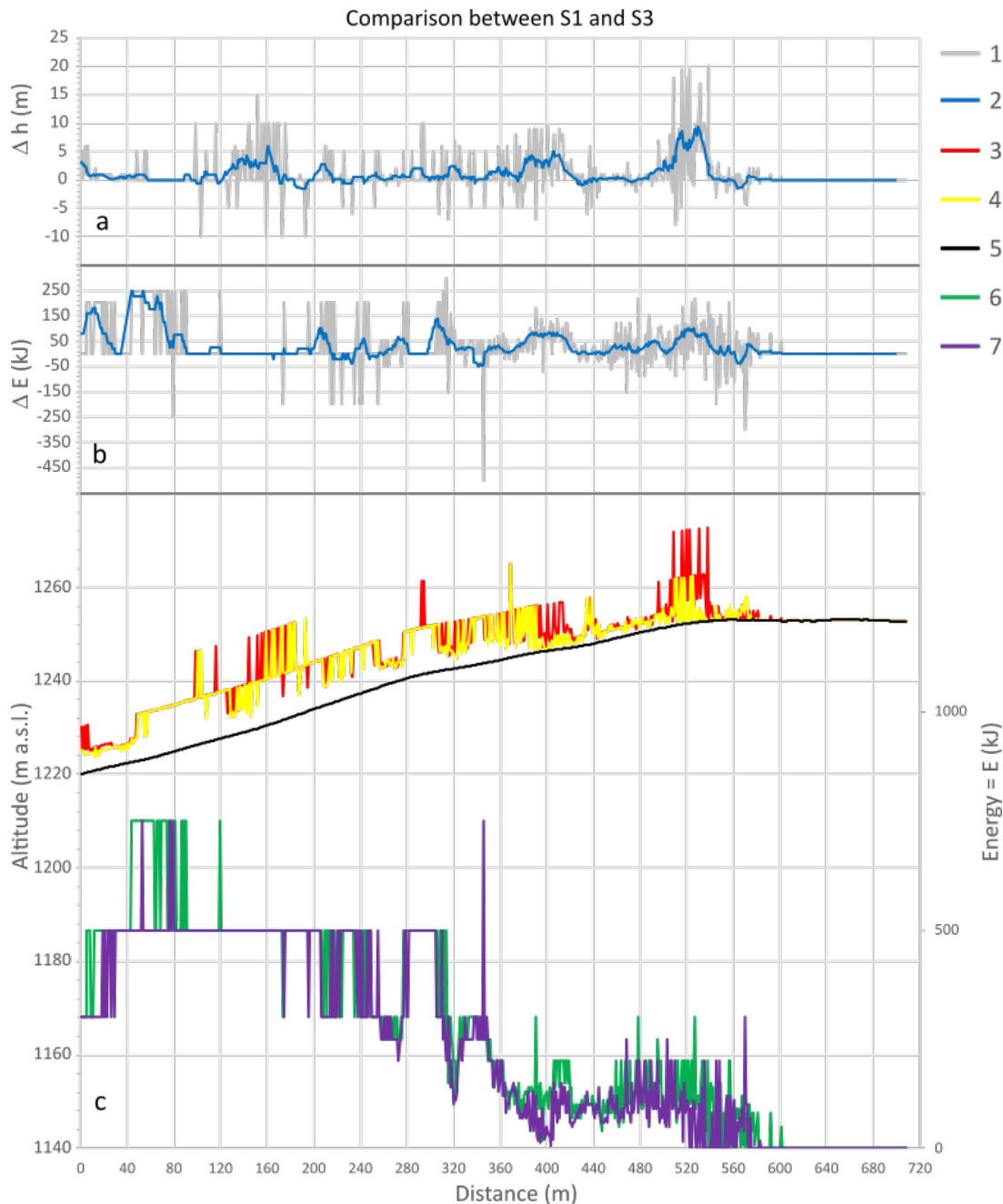
Figure 53: Main variations along the road path between S1 and S3 modelling results: a) variations of rebound heights; b) variation of maximum energies; c) maximum heights and energies recorded for S1 and S3 along the road path. 1= heights and energy variation envelopes; 2= 10 cells moving average; 3= S1 maximum heights envelope; 4= S3 maximum heights envelope; 5= road profile; 6= S1 maximum energies envelope; 7= S3 S1 maximum energies envelope.

The comparison between S2 and S4 scenarios allowed the quantitative estimation of the change in hazard patterns for the 100-year return period. Results are mapped in Figure 54 where variations in the maximum energies (Figure 54a) and maximum heights (Figure 54b) are plotted. The distribution of the energy variation shows how they tend to be unchanged over most of the study area (over about $11.2 \times 10^4 \, \mathrm{m}^2 \approx 57\%$), whereas they tend to slightly be reduced to 26%. On a limited portion of the same (about 17%) an increase can be noticed, instead, due to the deviatoric effect of the vegetation. The NBS implementation did not induce significant improvements in rebound heights, since no changes were detected over a large part of the studied area (about $12.7 \times 10^4 \, \mathrm{m}^2 \approx 65\%$).

The profiles of energy and height variations along the road path show a symmetry around 0 with both positive and negative values (Figure 55a, b). This could be explained with a spatial shift of most peaks more evident when observing the combined modelling output in Figure 55c. This highlights the minimal mitigating effect of NBS and forest cover when dealing with boulders of $1.00 \, \mathrm{m}^3$, since these seem to exert just a deviatoric effect without significantly affecting the rockfall intensity.

Figure 54: Main variations between the ante-operam (S2) and pos-operam (S4) scenarios for the volume class V=1m³ calculated from the difference S1-S3 for (a) maximum rockfall energies and (b) maximum rebound heights.

Figure 55: Main variations along the road path between S1 and S3 modelling results: a) variations of rebound heights; b) variation of maximum energies; c) maximum heights and energies recorded for S1 and S3 along the road path. 1 = heights and energy variation envelopes; 2= 10 cells moving average; 3 = S1 maximum heights envelope; 4 = S3 maximum heights envelope; 5= road profile; 6= S1 maximum energies envelope; 7 = S3 maximum energies envelope.

4.2.6   Concluding remarks

With this study, the effect of nature-based solutions (NBSs) in mitigating rockfalls on forested mountain slopes is investigated through a review of different rockfall simulation algorithms and the application of the most suitable one to investigate the effect of NBS at each study area. In this section, we discuss the most significant results of rockfall modelling in the forested slope of Artouste in the Pyrénées-Atlantiques (France) department, where different types of NBS are designed to be integrated with afforestation. The existing and planned NBS involve some punctual and areal interventions, affecting a limited area compared to possible rockfall source and propagation areas. They consist of wooden tripods, meshes, and masonry walls designed to fix unstable blocks along the slope. Some passive defence works, such as wooden rockfall barriers, are designed close to some source areas with the aim to intercept falling rocks before the increase of speed. All those measures are designed to be integrated and coupled with an expected mitigating effect of the forest.

After some evaluations, the modelling approach was oriented to a semi-probabilistic physical-based model applying Rockyfor3D software.

The goal is to verify the effectiveness of NBS solutions by comparing the modelling results of NBS scenarios, including afforestation, with baseline scenarios.

Field surveys recognized two main volume classes for rockfall, 0.25 m^3 and 1.00 m^3, associated with 10- and 100-year return period, respectively.

By integrating forest data with rockfall risk mitigation interventions and different blocks volumes, four different modelling scenarios were distinguished:

- Scenario 1: baseline with block size 0.25 m^3;
- Scenario 2: baseline with block size 1.00 m^3;
- Scenario 3: NBS with block size 0.25 m^3;
- Scenario 4: NBS with block size 1.00 m^3.

The main target of the study was to assess the mitigating effect of NBS in terms of variation of maximum rockfall energies and rebound heights on the slope and, specifically, along the road.

Comparing modelling results of the S1 and S3 scenarios related to blocks of 0.25 m^3, the mitigating effect of coupled NBS and forest is exhibited through a dampening of the highest peak values for both maximum rockfall energy and rebound height. On the other hand, NBS do not significantly affect the average values which are reduced only in few areas directly downslope to the designed wooden rockfall barriers. With such a block size, rockfall energy along the road after NBS implementation ranges between 200 and 500 kJ.

If blocks of 1 m^3 are considered, no significative improvements are observed with NBS introduction.

Also with regard to the maximum energy, no improvements are noted, except for some peaks in very limited areas. The most evident effect is a shift of the highest values of kinetic energy and rebound height, probably due to the deviatoric effect of block-trees impacts. Therefore, the stabilization interventions give a very local contribution, limited to a few areas with small extensions compared to the identified potential rockfall sources; passive defence structures such as wooden rockfall barriers are the most effective for stopping small boulders (volume of less than 0.25 m^3), while they have a marginal effect on blocks with a volume of 1.00 m^3. However, the combination of several orders of overlapping barriers was proven to stop most of the blocks providing a significant mitigation effect.

Based on modelling outputs, the designed interventions are not sufficient to significantly reduce the risk of rockfalls due to the very local effect of some types of NBS, their small spatial distribution, and low adsorption energies of wooden barriers and trees. However, they might be considered as an additional solution for dampening the rockfall intensity limiting the sizing and, thus, the economic and environmental impacts of other interventions such as steel rockfall barriers.

4.3 Rockfall modelling at Santa Elena, Biescas, Spain

4.3.1 Case study and hazard scenario

This case study is located about 35 km in the south side of Artouste, in the municipality of Biescas, Huesca province, Spain. It is located along one of the main routes crossing the Spain-France border in the central area of the Pyrenees Mountain passageway. On the Spanish side, the extension to the south way of the RD-934 is identified as A-136, and connects, with the main direction N-S, several cities and touristic localities of the Huesca province in the Aragona region.
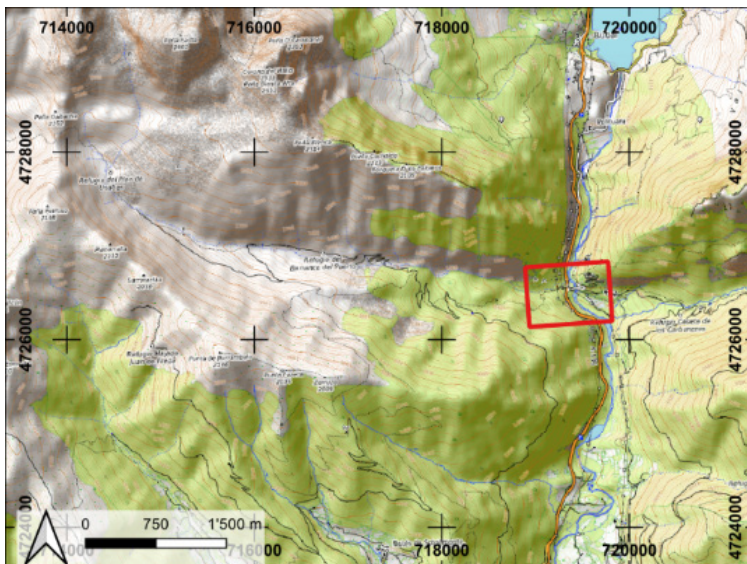
Figure 56. Study area location on base map from Open Street Map services. Reference system is ETRS89 – UTM zone 30N (EPSG: 25830)

Consistently with the Artouste case study, this road sector exhibits high traffic intensity, especially during summer and winter holidays and weekends, thus showing high exposure to possible hazardous phenomena affecting the road path. The high risk of this area is also related to the low visibility caused by a large road hump. The study site is at

the 3+350 km of road A-136, at an elevation between 977-1045 m a.s.l. Here the road crosses the mouth of the E-O oriented valley called Barranco del Puerto, to the south of the ridge dominated by Mount Corona del Mallo (2535 m.a.s.l.), at the crossroad with the Gallego river valley (Figure 56). To the south side of the crossroad, the road crosses small relief on the right of both the Barranco del Puerto and Gallego river valleys, which is 30 m high above the road level. Here moraine deposits outcrop on a slope with a mean angle of about 45°. The road crossing this slope is 150 m long. Here slopes exhibit discontinuous bushy vegetation cover with some large bare areas where localized erosive phenomena are active. Evidence of such erosion is provided by vertical gullies, the absence of vegetation, and abrupt morphologies at the slope scale. Consequently, every year several blocks of different sizes detach from the eroded moraine debris on the slope reaching the road, thus representing a dangerous threat to car drivers.

Several defence works have already been implemented in the slope above the road, mainly consisting of steel meshes anchored with rock bolts. The meshes are now broken at several points, and several rock bolts are fully exposed due to subsequent debris erosion. For these reasons, they are no longer considered effective.

Recent studies on risky phenomena affecting the A-136 road point out the susceptibility of this sector characterized by high landslide frequency (Figure 57).
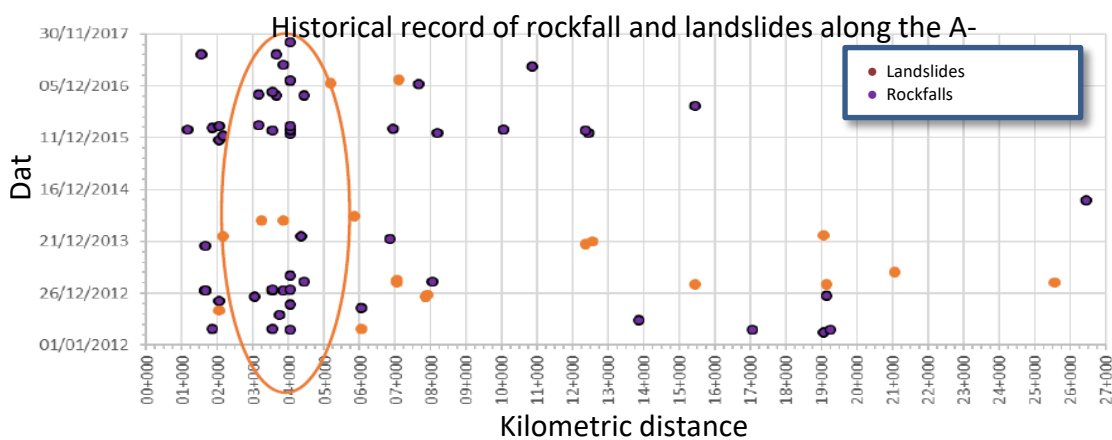
Figure 57. Landslides (orange dots) and rockfalls (purple dots) occurring along the A-136 road (Study of natural risks affecting the road A-136, Geoconsult Ingenieros Consultores, S.A., funded by AECT Espacio Protalet. The Santa Elena is highlighted with an orange oval.

4.3.2   Geological setting

From the geological viewpoint, the area is in the South Pyrenean Zone, just to the south side of the Central Pyrenees Belt axial area, where the metamorphic Hercynian core complex is directly overlain through a tectonic contact by Mesozoic to Cenozoic sedimentary successions pertaining to the Iberian plate.

To the south of the contact with the crystalline basement, the sedimentary successions are structured in a south-verging nappe-stack which shows its older terms to the north, along the interior ridges of Aragona (*Sierras Interiores*) (Figure 58). They consist of shallow-water limestones and grainstones (upper Cretaceous), forming the highest ridges, overlain by a calcareous-dolomitic succession (Paleocene), and a transgressive slope to basin deposits formed by marls and flinty limestones (Paleocene). The overlying sedimentary cover is formed by terrigenous marly and clastic turbiditic successions (Lower Eocene – Medium Eocene) (Figure 58). The younger terms of the sedimentary succession, outcropping more to the south, are represented by clastic continental deposits aged Upper Eocene to Oligocene.

Most recent deposits outcropping in the studied area are related to quaternary glacial activity and recent fluvial and slope dynamics. The glacial footprint is evidenced by deep-carved valleys often showing the typical U shape with steep slopes and by frequent glacial moraine deposits, extensively outcropping in the study area (Figure 58). The subsequent fluvial and slope dynamics is corroborated by the erosion of most glacial deposits and formation of alluvial fans at the mouth of lateral valleys intersecting the main valley of the Gallego river, and the formation of colluvial talus at the slope's foothill.

The study area is located at the relief base constituted by a moraine eroded by subsequent fluvial activity. It is constituted by incoherent tills made of very heterogeneous unsorted clastic deposits with heteromeric and polygenic gravels, blocks, and boulders, varying in size from a few millimetres to some meters. The texture of the deposit can be either clast-supported or matrix-supported by a clayey to a sandy matrix.

Currently, because of the matrix weathering and erosion, many outcropping blocks and boulders of varying sizes can get unsupported, losing their balance and detaching from the slope from different heights. This causes the onset of rockfalls threatening the road downslope.
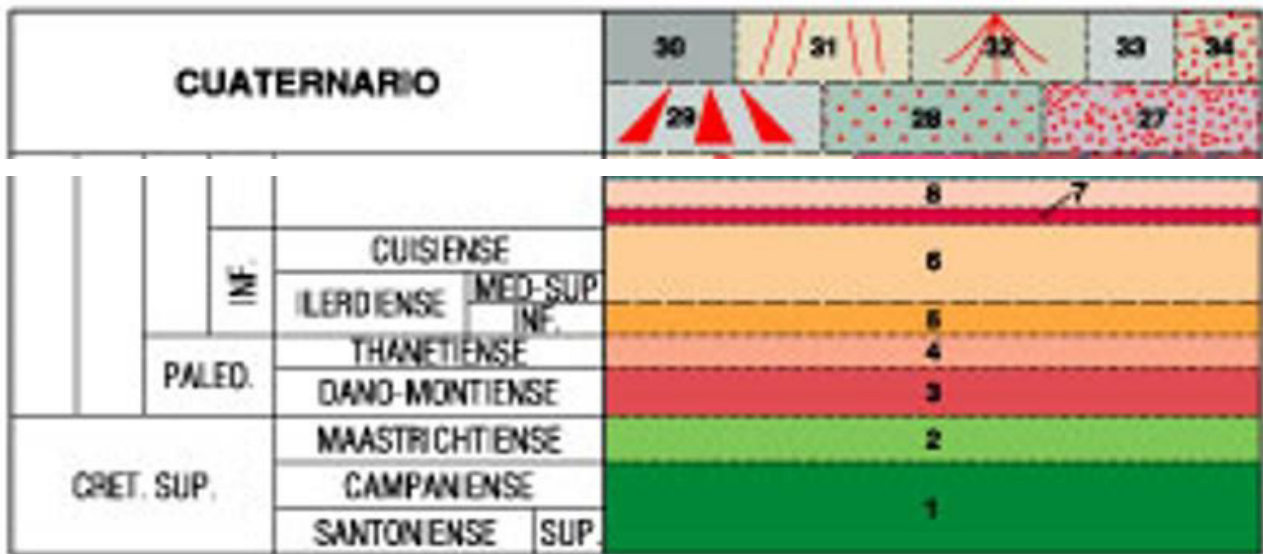
Figure 58: sketch from the geological map of Spain (scale 1:50.000) with its legend, the black rectangle locates the study area. 2 – Cretaceous limestones and grainstones (upper Cretaceous); 3 – Dolostones and limestones (Paleocene); 4 – Limestones (upper Paleocene); 5 – slope to basin marls and flinty limestones; 6 – turbiditic pelites and sandstones; 7 – Calcareous breccias and calcarenites from the Megacapa del Villana Fm.; 8 – turbiditic pelites and sandstones; 27 – Glacial deposits; 33 – actual alluvial deposits.
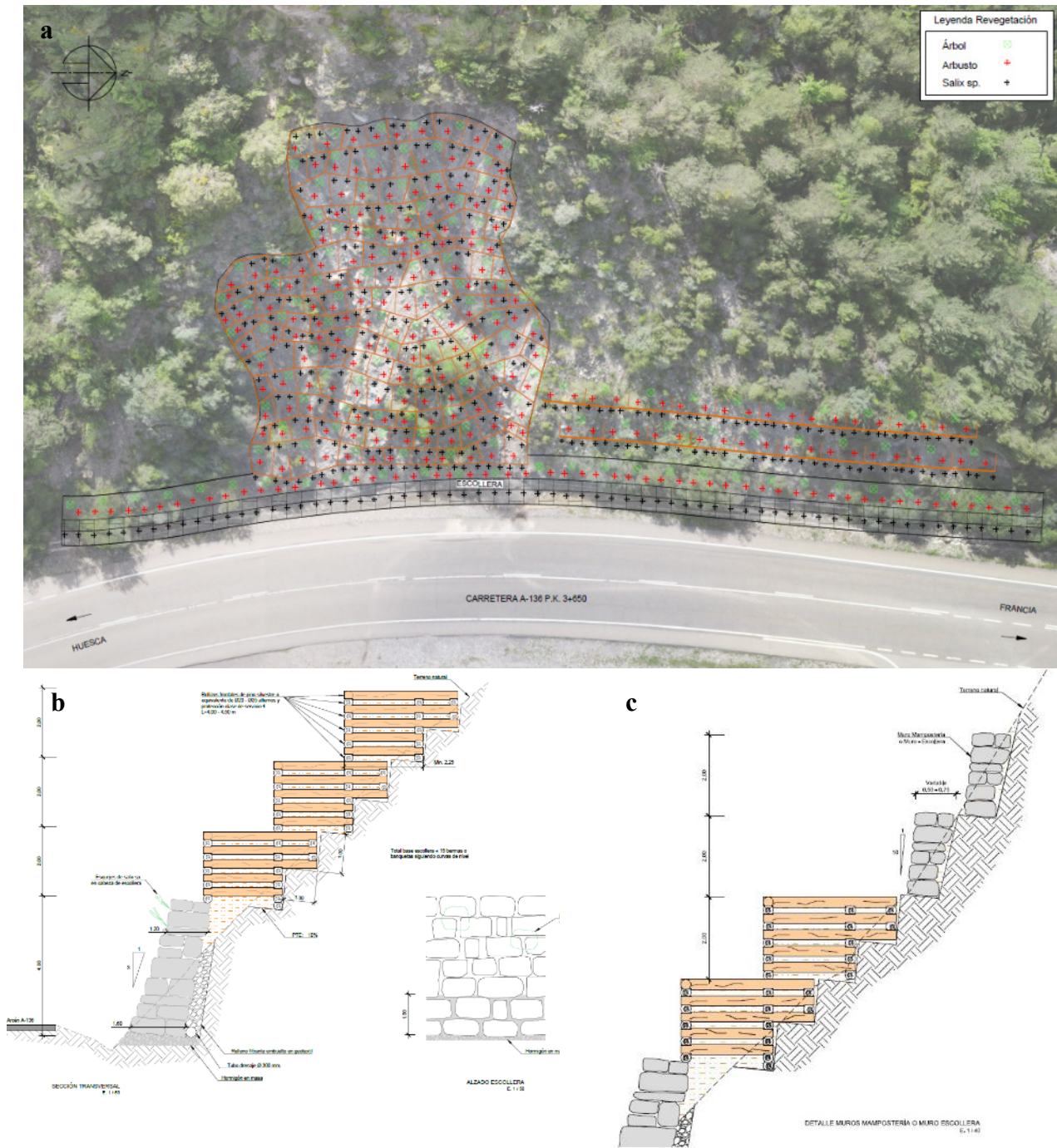
Figure 59. Excerpts from the design layouts. a) planimetry of the designed terraces and planted vegetation patterns; b) details on the basal masonry wall and upslope structures of wooden gabions used the terraces; c) details of masonry walls designed for preventing soil erosion in areas with steepest slopes.

4.3.3   Nature-Based Solutions (NBSs) designed

The solutions adopted to deal with the hazardous scenario here discussed and, thus, modelled for the assessment are the NBS designed in the frame of the PHUSICOS

project. They are aimed at reducing soil erosion of the outcropping moraine deposits on the slope, thus preventing boulder exposure and the consequential possibility of their detachment and rolling toward the road at the foothill. This is achieved by a reconfiguration of the current slope morphology to both limit the slope steepness and create favourable conditions for the growth of autochthonous vegetation after implantation (Figure 59a).

The slope re-profiling will be carried out in the central and most eroded area with terracing using gabions or wooden structures to support the earth covering the moraine bedrock (Figure 59a, b). The terraces will then be planted with autochthonous shrubs and trees aimed at both stabilizing the earth cover and reducing the aesthetic impact of the interventions. In some steep areas, masonry retaining walls are designed to prevent soil erosion and rock detachment (Figure 59c). On less steep lateral parts of the slope, less affected by soil erosion, slope stability and revegetation will be promoted by creating vegetated crib walls.

4.3.4   Methods

The most significant hazardous phenomenon in the study site is related to rockfall detaching from moraine deposits. Consequently, the hazard analysis and the assessment of the NBS effectiveness was carried out by modelling rockfall hazards at the slope scale.

In this study site, the slope affected by rockfall has a limited extension, and designed vegetation consisting of a mix of autochthonous shrubs and tree species is mainly aimed at stabilizing the terraces and reducing the intervention impacts, rather than intercepting the falling blocks. Moreover, the block sizes simultaneously detaching could be characterized by very different size and shape. For these reasons, tridimensional, physically based models should be applied, also being suitable to run simulations on large scales, by accounting for different block shapes and sizes simultaneously. Moreover, they should include the modelling of vegetation, even though neglecting the rock-tree impacts. RAMMS: ROCKFALL (Caviezel et al., 2019) was thus assessed to be the best-suited model to fulfill such requirements.

The hazard analysis was based on high-resolution input data provided by site managers (CTP-OPCC) and was oriented to assess the potential mitigating effect exerted by the designed NBSs.

To this aim, the assessment is based on comparing results of rockfall modelling for a baseline (S0, considering current slope morphology and vegetation cover) and an NBS scenario (S1, considering new slope shape and more extended vegetation cover). Since current defence works are considered to be ineffective, their action is neglected during simulations.

A single scenario was defined regarding the baseline conditions (S1), considering the simultaneous detachment of different-sized blocks. Indeed, since there is no evidence of

different detachment frequencies for different block sizes, it is reasonable to assume that erosion currently destabilizes both large and small blocks.

To model the NBS scenario (S2), only the slope morphology and the density of the vegetation cover was modified according to the design layouts. Conversely, to limit the possible bias on the mitigating effect introduced by a change in rockfall triggering locations, the source points, the block sizes and thus the assessment of NBS effectiveness were based on the comparison between S1 and S2.

4.3.4.1   Modelling setup

Input data required for modelling consists of a set of raster files (Tiff format) and shapefile (ESRI shp format), which spatially define the different parameters controlling rockfall propagation, such as the slope morphology (as a raster), the soil types (as polygonal shapefile), the vegetation cover (as polygonal shapefile) and the block position (as point shapefile). Spatial input data were arranged using the open source qGIS software. Other input data are the block shapes and the initial conditions.

The former can be both imported as a 3D model or selected within a library of rock models provided with the software, where users can define block size and density of each block type. The software automatically computes the initial conditions to start the rockfall propagation.

Table 16: soil types and descriptions

ID	Soil Type	Soil Stiffness	Description	Exemplary image (software manual)
1	Moraine debris	Hard	Rocks jump over ground. Mixture of large and small rocks. Usually without any vegetation.	
4	Paved road			
2	Thin soil cover and mountain meadows	Medium hard	Penetration depths are small. Ground is flat. Rocky debris is present. Shallow surface soil. Usually little (initial) vegetation.	
5	Unpaved roads			
3	Bedrock	Extra hard		

ID	Soil Type	Soil Stiffness	Description	Exemplary image (software manual)
7	Concrete and masonry structures		Ground is very hard and is marginally deformed by rocks. No vegetation and no surface soil.	
6	Vegetated soils	Medium	Meadow is deep but contains rock fragments. The meadow can be covered with vegetation. Soil structure of a medium deepness. Rank vegetation.	
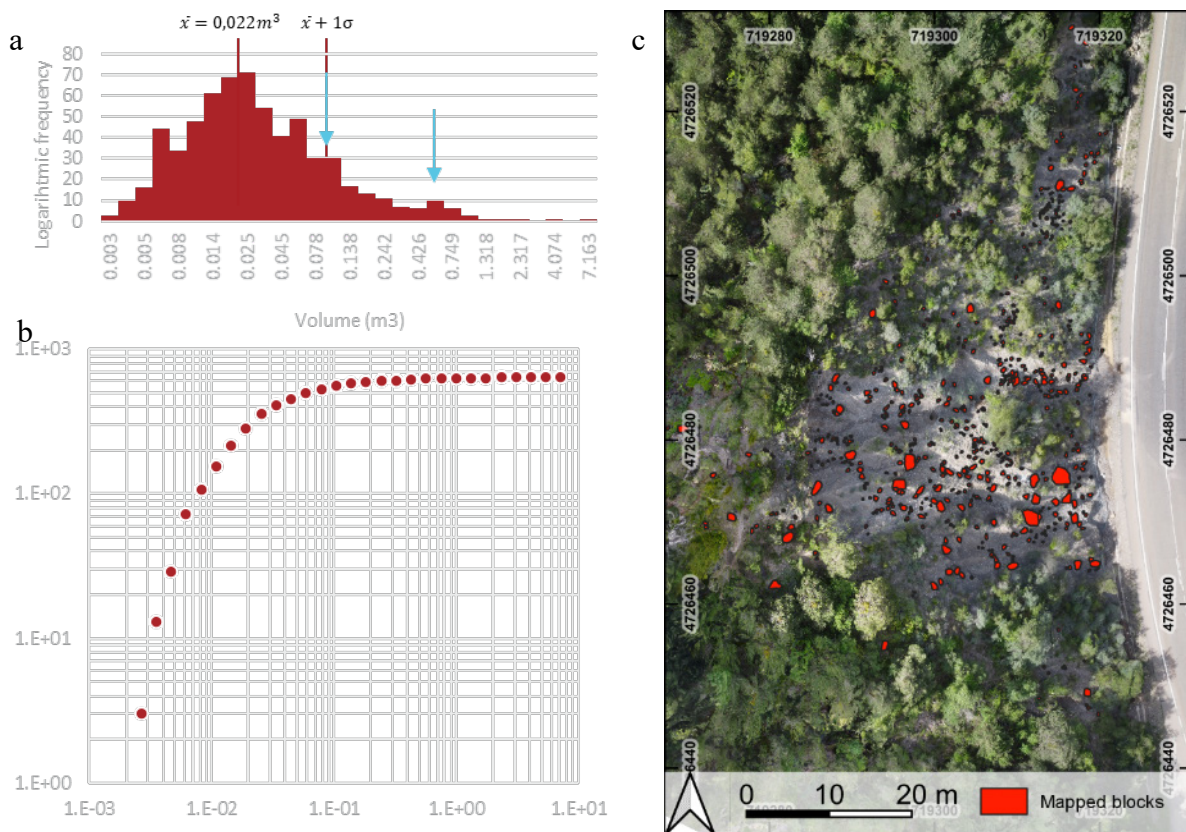
Figure 60: Statistical and spatial distribution of block volumes. a) histogram of the log-normal distribution of volume classes obtained according to Sturge's rule; b) dispersion diagram of the block volumes cumulative logarithmic frequency; c) Blocks mapped on the orthophoto.

A DTM accurately describes the slope morphology, suitably converted to be included in RAMMS:Rockfall. For this purpose, site owners carried out several campaigns of topographical surveys using both fixed and mobile terrestrial laser scanners (Faro Focus 3d and Geoslam Zeb-Horizon) aimed to reconstruct dense point clouds of the area and collecting ground data below the vegetation cover. Moreover, a close-range photogrammetric survey was carried out to get a realistic representation of the area through high-resolution orthophotos. Georeferencing of 3d models was based on differential real-time kinematic Global Navigation Satellite System (GNSS) positioning of several benchmarks installed in the surveyed area. Data processing included image and clouds alignment, dense point cloud reconstruction and filtering. This allowed creating a DTM with 20 cm cell size, and a planimetric orthophoto, 2 cm cell size, was applied to map the NBS and the model setup.

Soil types were mapped through remote sensing based on Unmanned Aerial Vehicles (UAV) imagery, which allowed detecting 6 different soil types for the baseline scenario. They are: 1) bare moraine debris, 2) thin soils and mountain meadows covering the debris, 3) bedrock, 4) paved roads, 5) unpaved roads, 6) soils covered with dense shrub and tree cover. An additional soil type was added for the NBS scenario, for takin in account the retaining wall at the slope base 7) concrete and masonry structures. According to the software manual, soil classes were classified, based on the stiffness, as follow (Table 16):
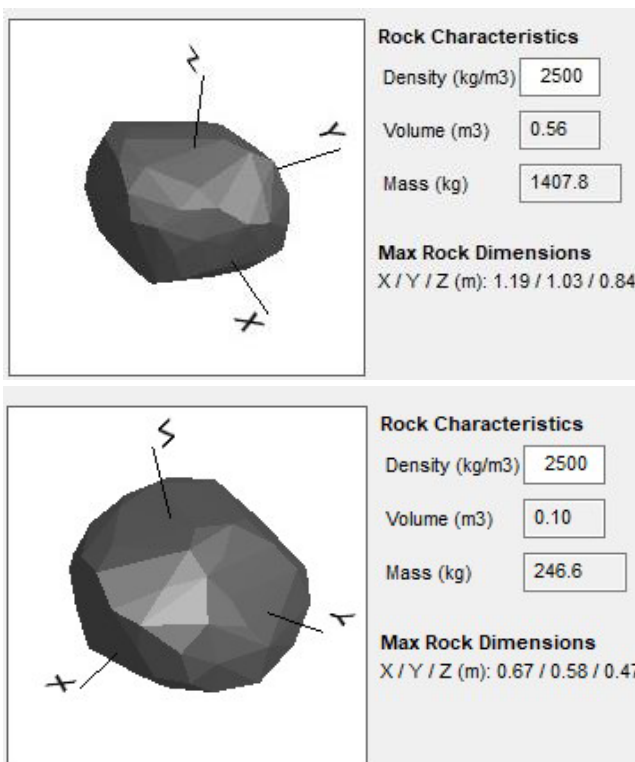
Figure 61: 3d model and dimensional parameters of simulated rock blocks: a) block with volume = 0.56 m3; b) block with volume = 0.10 m3

Based on UAV imagery, different vegetation cover types were detected. Three classes are suggested by the software manual, based on the vegetation density: 1) open forest with a density = 20 m^2/ha and a drag = 250 kg/s; 2) medium forest with a density = 35 m^2/ha and a drag = 500 kg/s; 3) dense forest with a density of 50 m^2/ha and a drag = 750 kg/s.

The block position was obtained by mapping individual blocks outcropping in the moraine debris. The mapping was carried out on UAV imagery and allowed to detect 638 blocks and boulders identified by polygons for which the two main dimensions were measured. To extract information on the possible block volume, the third dimension (generally in the vertical direction) was assumed equal to the shorter, considering flattened to slightly prolate shapes. This allowed estimating the block volumes between $0.02 – 5.4$ m^3. As shown in Figure 60, block volumes have a bi-modal distribution with the most frequent sizes below 0.1 m^2 and a second population with a peak around 0.56 m^3. These two classes were thus used as input for modelling.

The model setup also considered the average spatial densities of the two main classes of block sizes in areas without vegetation cover, which resulted in 0.125 blocks*m^{-2} (i.e. 1 block each 8m^2) and 0.016 blocks*m^{-2} (i.e. 1 block each 64m^2), respectively.

These values were applied to get spaced source points simulating the rockfall onset in areas disregarded due to vegetation cover. The data were also merged with the mapped points in the rockfall source shapefile.

Figure 61: Input maps used for rockfall simulation with RAMMS::Rockfall varying for the two modelled scenarios S1 and S2, including hill-shaded background showing ante opera and post opera slope morphology: a) Mapped soil types for S1; b) Mapped soil types for S2, according to the project layout; c) Mapped vegetation densities for S1; c) Mapped vegetation densities for S2.

The most suitable block shape was selected within the software library based on evidence from remote sensing on high-resolution digital images. The most suitable shape was the equidimensional, slightly oblate blocks in the library referred to as "real equant".

The modelling scenarios S1 and S2 differ in a) DTM describing the different slope shapes before and after NBS implementation; b) soil type, which changes due to the

earth cover of terraces (Figure 61 a, b); c) vegetation which varies in the area of terracing due to revegetation (Figure 61 b, c). More in detail, the soil type on terraces, according to the design layouts, could be considered as moderately stiff (medium); at the base of the slope is designed a retaining wall, which could be considered as extra hard (Figure 61b). In addition, after implantation and plant growth, terraces could be considered as covered by medium-dense vegetation (Figure 61d).

4.3.5   Modelling results and discussion

4.3.5.1   Scenario 1

The first modelling scenario (S1) represents the baseline, i.e., without including vegetation and NBS interventions, considering the two main classes of block volumes ($V_1 = 0.1$ m^3 and $V_2 = 0.56$ m^3). Not having any information on the rockfall frequency, no knowledge can be provided on return periods. Therefore, the assessment is based on rockfall susceptibility. Maps representing the most significant simulation results for this scenario are reported in Figure 62.

Figure 62a shows the maximum rebound heights (sampled at the 95th percentile), resulting always in smaller than 4 m, expect for very few events. The highest values are recorded in areas with steep slopes and scarps, frequently occurring in the central sector where erosion is more intense and rockfalls are more channelized (Figure 63). Since rockfalls are characterized by short runout due to the limited extension of the slope, rock blocks never reach velocities high enough to induce high jump heights.

Figure 62b shows the maximum kinetic energy corresponding to the 95th percentile of maximum energies recorded at each cell. It indicates that, consistently with jump height, rockfalls reach their highest intensity in a few small areas, namely in the central side of the slope, which is also the steepest. Here, large boulders outcrop and rockfalls reach higher velocity. Consequently, in these areas, few rockfall events can reach kinetic energy up to 300 kJ, whereas in the remaining areas rarely exceeds 100 kJ, with the highest frequencies below 25 kJ. Rockfall energy slightly increases to the slope base due to a slight velocity increase during the short propagation.

The rockfall reach probability is shown in Figure 62c, which points out that, due to the high frequency of rockfalls that channelize along the deepest gullies, the reaching probability can exceed 80% at the mouth of the gullies at the slope base, in the central side of the slope. In the other areas, rockfall channelling is much less evident and, therefore, reach probability never exceeds 40%. Consequently, the blocks preferentially accumulate along the road in the central and northern part of the slope (Figure 62d). Conversely, in the southern side, the presence of a low dipping surface in the middle of the slope can favour the accumulation of blocks detaching from the upslope areas (Figure 62d).

The main target of this study concerns the hazard affecting the road running at the slope base. To this aim, graphs showing the variation of the main parameters, such as the rebound heights and the block energies along with the slope base profile (Figure 63),

were generated. They show energy reaching 300 kJ in the central part of the transect (green line), whereas it is significantly lower in both the north and the south side, where, except for some peaks, it never exceeds 100 kJ.

The average rebound height (red line) is very low at the southern and northern end of the slope base, where it rarely exceeds 1 m. It gradually increases to the central part of the slope, instead, reaching 4 m. In a few cases, at the base, it can exceed 6 m, where channelized rockfalls reach their highest velocities. The general trend, however, correlates with the slope height, affecting the runouts length.
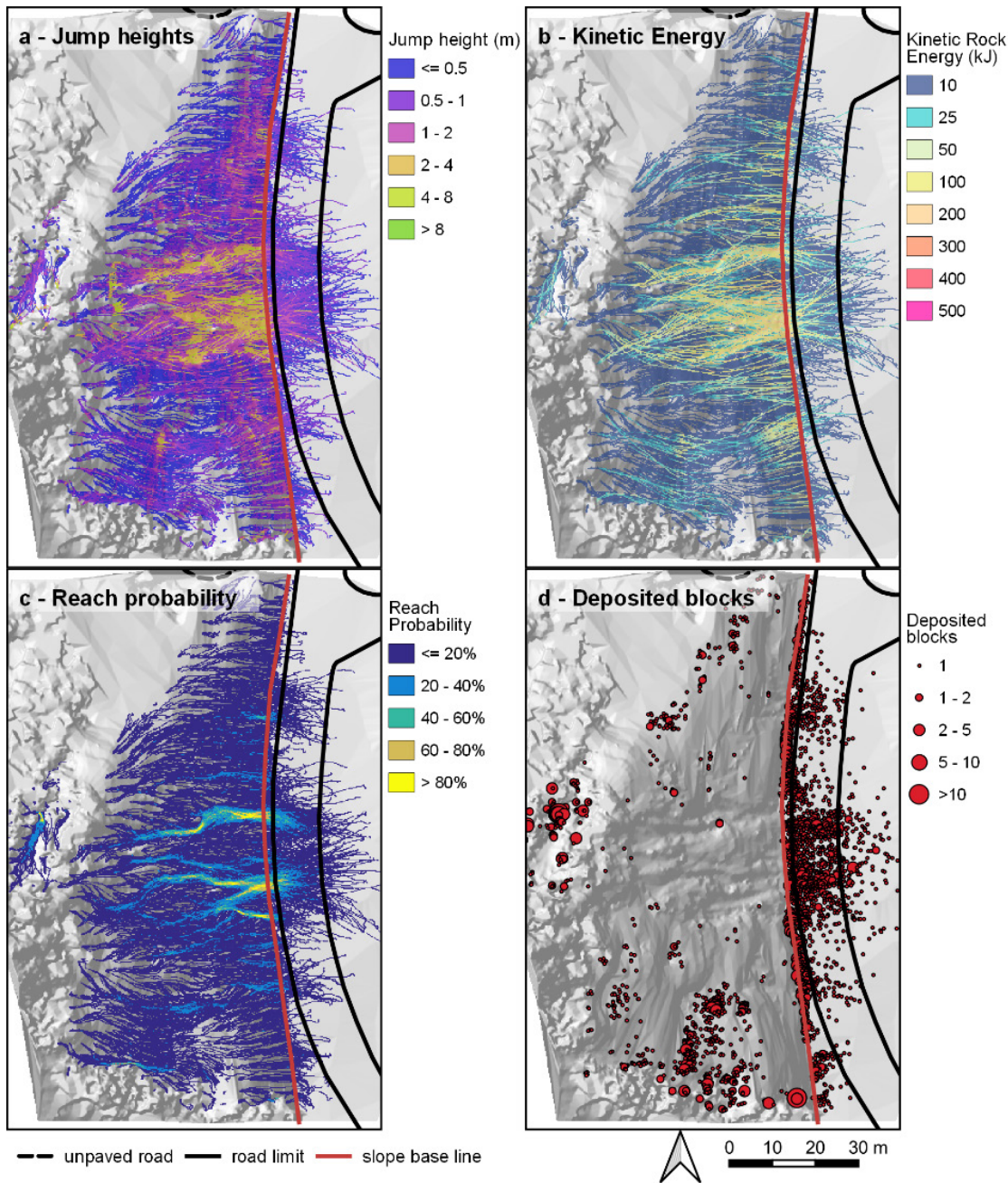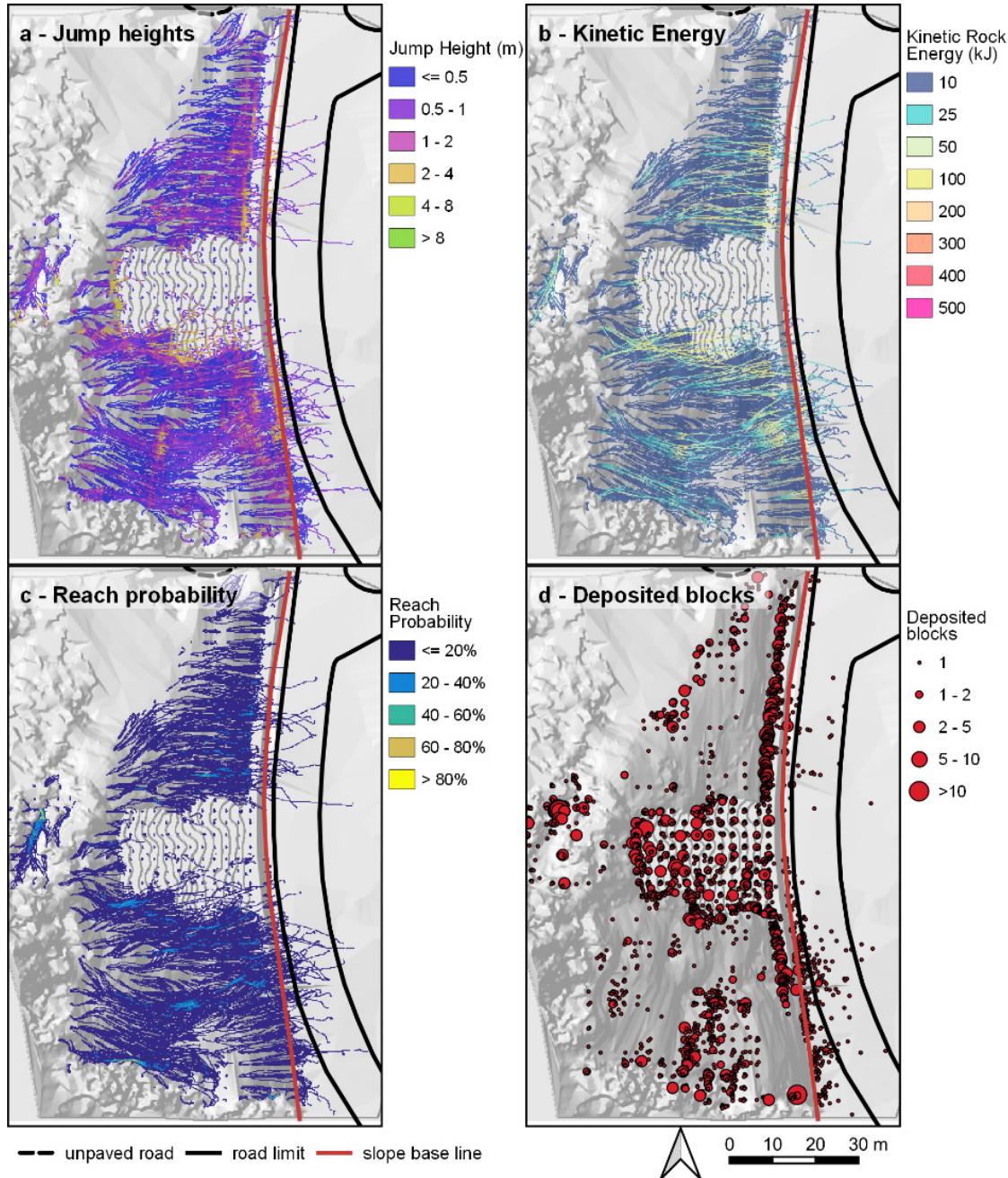
Figure 62: Output maps of rockfall modelling for Scenario 1. Main rockfall parameters represented are a) maximum rockfall energies sampled at 95th percentile (kJ); b) maximum rockfall rebound heights sampled at the 95th percentile (m); c) rockfall reach probabilities (%); d) number of deposited blocks at each cell
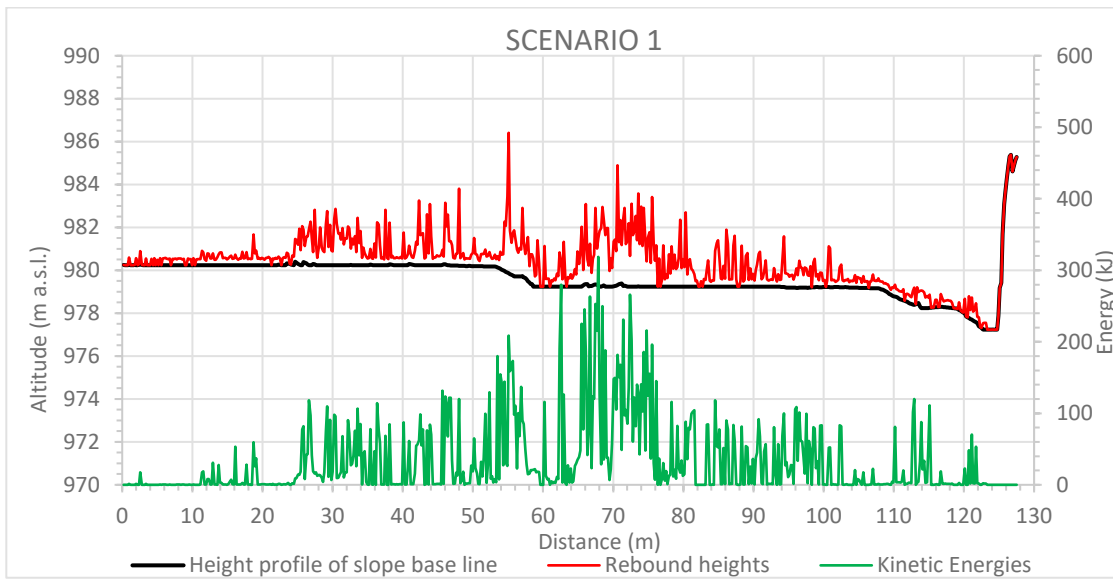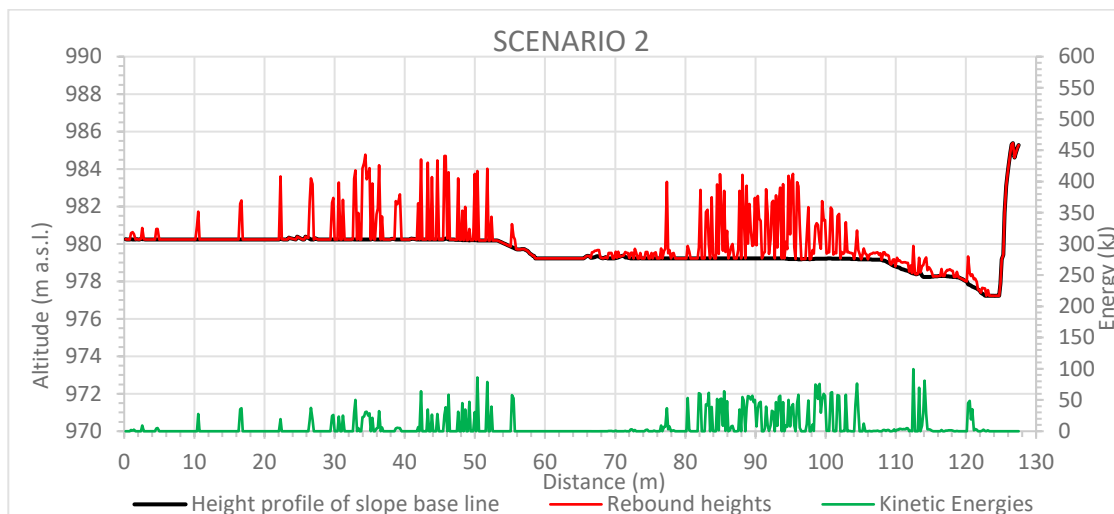
Figure 63. Modelled maximum energy and rebound height along the slope base, a few meters to the west of the road path (S1)

4.3.5.2 Scenario 2

Based on the same settings of both block position and size distribution, the S2 models the effects of NBSs, through a new DTM accounting for the updated slope morphology due to terracing and the new distribution of vegetation cover due to implantation of autochthonous species on terraces.

The resulting maps are reported in Figure 64, which, as for the S1, reports the distribution of max jump height (95th percentile), maximum rock kinetic energy (95th percentile), total reach probability, and the number of deposited blocks.

Observing the spatial distribution of maximum rockfall jump height (Figure 64a), it is worth noting that in the northern part of the area, rockfalls can reach the road in very few cases, with jumping height usually not higher than 1 m. In the slope's central side, rockfall does not propagate significantly and cannot reach the road. Rockfall energy (Figure 64b) shows a similar distribution. Indeed, it rarely reaches 100 kJ along the slope and on the top of the retaining wall at the slope base, where it dissipates most of its energy and occasionally affect the road with residual energies below 25 kJ. In the central part of the slope, rock movement is prevented by the terracing, and as a consequence, rockfalls can transfer very low energies during the very short paths after triggering.

Consequently, rockfall reach probability is also significantly affected by the designed NBS (Figure 64c); indeed, areas of rockfall channelling are avoided by the new slope configuration and reach probability only in very few and very localized cases, can exceed 20%. Rock deposition represented in Figure 64d highlights the effect of NBS in contrasting rockfall triggering and favouring rockfall deposition. Indeed, most of the blocks accumulate along the slope due to the mitigation effect of vegetation and terraces. When rockfalls reach the slope base, they accumulate mostly above the wall designed at

the slope base, and only in a few cases they can propagate further and accumulate on the road.

Figure 64. Output maps of rockfall modelling for Scenario 2. Main rockfall parameters represented are: a) maximum rockfall energy sampled at 95th percentile (kJ); b) maximum rockfall rebound height sampled at the 95th percentile (m); c) rockfall reach probability (%); d) number of deposited blocks at each cell.

Considering the transect designed at the slope base, which runs at the base of the retaining wall here designed, it is worth noting that rockfall height in a few individual

cases propagates beyond the wall (Figure 65). In such cases, they can reach jump heights quite similar to the height of the wall of around 4 m.

It could also be noticed that in the central part of the slope base, previously affected by the highest rebounds, the jump height is quite uniformly close to zero, mainly due to the absence of rockfall arrivals. Notwithstanding the high jump heights recorded, the energy content of rockfall passing the wall at the slope base is relatively low, rarely exceeding 50 kJ and, only in one case, resulting higher than 100 kJ. As above remarked, in the central part, terracing prevents rockfalls, and consequently, no energy is transferred.

Figure 65. Modelled maximum energy and rebound height along the slope base, a few meters to the west of the road path (S2)

4.3.5.3 Main changes in hazard patterns

Although the differences in hazard patterns induced by the integration of NBS are widely discussed in the previous section, a quantitative estimation of the variation of the main parameters characterizing rockfall hazard could help to quantify the mitigative effects of the designed solutions.

The distribution of such variations derived from the comparison between the baseline and the NBS scenarios (S1-S2) are shown in spatial way in Figure 66, which represent the changes in both rockfall jump height (Figure 66a) and kinetic energy (Figure 66b). Negative values prove a detrimental effect of NBS with an increase of the considered parameter. Conversely, positive values indicate a mitigating effect.
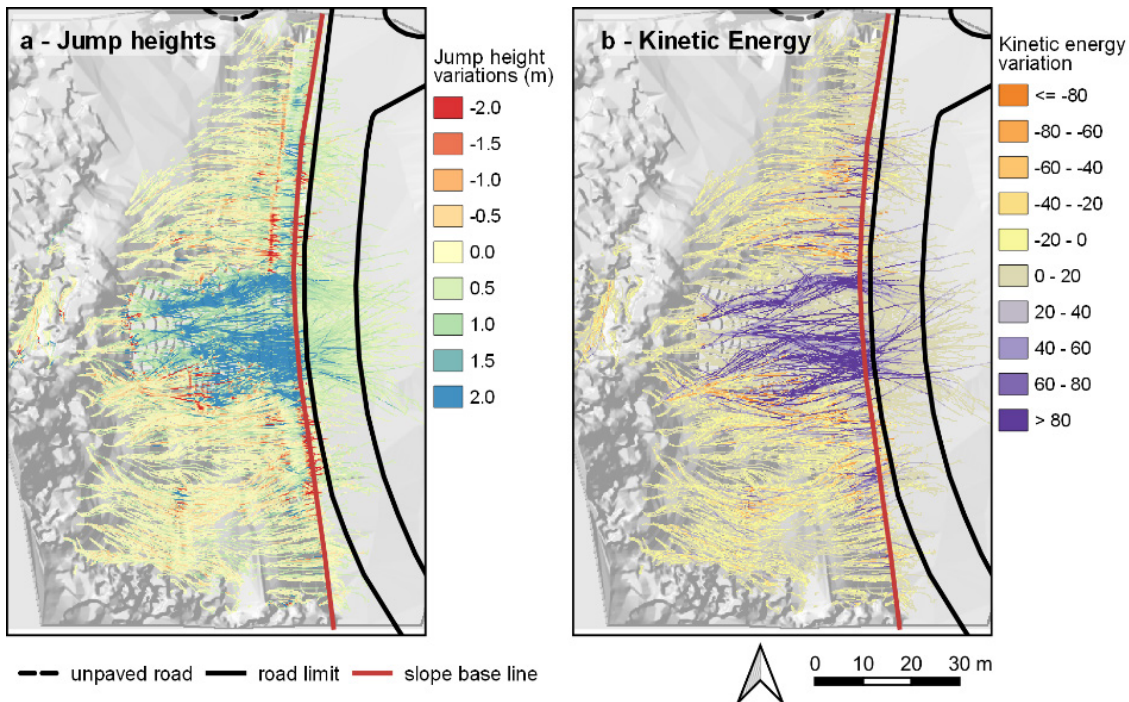
Figure 66. Main variations between the ante-operam (S1) and pos-operam (S2) scenarios concerning (a) maximum rockfall energy and (b) maximum rebound height.

The distribution of heights variation (Figure 66a) shows that a large rate of the slope rockfall height either does not significantly change or is slightly decreased, probably due to the more extended vegetation cover. Conversely, in the central part where terracing is done, the most relevant reduction of rockfall height is recorded due to the effect of terraces in preventing rock detachment and movement. Hoverer, it is worth noting a narrow strip close to the retaining wall at the slope base, characterized by an increase of rockfall jump height for blocks that can propagate beyond the wall, toward the road.
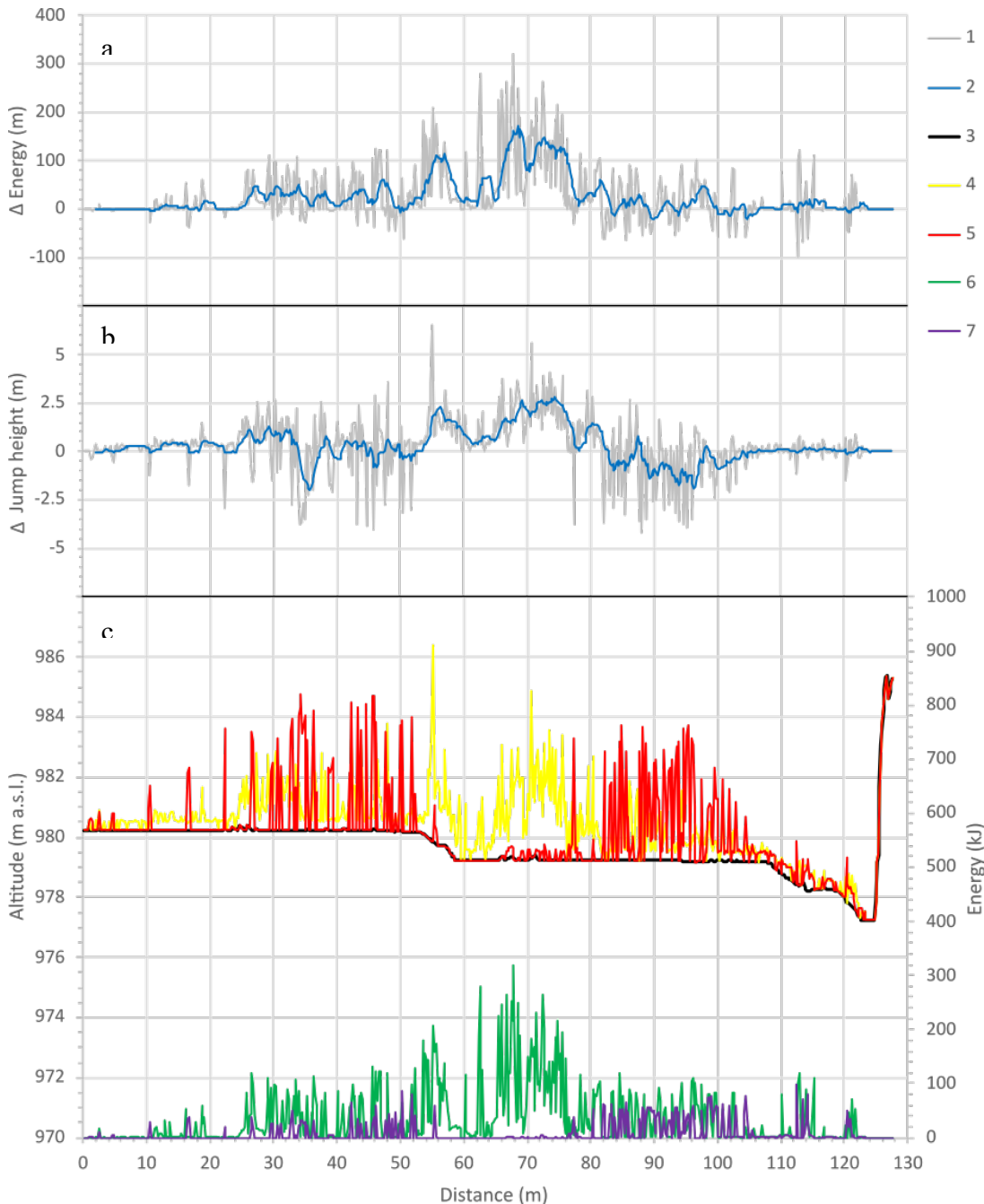
Figure 67. Main variations along the road path between S1 and S2 modelling results: a) variations of rebound height; b) variation of maximum energy; c) maximum height and energy recorded for S1 and S3 along the road path. 1 = heights and energy variation envelopes; 2 = 10 cells moving average; 3 = road profile; 4 = S1 maximum heights envelope; 5 = S2 maximum heights envelope; 6 = S1 maximum energies envelope; 7 = S2 maximum energies envelope.

The same trend could was observed for the rockfall energy (Figure 67b), which further shows the mitigative effect of designed NBSs. Indeed, rockfall energy is significantly mitigated in the area of NBS interventions with an energy reduction exceeding 80 kJ, particularly in the central area where rockfalls are prevented. It should also be noticed

that, also at the base of the retaining wall in the northern sector, energy is lowered, despite the increase of jump height. This indicates that the falling blocks dissipate much of their energy when impacting the wall, where indeed most of them are stopped.

To better understand the mitigative effects of NBS on road safety, the absolute variation of the transit height and energy is reported along the slope base, just to the west of the road path. Here, the main outputs of the comparing scenarios are reported together to make the analysis of the residual hazard on the road easier.

The comparison shows that the expected rockfall energy is significantly reduced over the whole path. Reduction is more intense in the central part, downslope to the terraced area, where energy is not higher than 300 kJ. In the northern and southern sectors, energy reduction is less evident (Δ < 100 kJ) due to both the milder effect of the revegetation and the lower rockfall kinetic energy related to shorter runouts.

Maximum rockfall height is also reduced over the whole path but more intensely in the central part, where the reduction is up to 6 m. In the northern and southern sides, despite a general milder reduction (Δh < 2.5 m), some cases are detected showing an increase up to 4 m of rockfall height due to some blocks jumping the wall.

4.3.6   Concluding remarks

The present analysis focuses on the hazard phenomena affecting the case study of Santa Elena, Biescas, in Spain. Here a slope on moraine debris facing one of the most important roads in the area is affected by intense erosion which caused debris denudation and excavation of deep gullies. The erosion of clayey and sandy matrix can provoke the detachment of rock boulders threatening the road users. Rock detached can present very different sizes since highly heteromeric outcropping blocks characterize the moraine debris.

To tackle this issue, some NBS are designed mainly consisting of slope terracing by means of wooden and masonry structures and subsequent revegetation. A retaining masonry wall is also planned at the slope base. Given the limited extension of the studied slope and the hazard scenario's peculiarities, considering the availability of high-resolution tridimensional data, the modelling approach was oriented to a deterministic physical-based model that allows fully evaluating the shape and the size of blocks.

The goal of the assessment was to verify the effectiveness of NBS by comparing the modelling results of an NBS scenario (S2) with a baseline scenario (S1).

Model input data were collected during field campaigns and remote sensing on high-resolution UAV imagery and terrestrial laser-scanning models.

The main target of the assessment was to assess the change in maximum rockfall energy and jump height, as a consequence of the mitigative effect of planned NBS both on the slope and along the investigated road transect.

Modelling results highlight that rockfalls are characterized by short runout related to the limited slope extension and, consequently, mostly show low energy content. The highest rockfall energy and height are recorded along some gullies in the central part of the slope where blocks channelize. As a consequence, also the reaching probability is the highest in these areas. In the current scenario, most of the blocks reach the slope base and the road. The terracing was proven to significantly limit the rockfall hazard since terraces both prevent rockfall detachment and hinder the movement of detached rocks. As a consequence, in the most hazardous area, corresponding to the main area of NBS implementation, the rock blocks accumulate on the terraces without reaching the road. In the remaining part of the slope, the largest part of detached rock can reach the slope stop when they impact on retaining wall. In only a few cases, rocks can jump over the wall after dissipating most of their kinetic energy. Therefore, compared to the current scenario, the hazard on the road is highly reduced, and the planned NBS can be considered as an effective approach, showing very few downsides, which, in any case, can be handled through few integrative interventions.

4.4   References

Bartelt, P., Bieler, C., Bühler, Y., Christen, M., Dreier, L., Gerber, W., Glover, J., Schneider, M., Glocker, C., Leine, R., 2013. RAMMS Rapid Mass Movements System-User Manual v1. 6 Rockfall: A Numerical Model for Rockfall in Research and Practice. WSL Institute for Snow and Avalanche Research SLF, Davos.

Bozzolo, D., Pamini, R., 1986. Simulation of rock falls down a valley side. Acta Mechanica 63, 113–130. https://doi.org/10.1007/BF01182543

Broilli, L., 1974. Ein Felssturz im Großversuch. pp. 69–78. https://doi.org/10.1007/978-3-7091-8372-4_9

Caviezel, A., Lu, G., Demmel, S.E., Ringenbach, A., Bühler, Y., Christen, M., Bartelt, P., 2019. RAMMS::ROCKFALL - A Modern 3-Dimensional Simulation Tool Calibrated on Real World Data.

Chang, W.-R., 1998. The effect of surface roughness on dynamic friction between neolite and quarry tile. Safety Science 29, 89–105. https://doi.org/10.1016/S0925-7535(98)00011-3

Christen, M., Bartelt, P., Gruber, U., 2007a. RAMMS-a modeling system for snow avalanches, debris flows and rockfalls based on IDL. Photogrammetrie Fernerkundung Geoinformation 2007, 289.

Christen, M., Bartelt, P., Gruber, U., 2007b. RAMMS-a modeling system for snow avalanches, debris flows and rockfalls based on IDL. Photogrammetrie Fernerkundung Geoinformation 2007, 289.

Collins, B.D., Stock, G.M., 2016. Rockfall triggering by cyclic thermal stressing of exfoliation fractures. Nature Geoscience 9, 395–400. https://doi.org/10.1038/ngeo2686

Cottaz, Y., Faure, R., 2008. Pir3D, an easy to use three dimensional block fall simulator. Landslides and Engineered Slopes. From the Past to the Future 319–322. https://doi.org/10.1201/9780203885284-C28

Crosta, G.B., Agliardi, F., 2004. Parametric evaluation of 3D dispersion of rockfall trajectories. Natural Hazards and Earth System Science 4, 583–598. https://doi.org/10.5194/NHESS-4-583-2004

Cruden, D. M., & Varnes, D. J. (1996). Landslide types and processes. Special Report - National Research Council, Transportation Research Board, 247, 36-75.

Dorren, L., 2017. FINT - Find Individual Trees User manual.

Dorren, L., Maier, B., Berger, F., 2006. Assessing protection forest structure with airborne laser scanning in steep mountainous terrain, in: Workshop on 3D Remote Sensing in Forestry. p. 242.

Dorren, L.K.A., 2015. Rockyfor3D (v5. 2) revealed—transparent description of the complete 3D rockfall model. EcorisQ paper (www. ecorisq. org).

Dorren, L.K.A., Berger, F., le Hir, C., Mermin, E., Tardif, P., 2005. Mechanisms, effects and management implications of rockfall in forests. Forest Ecology and Management 215, 183–195. https://doi.org/10.1016/j.foreco.2005.05.012

Dorren, L.K.A., Berger, F., Putters, U.S., 2006. Natural Hazards and Earth System Sciences Real-size experiments and 3-D simulation of rockfall on forested and non-forested slopes, Natural Hazards and Earth System Sciences.

ESRI, 2004. What is ArcGIS ? Environmental Systems Research Institute.

Evans, S.G., Hungr, O., 1993. The assessment of rockfall hazard at the base of talus slopes. Canadian Geotechnical Journal 30, 620–636. https://doi.org/10.1139/t93-054

Forte, G., Verrucci, L., di Giulio, A., de Falco, M., Tommasi, P., Lanzo, G., Franke, K.W., Santo, A., 2021. Analysis of major rock slides that occurred during the 2016–2017 Central Italy seismic sequence. Engineering Geology 290, 106194. https://doi.org/10.1016/J.ENGGEO.2021.106194

Frattini, P., Crosta, G.B., Agliardi, F., 2013. Rockfall characterization and modeling. Landslides 267–281. https://doi.org/10.1017/CBO9780511740367.023

Guzzetti, F., Crosta, G., Detti, R., Agliardi, F., 2002. STONE: a computer program for the three-dimensional simulation of rock-falls. Comput Geosci 28, 1079–1093. https://doi.org/10.1016/s0098-3004(02)00025-0

Hungr, O., Evans, S.G., 1988. Engineering evaluation of fragmental rockfall hazards, in: International Symposium on Landslides. 5. pp. 685–690.

Kirkby, M.J., Statham, I., 1975. Surface Stone Movement and Scree Formation. The Journal of Geology 83, 349–362. https://doi.org/10.1086/628097

Kupferschmid Albisetti, A.D., Brang, P., Schönenberger, W., Bugmann, H., 2003. Decay of Picea abies snag stands on steep mountain slopes. The Forestry Chronicle 79, 247–252. https://doi.org/10.5558/tfc79247-2

Lan, H., Derek Martin, C., Lim, C.H., 2007. RockFall analyst: A GIS extension for three-dimensional and spatially distributed rockfall hazard modeling. Computers & Geosciences 33, 262–279. https://doi.org/10.1016/j.cageo.2006.05.013

Li, L., Lan, H., 2015. Probabilistic modeling of rockfall trajectories: a review. Bulletin of Engineering Geology and the Environment 2015 74:4 74, 1163–1176. https://doi.org/10.1007/S10064-015-0718-9

Loye, A., Jaboyedoff, M., & Pedrazzini, A. (2009). Identification of potential rockfall source areas at a regional scale using a DEM-based geomorphometric analysis. *Natural Hazards and Earth System Sciences*, *9*(5), 1643-1653.

Pfeiffer, T.J., Bowen, T.D., 1989. Computer Simulation of Rockfalls. Environmental & Engineering Geoscience xxvi, 135–146. https://doi.org/10.2113/gseegeosci.xxvi.1.135

Pratt, C., Macciotta, R., Hendry, M., 2019. Quantitative relationship between weather seasonality and rock fall occurrences north of Hope, BC, Canada. Bulletin of Engineering Geology and the Environment 78, 3239–3251. https://doi.org/10.1007/s10064-018-1358-7

QGIS.org, 2021. QGIS Geographic Information System [WWW Document]. Open Source Geospatial Foundation Project.

Rammer, W., Brauner, M., Dorren, L.K.A., Berger, F., Lexer, M.J., 2010. Evaluation of a 3-D rockfall module within a forest patch model. Natural Hazards and Earth System Sciences 10, 699–711. https://doi.org/10.5194/nhess-10-699-2010

Schönenberger, W., Noack, A., Thee, P., 2005. Effect of timber removal from windthrow slopes on the risk of snow avalanches and rockfall. Forest Ecology and Management 213, 197–208. https://doi.org/10.1016/j.foreco.2005.03.062

Stevens, W.D., 1998. Rocfall: a tool for probabilistic analysis, design of remedial measures and prediction of rockfalls.

Stokes, A., Salin, F., Kokutse, A.D., Berthier, S., Jeannin, H., Mochan, S., Dorren, L., Kokutse, N., Abd.Ghani, M., Fourcaud, T., 2005. Mechanical Resistance of Different Tree Species to Rockfall in the French Alps. Plant and Soil 278, 107–117. https://doi.org/10.1007/s11104-005-3899-3

Woltjer, M., Rammer, W., Brauner, M., Seidl, R., Mohren, G.M.J., Lexer, M.J., 2008. Coupling a 3D patch model and a rockfall module to assess rockfall protection in mountain forests. Journal of Environmental Management 87, 373–388. https://doi.org/10.1016/j.jenvman.2007.01.031

5 Hazard modelling at Pyrenees case study affected by snow avalanche

5.1 Introduction

One of the PHUSICOS test site is the Midaou catchment in the municipality of Barèges, Département Hautes-Pyrénées in south-western France. The area is located on the southern slope od the Péne Det Pouri Mount (2587 m a.s.l.), which dips toward the valley of the Le Bastan river, where the village of Barèges is located. The slope degree mainly ranging between 30° and 50°, sometimes interrupted by vertical rockfaces, causes snow detachment occurring mainly in the highest part where vegetation cover is scarce, thus posing a serious threat to the village of Baréges to the foothill area. As a consequence, the village of Barèges was severely damaged in the past by snow avalanches. Two relevant events occurred in 1897 and 1907, causing extended damages and casualties. Since then, many different measures have been adopted in the release area consisting of snow bridges and terracing.
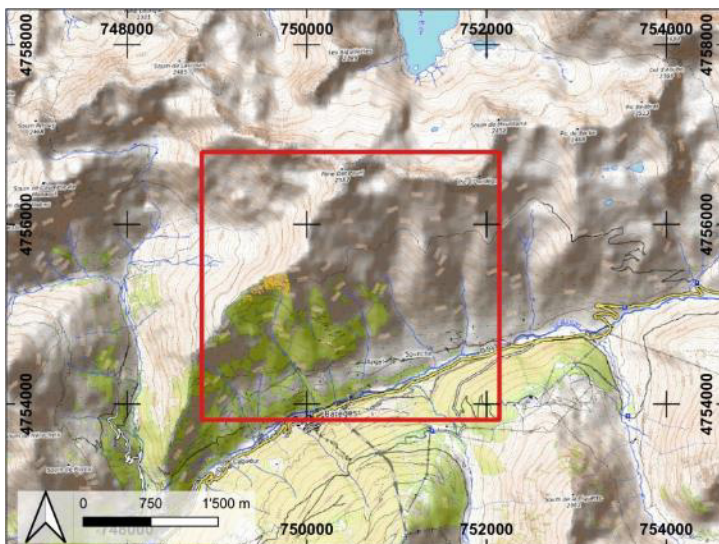
Figure 68. Study area location on base map from Open Street Map services. Reference system is ETRS89 – UTM zone 30N (EPSG: 25830)

One of the last events in 2013, affecting a military facility in the valley, pointed out the limited efficacy of existing measures. For this reason, new NBS measures were designed to integrate with the existing measures: they consist of the afforestation of the snow-avalanche release areas, with suitable tree species, in areas where soil cover thickness allows implantation. Furthermore, to protect growing trees, protective structures consisting of wooden tripods are installed on the implantation site to support the snow load, threatening small trees.
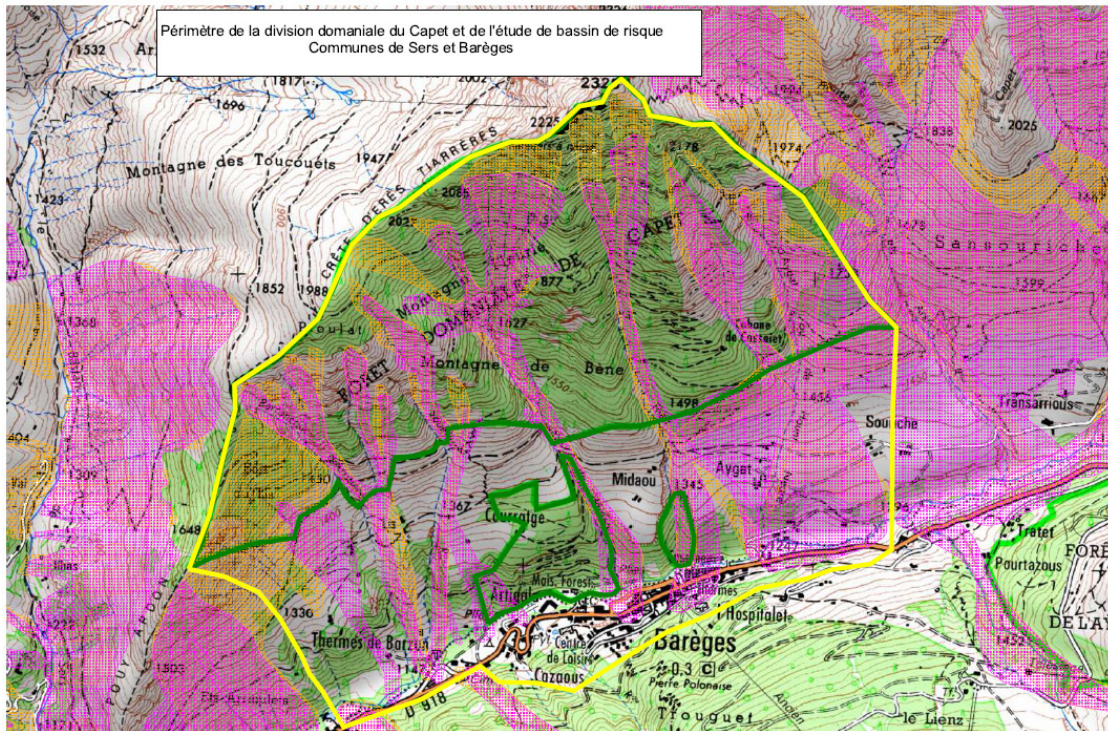
Figure 69. The valley side north of the village of Barèges. Avalanche paths are between the green areas and mainly follow gullies towards the valley and the village. Release areas of the two main gullies in the proposal are marked with red circles (Solheim et al., 2019).

5.2 Modelling approach

At the Capet Forest case study, the effectiveness of the planned measures was assessed by comparing a baseline scenario (without NBS and other mitigative measures) with a post-operam scenario (considering both NBS and grey existing measures) under the same conditions. This choice was due to the lack of relevant local nivo-meteorological data and the absence of well-characterized previous events.

The tests focussed on the afforestation at high altitudes as protection against the release of snow avalanches. To model the protective effect of the established forest, the run-out of snow avalanches with return periods in the (estimated) range 10–300 years has been simulated with the numerical model MoT-Voellmy carried out by NGI experts.

Figure 70. The type of wooden structures, made from local wood, planned for implementation to protect the plants from damage by snow creep during the first years. The structures will themselves also prevent release of snow avalanches (Solheim et al. 2019)a

5.3   Main modelling outcomes

The main results showed that both designed NBS and the existing mitigation measures can effectively reduce the probability of avalanche release from the highest parts of the potential release area. Nevertheless, avalanches could start at lower altitudes but with lower magnitude and shorter run-outs. Under extreme conditions similar to those recorded in 2013 (the snow covering the supporting structures completely and/or being unusually light and cohesionless), the snow avalanche release in the mitigated area upslope might still be possible but involving shallower depths of snow cover.

Detailed information about modelling approaches, methods and detailed analyses of modelling outcomes are discussed in the attached technical note in Annex 7 entitled "Assessment of the Effectiveness of Afforestation as a Nature-Based Solution Against Snow Avalanches in the Forêt du Capet, French Pyrenees" (Issler, 2022).

5.4 ANNEX 7 - Assessment of the Effectiveness of Afforestation as a Nature-Based Solution Against Snow Avalanches in the Forêt du Capet, French Pyrenees

Assessment of the Effectiveness of Afforestation as a Nature-Based Solution Against Snow Avalanches in the Forêt du Capet, French Pyrenees

Contents

Tables

Figures

Review and reference page

Abstract

One of the demonstration sites of the EU Horizon 2020 Research and Development project PHUSICOS is the Midaou catchment in the municipality of Barèges in the Département Hautes-Pyrénées in south-western France. The nature-based solution to be tested is afforestation at high altitudes as a protection against release of snow avalanches. To help in assessing the protective effect that can be expected once the forest has established itself, the run-out of snow avalanches with return periods in the (estimated) range 10–300 years has been simulated with the numerical model MoT-Voellmy.

The main results are that both the existing "gray" mitigation measures (terraces and snow bridges in the northern part of the catchment) and the planned afforestation strongly reduce the probability of avalanche release from the highest parts of potential release area. Avalanches will nevertheless start at lower altitude, but they will be less massive and have a reduced run-out. Under extreme conditions as in 2013 (the snow covering the supporting structures completely and/or being unusually light and cohesionless), a release may also comprise the protected areas, but there the fracture depth will be small.

It is difficult to assign return periods to the simulations because we lack (i) detailed nivo-meteorological data to estimate the fracture depth as a function of the return period, (ii) well characterized events for calibrating the model for this site, and (iii) first-hand knowledge of the area. Nevertheless, the comparison between avalanches with and without the "gray" and nature-based mitigation measures but otherwise identical conditions is expected to be quite robust and indicates that both mitigation approaches have similarly good effect.

1 Introduction

1.1 The PHUSICOS demonstrator project Midaou avalanche path, French Pyrenees

PHUSICOS is a large collaborative project in the framework of the European Union's Horizon2020 Research and Development program. Its goals are to further develop and adapt nature-based solutions (NBSs), to demonstrate the feasibility, effectiveness, efficiency and upscalability of NBSs, and to identify obstacles to their adoption as well as to point towards overcoming them (Solheim et al., 2021). These authors underline the important role of convincing the stakeholders of the effectiveness and economic efficiency of envisaged NBSs so the stakeholders will overcome their innate skepticism and will approve and support implementation of NBSs. Demonstrator projects in different rural or mountainous regions of Europe, addressing different types of natural hazards at a range of scales with a wide variety of mitigation measures, are therefore a central part of PHUSICOS.

The present Technical Note addresses the question of estimating the effectiveness of one such measure—afforestation of a release area—against one specific threat, namely snow avalanches, in the Midaou catchment in the municipality of Barèges, Département Hautes-Pyrénées in south-western France. This is one of the PHUSICOS test sites where implementation has progressed farthest. Nevertheless, the effectiveness of the afforestation cannot be seen at once for two main reasons: First, trees in a high-alpine environment (above 2000 m a.s.l. in this case) need at least about two decades to grow up to the point where they can prevent avalanche release. Moreover, during their early growth phase they are exposed to many environmental factors that can threat their survival. Second, large snow avalanches that pose a threat to settlements and thus put the protection measures to a test are episodic, typically with decades to centuries between successive occurrences.

Hence, the effectiveness of this mitigation measure can only be demonstrated by either pointing to locations where afforestation has proved successful over long periods of time under comparable topographic and climatic conditions, or by constructing realistic scenarios for extreme weather and snow-cover conditions conducive to the formation of large avalanches, whose run-out and effect on the endangered settlement is then modelled numerically.

1.2 How can one assess effectiveness and efficiency of NBSs?

The most appropriate measure for the effectiveness of a specific mitigation measure is the reduction of *risk*. The risk from snow avalanches or other natural hazards can be obtained by summing the *expected loss* of monetary or non-monetary values or human life over all scenarios, weighted with the probability of each scenario. The expected loss increases monotonically with the *intensity* connected to a scenario, which for snow

avalanches typically is quantified by the impact pressure. The probability of an event exceeding a given value of intensity decreases monotonically with the intensity.

The expected loss depends on the one hand on the *exposure* of the elements at risk, and on the other hand on the *vulnerability* of these elements. The exposure of buildings is 1 whereas the exposure of people inside an apartment building, say, is the number of inhabitants times the fraction of time they spend inside the house on average. The vulnerability of a structure can be taken as the cost of repair or replacement in the case of a hit, the vulnerability of persons as the probability of severe injury or death. In either case, the vulnerability is a monotonically increasing function of the intensity.

A complete quantitative risk assessment for the Midaou avalanche path with and without afforestation is beyond the scope of this study; both the exposure and vulnerability depend on the locale-specific circumstances that we do not know well. Moreover, this part of the assessment cannot easily be generalized. A less ambitious goal would be to estimate how the probability distribution function (PDF) of event intensity—expressed by the maximum impact pressure at a given location—varies along the path. These estimates should be made both for the situation prior to afforestation and after the new forest has attained its full effectiveness. With this information, the risk could be assessed quantitatively once exposure and vulnerability of buildings and people are specified.

The central element in such an analysis is the estimation of the release probability and of the PDFs of friction parameters and fracture depth that specify the dynamic behavior of, and initial conditions for, the run-out model. There is presently no validated and generally accepted method for calculating the release probability in a given potential avalanche release area. A promising first step is described by Gauer (2018); it has been implemented in a code for generating avalanche susceptibility maps (Issler, et al., 2020), but the required gridded daily nivo-meteorological input data are not available for the present study area.

For these reasons, a simpler approach has been chosen for the present study: Based on simple topographic criteria, general information about the dominant wind directions and expert judgment, two major and one minor potential release areas (PRAs) are selected. In the upper reaches of one of the two major areas, afforestation is progressing; in the upper reaches of the other, older mitigation measures (steel bridges and terraces supported by stone walls) are present. Both types of measures may be expected to reduce the release probability in their area by one to two orders of magnitude, and if a release nevertheless occurs, the avalanche mass will be much smaller than without the measure. In the third PRA, at lower altitude, no mitigation measures are present or planned; it serves as a reference for (qualitatively) assessing the residual risk to Barèges.

Numerical run-out simulations have been carried out for these three PRAs, considering the situation with and without mitigation measures. No quantitative estimate is given for the probability of each scenario. Qualitatively one may consider the scenarios with release in the upper reaches of the major PRAs as relatively frequent if there are no mitigation measures; they will be rare events if mitigation measures are present. Releases

from only the lower reaches are assumed to be infrequent but not rare. Finally, release from the minor PRA at lower altitude is also assumed infrequent.

1.3   Organization of the report

Section 2 presents the theoretical framework and summarizes the tools that were used. The simulation results are shown in different views in Section 3, followed by a critical discussion of their meaning and their uncertainties and error sources in Section 4. The avalanche flow model MoT-Voellmy, which was in this report, is described in Appendix A, while Appendix B outlines how a probabilistic risk analysis could be carried out if more nivo-meteorological data can be obtained and an existing model is developed further.

2   Analysis methods

2.1   Release areas

Avalanche release is a complex process determined by a multitude of factors and defies a purely deterministic description: The weather throughout the winter determines the depth, layering and physical properties of the snowpack, all of which vary strongly over short distances due to the local ground properties, differences in insolation, and snow drift.

Empirical rules for where (slab) avalanches can form have emerged from decades of observations:

- Almost always, potential release areas (PRAs) are characterized by slope angles in the range $28° \leq \theta \leq 60°$. Small islands with $\theta < 28°$ inside steeper terrain may, however, be included in the release.
- Fractures will not propagate across very sharp terrain shoulders.
- Lines along which the slope angle changes abruptly often place a limit on PRAs.
- Terrain in lee zones of the dominant wind direction, where drifting snow tends to deposit, is favored over windward zones. Similarly, bowl-shaped areas tend to catch snow whereas convex areas often are swept clear of snow.
- Fracture propagation across narrow "bottlenecks" (of width 10 m or less) is rare. So are "outstickers" (long and narrow zones sticking out of the main release area).
- Actual release areas typically comprise only a part of the PRA.

Few studies investigate the distribution of release-area size in a given path, e.g., (Maggioni and Gruber, 2003; Maggioni et al., 2006). Well-established, practical methods for determining the most likely extent of the release area under given conditions are still lacking. There are physical reasons why both very small and very large releases should be rarer than those of intermediate size. An approach that builds on ideas expounded some 40 years ago in (Lackinger, 1989) and combines them with elements of the

approach by Gauer (2018) is presently under development at NGI but not ready for application yet.

In view of these difficulties, a simplified procedure was chosen here:

- All terrain with a local slope angle in the range $28° < \theta < 60°$ was mapped and considered PRAs.
- These areas were divided into PRAs that can be considered separate even under the most extreme of circumstances (Figure 1).
- Among the resulting PRAs, two large ones to the Northwest (10+11) and the North (20+21) of the Midaou catchment and a somewhat smaller one (3) at lower altitude were selected and manually reduced somewhat to shapes that looked more realistic (mainly "outstickers" and "bottlenecks" were removed).
- The two large PRAs were subdivided (Figure 1) into upper (10, 20) and lower parts (11, 21) according to whether there are mitigation measures present (stone terraces and steel bridges in the case of the northern PRA, afforestation in the case of the north-western PRA).
- No attempt has been made to specify subareas of the selected PRAs for different return periods.
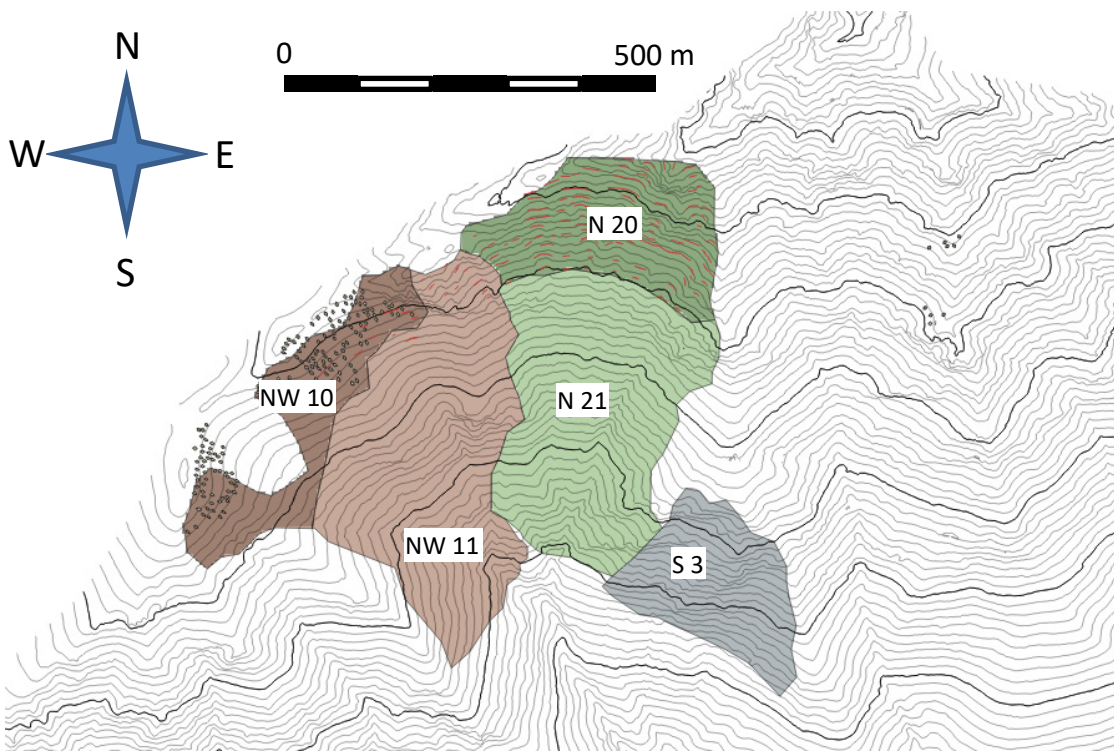

Figure 1. Studied release areas in the Midaou path: North-west (10, 11), North (20, 21), South (3). The dots in area 10 represent groups of planted trees while red lines in area 20 and in the northernmost corner of area 11 indicate existing support structures (terraces and steel bridges or nets). Equidistance 10 m

2.2   Release probability

In practical hazard mapping, the *release probability* of avalanches is usually either inferred from available observations or subjectively estimated (often only distinguishing between "relevant" and "irrelevant" avalanche paths). For example, the often-used Swiss guidelines for avalanche hazard mapping (Salm, et al., 1990; SLF, 1999) apply only to "extreme" avalanches with return periods of 30 years or more, but do not give criteria for estimating the return period of avalanches in a given path.

Recent years have seen significant progress in estimating the release probability of avalanches in a given potential release area (PRA) (Gauer, 2018): Daily (modeled and/or interpolated) data for air temperature, precipitation and snow height in the PRA are used to generate a large set of synthetic weather situations (typically 1–5 million), then a simple infinite-slope stability criterion is applied for each sample and the number of "releases" counted. For each simulated release event, one can evaluate the minimum required new-snow height and the corresponding fracture depth and thus find $d_0(T)$, the dependence of fracture depth on return period. This approach is implemented in the code NAKSIN (Issler et al., 2020), which is designed for automatically generating detailed and realistic avalanche susceptibility maps for extended areas.

Application of NAKSIN to the Midaou avalanche path was originally envisioned but had to be abandoned because the necessary input data—series of daily values of air temperature, precipitation and snow depth at or near the study area spanning several decades—are not available or could only be estimated with insufficient precision.

The one piece of information available for the Midaou path is that at least one avalanche has reached and damaged Barèges since the establishment of a cadastre of observed avalanches in the late 19th century. However, it is likely that avalanches release frequently in this catchment, where north-westerly winds will deposit significant amounts of snow under snowfall events and some degree of snow drift may also be expected without precipitation under north-westerly to north-easterly winds.

Drifting snow will deposit near the crest, i.e., in the upper reaches of the two major PRAs defined above. One may thus assume that dry-snow avalanches will most often start in the two uppermost PRAs. Descending on their path, such avalanches may often induce secondary releases farther along and to the sides of the path or entrain significant amounts of new snow where the snow temperature is low.

In contrast, the release probability of wet-snow avalanches may be higher in the lower parts of the major PRAs and in the minor PRA. Wet-snow avalanches tend to follow the topographic features more closely and often have a shorter run-out than dry-snow avalanches. One may expect that wet-snow avalanches pose a minor threat for Barèges, but this needs verification. Table 1 summarizes our qualitative assessment. We use the vague and non-standard terms "frequent", "occasional", "rare" and "very rare" on purpose to emphasize that they are only qualitative. With more information on avalanche events in this mountain side, they could be made semi-quantitative.

NGI

Table 1. Qualitative assessment of avalanche release probability in the selected potential release areas, disregarding mitigation measures

Release area	NW, upper (10)	NW, lower (11)	NW, both (10+11)	N, upper (20)	N, lower (21)	N, both (20+21)	S (3)
Dry-snow avalanches all path	Occasional	Rare	Very rare	Occasional	Rare	Very rare	Very rare
Transition dry-to-wet	Frequent	Occasional	Rarely	Frequent	Occasionally	Rare	Occasional
Wet-snow avalanches all path	Occasional	Frequent	Occasional	Occasional	Frequent	Occasional	Frequent

Not having surveyed the site and lacking information about the frequency of avalanche release in the catchment, estimating the return periods of different types of avalanches from the PRAs under consideration is guess-work. Only for illustration purposes, we indicate the following estimates: Frequent – $T = 0.5$–10 y, Occasional – $T = 10$–30 y, Rare – 30–100 y, Very rare – $T > 100$ y.

2.3 Effect of mitigation measures on release probability

The terraces and snow bridges constructed in the upper reaches of the northern PRA and the afforestation in the north-western PRA influence both the release probability and size of avalanches. Terraces are expected to prevent the formation of continuous weak layers longer than the distance between successive terraces, at least until the terrace walls are snowed in completely. Assume the retaining walls are vertical, the slope angle before construction of the terraces was ψ and now is $\phi < 30°$ on each terrace, and the horizontal distance is L. Then the height of the retaining walls is $H = L(\tan \psi - \tan \phi)$. Under the optimistic assumption that small slides or cornices from one terrace falling over the wall will not trigger a chain reaction of slides on the terraces below, the terraces will prevent avalanche release from their area up to a snow depth $h_{\max} = L \cdot (\tan \psi - \tan \phi)/2$. This estimate might be reasonable for low to moderate values of L, but for $L \gg 10$ m, a criterion like $h_{max} = L \cdot (\tan \chi - \tan \phi)/2$ with $\chi \sim 30$–$35°$ might be more realistic.

In the case of (almost) uninterrupted lines of steel bridges or nets spaced according to the established guidelines, the probability of avalanche release should be reduced by one to two orders of magnitude or more if the snow depth does not exceed the height of the structures. If it does, the fracture depth should be limited to the excess snow depth in most cases. If an avalanche is released from within the support structures, it may trigger the area below if the snow cover there is close to releasing, or the flowing avalanche may entrain significant amounts of new snow.

Fully developed non-deciduous forest stretching to near the crest in the afforestation zone will affect the avalanche hazard in several ways:

- The tree trunks tend to stabilize the snow cover.
- The formation of continuous weak layers is strongly inhibited if the stand is dense enough.
- Snow blowing over the crest is intercepted and deposited in more gently sloped terrain where avalanche release is not to be expected.
- Due to higher temperature in the forest stand and snow compactification by intercepted snow falling from the branches in small quantities, the snow-cover strength may be higher than in the free field, making avalanche release less likely.

The effectiveness of protection will, however, depend on the local topography, the present weather and snow conditions, and the state of the forest stand (density and age). Our tentative assessment of the release probabilities in the different PRAs with mitigation measures are listed in Table 2. While the trees in the afforestation area are growing up, the tripods protecting them will have a significantly smaller stabilizing effect than the final forest, mostly because of the absence of a snow-intercepting canopy, but also because of the larger distance between the tripods in deep snow packs.

Table 2. Qualitative assessment of avalanche release probability in the selected potential release areas, including mitigation measures: completed afforestation project in the upper north-western PRA, existing support structures and terraces in the upper northern PRA, no mitigation measures in the southern PRA

Release area	NW, upper (10)	NW, lower (11)	NW, both (10+11)	N, upper (20)	N, lower (21)	N, both (20+21)	S (3)
Dry-snow avalanches all path	Very rare	Rare	Very rare	Rare	Rare	Very rare	Rare
Transition dry-to-wet	Very rare	Occa-sional	Very rare	Occa-sional	Occa-sional	Rare	Occa-sional
Wet-snow avalanches all path	Rare	Fre-quent	Very rare	Occa-sional	Fre-quent	Rare	Fre-quent

2.4   Choice of model for run-out calculations

There are a multitude of depth-averaged 2D run-out models for snow avalanches available, among them RAMMS::AVALANCHE (Christen, et al., 2010), SAMOS-AT (Granig, et al., 2009) and Titan2D (Pitman, et al., 2003). In the present work, the code MoT-Voellmy, developed at NGI, has been used. It is also a depth-averaged 2D model implementing the Voellmy friction law, the parameters of which may be specified globally or vary across the path. The model accounts for the braking effect of forest in a controlled and physically meaningful way using information about the spatial distribution of the average number and breast-height diameter of trees in the path (furnished in raster files) and "removes" them once the bending moment exerted by the flow exceeds the bending strength. Furthermore, MoT-Voellmy features a physics-based entrainment

model depending only on the snow-cover strength and the flow variables, without empirical parameters. For further details, see Appendix A.

The simulations were run on a digital terrain model (DTM) forming a regular grid with resolution $\Delta X = \Delta Y = 5.0$ m, constructed from LiDAR data processed to a resolution of 1.0 m, spanning 1300 m from West to East and 2000 m from North to South (104,000 cells). The terrain rises from 1100 m a.s.l. on the valley floor to almost 2200 m a.s.l.

2.5   Initial conditions

Considering the scarcity of data, the fracture depths (measured perpendicular to the terrain) indicated in Table 3 were used in the simulations.

Table 3. Fracture depths d_0 used in run-out simulations

Release area	NW upper (10)	NW lower (11)	NW both (10+11)	N upper (20)	N lower (21)	N both (20+21)	S (3)
Without mitigation measures							
Frequent	0.5 m	0.5 m	—	0.5 m	0.5 m	—	0.3 m
Occasional	0.7 m	0.7 m	0.7/0.7 m	0.7 m	0.7 m	0.7 m	0.5 m
Rare	1.0 m	1.0 m	1.0 m	1.0 m	1.0 m	1.0 m	0.7 m
Very rare	1.5 m	1.3 m	2.0/1.0 m	1.5 m	1.3 m	2.0/1.0 m	1.0 m
With fully developed mitigation measures							
Frequent	—	—	—	—	—	—	—
Occasional	—	—	—	—	—	—	—
Rare	0.7 m	—	—	0.5 m	—	0.3/1.0 m	—
Very rare	1.0 m	—	0.5/1.5 m	0.7 m	—	0.5/1.5 m	—

An alternative would be to apply the method outlined in the Swiss guidelines (Salm, et al., 1990) for estimating the initial conditions for avalanches with long return periods (typically T = 30–300 years):

- ⌐ Terrain with an inclination 28–30° < θ < 50° is considered potential release area (PRA). The Swiss guidelines do not account for the empirical fact that the size of the actual release area increases with the return period T. In Norwegian practice, the upper limit is usually set to 55° or 60°.
- ⌐ It is assumed that the extreme-value distribution of the 3-days new snow depth, HN_{3d}, as a function of T, is directly related to the fracture depth, $d_0(T)$.
- ⌐ If $HN_{3d}(T)$ is approximately known (measured or interpolated) at an altitude Z_{ref} different from Z at the PRA to be assessed, an altitude gradient $\lambda = 0.05$ m/100 m $= 5 \times 10^{-4}$ is applied.
- ⌐ Depending on the degree of wind exposition of the PRA, $HN_{3d}(T)$ may be increased by $\Delta HN_{3d,w} = 0.35$–0.6 m.
- ⌐ An inclination factor $f(\theta) = \dfrac{0.291}{\sin\theta - 0.202\cos\theta}$ is finally applied to account for the shear stress increasing with inclination θ.

These prescriptions can be summarized in the formula

$$d_0(T) = \left[\text{HN}_{3d}(Z_{\text{ref}}, T) + \lambda \cdot (Z_{\text{PRA}} - Z_{\text{ref}}) + \Delta\text{HN}_{3d,w}\right] \cdot f(\theta). \qquad (1)$$

This approach has not been adopted here because it assumes that only the new snow (from the past three days) releases, excluding the possibility that a buried weak layer fails when the overload becomes too large. In this way, the real fracture depth tends to be underestimated. This is implicitly compensated by the traditional calibration of the friction parameters (SLF, 1999), but for reasons explained in Secs. 2.6 and 4.1 a different calibration is used here (Gauer, 2020).

For simulations with entrainment, raster files congruent with the DTM were constructed for the depth (b_0) and shear strength (τ_c) of the erodible snow cover. To capture the altitude dependence of the new-snow depth and the temperature and density dependence of the snow-cover shear strength, these quantities were made to depend on the altitude Z according to the formulas

$$
\begin{aligned}
b_0(Z) &= \left\{ \begin{matrix} 0 \\ 0.5 \end{matrix} \right\} \text{ m} + 0.0005 \text{ m}^{-1} \cdot Z, \\
\tau_c(Z) &= \left\{ \begin{matrix} 1000 \\ 875 \end{matrix} \right\} \text{ Pa} - 0.25 \text{ Pa m}^{-1} \cdot Z,
\end{aligned}
\qquad (2)
$$

with the upper value for $\tau_c(Z = 0)$ intended for frequent to occasional situations and the lower one for rare or very rare conditions.

2.6   Friction parameters

Voellmy-type models do not describe the complex transitions between different flow regimes. Consequently, their friction parameters μ and k are not material parameters that can be measured in the laboratory or derived from measurements of the snow-cover properties. Instead, they must be calibrated from measurements of real avalanche events. Their values depend on a multitude of factors like return period of the event to be simulated, the avalanche size, topographical properties of the avalanche path like degree of channelization and surface roughness, and the snow-cover properties at release time.

Traditionally, calibration of avalanche run-out models has focused on run-out distances because this is the main observable (Buser & Frutiger, 1980; SLF, 2017). With this calibration, μ-values typically are in the range 0.15–0.35, and k-values in the range 0.004–0.02. In avalanches whose speed also was measured (Salm & Gubler, 1985), the simulated speeds were too low, especially for large avalanches. McClung and Gauer (2018) have presented experimental evidence from a large variety of sources for the maximum avalanche speed to scale as the square of the total drop height. This observation points towards small values of k, i.e., a predominantly Coulomb-frictional behavior. As pointed out by Gauer (2020), the experimentally observed velocity profiles along the path are well reproduced by a friction law like pure Coulomb friction with a coefficient $\mu = 0.25$–0.35 and an additional, velocity-dependent, retardation due to snow entrainment. Based on these considerations, simulations were run with a set of constant friction-coefficient pairs (μ, k) as indicated in Table 4.

For additional studies, spatially variable friction coefficients $\mu(\boldsymbol{x})$ and $k(\boldsymbol{x})$ were also set up as raster files. As with the snow-cover depth and shear strength, the climate dependence of the friction parameters was approximated by applying an altitude gradient:

$$\mu(Z) = \left\{ \begin{matrix} 0.5 \\ 0.4 \end{matrix} \right\} - 1.0 \cdot 10^{-4} \text{ m}^{-1},$$

$$k(Z) = \left\{ \begin{matrix} 0.004 \\ 0.003 \end{matrix} \right\} - 1.0 \cdot 10^{-6} \text{ m}^{-1}.$$

(3)

In the Midaou path, these formulas give $0.39\ (0.29) > \mu > 0.28\ (0.18)$ for the dry friction, and $0.0029\ (0.0019) > k > 0.0018\ (0.0008)$ for the "turbulent" friction. The higher limits refer to the valley bottom and the lower ones to the ridge. In the braces, the larger values are assumed appropriate for events with a return period in the range 30–100 years, the smaller ones for return periods larger than 100 years.

Table 4. Indicative friction coefficients for different avalanche types in the Midaou path, for "frequent", "occasional", "rare" and "very rare" events. Only shaded values were used here

Event type	Return period	No erosion		With erosion		
		μ	k	μ	k	τ_c (Pa)
Mixed dry-snow avalanche	"Frequent"	0.35	0.008	0.35	0.003	450–725
	"Occasional"	0.30	0.007	0.32	0.002	450–725
	"Rare"	0.25	0.006	0.30	0.001	325–600
	"Very rare"	0.27	0.005	0.28	0.001	325–600
Wet-snow avalanche	"Frequent"	0.40	0.030	0.40	0.015	?
	"Occasional"	0.35	0.025	0.35	0.012	?
	"Rare", "very rare"	0.30	0.020	0.30	0.010	?

3 Simulation results

3.1 General features of the simulated avalanches

A characteristic feature of the Midaou path are the wide, bowl-shaped release areas that are progressively funneled into 20–30 m deep gullies. An immediate consequence of this topography is that avalanches get completely channelized unless they are very large and fast and that the flow depth in the gully may exceed the fracture depth by a factor of 10 or more.

3.2 Avalanches without mitigation measures

If there were no terraces, steel bridges or nets and no forest near the north-western crest, avalanches would most often release from the upper parts of the total PRAs because of wind-loading. An exception may occur in spring with wet-snow avalanches releasing first at lower altitudes. Under exceptional ("very rare") conditions, there may be releases comprising both the upper and lower parts of the PRAs, albeit with a lesser fracture depth away from the crest.

The following figures present simulation results corresponding to "frequent", "occasional", "rare" and "very rare" events. They are to be compared with simulations that attempt to mimic the situation with the existing and planned mitigation measures, shown in Section 3.3. As dry-snow avalanches pose a larger threat to Barèges than wet-snow avalanches, no attempt has been made here to simulate them.

The simulations in Figure 2 show that relatively small avalanches starting near the crestline with a fracture depth of 0.5 m can reach the valley floor and—in the case of avalanches from the northern release area—even cross the river if there are no mitigation measures. It is conceivable that the friction parameter values used in these simulations are too pessimistic for this site or that the return period of avalanches of this size is of the order of 30 y rather than the tentative estimate of 10 y.

The avalanche from the area N 20 fills the deep gully and even spills over in the bends. The mass of the avalanche from area NW 10 is smaller; it follows the gully bends essentially without spilling over. A fraction of the mass follows a smaller ravine almost to the valley floor. A real avalanche would likely stop earlier due to increased friction along the gully sides.
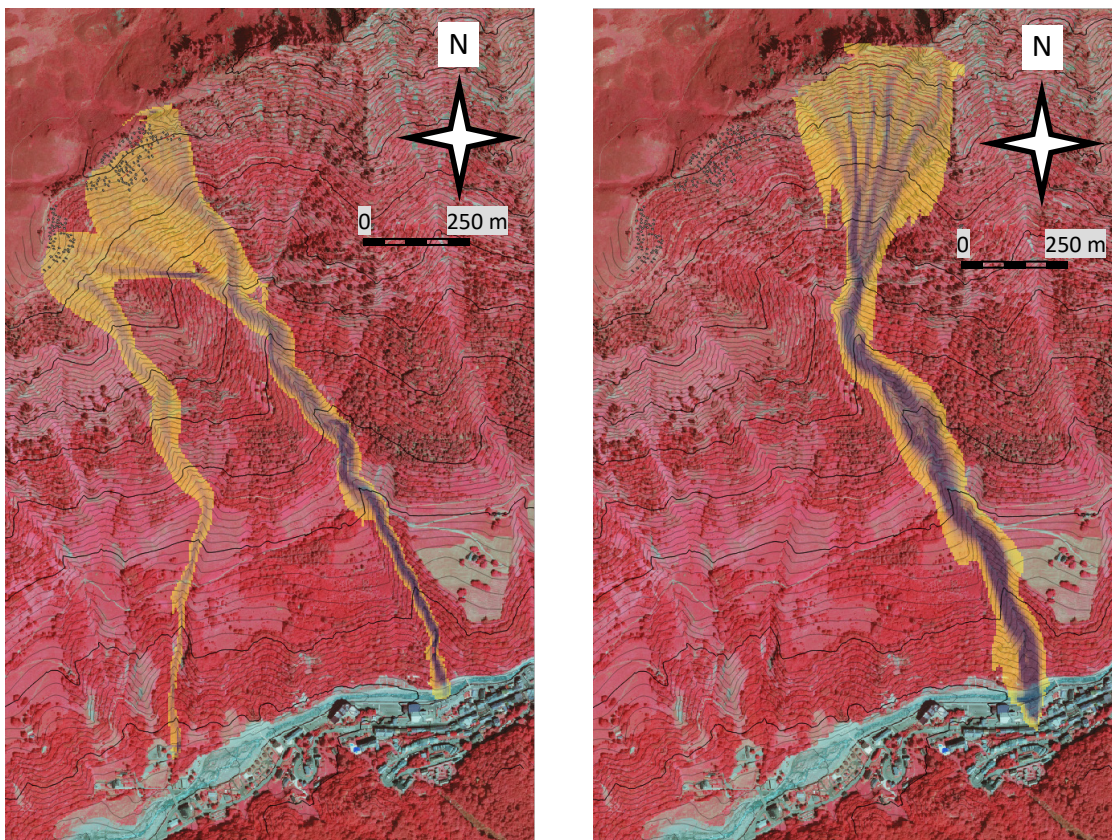

Figure 2. Simulated "frequent" avalanches from the north-western (NW 10, left panel) and northern (N 20, right panel). Assumed release depth 0.5 m, constant friction coefficients μ = 0.35, k = 0.003, entrainment enabled
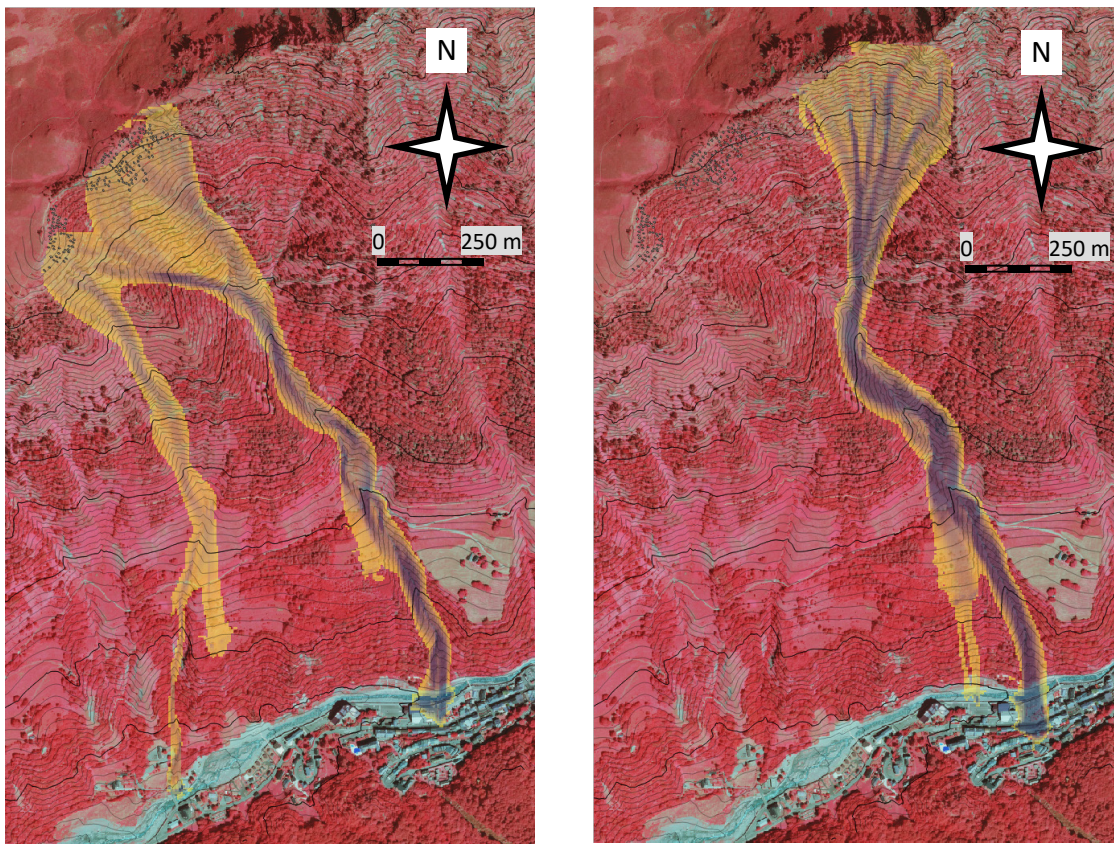
Figure 3. Simulated "occasional" avalanches from the north-western (NW 10, left panel) and northern (N 20, right panel). Assumed release depth 0.7 m, constant friction coefficients μ = 0.32, k = 0.002, entrainment enabled

The selected initial conditions for "occasional" avalanches (Figure 3) provide a 40% larger initial mass, and the friction is reduced by about 10%. The main branch of the avalanche from area NW 10 (left panel) advances farther, crosses the river and reaches the main street. The effect is, however, moderated by the mass loss due to spill-over of the front at a bend at about 1400 m a.s.l. The front is the fastest part of the avalanche and thus the first to overflow the embankment in a sharp bend. In this case, the over-flowing mass had low velocity after climbing up the embankment and stopped after a short distance. A similar effect is observed in the western branch of the W 10 avalanche, at a similar altitude. The mass remaining in the narrow channel advances only a short distance beyond the stopping point of the "frequent" avalanche.

A part of the avalanche from N 20 (Figure 3, right panel) leaves the gully at the same bend as the eastern branch of NW 10 but has more kinetic energy and so traverses the more gently inclined terrain beneath the bend. About 100 m above the valley floor, the slope becomes steeper again, allowing also this branch to reach the river.
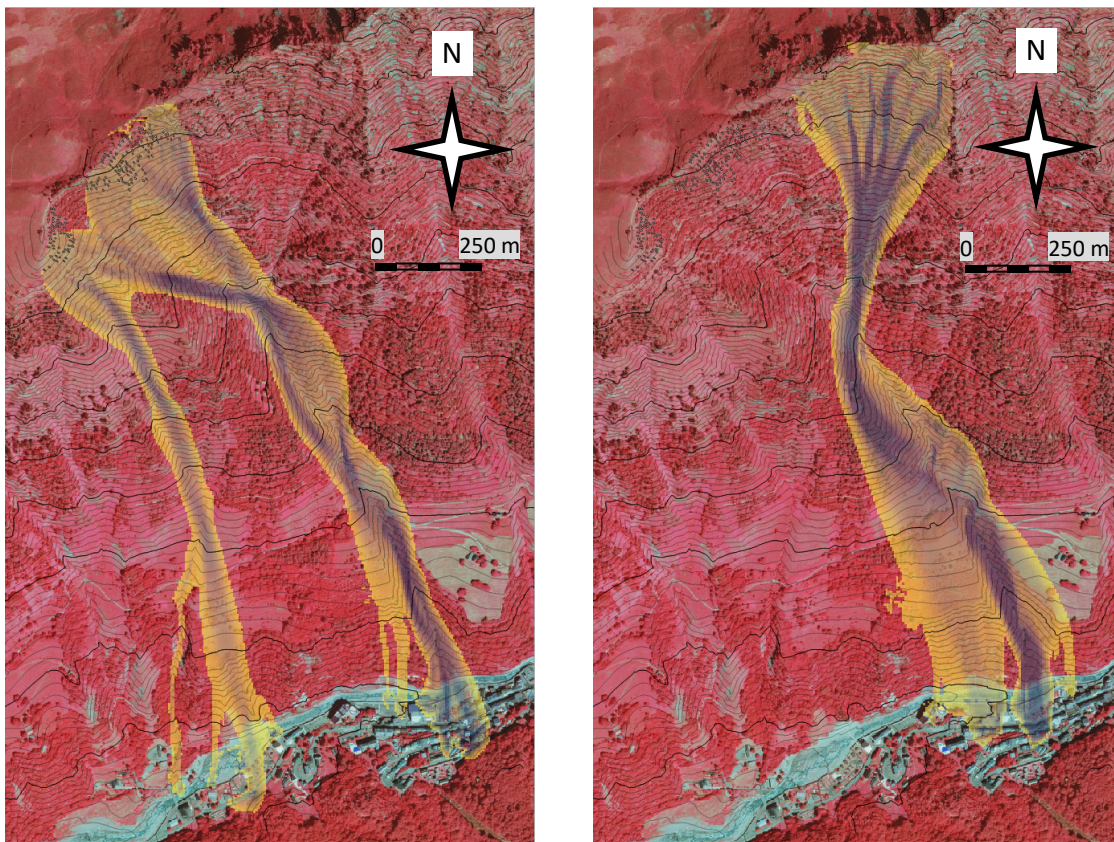
Figure 4. Simulated "rare" avalanches from the north-western (NW 10, left panel) and northern (N 20, right panel). Assumed release depth 1.0 m, constant friction coefficients μ = 0.30, k = 0.001, entrainment enabled

Both simulated "rare" avalanches would inflict severe damage on Barèges, but in different areas of the village. Under the assumed conditions, most of the mass of the minor branch of the NW 10 avalanche leaves the ravine at 1400 m a.s.l. and hits the western part of Barèges. The main branch creates a deep deposit in the eastern part of the village and climbs the counter-slope about 30 m.

Complex flow patterns develop in the main, eastern, branch (Figure 4, left panel): Snow from the southern part of NW 10 is funnelled into a ravine going almost due East before it reaches the main gully at 1650 m a.s.l. Much of the mass is too fast to follow the topography in the sharp 45° turn; at first, it continues almost horizontally on the north-eastern face of the gully, then gradually turns in a southern direction and reaches the main gully at 1400 m a.s.l. at an angle of 20–30°. The collision with snow flowing down the main gully causes mass to spill over the western embankment and to flow on the open slope down to the river. The mass staying in the main gully fills it to a large degree. At 1250 m a.s.l. two new branches are created—one following the main gully and turning to the south, and another spilling over the eastern gully flank and continuing in south-south-westerly direction. Both branches cross the village and ascend about 20 m on the counter-slope.

Analogous spill-over effects characterize the avalanche from the upper northern release area N 20 (Figure 4, right panel): At 1600 m a.s.l., only the slow tail follows the gully in a sharp 45° turn to a south-easterly direction. Much of the mass continues southwards; some of it is gradually pulled towards the main gully while a fraction passes a marked terrain shoulder and descends the open slope in south-south-easterly direction some 200 m east of the gully. It crosses the river and stops in the village; the deposit is about 200 m wide but shallower than the main deposit.

The latter is predicted to exceed 10 m in depth and to reach well beyond the main street. The damage from it is only limited because there are few houses in the area facing the main torrent of Midaou.
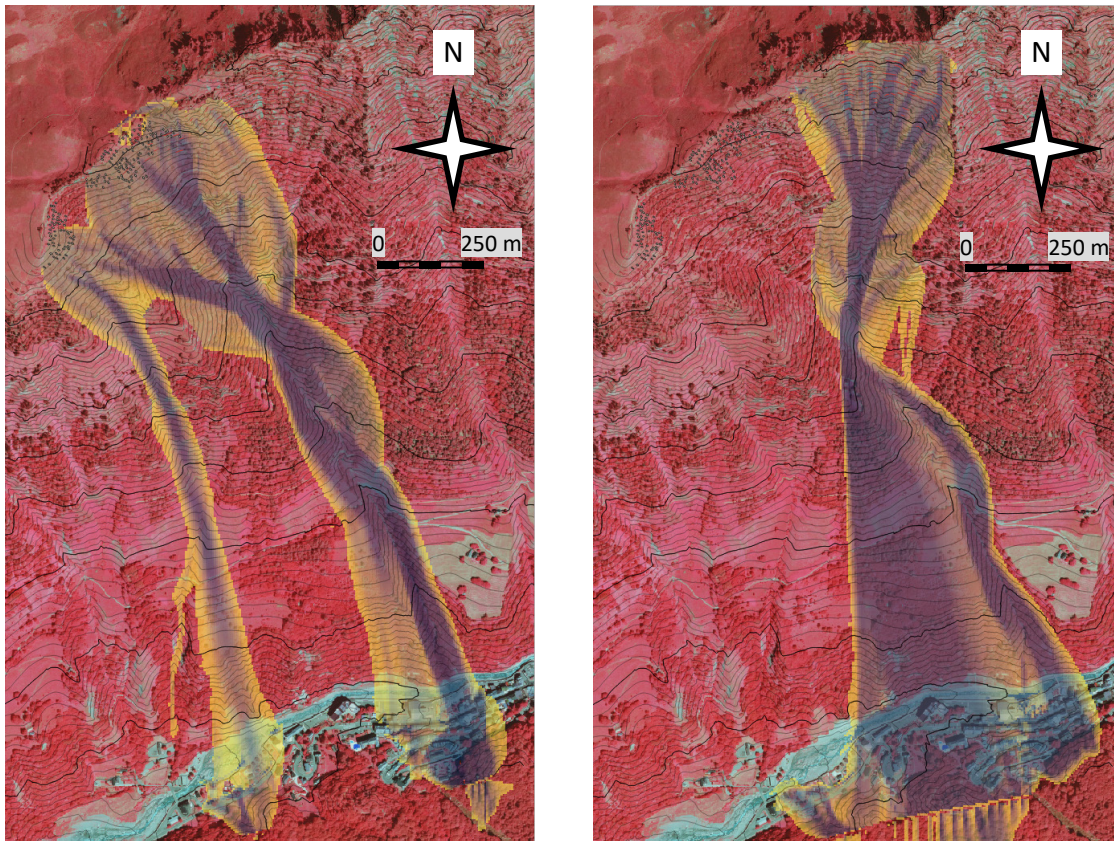

Figure 5. Simulated "very rare" avalanches from the north-western (NW 10+11, left panel) and northern (N 20+21, right panel) release areas. Assumed release depth 2.0 m in NW 10 and N 20, 1.0 m in NW 11 and N 21. Constant friction coefficients μ = 0.28, k = 0.001, entrainment enabled. The stripes at the lower edge are artifacts from the digital terrain model (no data in the lower right corner)

For "very rare" events with the upper and lower parts of the PRAs releasing simultaneously (NW 10+11, Figure 5, left panel or N 20+21, right panel), the tendencies observed in "rare" avalanches are even more pronounced: Snow from the south-westernmost part of PRA NW 10+11 almost completely leaves the ravine at the bend at 1400 m a.s.l. and

descends at high speed in a straight line, ascending about 50 m on the counter-slope. The relatively few houses in its deposit area would likely sustain severe damage. The main branch spills over the Midaou gully due to its large mass and covers a substantial part of Barèges in a very deep deposit. Its head ascends far on the counter-slope, crossing the boundary of the terrain model.

With the made assumptions about release mass and friction parameters, the avalanche from the northern PRA N 20+21 becomes so large and fast that its main component leaves the gully at the sharp bend at 1600 m a.s.l. and descends in a straight southern line over the open slope, covering most of Barèges. There is a curious prediction that the western fringe of the avalanche ascends along the eastern side of a pronounced terrain shoulder (visible in the middle of the lower border of the maps) into quite steep terrain. There, it does not stop but flows downhill along the western side of the shoulder and hits the westernmost part of Barèges from the south. Due to the limitations of the terrain model and the Voellmy model, it is difficult to assess whether this behavior is realistic or not. However, such a flow pattern has been observed at least in one instance in Switzerland during the severe 1999 winter (Teufen, 2005).

3.3   Avalanches in the presence of mitigation measures

One may expect that the mitigation measures can cope with "frequent", "occasional" and hopefully also "rare" avalanche situations so that avalanches release only from the areas NW 11, N 21, and S 3. The case of S 3 will be considered separately in Sec. 3.4.

The simulations shown in Figure 6 suggest that avalanche events with return periods up to about 100 y should not pose a major threat to Barèges. However, the avalanche from area NW 11 stops only at the river, slightly lower friction coefficients or a larger fracture depth would mean that it reaches the northernmost buildings of Barèges. Interestingly, the avalanche from N 21 runs about 200 m shorter.

Both avalanches become completely channeled in the deep and narrow gully not far from the stauchwall. This is important because they cannot entrain large amounts of snow in the gully. However, the simulated flow depths exceed 10 m in both cases. A large deposit in the river may block it and cause problems in the spring.

The release area of "very rare" avalanches situations may comprise the upper areas NW 10 or N 20 as well, albeit with moderate fracture depths only. The simulations shown in Figure 7 were run with the same friction coefficients as those in Figure 6, only the release area and the mean fracture depth are significantly larger. These simulations should therefore be considered "optimistic" from the point of view of the inhabitants of Barèges. The avalanche from the NW area crosses the river and the main street of the village; it would cause significant damage. The avalanche essentially is contained by the gully but fills it bank-full and overflows a little at one bend.
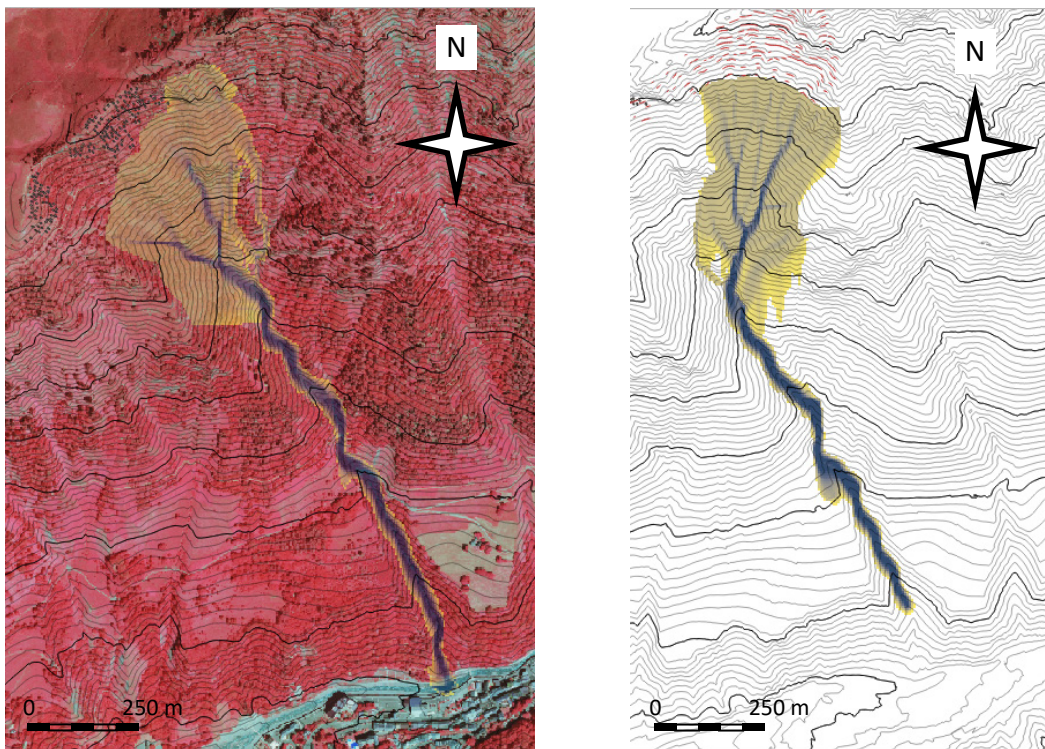
Figure 6. Simulated run-out of "rare" avalanches in the presence of mitigation measures, released from the lower parts of the western (left panel) and northern (right panel) release areas. The fracture depth was 1.0 m in both cases, the friction coefficients were set to μ = 0.30 and k = 0.001, and erosion enabled. Without the false-color orthophoto as background, the existing defense structures in N 20 are readily seen (right panel)

Surprisingly, the situation is completely different for the avalanche from the northern area: Its front attains a speed exceeding 60 m s^{-1} at the 60° bend at 1700 m a.s.l., which has a curvature radius of only about 100 m. A large fraction of its mass overflows the outer bank and descends over the open slope to the west of the gully. There, it can entrain much more mass because of its greatly increased width. It crosses (and dams) the river over a length of some 300 m, continues for about 200 m across Barèges and climbs about 40 m up the counter-slope. Similar behavior is observed by simulating the NW avalanche with the friction coefficient reduced by only 0.01 to μ = 0.27.

This simulation should not be dismissed as unrealistic: Avalanches of this size and devastating effect have been released artificially at several test sites, e.g. at Vallée de la Sionne in Switzerland, Ryggfonn in Norway and Shiai-dani in Japan. Moreover, spontaneously released avalanches of comparable or larger size, with a large powder-snow cloud component, have repeatedly occurred in the Pyrenees, e.g. at Àrreu in 1803 (Oller, et al., 2020) and at Arinsal in 1996 (Furdada, et al., 2020).
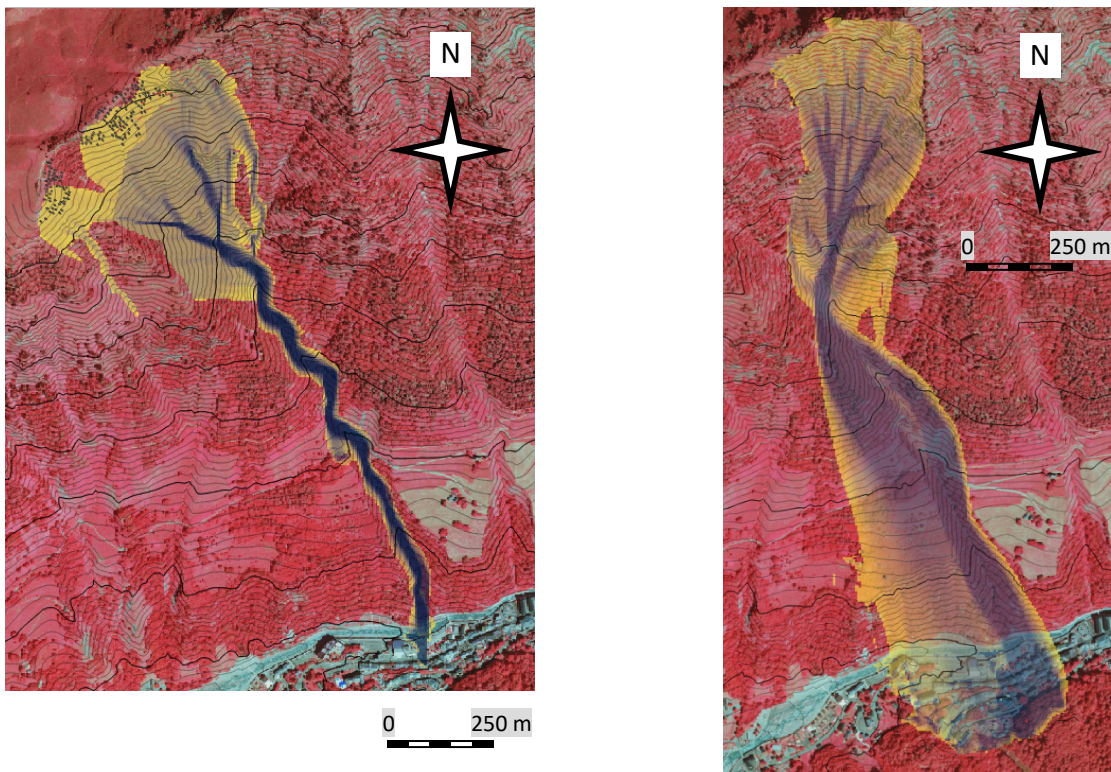
Figure 7. Simulated run-out of "very rare" avalanches from the north-western (NW 10+11, left panel) and northern (N 20+21, right panel) release areas, accounting for the existing and planned mitigation measures. In both cases, a fracture depth of 0.5 m was assumed in the up-per, mitigated parts NW 10 and N 20, whereas $d_0 = 1.5$ m was used in the lower parts NW 11 and N 21. The friction parameters were set to constant values of $\mu = 0.30$ and $k = 0.001$; en-trainment was enabled

3.4 Avalanches unaffected by mitigation measures

As the most relevant example of avalanches releasing from areas not influenced by the existing or planned mitigation measures, dry-snow avalanches originating in the south-ern PRA S 3 are simulated with fracture depths of 0.7 m (corresponding to "occasional" or "rare" avalanches) and 1.0 m (very rare avalanches). The results for the maximum flow/deposition depth are shown in Figure 2. For occasional avalanches, friction coeffi-cients varying with altitude in the range 0.3–0.4 according to Eq. (3) and the larger val-ues of shear strength in Eq. (2) were used, whereas the "very rare" avalanche was simu-lated with $\mu = 0.3$ (rather than 0.28, accounting for the lower altitude), $k = 0.001$ and the lower shear-strength values in Eq. (2).

Somewhat surprisingly, the lower release mass and the increased friction do not allow the "frequent" and "occasional" avalanches to accelerate to high speed before they enter the main gully of Midaou. For this reason, they do not spill over the western gully side. The gully is relatively gently inclined from 1600 to 1300 m a.s.l., so that the "frequent" avalanche stops at altitude 1400 m a.s.l while the "occasional" event continues to 1300 m a.s.l., still at a safe distance from Barèges.
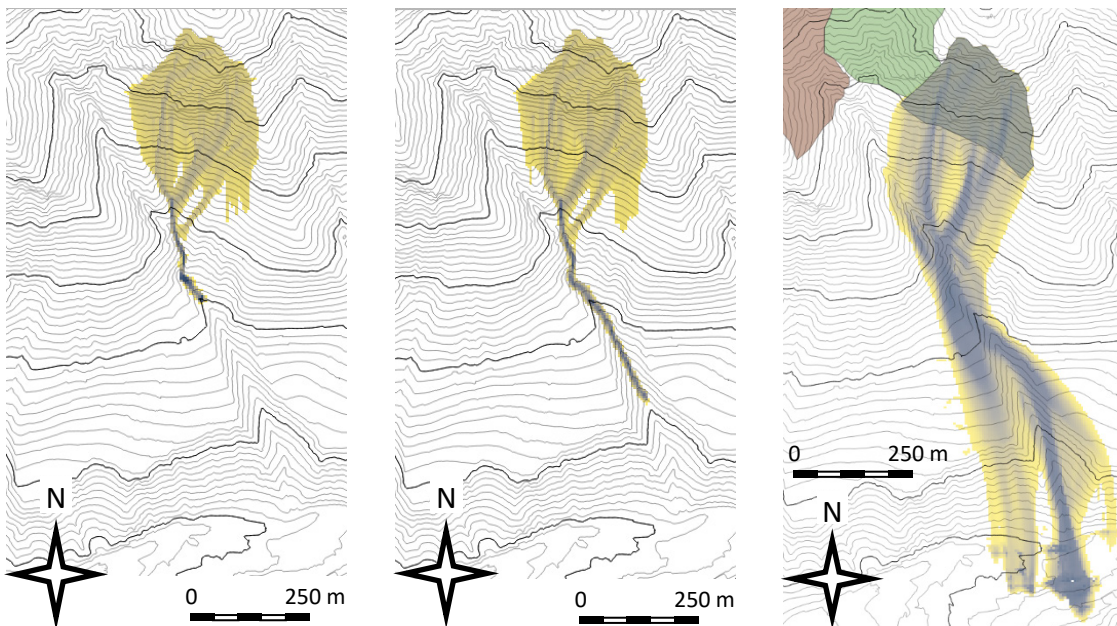
Figure 8. Maximum flow depth of "frequent" (left panel), "occasional" (middle panel) and "very rare" avalanches (right panel) from release area S 3. For "frequent" and "occasional" avalanches, a fracture depth of 0.7 m was assumed while 1.0 m was assumed for the "very rare" case. The maximum flow/deposit depth exceeds 10 m in the gully and—for the extreme case—even on the counter-slope due to massive entrainment

For a meaningful assessment of the effectiveness of the "gray" and "green" mitigation measures, one must also consider the remaining avalanche hazard from other release areas in the Midaou catchment. As the most representative PRA not affected by the mitigation measures, the PRA S 3 has been simulated. For initial conditions of "frequent" and "occasional" avalanches (Figure 8, left and middle panel, respectively) surprisingly short run-out distances were obtained. The Midaou gully contains such avalanches because they do not reach very high speeds when they enter the main gully. These findings are consistent with the fact that Barèges is not frequently hit by avalanches.

A completely different picture arises for "very rare" avalanche events from S 3 (Figure 8, right panel): A substantially larger initial mass and lower friction lead to large flow depths and high speeds. A substantial fraction of the avalanche mass crosses the Midaou gully and descends on the open slope to the east of the gully. Its mass and speed allow it to cross the river, traverse Barèges completely, 50–100 m wide, and ascend about 20 m on the counter-slope. The flow in the main gully is even more devastating, advancing considerable farther and higher up, with a deep deposit. In addition, a minor branch spills over the eastern sidewall of the gully and descends to the river. Altogether, this avalanche has a destructive effect that is comparable to "very rare" events originating in the north-western and northern release areas in the presence of mitigation measures.

4 Discussion and conclusions

When trying to quantify the effectiveness and cost–benefit ratio of the NBS, several aspects must be considered: First, the simulations presented in Sec. 3 are fraught with large uncertainties that must be reflected appropriately in the estimate of the risk reduction achieved by mitigation measures. This point will be discussed in Sec. 4.1. Second, the pre-dating "gray" mitigation measures reduce the risk considerably on their own and thus diminish the benefit from the NBS in absolute numbers. (Strictly speaking, this inference is also uncertain because it is not precisely known whether an equally severe avalanche situation has arisen in the surroundings of Barèges since the event in 1907 that led to the construction of the terraces and supporting structures.) Moreover, the mitigation measures were presumably constructed where the release probability was considered highest. Thus, the afforestation area (NBS) in the north-western part of the PRA has *a priori* a lower effectiveness in terms of damage reduction than if it had been placed in the northern area instead of the "gray" mitigation measures. As this question is mostly of economic interest, it will not be dealt with further in the report.

4.1 Uncertainties in the avalanche simulations

Visualizations of avalanche simulations have an enormous (subliminal) persuasive power, especially if they use judiciously chosen colors. It is all the more important to critically discuss, and constantly be aware of, the large uncertainties involved in such calculations. They arise from (i) our insufficient knowledge of the initial conditions as a function of the return period, (ii) uncertainty in the choice of the friction coefficients, and (iii) the shortcomings of the flow model.

Uncertainties in the initial conditions

The choice of *release areas* is largely dictated by the topography and to some degree by the local wind conditions. The uncertainty in the maximum possible extent of the release area is not too large, but frequent and occasional avalanches will release only from smaller areas within the PRAs. Taking the entire areas NW 11, N 21 and S 3 is likely to overestimate the volume and run-out distance of avalanches with return periods below 100 y (provided the estimated fracture depth is close to its true value and the model together with the chosen friction parameters is trustworthy).

The *fracture depth for a given return period*, $d_0(T)$, is fraught with a very large uncertainty in this particular case, perhaps as much as $^{+50\%}_{-30\%}$. This uncertainty is a major source of uncertainty in the run-out distance. It could be reduced through a detailed analysis of all existing nivo-meteorological data, including interpolation from the closest weather stations to the study area. However, even if the statistics of snow depth and snowfall height are well known, assumptions are necessary about the location of the weak layer along which the fracture occurs. In a south-facing slope in the Pyrenees, solar radiation will in many cases only allow the interface between old and new snow to fracture, but in some cases buried weak layers may nevertheless survive until the next major snowfall, potentially leading to large fracture depths.

There is little doubt that blowing snow is a major factor in this catchment. The Swiss guidelines (Salm, et al., 1990) recommend increasing the new-snow depth extrapolated from meteorological stations by 0.3–0.5 m (as an average over the entire release area) if the release area is in the lee of the predominant wind direction. Experience from Norway suggests that even more should be added in particularly exposed areas. When it comes to "very rare" avalanches, the uncertainty becomes even larger because the wind conditions before the release and under the snow storm likely are extraordinary. In such cases, it cannot be excluded that the avalanche release areas extend into the forest or into the snow-covered terraces or supporting structures.

Without first-hand knowledge of the site and the general winter conditions in an unfamiliar mountain range, it was decided to assume different values of d_0 ranging from relatively small to large and not to assign definite return periods to them. One may attempt to attach a quantitative meaning to the vague terms "frequent", "occasional", "rare" and "very rare" *a posteriori* by comparing the simulation results to records of historical avalanches, if they exist.

Uncertainties due to shortcomings of the model

Voellmy-type models are presently used almost universally for avalanche run-out calculations, but they have important shortcomings that users must keep in mind when interpreting the simulation results. The key weaknesses are the following:

- They describe only the dense-flow regime, but it is well known from observations and experiments that there are the suspension flow regime (the "powder-snow cloud") of low density and an intermediate-density regime, variably termed "light-flow", "saltation layer", "intermittency regime" or "fluidized flow". The Voellmy-type models cannot describe suspension flow at all, but in the case of large avalanches (and likely also in the Midaou path) this component may become strong and cause extensive damage due to its very long run-out and its capacity to climb high up on the counter-slope. By tweaking the friction parameters, the run-out and high speed of the fluidized flow can be approximately captured by the model, but the distribution of deposited mass will differ significantly from reality, and pressures in the distal area are either overestimated by a factor of roughly 3 or underestimated in the area reached by the dense flow.

- The Voellmy friction law Eq. (8)—specifically, the dependence on the square of the speed—is known to be inadequate for avalanche flow. The main reason for this discrepancy is that the flowing snow expands with increasing speed, which leads to a much milder growth of the shear stress with the flow velocity. Therefore, Voellmy-type models tend to underestimate the velocity of large avalanches if the most popular calibration of friction parameters (SLF, 2017) is used. Too low flow speeds can lead to serious errors even in the avalanche trajectory if there are sharp bends where a sufficiently rapid flow can leave the gully. This is indeed the case at several locations in the Midaou path. The simulations presented in Sec. 3 try to remedy this problem to some degree by choosing a calibration with larger values of μ and very low values of k.

⌐ The thermal and mechanical properties of the snow cover are known to have a profound impact on the behavior of snow avalanches, but the Voellmy-type models can account for these effects only indirectly if spatially variable values are prescribed for the friction parameters, with both μ and k increasing with snow-cover temperature.

Uncertainties in the friction parameters

The conventional calibration of Voellmy-type models (SLF, 2017) has been used and refined over several decades. With the recommended values, run-out distances are well predicted for large parts of the Alps, provided underestimation of the velocity does not lead to the flow choosing the wrong path. When the model is applied to avalanches in Norway, the implicit temperature dependence of the friction parameters (through an altitude dependence as a proxy) in (SLF, 2017) needs to be adjusted to account for the climate differences. Some adjustment would probably also be required when applying the model to the Pyrenees, adding to the uncertainty.

Due to the importance of simulating realistic velocities, the calibration with larger μ-values and lower k-values suggested by Gauer (2020) has been adopted in this study. It has the disadvantage that it is much less tested than the traditional one, and there are no specific recommendations yet as to the dependence of these values on the target return period, the avalanche size, the climatic conditions, and possibly the terrain features (degree of channelization). Moreover, entrainment is an intrinsic part of this approach, and one ought to have guidelines for choosing the shear strength of the snow (τ_c) as a function of return period and climatic conditions.

In the absence of such guidelines, a set of different values within a reasonable range have been used here. This leaves the question open which return periods these values correspond to, i.e., how "frequent", …, "very rare" can be made quantitative. If there were sufficiently many records of observed run-out distances, such a calibration would be possible. The recorded event of 1907 is probably closest to the "occasional" event of Figure 3, right panel if one assumes it released from N 20. Considering that the French National Forest Service has kept records for 120–150 y, one may be tempted to associate the "occasional" simulations with a return period around 100 y. However, the release probability was strongly reduced not long afterwards by the construction of terraces and later supporting structures. If one assumes that these mitigation measures were successful, the effective observation period for the northern release area is reduced to perhaps 50 y and one would estimate a return period of 30–50 y for that class of event, based on maximum likelihood under very scarce information. However, the effective observation period for the non-mitigated north-western PRA is indeed 120–150 y. However, this does not necessarily mean that the "occasional" friction parameters correspond to $T \gtrsim$ 100 y if the release probability itself is of the order of 0.01 y^{-1}. A detailed comparison of the two PRAs would be needed to arrive at more certain estimates.

4.2 The protective effect of the mitigation measures

Terraces and supporting structures in the northern PRA

Comparison of the right panels of Figs. 3, 4 and 6 suggests that the existing "gray" mitigation measures diminish the avalanche hazard in Barèges significantly: Under the made assumptions for initial conditions and friction parameters, even "frequent" avalanches cross the river without the mitigation measures whereas only "very rare" events will do so with the supporting structures in place. However, under those exceptional circumstances the damage in Barèges would still be devastating.

There are reasons to think that this conclusion may be too optimistic. First, situations where the retaining structures and terraces are completely covered by snow might occur more frequently than "very rarely". When this happens, the probability for an avalanche to be released is difficult to quantify reliably, but to judge from experiences during the winter 1999 in the Alps it is significant. Second, there seem to be many openings in the rows of defense structures, which also increase the release probability. Again, it si difficult to estimate the order-of-magnitude of this effect, and to the author's knowledge, there are no quantitative investigations of the effect of openings on release probability. Studies of avalanches released in forests suggest that the mitigative effect of forest stands sharply decreases if there are openings wider than about 10 m and longer than 20–30 m. In the case of retaining structures or terraces, where there is no interception effect from the tree canopy, the critical gap width might be smaller.

Afforestation in the north-western PRA

The benefit from afforestation in the upper north-western release area (Figs. 3 and 4 vs. Fig. 6, left panels) appears even larger. "Rare" and "very rare" avalanches events without forest are predicted to cause considerable/large damage in Barèges whereas the damage would be limited to a small area and probably not be severe under "very rare" avalanche events if the protective forest is present.

However, the following points must be considered in assessing the benefit for Barèges:

- Avalanches from the north-western release area appear to be a lesser threat to the village than those from the northern area. Thus, a satisfactory safety level is also contingent on effective mitigation of the northern area (see previous paragraph).
- The run-out distance (and the wrought damage) of avalanches from the north-western area is quite sensitive to the choice of friction parameters and/or the assumptions about the fracture depth. A moderate reduction of μ for "very rare" events will produce substantially more damage.

Nevertheless, afforestation appears to be an effective (and presumably also cost-effective) measure to reduce the avalanche risk in Barèges, provided effective mitigation of the northern area is assured. This finding suggests that afforestation at and near the crest of the northern area N 20—if feasible—would be an effective means to improve the over-all hazard situation: The probability of the defense structures to get covered by drifting snow would be reduced substantially, and perhaps even the problem of the gaps in the existing rows could be solved by planting groups of trees in these gaps.

Residual risk due to non-mitigated PRAs

Somewhat surprisingly, the run-out distance, area and deposited mass of avalanches originating in the low-lying south-eastern area S 3 appear to be very sensitive to the initial conditions and assumed friction parameter values (Figure 8). Neither does the assumed release depth of 1.0 m for a "very rare" event appear particularly large—even in the absence of blowing snow—nor is a value of $\mu = 0.30$ with $k = 0.001$ to be considered low. Under these circumstances, estimates of the hazard level are particularly uncertain. However, comparing area S 3 to N 21 or NW 11, it appears more likely that the run-out of "occasional" and "rare" avalanches from S 3 is underestimated than the one of "very rare" events being massively overestimated.

If this assessment is correct, one must conclude that there is a substantial residual risk due to these avalanches, which is not mitigated by any measures so far. If, furthermore, "rare" events have a return period of the order of 100–150 y and "very rare" events of about 300 y, sufficient safety of Barèges against snow avalanches according to the French regulations cannot be achieved without mitigation measures in the release area S 3. This concern disappears, however, if one were to conclude that "very rare" events as characterized here have a return period well above 300 y.

The simulation results indirectly show that afforestation in area S 3—provided it is feasible—would provide a significant reduction of the avalanche hazard because not only the probability of a release would be reduced by perhaps an order of magnitude, but also the probable release depth should be smaller, and/or the friction of the avalanche increased. A "very rare" event under such conditions would likely resemble a "rare" avalanche without mitigation measures and not reach Barèges.

Options for reducing the residual risk

From the discussion above, it results that there are three main sources of residual risk and that the total residual risk may be larger than the target laid down in the French legislation. The following brief discussion of different options for reducing the total risk must be considered tentative because of the large uncertainties in the estimates of residual risk from each PRA and the combined residual risk.

- ⅂ The simulations in Secs. 3.3 and 3.4 suggest that the largest risk contributions are from "very rare" events originating from the PRAs N 20+21 and S 3. Measures in PRA NW 10 and 11 would therefore not have highest priority.
- ⅂ The simulations from PRA N were carried out assuming that the terraces and supporting structures prevent almost all avalanche releases, provided these structures are not snowed in completely. This assumption is hard to justify if there are significant gaps in the rows or if the distances between rows exceeds the maximum recommended distance under the given terrain conditions. If any of these assumptions are not fulfilled, it will likely be best to concentrate the mitigation effort on PRA N 20 first.
- ⅂ If the mitigation measures in PRA N 20 are not up to today's standards, there are two options: (i) close the gaps or (ii) plant forest near the crest to reduce the amount of blowing snow. The first approach is the standard (and presumably

more expensive) one. It will improve the effectiveness of the measures under non-extreme snow conditions, but the probability of overfilling is not reduced. The second approach reduces the probability of overfilling without eliminating it; moreover, the probability of avalanches releasing from within the mitigation works is somewhat reduced but by no means eliminated. An important consideration is, however, whether the wind and soil conditions are conducive to afforestation or not.

⌐ PRA S 3 is at lower altitude and much less exposed to snow blowing over the crest. Both factors would seem to favor afforestation and perhaps also diminish its costs. Again, terrain and soil conditions need to be considered; also, this area is rather steep. Partial afforestation, starting from the upper end of the PRA, is also an option. Avalanches could still release from the lower parts, but they will have less mass and lower speed at the critical bend, greatly reducing their chance of damaging Barèges.

If additional mitigation measures are to be planned, refined numerical simulations will be useful, e.g., to estimate the expected shortening of run-out if trees are planted in PRA S 3 to different altitudes. Given the considerable investments of such mitigation, it would be recommendable to carry out a much more thorough investigation of the avalanche history of Barèges and of the nivo-meteorological conditions along the path. This would open for estimates of the return period of avalanches releasing in different parts of the catchment and narrow down the range of likely friction parameters. Research and development work will hopefully soon lead to a more constrained alternative calibration of Voellmy-type models and thus more reliable estimates of the run-out for different return periods.

Acknowledgements

References

Buser, O. & Frutiger, H., 1980. Observed maximum runout distance of snow avalanches and determination of the coefficients μ and ξ. *Journal of Glaciology,* 26(94), 121–130, DOI 10.3189/-s0022143000010662.

Christen, M., Kowalski, J. & Bartelt, P., 2010. RAMMS: Numerical simulation of dense snow avalanches in three-dimensional terrain. *Cold Regions Science and Technology,* **63**(1), 1–14, DOI 10.1016/-j.coldregions.2010.04.005.

Furdada, G. et al., 2020. The avalanche of Les Fonts d'Arinsal (Andorra): An example of a pure powder, dry snow avalanche. *Geosciences,* **10**(4), 126, DOI 10.3390/geosciences10040126.

Gauer, P., 2018. *Avalanche probability: slab release and the effect of forest cover. In: Proceedings of the* International Snow Science Workshop 2018, Innsbruck, Austria, 76–83. URL http://arc.lib.montana.edu/-snow-science/objects/ISSW2018_P01.13.pdf.

Gauer, P., 2020. Considerations on scaling behavior in avalanche flow: Implementation in a simple mass block model. *Cold Regions Science and Technology,* **180**, 103165, DOI 10.1016/j.coldregions.-2020.103165.

Granig, M., Sampl, P., Tollinger, C. & Jörg, P., 2009. *Experiences in avalanche assessment with the powder snow avalanche model SamosAT. In:* Proceedings of the International Snow Science Workshop 2009, Davos, Switzerland, p. 514–518. URL: https://arc.lib.montana.edu/snow-science/item/293.

Issler, D., 2020. The 2017 Rigopiano avalanche – dynamics inferred from field observations. *Geosci.,* **10**(11), 466, DOI 10.3390/geosciences10110466 .

Issler, D., Gleditsch Gisnås, K. & Domaas, U., 2020. *Approaches to including climate and forest effects in avalanche hazard indication maps in Norway.* Oslo, Norway:Norwegian Geotechnical Institute, NGI Technical Note 20150457-10-TN. URL https://www.nve.no/media/10589/20150457-10-tn.pdf.

Issler, D., Jónsson, Á., Gauer, P. & Domaas, U., 2016. *Vulnerability of houses and persons under avalanche impact – the avalanche at Longyearbyen on 2015-12-19. In:* Proceedings of the International Snow Science Workshop 2016, Breckenridge, Colorado. http://arc.lib.montana.edu/snow-science/-objects/ISSW16_O16.03.pdf

Lackinger, B., 1989. Supporting forces and stability of snow-slab avalanches: a parameter study. *Annals of Glaciology,* **13**, 140–145, DOI 10.1017/s0260305500007783.

McClung, D. M. & Gauer, P., 2018. Maximum frontal speeds, alpha angles and deposit volumes of flowing snow avalanches. *Cold Regions Science and Technology,* 153(1), p. 78–85, DOI 10.1016/-j.coldregions.2018.04.009.

Oller, P., Fischer, J.-T. & Muntán, E., 2020. Multidisciplinary approach to reconstruct the historic avalanche that destroyed the village of Àrreu in 1803, Catalan Pyrenees. *Geosciences,* **10**(5), 169, DOI 10.3390/geosciences10050169.

Pitman, E. B. et al., 2003. Computing granular avalanches and landslides. *Phys. Fluids,* **15**, 3638–3648, DOI 10.1063/1.1614253.

Salm, B., Burkard, A. & Gubler, H. U., 1990. *Berechnung von Fliesslawinen. Eine Anleitung für Praktiker mit Beispielen.* Davos, Switzerland: Swiss Federal Institute for Snow and Avalanche Research (SLF).

Salm, B. & Gubler, H., 1985. Measurement and analysis of the motion of dense flow avalanches. *Annals of Glaciology,* **6**, 26–34, DOI 10.3189/1985AoG6-1-26-34.

SLF, 1999. *Neue Berechnungsmethoden in der Lawinengefahrenkartierung [New calculation methods in avalanche hazard mapping].* Davos, Switzerland: Swiss Federal Institute for Snow and Avalanche Research (SLF).

SLF, 2017. *RAMMS::AVALANCHE User Manual.* Davos, Switzerland: WSL Institute for Snow and Avalanche Research SLF.

Teufen, B., 2005. *Rekonstruktion eines sehr ungewöhnlichen Lawinenereignisses: Kandersteg, Üschene, Februar 1999 [Reconstruction of a very unusual avalanche event: Kandersteg, Üschene, February 1999].* URL: http://snf.ngi.no/reports/teufen_Bericht_Ueschene_1999.pdf.

Appendix A   Brief description of MoT-Voellmy

The code MoT-Voellmy, created at NGI in 2011/2012 and modified since, is a simple model for simulating the motion of dense snow avalanches over curved terrain. With a suitable choice of the friction parameters, it can also be applied to rock avalanches and submarine debris flows. Like most models of gravity mass flows presently in use, MoT-Voellmy uses depth-averaging, i.e., it reduces the computational effort by one to two orders of magnitude by describing the flow in terms of the local flow depth $h(x, y, t)$ and the average velocity across the flow depth, $\overline{\boldsymbol{u}}(x, y, t) = \frac{1}{h(x,y,t)} \int_0^{h(x,y,t)} \boldsymbol{u}(x, y, z, t)$.

MoT-Voellmy assumes the terrain topography to be in a local Euclidean (typically UTM) coordinate system (X, Y, Z), with Z in the vertical direction and formatted as a standard ESRI ASCII Grid raster file as used in GIS applications. For meaningful simulations, the grid spacing should be in the range 2–10 m; in coarser grids, dynamically relevant terrain features are lost, whereas the snow cover smoothens the terrain roughness present in finer grids. From this input data, the program derives a curved, non-orthogonal coordinate system (x, y, z) in which the surface $z = 0$ follows the terrain. When projected vertically on the (X, Y)-plane, the coordinate lines $(x, y = \text{cst.}, z = 0)$ and $(x = \text{cst.}, y, z = 0)$ coincide with the X- and Y-coordinate lines, respectively. The z-direction is perpendicular to the local tangent plane to the surface. MoT-Voellmy calculates the metric tensor and the curvature tensor on the curved surface $z = 0$ to compute the norm of the velocity vector and centrifugal forces correctly. The length of the vector $\overline{\boldsymbol{u}}$ must be calculated as

$$\overline{\boldsymbol{u}}^2 = G_{xx} \overline{u}_x^2 + G_{yy} \overline{u}_y^2 + 2 G_{xy} \overline{u}_x \overline{u}_y, \tag{4}$$

and the apparent gravitational acceleration in the bed-normal direction, g_z', is

$$g_n' = g_z + \kappa_{\boldsymbol{u}} \overline{\boldsymbol{u}}^2, \tag{5}$$

with $\kappa_{\overline{\boldsymbol{u}}}$ the surface curvature in the direction of $\overline{\boldsymbol{u}}$.

The governing equations are the (depth-averaged) balance equations of mass and momentum on the curved surface:

$$\partial_t(\rho h) + \boldsymbol{\nabla}_{||} \cdot (\rho h \overline{\boldsymbol{u}}) = q_e, \tag{6}$$

$$\partial_t(\rho h \overline{\boldsymbol{u}}) + \boldsymbol{\nabla}_{||} \cdot (\rho h \overline{\boldsymbol{u}\boldsymbol{u}}) = -\boldsymbol{\nabla}_{||}\left(\tfrac{1}{2}\rho g_n' h^2\right) + \rho \boldsymbol{g}_{||} h - \boldsymbol{\tau}_b. \tag{7}$$

The gradient operator $\boldsymbol{\nabla}_{||}$ acts only in the x- and y-directions. The flow density, ρ, is considered constant in this model—an unrealistic assumption, but a major simplification presently applied in almost all snow avalanche models. q_e is the mass entrained from the snow cover per unit time and unit area, and $\boldsymbol{\tau}_b$ is the bed shear stress (acting in the tangent plane). The first equation states that the rate of change of the avalanche mass in a fixed infinitesimal column perpendicular to the terrain (the first term) is equal to the mass entrainment rate from the snow cover (the third term) minus the difference between the mass outflux and influx through the lateral boundaries of the column (second term). Similarly, the first term in Eq. (8) is the rate of momentum change in the infinitesimal

column and the second term the difference between lateral outflux and influx of momentum. Acceleration due to the gradient of the normal stresses (modelled as hydrostatic pressure $\int_0^h \rho\, g_n'(h-z)\mathrm{d}z = \frac{1}{2}\rho g_n' h^2$) is described by the first term on the right-hand side of Eq. (8). The next term is the driving force due to gravity, while the last term contains the effects of friction along the snow-cover–avalanche interface. As the name of the model indicates, the Voellmy friction law is assumed:

$$\boldsymbol{\tau}_b = -\frac{\overline{\boldsymbol{u}}}{|\overline{\boldsymbol{u}}|}\rho(\mu g_n' h + k\overline{\boldsymbol{u}}^2) \qquad (8)$$

μ and k are the dimensionless coefficients of Coulomb friction and "turbulent" drag, respectively. Note that centrifugal forces proportional to $\overline{\boldsymbol{u}}^2$ lead to increased or decreased Couomb friction, cf. Eq. (6), and that other models like RAMMS::AVALANCHE use the dimensional parameter $\xi \equiv g/k$.

Notable features of MoT-Voellmy, rarely found in other models, are the following:

- ⌐ *Entrainment of the snow cover* can be included in the simulation. The entrainment rate depends on the shear strength of the snow cover, τ_c, the shear stress (9), and the velocity of the avalanche:

$$q_e = \begin{cases} 0 & \text{if } |\tau_b| \le \tau_c, \\ \dfrac{|\boldsymbol{\tau}_b| - \tau_c}{|\overline{\boldsymbol{u}}|} & \text{if } |\tau_b| > \tau_c. \end{cases} \qquad (9)$$

  This formula presents a dynamically consistent model of basal entrainment and yields plausible results with realistic values for the shear strength of new snow, but there is presently not enough experimental data to allow a stringent validation of the model.

- ⌐ *Braking effect of forest:* MoT-Voellmy does not explicitly calculate the flow around each tree but modifies the friction coefficients μ and k in each cell of the computational grid by amounts $\Delta\mu(\overline{u}, h, n \cdot D, \tau_c)$, $\Delta k(\overline{u}, h, n \cdot D, \tau_c)$, depending on the instantaneous values of the velocity and flow depth as well as the number of trees per unit area, *n*, and their average diameter, *D* (Issler et al., 2020). These functions are derived from laboratory experiments and numerical simulations of granular flows against a cylindrical obstacle. Again, there is little experimental data from snow avalanches available to validate this relatively simple model.

- ⌐ *Forest destruction:* Large avalanches flowing through a forest may destroy it completely and over large areas, e.g., (Issler, 2020). This will greatly reduce the braking effect of the forest for the parts of the avalanche arriving after the trees have been felled. MoT-Voellmy attempts to account for this by reducing *n* in the expressions for $\Delta\mu$ and Δk from its initial value n_0 to 0 according to

$$n(t) = n_0 \exp[-\lambda(t - t_c)] \qquad (10)$$

  as soon as the overturning or breaking moment exerted on the trees exceeds a critical value at some time t_c. The breaking moment as well as the decay constant λ increase with the tree diameter.

NGI

Appendix B   Outline of a probabilistic method for assessing the risk reduction due to afforestation

The discussions under the consortium meeting on Dec. 2, 2021 showed that a procedure for assessing the cost–benefit ratio of NBSs against natural hazards would be of great value. In such analyses, the estimation of risk reduction afforded by the NBS is a key factor on the benefit side. This case study at the Forêt du Capet allows to illustrate how the computations carried out could be extended to provide a quantitative risk analysis.

Denote the *expected annual loss* (of human lives, material or immaterial goods, expressed in suitable units) or *risk* at a given location without any mitigation measures by R_0, and let R_1, R_2, … be the corresponding expected annual losses after implementing specific mitigation measures. Then the *benefit* from mitigation measure i is given by $R_0 - R_i$. Quantifying the associated cost C_i is a different issue and will not be discussed here. The risk can be decomposed as a weighted *sum over scenarios S* for the considered hazard, where a scenario typically is associated with a specific *intensity I_S* of the hazardous event. Where the hazard is present in the study area, there may be objects at risk (persons, buildings and infrastructure, an archeological site, the beauty of an undamaged landscape, …). Each object j has an associated location x_j, *exposure E_j* indicating the fraction of the time when object j is present at x_j in the hazardous area ($E = 1$ for buildings and most infrastructure, $E \leq N$ if up to N persons can be present). Another central quantity is the *vulnerability $V_j(I_S)$*, which represents the expected loss (measured in suitable units) if object j is hit by an event of intensity I_S.

From these building blocks, the risk can be calculated as

$$R = \sum_S \sum_j P(S) E_j V_j(I_S). \tag{11}$$

$P(S)$ is the (annual) probability of scenario S occurring. In the case at hand, where snow avalanches are the only hazard considered, the sum over scenarios may be replaced by a sum or integral over the intensity. If we characterize the intensity by the maximum pressure, p_{max}, that the avalanche exerts on the object to, we may rewrite Eq. (12) as

$$R = \sum_j \int_0^\infty P_j(p_{max}) E_j V_j(p_{max}) \mathrm{d}p_{max}. \tag{12}$$

(For simplicity, p_{max} will be replaced by p in the following) The maximum pressure in an avalanche event varies strongly with location within the avalanche path; this is accounted for by using different PDFs P_j for different locations x_j. Depending on the type of object, the maximum load, $F_{max}(x_j)$, or the maximum moment, $M_{max}(x_j)$, may be more suitable quantities for measuring the avalanche intensity.

Specifying the exposures E_j typically is a task to be carried out by the stakeholder, who either has relevant information or wishes to define a specific situation. Regarding vulnerability, it may be useful to split this function up further: For buildings, the relative

vulnerability, i.e., the fraction of its monetary value or usefulness that is lost, depends mostly on the type of construction (from simple wood-frame building to reinforced concrete) while its original value W depends on many other factors like the size of the building. One may then set $V_j(p) = W \cdot v_j(p)$, with $v_j(p)$ ranging from 0 to 1. For persons inside buildings, the survival chance depends mainly on the degree to which the structure of the building retains voids free of debris and snow. This suggests expressing the vulnerability of persons as a function of the *degree of damage*, D, to the building. D, in turn, depends on both the type of building and the pressure p (Issler, 2020). Work is ongoing at NGI to improve preliminary estimates of the vulnerability of persons in buildings (Issler, et al., 2016) (Issler, 2020) and to estimate the pressure dependence of the vulnerability of relevant building types by means of structural simulations.

The remaining task is to obtain the PDFs of avalanche pressure at the locations x_j within the *study area*. The *process area* comprises the study area and all avalanche paths that might reach the study area. Assume that events with a return period up to T_t years should be considered. A possible approach consists of the following steps:

1. Find all potential release areas (PRAs) in the process area.
2. Depending on the size of the process area, generate synthetic daily weather and snow cover data corresponding to at least $100\ T_t$ winters, either for the process area as a whole or, if the process area is large and has large altitude differences, for each PRA. How this can be done, depends on the availability of nivo-meteorological data. In most cases data from different (near-by) meteorological stations must be interpolated. Unless there are measurements over a period $T \gtrsim T_t/3$, there will be significant uncertainty regarding the tail of the distribution.
3. For each "synthetic day" in each PRA, check whether the snow cover is stable or not and count the unstable situations. If an avalanche is predicted, calculate the minimum slab thickness for instability and record it.
4. For each release event (or for a random sample of at least ~100 events), determine the corresponding release depth and the friction values for the flow, following an appropriate PDF, which preferably is correlated with the (synthetic) nivo-meteorological data that produced this "event".
5. Simulate this "event" with a suitable dynamical run-out model and record, for each object location j, the maximum impact pressure $p_{max}(x_j)$, the maximum load $F_{max}(x_j)$, or the maximum moment, $M_{max}(x_j)$, depending on how the vulnerability function of the object is formulated.
6. For each object location j, appropriately weight each simulated event and extract the PDFs for maximum impact pressure, load or moment at x_j.
7. Compute the resulting probability distribution of the degree of damage of the object and then, for buildings, the probability distribution of severe injury or death for their inhabitants.
8. Finally, use the exposure data to compute the expected losses.

The code NAKSIN (Nye AktsomhetsKart for Snøskred I Norge = New snow-avalanche susceptibility maps for Norway) implements most aspects of steps 1–5 using nivo-meteorological and forest data that is openly accessible for the entire country (Issler, et al., 2020). Some modifications would be necessary, however:

⌐ If the nivo-meteorological time series used by NAKSIN cannot be obtained for the study area, they either must be generated artificially based on expert assessment of the local conditions, or useful proxies must be found.

⌐ Instead of simulating only a single avalanche run-out per PRA, with parameters corresponding to an event with the selected target return period T_t, all the samples predicting a release should be simulated. (To keep the number of run-out calculations manageable, a subset should be randomly selected for PRAs with high release probability.)

⌐ For each selected "event", the friction parameters for the run-out calculation must be chosen randomly, but they should correlate with the nivo-meteorological conditions of this sample.

⌐ The values of p_{max}, F_{max} and/or M_{max} at the object locations x_j must be extracted and stored.

⌐ Routines for extracting the PDFs of interest must be included.

⌐ To make the approach more realistic, an algorithm for finding the subarea of the PRA that has highest release probability under the given conditions of each synthetic event should be developed and implemented.

For future reference, some technical issues that will arise in the implementation of the procedure outlined above are briefly discussed below:

⌐ Under the simplifying assumption that the avalanche density is constant (a value $\rho_f = 250\,\mathrm{kg\,m^{-3}}$ appears reasonable), the maximum impact pressure at the location x_j in each run-out simulation is approximated by the formula

$$p_{max}(x) \approx \frac{1}{2} C_d \rho_f \bar{u}_{max}^2(x) + \frac{1}{2} \rho_f g [h_s(x) + h_f(x)], \qquad (13)$$

where C_d is the drag coefficient of the object hit by the avalanche, h_s is the snow height, and h_f is the height of the avalanche flow. For cylindrical objects like trees or pylons, one may use $C_d \approx 1 + 5\,\mathrm{Fr}^{-2}(x)$, with the Froude number given by $\mathrm{Fr} = \bar{u}/\sqrt{gh}$. For objects like houses that are much wider than the flow depth, $C_d \gtrsim 2$ appears more appropriate.

⌐ If the annual release probability of the avalanche path is P_{rel}, and a total of N simulations have been carried out, an epoch of duration $T = N/P_{rel}$ has been simulated. The *cumulative PDF* of impact pressure at location x_j is then obtained by sorting the simulations in descending order with respect to the rank, $s = 1, 2, \ldots, N$, of their maximum pressures $p_{max}(x_j, s)$, i.e.,

$$p_{max}(x_j, 1) > p_{max}(x_j, 2) > \ldots > p_{max}(x_j, N). \qquad (14)$$

The annual probability of $p \geq p_{max}(x_j, s)$ is then

$$P_j(p) = \frac{s \cdot P_{rel}}{N}. \qquad (15)$$

If $p \geq p_{max}(x_j, 1)$, one may set $s = 0$ in this formula to obtain $P_j(p) = 0$.

⌐ Pressure maps for some design probability P_{design} (e.g., $0.01\,\mathrm{y^{-1}}$) are obtained by interpolating the cumulative PDFs of impact pressure at each object location to

find the pressure p_j for which $P_j(p_j) = P_{\text{design}}$. Such maps are important for land-use planning in countries where the maximum impact pressure for some P_{design} must not exceed some critical value in constructible areas.

- To obtain reliable information about the PDFs for $p_{\max}(x_j)$, many simulations with initial conditions and friction parameters distributed according to their respective PDFs must be carried out using Monte Carlo techniques. In the present case, there are five random input parameters: the release area A_f, the fracture depth d_f averaged over the area, the shear strength of the snow cover τ_c, and the friction parameters μ and k. One would then need about $20^5 \approx 3 \cdot 10^6$ simulations. One can, however, lessen the computational burden by (i) imposing correlations between some of the parameters and (ii) using Latin Hypercube Sampling (LHS). For the snow-cover shear strength, the value used in the stability calculation may be used; a fixed relation $k(\mu)$ appears plausible. The size of the release area, A_f, is obtained from the calculation of release probability in advanced models or can be expressed as a function of the fracture depth, d_f to be correlated as $A_f = F(d_f)$, where F is a monotonically increasing function of d_f. In LHS, each dimension of the parameter space is divided into M intervals with equal probability $1/M$ according to the respective PDF. M quasi-random samples are generated such that each interval in each parameter-space dimension is populated exactly once.

- Despite the good results that can be obtained with relatively few Monte Carlo samples if LHS is used, it is still important to use a highly efficient flow-simulation code tightly integrated with the LHS sampling to achieve a practically usable tool. To this end, MoT-Voellmy was extended to read a list of M parameter-value samples generated by a simple yet flexible Python script and to run M simulations with these parameter sets in a user-specified number of parallel processes. This code can be developed further to implement more of the features mentioned above.

Kontroll- og referanseside/ Review and reference page

Dokumentinformasjon/*Document information*		
Dokumenttittel/*Document title*		**Dokumentnr./***Document no.*
Assessment of the Effectiveness of Afforestation as a Nature-Based Solution Against Snow Avalanches in the Forêt du Capet, French Pyrenees		20180404-02-TN
Dokumenttype/*Type of document*	**Oppdragsgiver/***Client*	**Dato/***Date*
Teknisk notat / Technical note	European Commission, Horizon2020 Program	2022-02-16
Rettigheter til dokumentet iht kontrakt/ *Proprietary rights to the document according to contract*		**Rev.nr.&dato/***Rev.no.&date*
Oppdragsgiver / Client		0 /
Distribusjon/*Distribution*		
FRI: Kan distribueres av Dokumentsenteret ved henvendelser / FREE: Can be distributed by the Document Centre on request		
Emneord/*Keywords*		
Nature-Based Solutions, Afforestation, Snow avalanches, Numerical simulation		

Stedfesting/*Geographical information*	
Land, fylke/*Country*	**Havområde/***Offshore area*
France	
Kommune/*Municipality*	**Feltnavn/***Field name*
Barèges, Hautes-Pyrénées	
Sted/*Location*	**Sted/***Location*
Midaou gully	
Kartblad/*Map*	**Felt, blokknr./***Field, Block No.*
UTM-koordinater/*UTM-coordinates* Zone: East: North:	**Koordinater/***Coordinates* Projection, datum: East: North:

Dokumentkontroll/*Document control*

Kvalitetssikring i henhold til/*Quality assurance according to NS-EN ISO9001*

Rev/ *Rev.*	Revisjonsgrunnlag/*Reason for revision*	Egenkontroll av/ *Self review by:*	Sidemanns-kontroll av/ *Colleague review by:*	Uavhengig kontroll av/ *Independent review by:*	Tverrfaglig kontroll av/ *Interdisciplinary review by:*
0	Original document	2022-02-14 Dieter Issler	2022-02-10 Anders Solheim		

Dokument godkjent for utsendelse/ *Document approved for release*	Dato/*Date*	Prosjektleder/*Project Manager*
	16 February 2022	Amy M. P. Oen

NGI (Norwegian Geotechnical Institute) is a leading international centre for research and consulting within the geosciences. NGI develops optimum solutions for society and offers expertise on the behaviour of soil, rock and snow and their interaction with the natural and built environment.

NGI works within the following sectors: Offshore energy – Building, Construction and Transportation – Natural Hazards – Environmental Engineering.

NGI is a private foundation with office and laboratories in Oslo, a branch office in Trondheim and daughter companies in Houston, Texas, USA and in Perth, Western Australia

www.ngi.no

NGI OSLO
TRONDHEIM
HOUSTON
PERTH